



HAL
open science

Production of biocarbon catalysts for NO_x decomposition, WGS and RWGS

Théodore Graul

► **To cite this version:**

Théodore Graul. Production of biocarbon catalysts for NO_x decomposition, WGS and RWGS. Chemical and Process Engineering. Ecole des Mines d'Albi-Carmaux, 2023. English. NNT : 2023EMAC0017 . tel-04813435

HAL Id: tel-04813435

<https://theses.hal.science/tel-04813435v1>

Submitted on 2 Dec 2024

HAL is a multi-disciplinary open access archive for the deposit and dissemination of scientific research documents, whether they are published or not. The documents may come from teaching and research institutions in France or abroad, or from public or private research centers.

L'archive ouverte pluridisciplinaire **HAL**, est destinée au dépôt et à la diffusion de documents scientifiques de niveau recherche, publiés ou non, émanant des établissements d'enseignement et de recherche français ou étrangers, des laboratoires publics ou privés.

Université Fédérale



Toulouse Midi-Pyrénées

THÈSE



IMT Mines Albi-Carmaux
École Mines-Télécom

En vue de l'obtention du

DOCTORAT DE L'UNIVERSITÉ DE TOULOUSE

délivré par

IMT – École Nationale Supérieure des Mines d'Albi-Carmaux

présentée et soutenue par

Théodore GRAUL

le 5 décembre 2023

Titre :

**Production of biocarbon catalysts for
NO_x decomposition, WGS and RWGS**

École doctorale et discipline ou spécialité :

MEGEP : Génie des procédés et de l'environnement

Unité de recherche :

Centre RAPSODEE, UMR CNRS 5302, IMT Mines Albi

Directeur de thèse :

Ange NZIHOU, Professeur, IMT Mines Albi

Autres membres du jury :

Marco BARATIERI, Professeur, Free University of Bozen/Bolzano, Italie, Rapporteur

Roger GADIOU, Professeur, IS2M, Rapporteur

Catherine AZZARO-PANTEL, Professeure, ENSIACET, Présidente

Pascal FONGARLAND, Professeur, CPE Lyon, Examineur

Laurent VAN DE STEENE, Ingénieur de Recherche, CIRAD Montpellier, Examineur

María GONZÁLEZ MARTÍNEZ, Maître-assistante, IMT Mines Albi, Encadrante

Typhaine FOX, Directrice, EIZHY, Invitée

Acknowledgments

I would like to first begin by saying a massive thank you to everyone who took part in this adventure with me. I'm sure I'll forget some names here but I won't forget nor the faces of the people who helped me see this to the end neither what you represent to me.

First and foremost, thank you Ange and María, for directing and supervising this research work for the past 3 years (and a half). Most importantly, thank you for giving me this opportunity and the many yet to come. Thank you for lifting me up and helping me achieve this project. And I don't want to say till its end because it looks like there is still a lot of work coming out of the thesis (Sorry both of you, it seems you'll be quite occupied! But I'll try and help where I can and I hope and know we'll still work together!).

I would like to also thank the jury for your presence and attention during the review of the thesis and the defence. You have seen and acknowledged the importance of our work. You have even given various aspects to work on that will amplify the scope of this work. I can't wait to see the outcomes and I think it is the same for you! Thank you again for your insight.

Thank you Typhaine and Eizhy and the European H2020 Mobile Flip project for it is thanks to you that this thesis came so far. The choice and reception of biomass was quite difficult in this project and you made this difficulty easier to bare. Going forward, the team will be working hard on the topic of the thesis as we have managed to show the potential of your multifaceted bioresources. Thank you in advance for continuing to collaborate with them! And thank you once more for your help!

Speaking of the team, un grand merci à Alex, Antoine, Céline, Christine, Denis, Isabelle, Jean-Marie, Jenny, Laurent, Louise, Michaël, Pierre, Séverine, Sylvie et Teresa! Vous m'avez toujours prêté une oreille et même vos mains quand j'avais des questions ou des problèmes, et c'est grâce à vous que la thèse a pu battre son plein. Même en dehors de la thèse, vous avez enrichi ma culture scientifique et générale (et aussi culinaire!). Et ce n'est pas que moi! Vous avez été et êtes là aussi pour toutes les générations passées et à venir de chercheurs de toute âge, et on ne saura jamais assez vous remercier pour votre aide. (Et aussi, j'espère qu'on vous payera les TP, c'était bien l'ATG en tant qu'étudiant avec Céline et Doan).

Merci à l'équipe de chercheurs avec qui j'ai pu beaucoup partagé de connaissances (et pour certain du chocolat!), enseigné, et discuté d'aspects qui vont au-delà de la thèse comme les post-doc et les postes d'enseignant-chercheur. Et parlé manger. Merci beaucoup Dimitri, Doan, Elsa, Fabienne, Fabien, Javier, Jean-Jacques, Marion, Nathalie, Patricia, Rachel, Suênia, Thomas, Vincent et Yasmine.

En parlant de personnes que j'embête un peu trop (ou pas assez!), je souhaite vous remercier énormément Chrystel, Marie et Valérie. J'ai adoré discuter avec vous trois et merci sincèrement de nous dépanner à chaque fois avec Sirepa, GED, les stagiaires, la thèse, ... Sur beaucoup d'aspects. Avec les techniciens, sans vous, on n'arrivera pas aussi loin. Merci beaucoup ! (D'ailleurs Chrystel si ton fils veut toujours aller à Madrid n'hésite pas à lui passer mes infos 😊.)

Et là, c'est la partie où je m'excuse. Je suis quasiment sûr que je vais oublier quelqu'un. Si c'est le cas, on peut négocier en chocolat ? En tous cas (et pour toutes les personnes oubliées ou non), merci énormément à mes collègues de travail, de bureau, de repas, de congrès, d'alcool, de bus, [Longum est index]. Je souhaite vous remercier mais aussi vous encourager dans vos entreprises. Vous êtes géniaux et le fruit de vos travaux ne peuvent qu'égaliser votre grandeur/génialité (oui c'est un mot). I'll say it in English to guarantee it's understood. To all my colleagues past and present: you are amazing and the result of your labor will be the reflection of your own greatness. Thank you very much and I'll make sure not to forget you all, Abdu, Abdul, Ahmed, Aissatou, Akaber, Alejandro, Amal, Amel, Ben, Bénit, Brenda, Canio, Carla, Carlos, Charles, Damien, Eli, Emmanuel, Floriane, Freda, Gloria, Guillaume, Hamado, Houssein, Huan, Huyn, Isis, Jean-Régis, Jenny, Julien, João, Kaitlyn, Keji, Khadija, Layde, Lina, Ludovic, Malek, Manel, Manon, Sister Maria, Marie, Marie-Anne, Maroua, Maxime, Mohamad, Morgane, Mu, Nafissatou, Najib, Petros, Rémi, Salomé, See Leng, Séverin, Shamala, Sherin, Théotime, Thomas, Uriel, Valentin, Vincent, Yasmine, Yi, Zac et Zili.

Je souhaite enfin remercier mes « petits », mes amis et ma famille. C'est à vous que je dédis ce manuscrit. Vous que j'ai vu grandir et pour certaines qui m'ont vu grandir (je pense à vous Albane, Amandine, Arielle, Cass, Clément, Joris, Manon) pendant et avant la thèse. Il faudrait que je trouve une façon de vous remercier pour votre soutien au cours de ces trois dernières années (et plus). Pour les petits, préparez-vous pour le Gala 😊! Et finalement, pour ma famille, Louis et ma famille étendue, merci d'avoir été là pour ces trois dernières années et de m'avoir aidé à respirer quand il y en avait besoin et à me faire découvrir et à me pousser à aller plus loin que la thèse.

Merci à tous, merci pour cette expérience, merci pour le livre de recette grâce auquel je vais pouvoir garder une partie d'Albi peu importe où j'irai y compris dans cette nouvelle aventure à Madrid à l'UC3M.

Merci encore une fois, énormément et sincèrement! J'espère vous revoir bientôt!

Table of contents

Acknowledgments	3
Table of contents	5
List of abbreviations	9
Résumé long	10
R.I. Introduction	10
R.1. Matériel et méthodes	11
R.2. NO _x decomposition using Ni- and Fe-loaded biocarbon	13
R.3. Nickel and iron-doped biocarbon catalysts for reverse water-gas shift	15
R.4. Nickel and iron biocarbon catalysts for water-gas shift reaction	16
R.CP. Conclusions et perspectives	18
Introduction	21
I.1. Thermochemical conversion of bioresources	21
I.2. Catalysis by metals in conversion processes; biomass, biocarbon and inherent metals	24
I.3. Objective of the thesis	29
References.....	30
Chapter 1	34
Materials and Methods.....	34
1.1. Introduction	34
1.2. Preparation of catalysts	34
1.3. Characterization of catalysts.....	40
1.3.1. Ultimate analysis: CHNS and ICP.....	40
1.3.2. Moisture and ash Content	42
1.3.3. TGA-DSC: Thermal stability and regenerability	44
1.3.4. Adsorption-desorption isotherms: specific surface area and pore type	46
1.3.5. Microscopy: dispersion and phases of metals, structure and porosity of biocarbon surface.....	47
1.3.6. TPX: Gas adsorption and surface groups	48
1.3.7. XRD: main organic and inorganic speciation	51
1.3.8. Summary	51

1.4. Direct decomposition of NO _x	52
1.5. WGS and rWGS experiments	57
1.6. Thermodynamic and process modelling.....	61
1.7. Conclusion	62
References.....	64
Chapter 2	67
NO _x decomposition using nickel and iron-loaded biocarbon	67
2.1. Introduction	68
2.1.1. NO decomposition mechanisms	68
2.1.2. Biocarbon for NO decomposition	70
2.1.2.1. Biocarbon structure.....	70
2.1.2.2. Biocarbon metallic elements.....	70
2.1.3. Objective of this study	71
2.2. Materials and methods	72
2.2.1. Preparation of biocarbon catalysts.....	72
2.2.2. deNO _x experiments	73
2.2.3. Characterization techniques	75
2.3. Results and discussion	75
2.3.1. Biocarbon characterization	75
2.3.1.1. Elemental composition.....	75
2.3.1.2. Surface characterization.....	77
2.3.2. deNO _x experiments	79
2.3.2.1. deNO _x performance, NO analysis.....	79
2.3.2.1.a. Effects of temperature	80
2.3.2.1.b. Effects of biomass	81
2.3.2.1.c. Effects of impregnated metals	81
2.3.2.1.d. Effects of metal content	82
2.3.2.1.e. Catalyst deactivation	83
2.3.2.2. deNO _x performance, N ₂ analysis	84
2.3.2.3. Other gases.....	85
2.4. Conclusions	88
References.....	90

Chapter 3	95
Nickel and iron-doped biocarbon catalysts for reverse water-gas shift.....	95
3.1. Introduction	96
3.1.1. Pyrolysis for biocarbon production.....	97
3.1.2. The effect of inorganic elements in RGWS	99
3.1.2.1. Alkali metals	99
3.1.2.2. Alkaline-earth metals	100
3.1.2.3. Transition metals.....	101
3.1.2.4. Lanthanides	104
3.1.2.5. Post-transition metals	104
3.1.2.6. Metalloids and nonmetals.....	105
3.1.2.7. Synergies between inorganic elements	105
3.2. Materials and methods	107
3.2.1. Preparation and utilization of the biocarbon catalysts	107
3.2.1.1. Production of biocarbon catalysts	107
3.2.1.2. Utilization of biocarbon catalysts in RWGS	109
3.2.2. Performance of the biocarbon catalysts.....	111
3.3. Experimental results	111
3.3.1. Performance of the biocarbon catalysts for RWGS	111
3.3.1.1. Type of bioresource.....	113
3.3.1.2. Inorganic elements.....	114
3.3.1.3. Surface properties and functional groups.....	117
3.3.2. Comparison with other catalysts	122
3.3.2.1. Rust and Fe-doped alumina	123
3.3.2.2. Influence of the pre-reduction stage	124
3.3.2.3. Influence of a long residence time	124
3.4. Conclusion and perspectives.....	125
References.....	127
Chapter 4	135
Nickel and iron biocarbon catalysts for water-gas shift reaction	135
4.1. Introduction	136
4.1.1. Operating conditions for WGS and their impact	137

4.1.1.1. Catalysts & kinetic parameters	137
4.1.1.2. Temperature.....	141
4.1.1.3. Pressure	142
4.1.1.4. Gas hourly space velocity and contact time	142
4.1.1.5. Steam/carbon ratio	142
4.1.1.6. Reactor configuration.....	143
4.1.1.7. Summary of the impact of operating conditions on WGS	144
4.2. Materials and methods	147
4.2.1. Preparation and utilization of the biocarbon catalysts	147
4.2.2. Performance of the biocarbon catalysts.....	149
4.3. Biocarbon-catalyzed WGS results: simulation, test and impact of variation of temperature and water partial pressure.....	149
4.3.1. Kinetic and thermodynamic simulations of WGS reaction conditions.....	149
4.3.1.1. Setting gases preheating temperature prior WGS reactor	150
4.3.1.2. Kinetic and thermodynamic simulations of the WGS reaction.....	152
4.3.2. WGS reaction	156
4.3.2.1. Influence of the temperature.....	156
4.3.2.2. Influence of the steam excess	159
4.3.2.3. Reaction performances	160
4.3.2.4. Kinetic parameters	162
4.4. Conclusion and perspectives.....	165
References.....	166
General conclusion.....	171
Perspectives.....	174
Appendix A	176
Non-retained biocarbon: preparation and characteristics.....	176
A.1. Operating conditions, description and initial choice.....	176
A.2. Conclusion.....	179
References.....	179
List of figures	180
List of tables.....	182

List of abbreviations

BC: biocarbon, understood as biochar
RF: raw fern biocarbon
FNI: fern biocarbon impregnated with Ni
FFe: fern biocarbon impregnated with Fe
RW: raw willow biocarbon
WNI: willow biocarbon impregnated with Ni
WFe: willow biocarbon impregnated with Fe
FNiFe: fern biocarbon impregnated with both Ni and Fe
FNI*: fern biocarbon impregnated with different Ni content than FNI
FFe*: fern biocarbon impregnated with different Fe content than FFe

BET: Brunauer–Emmett–Teller
BM: biomass
cat.: catalyst
CHNS: carbon, hydrogen, nitrogen, sulfur elemental content
DeNO_x: NO_x decomposition
Eq.: equation
FTS: Fischer-Tropsch synthesis
GHG: green-house gas
GHSV: gas hourly space velocity
HyPr-RING: hydrogen production by reaction integrated novel gasification
ICP-AES: Inductively coupled plasma atomic emission spectroscopy
IWI: insipient wetness impregnation
L–H: Langmuir–Hinshelwood
P: pressure
pr.: promoter
PR-BM: Peng Robinson – Boston Mathias
r: kinetic rate
RDS: rate determining step
RSD: relative standard deviation
RWGS: reverse water-gas shift reaction
S: selectivity
S/C or CO: steam to carbon or carbon monoxide ratio
SCR: selective catalytic reduction
SEM: scanning electron microscopy
sup.: support
T: temperature
TEM: transmission electron microscopy
TGA-DSC: thermogravimetric analysis – differential scanning calorimetry
TPD: temperature programmed desorption
TPO: temperature programmed oxidation
TPR: temperature programmed reduction
 \dot{V} : volumetric flow
WGS: water-gas shift
WI: wetness impregnation
X: conversion
XRD: X-ray diffraction

Résumé long

R.I. Introduction

Les émissions de gaz à effet de serre (GES) doivent impérativement être réduites afin respecter les Accords de Paris (2015) signés par 195 pays, dont l'objectif est d'empêcher le dépassement du réchauffement climatique de 2°C. Ceci concerne surtout le dioxyde de carbone (CO₂) et le méthane (CH₄) mais aussi d'autres gaz qui appartient à la famille des oxydes d'azote (NO_x), comme le protoxyde d'azote (N₂O), qui impactent la santé en plus de l'environnement. L'hydrogène (H₂) vert, produit de manière neutre en carbone par thermoconversion des bioressources, peut contribuer significativement à la transition énergétique et écologique. Le traitement des émissions des procédés de thermoconversion est aussi crucial pour ce but, incluant la conversion des NO_x formés dans les procédés oxydants utilisant de l'air à haute température. Ces procédés opérant sous l'effet de la chaleur requièrent des catalyseurs pour en limiter le besoin et les coûts associés. Les métaux catalytiques utilisés sont essentiellement des métaux nobles, de transition ou post-transition. Ces métaux sont généralement coûteux et peu respectueux de l'environnement en raison de leur rareté et des procédés employés pour les extraire du milieu naturel. Il existe toutefois des moyens de prélever du sol des métaux catalytiques écologiquement et à faible coût : la phytoremédiation. Les plantes de phytoremédiation extraient les métaux du sol par adsorption au cours de leur croissance. Certaines espèces dites hyperaccumulatrices développent des capacités extraordinaires d'extraction de ces métaux (jusqu'à plus de 1%*m*). Leur traitement thermique permet ensuite une exposition et dispersion de ces métaux dans la structure carbonéuse obtenue (biocarbonate). Cette structure, qui agit comme support biosourcé du catalyseur, présente des propriétés favorisant leur action, notamment de fortes surfaces spécifiques ou de la basicité de surface avec fonctions oxygène (O) réductibles.

Dans ce contexte, l'objectif de cette thèse est la production de catalyseurs biosourcés riches en métaux catalytiques pour des applications dans les domaines de l'énergie et de l'environnement. Dans notre cas, l'étude a porté sur la réaction de gaz à l'eau directe et inverse (WGS et RWGS, respectivement) et la décomposition directe de NO_x (deNO_x). Les catalyseurs biosourcés produits seront caractérisés en détail et testés dans les applications sélectionnées, dont les dispositifs expérimentaux ont été mis au point et optimisés au cours de cette thèse, afin de relier les propriétés catalytiques de ces matériaux aux mécanismes associés à ces transformations. Ceci promeut une approche d'économie circulaire sur la réutilisation des plantes de phytoremédiation pour produire des catalyseurs biosourcés, respectueux de l'environnement, pour la conversion de gaz en vecteurs énergétiques et la destruction de polluants comme les NO_x.

R.1. Matériel et méthodes

Les biosources choisies pour cette étude sont la fougère et le saule, des plantes utilisées en phytoremédiation. A leur réception, ils ont été broyés à granulométrie connue (10 et 6 mm respectivement). Ils ont ensuite été pyrolysés sous N_2 suivant une chauffe lente à $2^\circ C/min$ dès la température ambiante à $800^\circ C$, suivi d'un palier d'une heure à $800^\circ C$, dans un four carbolite. Les deux biomasses ont été imprégnées avant ou après pyrolyse par voie humide avec de fortes teneurs en nitrates de fer (Fe) ou de nickel (Ni) afin d'imiter l'hyperaccumulation et de mettre particulièrement en valeur le rôle de ces métaux. La température maximale de pyrolyse a été déterminée par simulation thermodynamique de la pyrogasification de la fougère avec FactSage, de manière à maximiser la rétention des espèces métalliques présentant un effet catalytique. L'analyse thermogravimétrique (ATG) a permis de déterminer la vitesse de chauffe garantissant le régime chimique pour la production de biocarbone. La vitesse de chauffe la plus faible respectant ce critère a été choisie afin de permettre le développement maximal de la porosité et de la surface spécifique du biocarbone. Les biocarbones produits ont ensuite été broyés et tamisés afin de déterminer leur granulométrie ($<125 \mu m$).

Les biocarbones se sont montrés stables jusqu'à $500^\circ C$ via les analyses ATG, avec une très faible perte de masse sous 24h ($<10 \% m$). La composition organique des biocarbones a été obtenue par combustion flash (CHNS, Flash 2000) de la matière organique du biocarbone résultant en la production d'azote, de dioxyde de carbone, de vapeur d'eau et de dioxyde de soufre (N_2 , CO_2 , H_2O et SO_2 respectivement). Ces gaz ont été séparés, identifiés et étalonnés au préalable. La composition inorganique a été déterminée par spectrométrie optique d'émission atomique à plasma à couplage inductif (ICP-OES). Le biocarbone a été minéralisé auparavant et introduit au niveau d'un plasma où pour un élément atomique donné correspond une longueur d'onde. A cette longueur d'onde et en étalonnant les intensités correspondantes à des solutions de concentration connue, on peut déterminer la quantité de métal dans la solution de biocarbone minéralisé. Les biocarbones de saule tendent à avoir plus d'éléments organiques, tandis que les biocarbones de fougère sont plus riches d'éléments inorganiques, effet qui est renforcé par l'imprégnation. Les teneurs en humidité et en cendres des biocarbones ont été déterminées à travers un analyseur d'humidité et par ATG sous air. Ceci a confirmé la forte présence d'espèces inorganiques dans les biocarbones de fougère.

Les isothermes d'adsorption-désorption de N_2 ont permis de calculer les surfaces spécifiques et d'identifier le possible type de porosité des biocarbones. En l'occurrence, le type semblait être II selon la classification de l'IUPAC, correspondant à des adsorbants non poreux ou macroporeux, alors que la présence d'hystérèse semble indiquer la possible présence de micropores. La microscopie électronique à balayage et à transmission a permis d'identifier la présence de phases métalliques et leur dispersion. La diffraction de

rayons X (DRX) permet d'informer davantage sur les phases cristallines majoritaires et donc sur la spéciation des métaux si détectés. Un programme de désorption, oxydation et réduction, en utilisant respectivement de l'ammoniac (NH_3), du CO_2 et du H_2 , en température a permis de déterminer le type de fonctions de surface selon le gaz introduit, leur quantité selon le volume de gaz adsorbé, et la force d'adsorption des fonctions selon la température maximale de pic. En combinaison avec un programme de désorption sous He, en analysant les gaz produits grâce à un μGC couplé et en se basant sur des valeurs rapportées, il est possible de déterminer la nature des fonctions de surface. Des tests sur la réutilisation des catalyseurs ont été effectués par ATG à calorimétrie différentielle à balayage (DSC) pour observer la désorption de gaz possiblement adsorbés.

Les catalyseurs biosourcés ont été testés en deNO_x en observant l'influence de la présence du catalyseur et de la température sur la décomposition du monoxyde d'azote (NO) dilué dans de l'argon (Ar). Ils ont été introduits dans un réacteur à lit fixe et courant descendant chauffé par un four Heraeus (**Fig. 1.12**). Les gaz produits sont nettoyés de goudrons et d'humidité à l'aide de trois barboteurs avant d'être analysés en μGC et par un analyseur de NO_x . La température maximale étudiée ne dépasse pas celle de stabilité obtenue par ATG (500°C). L'efficacité des catalyseurs a été exprimé en fonction d'un taux de réduction de NO .

Les catalyseurs ont aussi été testés en RWGS en introduisant H_2 et CO_2 dilués dans Ar , dans un réacteur sous pression à lit fixe à courant descendant et chauffé par un four carbolite (**Fig. 1.15**). Le gaz produit est privé d'eau grâce à une combinaison de condensation et piège à gel de silice pour ne pas endommager le μGC qui permet l'analyse de ces gaz. La température d'étude a été choisie (400°C) afin d'être dans des conditions de Fischer-Tropsch à haute température sans dépasser la stabilité du catalyseur. Deux campagnes ont été réalisées et la configuration expérimentale a été améliorée afin d'intégrer l'analyse continue par μGC des gaz et faire un meilleur suivi de la réaction. Les catalyseurs les plus actifs en RWGS (fougère) ont enfin été testés en WGS en introduisant H_2O et CO dilués dans Ar , dans le même réacteur que celui de RWGS. La température de préchauffe et la réaction ont été simulées par Aspen Plus. Pour la suite, l'influence de la température et du débit d'eau a été étudiée en présence des catalyseurs.

Les deux installations pour deNO_x et pour WGS/RWGS ont été développées, mises au point et optimisées au cours de cette thèse. Une de leur originalité est de permettre une quantification continue des gaz produits afin de décrire en détail les mécanismes associés à ces transformations. Elles constituent une avancée fondamentale dans le plateau expérimental et analytique du Centre RAPSODEE et servent déjà de référence dans des travaux en cours et futurs.

R.2. NO_x decomposition using Ni- and Fe-loaded biocarbon

La décomposition des oxydes d'azote (NO_x) passe principalement par la réaction de décomposition directe du monoxyde d'azote (NO), gouvernée par les mécanismes de Langmuir-Hinshelwood et d'Eley-Rideal. Les catalyseurs commerciaux, dont une révision bibliographique a été faite dans le chapitre correspondant, sont coûteux et peuvent requérir des fortes températures d'utilisation. Ainsi, les catalyseurs biosourcés présentent un intérêt catalytique et commencent à être utilisés pour la décomposition de NO_x (deNO_x) sans agents réducteurs comme l'ammoniac. Pour pouvoir être actif pour cette réaction, la préparation du catalyseur biosourcé est cruciale. Elle permet le développement d'une surface spécifique suffisamment élevée dotée de groupes fonctionnels actifs pour permettre la participation à la réaction aux éléments métalliques qui la composent. Le mécanisme de réaction en présence de métal a été détaillé, et la fonctionnalité du fer (Fe) et du nickel (Ni) a été discutée.

Les catalyseurs utilisés dans le cadre de cette étude ont été préparés comme présenté précédemment. Il s'agit de biocarbone de fougère et de saule non imprégnés et imprégnés avant pyrolyse dopés au Fe, au Ni et au Fe et Ni. Il y a également deux biocarbone de fougères fortement dopés au Fe et Ni. L'efficacité des catalyseurs biosourcés pour la deNO_x a été définie comme X_{NO} , qui est le ratio de NO converti par rapport au contenu initial en NO de l'effluent gazeux. Les caractéristiques de ces catalyseurs ont permis d'avoir une meilleure compréhension du mécanisme réactionnel en deNO_x. Ainsi, la forte présence de métaux dans les catalyseurs à base de fougère a montré des effets catalytiques ou promoteurs selon les espèces et les métaux catalytiques, tout en améliorant la structure électronique des catalyseurs biosourcés. Toutefois, ces catalyseurs peuvent perdre en activité si les sites sont peu dispersés ou encapsulés par la silice ou le carbone, ce qui peut se traduire dans une faible surface spécifique, ou si les sites ont peu de contact avec les gaz car le biocarbone en adsorbe peu, ce qui a été observé pour les catalyseurs de fougère.

Les catalyseurs biosourcés ont été comparés quand X_{NO} atteint le régime permanent, ce qui a lieu au bout de 50min. Dans ces circonstances, X_{NO} montre une augmentation croissante et non linéaire avec la température (**Fig. 2.5**). La présence d'un métal catalytique permet une meilleure activité pour la deNO_x, mais seulement quand ces métaux sont dans un état facilement réversible (Ni métallique). Ceci explique l'activité des métaux à 500°C. Cependant, ce n'est pas le cas à 350°C, où l'augmentation de X_{NO} est moins importante pour les catalyseurs biosourcés peu actifs. Le choix de la bioressource a également influencé X_{NO} , supérieur à basse température (200-350°C) pour les catalyseurs à base de fougère, puis inversement à 500°C pour ceux de saule. Cette activité à basse température a été liée à la présence de ses métaux inhérents. Néanmoins, à plus forte température, l'activité des métaux inhérents est comparable et donc le saule, qui peut approvisionner

davantage ces métaux de NO actif grâce à sa plus grande quantité de sites basiques et réducteurs, réagit plus avec NO. L'effet des métaux a aussi été comparé et une plus forte activité de ces métaux a été attribuée à leur disponibilité, à savoir leur potentiel à être encapsulé ou peu dispersé par la surface des catalyseurs biosourcés. De plus, aucun effet synergique entre Fe et Ni n'a été détecté. L'impact de la teneur en métaux a aussi été étudié. Une forte augmentation de cette teneur augmente légèrement X_{NO} et impacte la surface spécifique des catalyseurs, et donc la disponibilité du métal. Ainsi, une augmentation de la teneur d'un métal dans le catalyseur n'est peut-être pas intéressante, surtout dans une optique de réduction de coûts. Finalement, la désactivation des catalyseurs a été discutée. Un impact significatif sur X_{NO} n'a pas été visualisé pendant la durée de la réaction (4h), mais a été vu sur la perte de masse des catalyseurs, de l'ordre de 5 %m pour les catalyseurs biosourcés à base de Ni ou Fe et allant jusqu'à 10 %m pour les non imprégnés. Cette perte de masse est associée à la volatilisation du carbone et possiblement des groupes fonctionnels qui désorbent sous forme de CO et CO₂.

En plus du suivi de la concentration de NO, d'autres gaz comme N₂, O₂, CO, CO₂ et H₂ ont été monitorés. Malgré qu'elle ait été normalisée, la teneur de N₂ a augmenté pendant la réaction, associée à la décomposition directe du NO. Une désactivation à haute température des catalyseurs à base de fougère, reliée à la production de CO₂, a été associée à une désactivation par la silice. Un suivi de la production de CO semblait indiquer une désorption liée à la montée en température plutôt qu'à la réaction, et qui était plus important avec les échantillons ayant perdu le plus de masse. En comparaison au CO₂, peu de CO a été désorbé. La présence de ces gaz peut indiquer une plus forte exposition des métaux, qui peuvent ainsi participer davantage à la deNO_x. Une faible désorption de H₂ a aussi été détectée à 350 et 500°C et peut directement impacter la réaction.

La meilleure performance en deNO_x était atteinte par le catalyseur à base de saule et imprégné au Ni ($X_{NO} = 30.6\%$ à 500°C). Ceci a été lié à la combinaison de Ni fortement actif avec une forte capacité d'adsorption du NO de la part du saule. A basse température (<350°C), les catalyseurs les plus performants étaient à base de fougère, en raison de leur forte teneur métallique, ce qui peut être catalytique ou promouvoir des métaux catalytiques. Ceci semble indiquer qu'une forte teneur métallique n'est pas nécessaire pour la réaction deNO_x, mais plutôt le choix des métaux présents. La performance des catalyseurs en deNO_x a aussi pu être reliée à la teneur en N₂ des gaz sortants, ainsi qu'à la désorption de CO₂, CO et H₂, ce qui peut impacter directement la réaction. Ceci entraîne une perte de masse à considérer en vue de stabiliser davantage la matrice carbonée pour la réutilisation ou l'utilisation à plus haute température de ces catalyseurs biosourcés. De plus, des études utilisant ces catalyseurs avec des effluents réels permettraient d'analyser leurs

performances en présence d'autres espèces chimiques qui peuvent aussi subir une adsorption ou dégradation catalytique via ces matériaux.

R.3. Nickel and iron-doped biocarbon catalysts for reverse water-gas shift

La review bibliographique a permis de déterminer les conditions de production du biocarbone, ainsi que les métaux catalytiques ou ayant un rôle promoteur ou de support (Table 3.1), pour son utilisation en tant que catalyseur biosourcé pour la réaction inverse de gaz à l'eau (RWGS). La pyrolyse à haute température avec des vitesses de chauffe faibles et des longs temps de séjour a été choisie afin de développer dans le biocarbone des propriétés intéressantes pour la catalyse (porosité, dispersion et exposition des métaux...). Les métaux catalytiques sont souvent nobles, des métaux de transition ou des lanthanides. Les supports ou promoteurs sont des alcalins et alcalino-terreux (AAEM) et des métaux post-transition.

Les catalyseurs biosourcés ont été préparés suivant la méthodologie présentée précédemment. Des biocarbones de saule ou de fougère imprégnés avant ou après pyrolyse au Ni ou Fe ont été utilisés, ainsi qu'un biocarbone de fougère imprégnée avant pyrolyse au Fe et au Ni, de la rouille (Fe_2O_3) et une alumine dopée au Fe ($\text{Fe-Al}_2\text{O}_3$). Des valeurs à l'équilibre thermodynamique à 400°C en RWGS ont été calculés.

Les catalyseurs biosourcés ont montré une forte sélectivité pour le CO comparé à la rouille (88-100% contre 81%), et malgré une prédominance thermodynamique reportée pour la formation de CH_4 (Table 3.3). D'autres catalyseurs commerciaux peuvent atteindre une sélectivité approchant 100% mais nécessite une promotion par d'autres métaux comme le potassium (K). La conversion de CO_2 pour la plupart des catalyseurs biosourcés dépasse celle de $\text{Fe-Al}_2\text{O}_3$ (au plus 17,2% comparé à 7,6%). Leur performance est néanmoins faible par comparaison à la rouille (29.6%), or d'autres catalyseurs commerciaux indiqués en littérature (proche de l'équilibre, soit ici 35%). Toutefois, ils bénéficient d'une performance stable avec une conversion maintenue pendant 288h là où des catalyseurs commerciaux sont désactivés par frittage métallique ou par encrassement par dépôt de carbone à des temps de réactions moindres. Ces performances catalytiques ont été attribuées à la capacité de rétention de Fe et Ni au cours de l'imprégnation des catalyseurs, et au maintien des métaux inhérents des biomasses qui peuvent améliorer les propriétés électroniques des sites actifs et faciliter l'adsorption et la dissociation des gaz réactifs CO_2 et H_2 . En plus de la présence d'AAEM, les biocarbones présentent des fonctions de surface qui, en coordination avec Ni et Fe, forment des lacunes d'oxygène après réduction qui permettent une meilleure adsorption et activation du CO_2 . Cet ensemble de propriétés est responsable des meilleures performances par les catalyseurs de fougère par opposition à ceux de saule. L'imprégnation pouvait aussi affecter l'activité des catalyseurs, soit dû à un blocage de porosité par dépôt métallique et donc limiter l'accès aux sites actifs, soit en créant davantage de sites pour plus

d'échanges électroniques. Ceci explique pourquoi certains biocarbones de fougère sont bien plus actifs que d'autres comme celui imprégné au Ni après pyrolyse, celui imprégné au Fe avant pyrolyse et le biocarbone bimétallique imprégné avant pyrolyse.

Des études supplémentaires peuvent permettre d'éclaircir ce lien performant de liaison métal-surface. Cette conversion peut être améliorée en modifiant la structure du catalyseur ou en utilisant le catalyseur sans pré-réduction (augmentation de la conversion de 1.7%). De plus, la stabilisation à haute température des catalyseurs biosourcés avec (H₂O) ou sans activation (graphitisation) peut promouvoir une meilleure conversion en effectuant la RWGS à plus haute température grâce à l'aspect endothermique de la réaction, tout en maintenant le caractère sélectif des catalyseurs biosourcés. Il est aussi possible d'étudier l'utilisation des catalyseurs dans des réactions utilisant la RWGS comme la synthèse Fischer-Tropsch (FTS) ou la synthèse de méthanol (CAMERE).

R.4. Nickel and iron biocarbon catalysts for water-gas shift reaction

L'état de l'art sur l'influence et l'importance des conditions opératoires sur la réalisation de la WGS a été analysé afin de déterminer les conditions de réaction à tester avec les catalyseurs biosourcés. En plus d'agir sur un déplacement de l'équilibre, le choix des conditions opératoires peut empêcher la réaction de parvenir à son équilibre thermodynamique, d'où l'importance de l'activité cinétique des catalyseurs. A cet effet, des expressions de vitesses de réaction ont été exposées avec des constantes cinétiques mentionnées pour des réactions catalysées par des métaux nobles et non-nobles. La température tend à améliorer les vitesses cinétiques mais la conversion à l'équilibre thermodynamique est amoindrie en raison de la nature exothermique de WGS. La pression peut favoriser le sens direct de la WGS en raison d'une possible perméation des gaz produits. La vitesse spatiale des gaz et leur temps de séjour contribue à exposer les réactifs moins ou plus longtemps respectivement à la surface du catalyseur ce qui peut diminuer ou augmenter respectivement la production de gaz produits par la réaction. Le taux de vapeur par rapport aux composés carbonés peut améliorer la consommation des réactifs suite à un déplacement de l'équilibre de la réaction dans la direction des produits suite à la présence excessive d'un réactif. La configuration du réacteur peut influencer la réaction, par exemple en la déplaçant dans la direction des produits grâce à des membranes permettant d'extraire ces derniers ou grâce à des contacts réactifs-catalyseurs plus longs à cause de hauteurs de lit plus importantes. L'impact de ces différentes conditions opératoires a été synthétisé.

Les catalyseurs ont été préparés suivant la méthodologie présentée précédemment. Les catalyseurs utilisés dans cette étude ont été des biocarbones de fougère imprégnés avant ou après pyrolyse au Ni ou Fe, en plus du biocarbone bimétallique de fougère imprégné avant pyrolyse, la rouille (Fe₂O₃) et un biocarbone

bimétallique imprégné après pyrolyse. Pour le test en WGS, la température de réaction a été augmentée par paliers de 20°C toutes les 1h30 à partir de 180°C avec excès de vapeur par rapport au monoxyde de carbone (S/C) de 5,5. A température finale, l'excès de vapeur a été modifié à 1,4, 2,8 et 20,7 pour certains catalyseurs. Le procédé expérimental a été simulé avec la variation de la température de réaction et celle du débit d'eau liquide en utilisant Aspen Plus, et deux types de réacteurs ont été étudiés : un réacteur Gibbs pour une réaction en conditions thermodynamiques sur la base de calculs en équilibre thermodynamique, et un réacteur à écoulement piston pour simuler des conditions cinétiques basées sur des paramètres cinétiques reportés en littérature. La conversion de CO des conditions thermodynamiques était supérieure à 99%, représentatif de la réaction exothermique, et augmentait avec la pression partielle de vapeur et diminuait avec la température, représentatif des principes d'équilibre. L'augmentation des deux paramètres entraînait aussi une augmentation de la sélectivité envers CO₂ (min 75%) due à des paramètres plus favorables pour la réaction de WGS que la méthanation. Pour la simulation en conditions cinétiques, la température n'influe pas. La pression de vapeur a par contre permis une conversion maximale de 3.3% à 0.12 mL/min d'eau. Cet optimum est lié à un surplus d'eau qui entraîne un besoin plus important d'énergie pour faire réagir la vapeur supplémentaire et limitant l'énergie disponible à la réaction. De plus, ces conditions permettent d'atteindre une sélectivité de 100%. Les deux situations semblent avoir des effets contraires avec des faibles conversions pour des conditions cinétiques par rapport à la thermodynamique. Ainsi, selon la situation expérimentale, il est possible que la réaction puisse avoir des performances faibles mais justifiées à la vue des conditions opératoires.

L'impact de la variation de la température sur la production de CO₂, la conversion de CO et la sélectivité en CO₂ a été observé en WGS pour les catalyseurs biosourcés produits (Table 4.12). Les valeurs de production et de conversion étaient faibles en base volumique, ce qui était moins le cas en base massique. Cependant, les valeurs obtenues étaient cohérentes avec la cinétique simulée. La production de CO₂ a augmenté avec la température mais la désactivation des catalyseurs aussi. Une comparaison de cette production en fonction de la température et des catalyseurs a montré une plus forte activité des catalyseurs biosourcés, par rapport à la rouille, à base de Ni par rapport à ceux à base de Fe. Ceci aurait été lié au caractère plus réductible, car plus de groupes réductibles, à plus basse température (première température de désorption d'H₂ faible) des catalyseurs à base de Ni et donc ils n'ont pas eu besoin de plus d'énergie pour changer d'état en plus de réagir avec les réactifs gazeux. D'autant plus, les barrières énergétiques ont pu être amoindries grâce à la présence d'autres métaux comme les alcalins et les alcalino-terreux, présents en grande quantité dans la fougère, et grâce aux sites déficients en O, qui partagent une forte affinité avec les réactifs H₂O et CO, obtenus par réduction des groupes fonctionnels oxygénés provenant de la surface du biocarbone. La surface

spécifique développée par imprégnation ne semblait pas affecter ni l'accessibilité des sites actifs ni l'activité des catalyseurs et donc la forte surface suite à la graphitisation du biocarbone par Fe n'a pas semblé impactant pour la réaction de WGS. Cette comparaison a permis de plus d'établir un ordre d'activité des catalyseurs pour la réaction. La sélectivité en CO₂ était supérieure à 85% et s'améliorait avec la température. Ceci était lié à l'inhibition de la méthanation pour cause de son caractère exothermique plus important que celui de WGS. L'augmentation de S/C a permis de légèrement augmenter la production de CO₂ et la conversion et a eu peu d'effet sur la sélectivité (>97%). En effet, un plus grand excès d'un réactif favoriserait la production des produits de la réaction.

Des paramètres cinétiques ont pu être déterminés par loi d'Arrhenius et cinétique simplifiées, mais aucune corrélation entre l'ordre d'activité pour la réaction et ces valeurs n'a pu être établi. Ces valeurs étaient comprises entre 5.2 et 92.1 kJ/mol pour l'énergie d'activation et entre 2.2×10^{-1} et 2.2×10^8 pour la constante cinétique rapportée à celle de la rouille, cette dernière étant plus élevée pour les catalyseurs à base de Ni. Bien que ces valeurs soient dispersées, elles sont de l'ordre de magnitude de celles reportées en littérature.

Pour conclure, les catalyseurs biosourcés ont été testés en WGS. La cinétique de la réaction a été promue par augmentation de la température et l'excès de vapeur. Elle a d'autant plus été améliorée par les catalyseurs biosourcés surtout à base de Ni, et surtout celui imprégné avant pyrolyse au Fe et au Ni (10% de conversion) qui a bénéficié de l'effet synergique de ces deux métaux. L'efficacité des catalyseurs biosourcés de Ni a été liée leur capacité à être actifs à basse température, en combinaison des métaux inhérents à la fougère qui abaissent les barrières énergétiques, et des sites déficients en O créés par réduction des nombreux sites oxygénés du biocarbone. Des paramètres cinétiques ont été établis et qui, malgré le manque d'une relation explicite avec l'ordre d'activité des catalyseurs pour la WGS, sont cohérents avec les résultats et la littérature. Ceci semble montrer qu'il y a des caractéristiques qui peuvent subtilement affecter la cinétique de la réaction et qui peuvent faire l'objet de futures études. De plus, les propriétés des catalyseurs biosourcés et les conditions opératoires pourraient être optimisées afin de diriger la réaction de WGS vers l'équilibre thermodynamique.

R.CP. Conclusions et perspectives

Cette thèse a montré qu'il est possible de développer des procédés permettant de mitiger les émissions utilisant des catalyseurs biosourcés au lieu des catalyseurs commerciaux afin de réduire l'impact sur l'environnement. Ainsi, cette thèse se focalise sur la production de catalyseurs à base de bioressources et testés en réactions de décomposition de NO_x (deNO_x), de gaz à l'eau indirect (RWGS) et direct (WGS).

Le chapitre de matériels et méthodes a permis de faire l'état sur la création des catalyseurs biosourcés à base de fougère et de saule et imprégné avant et après pyrolyse au fer (Fe) et nickel (Ni). Ils ont été pyrolysés à 800°C à 2°C/min sous N₂ suivi d'un isotherme d'une heure. Ils ont été caractérisés en termes de teneur en éléments organiques (CHNS) et inorganique (ICP-AES), de dispersion inorganique sur la matrice organique (MEB/MET), de stabilité thermique (ATG-DSC), de surface spécifique (BET), de propriétés texturales et de fonctions chimiques de surface (TPD, TPR, TPO, DRX). Les installations expérimentales développées, mises au point et optimisées dans leur intégralité, ont été présentées.

L'étude de la deNO_x à travers les catalyseurs biosourcés a permis de montrer leur intérêt pour cette application. Ils bénéficient de métaux dispersés ayant un rôle catalytique ou promoteur de catalyseur et d'une surface permettant d'adsorber avec facilité les NO_x. Il s'agit notamment du saule qui bénéficie de propriétés texturales meilleures que la fougère qui malgré sa quantité plus importante de métaux inhérents ne possède pas une bonne accessibilité à ces métaux. L'augmentation de la température a permis aussi d'améliorer les performances en deNO_x.

L'étude des catalyseurs biosourcés en RWGS a montré l'intérêt de bioressources fortement riches en métaux inhérents comme la fougère. Ces métaux ont une part plus active en RWGS qu'en deNO_x car ils contribuent promouvoir les espèces catalytiques et améliorer la réception et l'activation des gaz. De plus, ils sont extrêmement stables avec une activité continue allant jusqu'à 288h comparé à la rouille qui malgré sa conversion approchant l'équilibre thermodynamique (30<35%) a été fortement désactivée en 24h.

L'étude en WGS des catalyseurs biosourcés était complémentaire à celle de RWGS et seuls les catalyseurs à base de fougère ont été testés. La température a été augmentée de 180 à au moins 280°C par paliers de 20°C et l'excès de vapeur de 1.4 à 20.7. Tous deux ont contribué à améliorer les performances des catalyseurs, ce qui était cohérent avec la simulation de la réaction et la littérature. Les catalyseurs les plus performants étaient à base de Ni en raison de leur réduction facile qui bénéficie des effets cumulés des métaux promoteurs et des sites déficients en O issus de la réduction des groupes oxygénés du biocarbone. L'application de la loi d'Arrhenius a aussi permis de déterminer les paramètres cinétiques de la réaction catalysée et n'a pas montré d'ordre lié à l'activité des catalyseurs mais les résultats semblaient cohérents avec les résultats et la littérature.

A travers ces trois applications, la versatilité des catalyseurs biosourcés a été mise en avant. Ils combinent des propriétés différentes qui permettent une bonne adsorption et activation des gaz et qui bénéficient de métaux catalytiques et promoteurs bien dispersés. Pour exploiter au maximum le potentiel des catalyseurs biosourcés, d'autres biomasses ou déchets riches en métaux pourraient être explorées, ainsi que

l'optimisation des propriétés de ces catalyseurs via des procédés d'activation ou la stabilisation thermique de la matrice carbonée afin de pouvoir l'utiliser dans des applications haute température telles que le reformage.

Introduction

The Paris Agreement, signed in 2015 by 195 nations, set the conditions to hold the rise in temperatures from global warming at 2°C and reduce greenhouse gas (GHG) emissions [1]. This mainly concerns carbon dioxide (CO₂) and methane (CH₄) which constitute the majority of GHG [2]. However, other minor GHG such as the nitrous oxides (NO_x) are also responsible for severe environmental and health issues among photochemical smog, acid rain and ozone layer depletion [3]. Hydrogen (H₂), an energy vector that can be produced through carbon-neutral processes such as thermochemical conversion of bioresources and biowastes or electrolysis, may play a significant role in reducing GHG emissions. These thermochemical conversion routes, such as biogas reforming and bioresources gasification may be enhanced by the use of catalysis.

1.1. Thermochemical conversion of bioresources

Thermochemical conversion of bioresources consists of a chemical transformation through heat under oxygen-free or limited atmosphere, as opposed to combustion. The yield of solid, liquid and gas products obtained by thermochemical conversion is strongly dependent to the selected conversion route (**Fig. 1.1**) and operating conditions (Table 1.1).

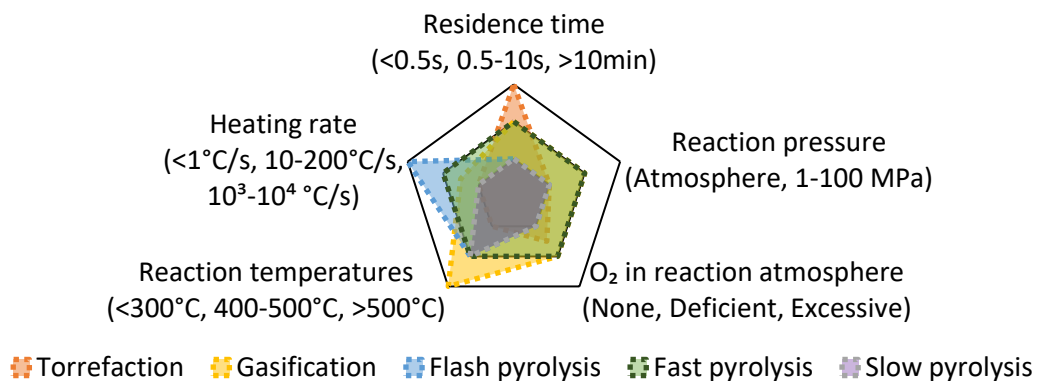
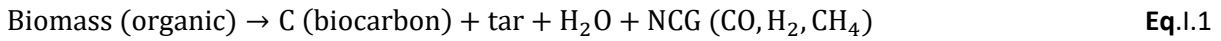


Fig. 1.1. Different types of thermochemical conversion [4]

Table I.1. Product distribution for different types of thermochemical conversion [5]

Thermochemical conversion type	Typical operating conditions		Product distribution		
	Temperature (°C)	Heating rate (°C.min ⁻¹)	Solid	Liquid (wt%)	Gas
Torrefaction	200 – 300	<1	30 – 85	0	10 – 60
Slow pyrolysis	300 – 700	1 – 100	15 – 40	20 – 55	15 – 60
Fast pyrolysis	450 – 550	>1000	10 – 35	50 – 70	5 – 30
Flash pyrolysis	300 – 800	>1000	12 – 40	-	60 – 70
Gasification	800 – 1200	Variable	0 – 10	5	85 – 100

Pyrolysis consists in the transformation of bioresources using heat and inert gases. This produces a solid product called biocarbon, understood as biochar, a liquid product from condensable gases called tar and a gaseous product from non-condensable gases (NCG) (Eq.I.1).



Pyrogasification is the combination of slow pyrolysis, from ambient temperature to gasification temperature (Table I.1) at slow pyrolysis heating rates and under inert atmosphere, followed by gasification, where a gasifying agent is introduced for a specific residence time at gasification temperature (800 to 1200°C). As a result, biocarbon, tar and gaseous products are obtained through primary and secondary reactions (Fig. I.2).

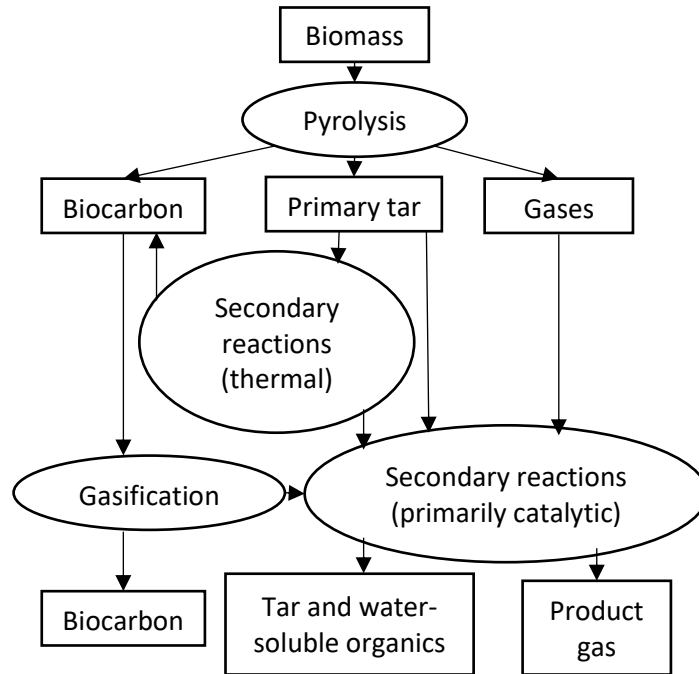


Fig. I.2. Pyrogasification steps [6]

Primary reactions can be represented by 3 mechanisms [7]:

- Biocarbon formation consists in converting biomass to biocarbon by forming aromatic polycyclic

structures. It concerns intra- and intermolecular rearrangement reactions that form stable bonds. This reaction produces water and NCGs. This can be catalyzed to maximize the production of biocarbon.

- Depolymerization is the rupture of monomers contained in the polymers, reducing the degree of polymerization of the biomass. This rupture continues till production of volatile molecules that are condensable at ambient temperature (tar).
- Fragmentation results in the formation of covalent bonds to form condensable gases and NCGs.

Secondary reactions consist in 2 competing mechanisms:

- Cracking represents broken gaseous bonds to form even lighter molecules. It is similar to fragmentation.
- Recombining is the formation of heavier molecules. It is responsible for the production and deposit of coke (solid carbonaceous particles) on the surface of biocarbon and catalysts.

Gasification is the production of NCGs, which mainly includes syngas composed by H₂ and carbon monoxide (CO). Operating conditions, namely temperature, heating rate and gasifying agent, will push different reactions towards the production of certain gases such as CO or H₂ (Table I.2) due to thermodynamic equilibrium principles. Indeed, high temperatures will favor endothermic reactions such as Boudouard reaction (Eq.I.2) and high pressures will influence reaction towards the formation of the least gaseous products (for ex., Eq.I.3 would be inhibited). A reactant in excess will drive reactions towards products. To maximize H₂ production, the operating conditions of water-gas shift (WGS, Eq.I.4) and reforming reactions (Eq.I.5 and I6) also need to be optimized.

Table I.2. Examples of reactions that can occur during pyrogasification [8]

Reaction		Standard enthalpy of reaction (kJ/mol)
Boudouard reaction: $C + CO_2 \rightarrow 2CO$	Eq.I.2	+ 172.1
$C + \frac{1}{2}O_2 \rightarrow CO$	Eq.I.3	- 110.7
Water-gas shift: $CO + H_2O \leftrightarrow CO_2 + H_2$	Eq.I.4	- 41.2
Dry reforming: $C_nH_m + nCO_2 \rightarrow 2nCO + \left(\frac{m}{2}\right)H_2$	Eq.I.5	
Steam reforming: $C_nH_m + nH_2O \rightarrow nCO + \left(n + \frac{m}{2}\right)H_2$	Eq.I.6	
$C + O_2 \rightarrow CO_2$	Eq.I.7	- 405.8

H₂ can also be used to form derivatives with the same objective of reducing emissions. This is the case for reverse WGS (RWGS, Backwards reaction of Eq.I.7) where H₂ and CO₂ are consumed. RWGS is usually implied in downstream reactions such as Fischer-Tropsch synthesis (FTS) and “carbon dioxide hydrogenation to form methanol via a reverse-water-gas-shift reaction” (CAMERE) to form long-chain

hydrocarbons or methanol respectively [9,10]. Additionally, other gaseous emissions such as NO_x can be abated using selective reduction (catalytic or not) or by direct decomposition (**Eq.1.8**) [3,11].



Operating conditions such as the temperature, heating rate, residence time or catalysts influence the reaction mechanism. They could increase the yield of wanted products like biocarbon and decrease the yield of others such as tar or coke that restrict access to active sites in catalysts. To reach equilibrium faster, catalysts may also be used. If the equilibrium is too long to reach then the capacity of the catalysts to affect the kinetics of these reactions is crucial.

I.2. Catalysis by metals in conversion processes; biomass, biocarbon and inherent metals

Catalysts for thermochemical conversion processes include noble, transition and post-transition metals (Table I.3). Recent studies (2022) report the use of nickel (Ni) in coordination with aluminum and cerium oxide (Al₂O₃ and CeO₂ respectively) for WGS and RWGS (**Fig. I.3**). For DeNO_x, reported catalysts figure among zeolites and titanium oxide (TiO₂, **Fig. I.4**).

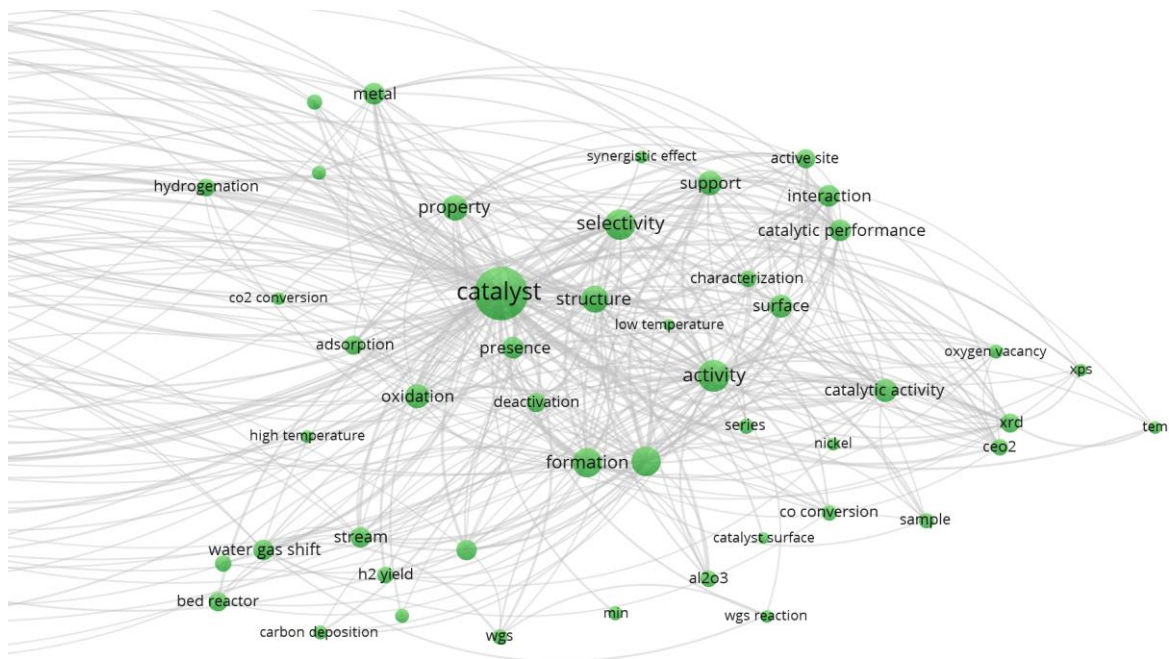


Fig. I.3. Wordmap by VOSviewer of 100 most used terms related to WGS catalysts from 1649 articles from ScienceDirect since 2022, focus on the catalytic cluster

Non-lignocellulosic biomass are for example manure and algae [21]. Manures have been studied in pyrolysis for biocarbon production [22–24]. Lignocellulosic biomass is principally composed of cellulose, hemicellulose and lignin (**Fig. 1.5**).

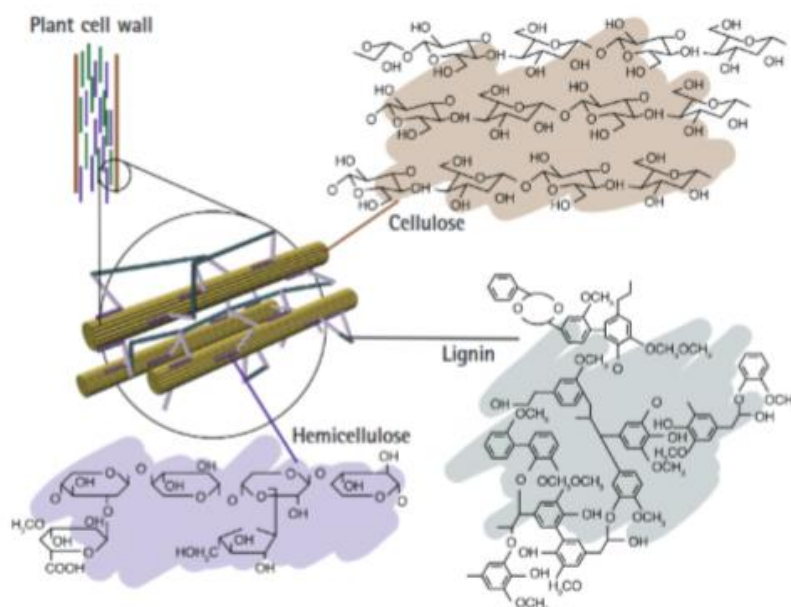


Fig. 1.5. Macromolecules composing lignocellulosic biomass [25]

Their content influences product distribution in thermochemical conversion (Table I.4), as they are degraded at different intervals of temperature [7,26]:

- Hemicellulose is degraded between 220 and 315°C. This can be explained by its amorphous polysaccharide-based structure and the presence of weaker bonds compared to other components.
- Cellulose is degraded between 250 and 350°C. Its polysaccharide-based structure presents a higher degree of crystallinity than that of hemicelluloses, which explains its degradation at higher temperatures. Cellulose contributes to the formation of tar.
- Lignin is degraded between 200 and 500°C. This large interval is due to the heterogeneity of lignin structures and its mixture of weaker and stronger bonds. Lignin contributes to the formation of biocarbon.

Table I.4. Product distribution from fast pyrolysis (>100°C/min) depending on lignocellulosic material [7]

	Biocarbon	Tar	Water	Gas
	<i>Yield (moisture free wt%, from different reactors between 500 and 800°C)</i>			
Cellulose	< 15	40 – 70	5 – 15	12 – 30
Hemicelluloses	20 – 30	20 – 35	20 – 30	22 – 35
Lignin	30 – 45	15 – 35	8 – 15	12 – 35

Modifying the product distribution obtained in bioresource pyrolysis is also possible by adjusting parameters such as a residence time, slower heating rate or the use of catalysts. Catalyzing pyrolysis not only means lowering the heat requirements for the conversion but also enhancing tar and coke conversion in the selected operating conditions.

There are 4 main types of lignocellulosic biomass [26]:

- Primary residues are byproducts of agriculture and silviculture (straw, wood, etc.).
- Secondary residues are byproducts of biomass transformation (sawdust, wood chips ...).
- Tertiary residues or contaminated biomass are the byproducts of used biomass-based products such as waste wood (CCA or Chrome Copper Arsenic/CCB or Chrome Copper Boron woods and others).
- Energetic cultures are crops dedicated to energetic valorization of biomass (short rotation coppice, such as miscanthus, for example).

Primary residues and energetic cultures can be naturally rich in metal elements, as it is the case of hyperaccumulators or phytoremediators, which contribute in soil remediation by extracting inorganic elements. Hyperaccumulators are studied because, by definition, they present a certain quantity of metal that surpasses a defined threshold (Table I.5). *Thlaspi caerulescens* has been studied as Ni hyperaccumulators [27–30], as well as *Noccaea caerulescens* [31], *Brassicae* and especially *Alyssum murale* [27,30,32–34]. *Pteridophytes* (ferns) have been studied as potential hyperaccumulators of arsenic (As) that can have high content in Ni [35–39]. Based on these studies and other complementary ones, a database of hyperaccumulators was created, which can sort plants on the type of metal accumulated, the plants location and many other criteria [40].

Table I.5. Metal thresholds for hyperaccumulation in plants [40]

Element	As	Cd	Cu	Co	Mn	Ni	Pb	Rare earth	Se	Tl	Zn
Threshold ($\mu\text{g/g}$)	1000	100	300	300	10000	1000	1000	1000	100	100	3000

Abundant or short rotation plants with a relatively high inorganic content may also present an interest for metal elements recovery. Sorghum has been studied for phytoremediation and bioenergy production [41]. Mays has been studied for zinc (Zn), cadmium (Cd), copper (Cu), lead (Pb) and Ni phytoextraction [27,30,42]. Ragweed has been studied for Pb extraction [30]. Mustard, tobacco and sunflower have been studied for Zn, Cd and Cu phytoextraction [27]. Non hyperaccumulating *brassicae* have been studied for chromium (Cr), Cd, Ni, Zn, Cu and Pb phytoextraction [43]. Reed and canary grass have been studied for Ni phytoextraction [42]. *Arundo donax* (giant reed) and *Broussonetia papyferia* (paper mulberry) have been studied for Cd, Cu and Pb phytoremediation and applied in pyrolysis [44].

Manchurian walnuts have been studied in pyrolysis as an abundant species possessing alkali and alkaline-earth metals (AAEMs) [45]. Finally, wooden species such as willow, poplar, oak or beech have been studied for thermal treatment (pyrolysis, gasification and incineration) and Cu, Zn, Cd, Cr, Ni, Pb and iron (Fe) phytoextraction [28,42,46–55].

Contaminated bioresources, as well as ash from bioresources thermochemical transformation, are also candidates for the production of biocarbon catalysts. CCB wood has been studied for catalytic hydroliquefaction [56]. CCA Wood has been studied for its Cu, Cr and As contents in combustion and pyrolysis [57–59]. Ash from bioresources and their addition in thermochemical conversion processes have been studied as a catalyst or as a potential catalytic support [60–64]. Coal ash has been studied in catalytic pyrolysis for syngas production [65].

The thermal treatment of these bioresources then results in a highly aromatic and thermally stable biocarbon enriched with metals that is porous, heat and electron conductive and with a surface containing basic and acid functions [66]. These different properties are interesting for catalysis as they facilitate access to active sites while providing energy to adsorb and dissociate reactive gases [67].

1.3. Objective of the thesis

The objective of this thesis is the production of robust and stable biocarbon catalysts from biomass inherently rich in metal species by pyrolysis and their use in WGS, RWGS and deNO_x reactions.

The work developed promotes a circular economy approach in the way that plants from phytoremediation have been used for the production of eco-friendly biocarbon catalysts for the production of energy vectors, such as H₂ from renewable resources, produced by direct and reverse water-gas shift (WGS and RWGS), as well as for the decomposition of NO_x pollutants (deNO_x).

The following chapters and sections introduce the production, characterization and use of the biocarbon catalysts in deNO_x, RWGS and WGS, as well as the associated mechanisms and performances. The last chapter then provides a conclusion and perspectives to this study.

References

- [1] United Nations Treaty Collection n.d. https://treaties.un.org/Pages/ViewDetails.aspx?src=IND&mtdsg_no=XXVII-7-d&chapter=27&clang=_en#4 (accessed June 9, 2021).
- [2] Jeffry L, Ong MY, Nomanbhay S, Mofijur M, Mubashir M, Show PL. Greenhouse gases utilization: A review. *Fuel* 2021;301:121017. <https://doi.org/10.1016/j.fuel.2021.121017>.
- [3] Skalska K, Miller JS, Ledakowicz S. Trends in NO_x abatement: A review. *Science of The Total Environment* 2010;408:3976–89. <https://doi.org/10.1016/j.scitotenv.2010.06.001>.
- [4] You S, Ok YS, Tsang DCW, Kwon EE, Wang C-H. Towards practical application of gasification: a critical review from syngas and biochar perspectives. *Critical Reviews in Environmental Science and Technology* 2018;48:1165–213. <https://doi.org/10.1080/10643389.2018.1518860>.
- [5] Sajjadi B, Chen W-Y, Egiebor N. A comprehensive review on physical activation of biochar for energy and environmental applications. *Reviews in Chemical Engineering* 2018;35. <https://doi.org/10.1515/revce-2017-0113>.
- [6] Baker EG, Mudge LK. Mechanisms of catalytic biomass gasification. *Journal of Analytical and Applied Pyrolysis* 1984;6:285–97. [https://doi.org/10.1016/0165-2370\(84\)80023-6](https://doi.org/10.1016/0165-2370(84)80023-6).
- [7] Collard F. X. BJ. A review on pyrolysis of biomass constituents: Mechanisms and composition of the products obtained from the conversion of cellulose, hemicelluloses and lignin n.d. http://publications.cirad.fr/une_notice.php?dk=574780 (accessed June 14, 2021).
- [8] Shen Y. Chars as carbonaceous adsorbents/catalysts for tar elimination during biomass pyrolysis or gasification. *Renewable and Sustainable Energy Reviews* 2015;43:281–95. <https://doi.org/10.1016/j.rser.2014.11.061>.
- [9] Bown RM, Joyce M, Zhang Q, Reina TR, Duyar MS. Identifying Commercial Opportunities for the Reverse Water Gas Shift Reaction. *Energy Technology* 2021;9:2100554. <https://doi.org/10.1002/ente.202100554>.
- [10] Joo O-S, Jung K-D, Moon I, Rozovskii AY, Lin GI, Han S-H, et al. Carbon Dioxide Hydrogenation To Form Methanol via a Reverse-Water-Gas-Shift Reaction (the CAMERE Process). *Ind Eng Chem Res* 1999;38:1808–12. <https://doi.org/10.1021/ie9806848>.
- [11] Roberts CA, Paidi VK, Shepit M, Peck TC, Stamm Masias KL, van Lierop J, et al. Effect of Cu substitution on the structure and reactivity of Cu_xCo_{3-x}O₄ spinel catalysts for direct NO_x decomposition. *Catalysis Today* 2021;360:204–12. <https://doi.org/10.1016/j.cattod.2020.05.050>.
- [12] Farjana SH, Huda N, Parvez Mahmud MA, Saidur R. A review on the impact of mining and mineral processing industries through life cycle assessment. *Journal of Cleaner Production* 2019;231:1200–17. <https://doi.org/10.1016/j.jclepro.2019.05.264>.
- [13] Dudka S, Adriano DC. Environmental Impacts of Metal Ore Mining and Processing: A Review. *Journal of Environmental Quality* 1997;26:590–602. <https://doi.org/10.2134/jeq1997.00472425002600030003x>.
- [14] Nzihou A, editor. *Handbook on Characterization of Biomass, Biowaste and Related By-products*. Springer International Publishing; 2020. <https://doi.org/10.1007/978-3-030-35020-8>.
- [15] Qu'est-ce que la biomasse ? Comment ça marche ? TotalEnergies Services France 2019. <https://www.services.totalenergies.fr/mes-deplacements/tout-savoir-sur-les-carburants-total/biomasse-comment-ca-marche> (accessed June 9, 2021).
- [16] Bio-waste – European Biomass Industry Association n.d. <https://www.eubia.org/cms/wiki-biomass/biowaste/> (accessed June 20, 2021).
- [17] Agrafioti E, Bouras G, Kalderis D, Diamadopoulou E. Biochar production by sewage sludge pyrolysis. *Journal of Analytical and Applied Pyrolysis* 2013;101:72–8. <https://doi.org/10.1016/j.jaap.2013.02.010>.
- [18] Chanaka Udayanga WD, Veksha A, Giannis A, Lisak G, Chang VW-C, Lim T-T. Fate and distribution of heavy metals during thermal processing of sewage sludge. *Fuel* 2018;226:721–44. <https://doi.org/10.1016/j.fuel.2018.04.045>.

- [19] Lu T, Yuan H, Wang Y, Huang H, Chen Y. Characteristic of heavy metals in biochar derived from sewage sludge. *J Mater Cycles Waste Manag* 2016;18:725–33. <https://doi.org/10.1007/s10163-015-0366-y>.
- [20] Wang X, Li C, Li Z, Yu G, Wang Y. Effect of pyrolysis temperature on characteristics, chemical speciation and risk evaluation of heavy metals in biochar derived from textile dyeing sludge. *Ecotoxicology and Environmental Safety* 2019;168:45–52. <https://doi.org/10.1016/j.ecoenv.2018.10.022>.
- [21] Li D-C, Jiang H. The thermochemical conversion of non-lignocellulosic biomass to form biochar: A review on characterizations and mechanism elucidation. *Bioresource Technology* 2017;246:57–68. <https://doi.org/10.1016/j.biortech.2017.07.029>.
- [22] Zeng X, Xiao Z, Zhang G, Wang A, Li Z, Liu Y, et al. Speciation and bioavailability of heavy metals in pyrolytic biochar of swine and goat manures. *Journal of Analytical and Applied Pyrolysis* 2018;132:82–93. <https://doi.org/10.1016/j.jaap.2018.03.012>.
- [23] Zhang P, Zhang X, Li Y, Han L. Influence of pyrolysis temperature on chemical speciation, leaching ability, and environmental risk of heavy metals in biochar derived from cow manure. *Bioresource Technology* 2020;302:122850. <https://doi.org/10.1016/j.biortech.2020.122850>.
- [24] Zhang Q, Ye X, Li H, Chen D, Xiao W, Zhao S, et al. Cumulative effects of pyrolysis temperature and process on properties, chemical speciation, and environmental risks of heavy metals in magnetic biochar derived from coagulation-flocculation sludge of swine wastewater. *Journal of Environmental Chemical Engineering* 2020;8:104472. <https://doi.org/10.1016/j.jece.2020.104472>.
- [25] Said M. Comportements et rôles des métaux lourds au cours de la pyro-gazéification de la biomasse : études expérimentales et thermodynamiques. phdthesis. Ecole des Mines d'Albi-Carmaux, 2016.
- [26] Shankar Tumuluru J, Sokhansanj S, Hess JR, Wright CT, Boardman RD. REVIEW: A review on biomass torrefaction process and product properties for energy applications. *Industrial Biotechnology* 2011;7:384–401. <https://doi.org/10.1089/ind.2011.7.384>.
- [27] Kayser A, Wenger K, Keller A, Attinger W, Felix HR, Gupta SK, et al. Enhancement of Phytoextraction of Zn, Cd, and Cu from Calcareous Soil: The Use of NTA and Sulfur Amendments. *Environ Sci Technol* 2000;34:1778–83. <https://doi.org/10.1021/es990697s>.
- [28] Keller C, Ludwig C, Davoli F, Wochele J. Thermal Treatment of Metal-Enriched Biomass Produced from Heavy Metal Phytoextraction. *Environ Sci Technol* 2005;39:3359–67. <https://doi.org/10.1021/es0484101>.
- [29] Reeves RD, Schwartz C, Morel JL, Edmondson J. Distribution and Metal-Accumulating Behavior of *Thlaspi caerulescens* and Associated Metallophytes in France. *International Journal of Phytoremediation* 2001;3:145–72. <https://doi.org/10.1080/15226510108500054>.
- [30] Huang JW, Cunningham SD. Lead phytoextraction: species variation in lead uptake and translocation. *New Phytologist* 1996;134:75–84. <https://doi.org/10.1111/j.1469-8137.1996.tb01147.x>.
- [31] Kozhevnikova AD, Seregin IV, Aarts MGM, Schat H. Intra-specific variation in zinc, cadmium and nickel hypertolerance and hyperaccumulation capacities in *Noccaea caerulescens*. *Plant Soil* 2020;452:479–98. <https://doi.org/10.1007/s11104-020-04572-7>.
- [32] Relationship between the Ni hyperaccumulator *Alyssum murale* and the parasitic plant *Orobanche nowackiana* from serpentines in Albania | SpringerLink n.d. <https://link.springer.com/article/10.1007/s11284-018-1593-1> (accessed October 26, 2020).
- [33] Shallari S. Biodisponibilité du nickel du sol pour l'hyperaccumulateur *Alyssum murale*. These de doctorat. Vandoeuvre-les-Nancy, INPL, 1997.
- [34] Shallari S, Echevarria G, Schwartz C, Morel JL. Availability of nickel in soils for the hyperaccumulator *Alyssum murale* (Waldst. Kit.), 1999.
- [35] Metal Hyperaccumulating Ferns: Progress and Future Prospects. <https://www.eurekaselect.com/117475/chapter> (accessed June 14, 2021).

- [36] Zhaol FJ, Dunham SJ, McGrath SP. Arsenic Hyperaccumulation by Different Fern Species. *The New Phytologist* 2002;156:27–31.
- [37] Akomolafe G, Dedeké, S.A S. TOLERANCE MECHANISMS IN PTERIDOPHYTES (FERNS) AND THEIR USE AS REMEDIATORS OF HEAVY METAL CONTAMINATED SITES, 2013.
- [38] Bondada BR, Ma LQ. Tolerance of Heavy Metals in Vascular Plants: Arsenic Hyperaccumulation by Chinese Brake Fern (*Pteris Vittata* L.). In: Chandra S, Srivastava M, editors. *Pteridology in the New Millennium: NBRI Golden Jubilee Volume*, Dordrecht: Springer Netherlands; 2003, p. 397–420. https://doi.org/10.1007/978-94-017-2811-9_28.
- [39] Chang J-S, Yoon I-H, Kim K-W. Heavy metal and arsenic accumulating fern species as potential ecological indicators in As-contaminated abandoned mines. *Ecological Indicators* 2009;9:1275–9. <https://doi.org/10.1016/j.ecolind.2009.03.011>.
- [40] A global database for plants that hyperaccumulate metal and metalloid trace elements - Reeves - 2018 - *New Phytologist* - Wiley Online Library n.d. <https://nph.onlinelibrary.wiley.com/doi/full/10.1111/nph.14907> (accessed October 26, 2020).
- [41] Al Chami Z, Amer N, Smets K, Yperman J, Carleer R, Dumontet S, et al. Evaluation of flash and slow pyrolysis applied on heavy metal contaminated *Sorghum bicolor* shoots resulting from phytoremediation. *Biomass and Bioenergy* 2014;63:268–79. <https://doi.org/10.1016/j.biombioe.2014.02.027>.
- [42] Korzeniowska J, Stanisławska-Głubiak E. Phytoremediation potential of *Phalaris arundinacea*, *Salix viminalis* and *Zea mays* for nickel-contaminated soils. *Int J Environ Sci Technol* 2019;16:1999–2008. <https://doi.org/10.1007/s13762-018-1823-7>.
- [43] Kumar PBANanda, Dushenkov Viatcheslav, Motto Harry, Raskin Ilya. Phytoextraction: The Use of Plants To Remove Heavy Metals from Soils. *Environ Sci Technol* 1995;29:1232–8. <https://doi.org/10.1021/es00005a014>.
- [44] Han Z, Guo Z, Zhang Y, Xiao X, Xu Z, Sun Y. Pyrolysis Characteristics of Biomass Impregnated with Cadmium, Copper and Lead: Influence and Distribution. *Waste Biomass Valor* 2018;9:1223–30. <https://doi.org/10.1007/s12649-017-0036-5>.
- [45] Zhao Y, Feng D, Zhang Y, Huang Y, Sun S. Effect of pyrolysis temperature on char structure and chemical speciation of alkali and alkaline earth metallic species in biochar. *Fuel Processing Technology* 2016;141:54–60. <https://doi.org/10.1016/j.fuproc.2015.06.029>.
- [46] Meers E, Vandecasteele B, Ruttens A, Vangronsveld J, Tack FMG. Potential of five willow species (*Salix* spp.) for phytoextraction of heavy metals. *Environmental and Experimental Botany* 2007;60:57–68. <https://doi.org/10.1016/j.envexpbot.2006.06.008>.
- [47] Stals M, Thijssen E, Vangronsveld J, Carleer R, Schreurs S, Yperman J. Flash pyrolysis of heavy metal contaminated biomass from phytoremediation: Influence of temperature, entrained flow and wood/leaves blended pyrolysis on the behaviour of heavy metals. *Journal of Analytical and Applied Pyrolysis* 2010;87:1–7. <https://doi.org/10.1016/j.jaap.2009.09.003>.
- [48] Šyc M, Pohořelý M, Kameníková P, Habart J, Svoboda K, Punčochář M. Willow trees from heavy metals phytoextraction as energy crops. *Biomass and Bioenergy* 2012;37:106–13. <https://doi.org/10.1016/j.biombioe.2011.12.025>.
- [49] Šyc M, Pohořelý M, Jeremiáš M, Vosecký M, Kameníková P, Skoblia S, et al. Behavior of Heavy Metals in Steam Fluidized Bed Gasification of Contaminated Biomass. *Energy Fuels* 2011;25:2284–91. <https://doi.org/10.1021/ef1016686>.
- [50] Vysloužilová M, Tlustoš P, Száková J. Cadmium and Zinc Phytoextraction Potential of Seven Clones of *Salix* spp. Planted on Heavy Metal Contaminated Soils. *Plant, Soil and Environment* 2003;49. <https://doi.org/10.17221/4191-PSE>.
- [51] Wani KA, Sofi ZM, Malik JA, Wani JA. Phytoremediation of Heavy Metals Using *Salix* (Willows). In: Bhat RA, Hakeem KR, Dervash MA, editors. *Bioremediation and Biotechnology, Vol 2: Degradation of Pesticides and Heavy Metals*, Cham: Springer International Publishing; 2020, p. 161–74. https://doi.org/10.1007/978-3-030-40333-1_9.

- [52] Mosseler A, Major JE. Phytoremediation Efficacy of *Salix discolor* and *S. eriocephala* on Adjacent Acidic Clay and Shale Overburden on a Former Mine Site: Growth, Soil, and Foliage Traits. *Forests* 2017;8:475. <https://doi.org/10.3390/f8120475>.
- [53] BRAC de la PERRIERE N, DANIEL M. Etude sur la pertinence d'une filière de taillis à courte rotation dans le Rhône. HESPUL; 2008.
- [54] Vervaeke P, Tack FMG, Navez F, Martin J, Verloo MG, Lust N. Fate of heavy metals during fixed bed downdraft gasification of willow wood harvested from contaminated sites. *Biomass and Bioenergy* 2006;30:58–65. <https://doi.org/10.1016/j.biombioe.2005.07.001>.
- [55] Wang S, Shi X, Sun H, Chen Y, Pan H, Yang X, et al. Variations in Metal Tolerance and Accumulation in Three Hydroponically Cultivated Varieties of *Salix integra* Treated with Lead. *PLOS ONE* 2014;9:e108568. <https://doi.org/10.1371/journal.pone.0108568>.
- [56] Kinata SE, Loubar K, Paraschiv M, Tazerout M, Belloncle C. Catalytic hydroliquefaction of charcoal CCB (copper, chromium and boron)-treated wood for bio-oil production: Influence of CCB salts, residence time and catalysts. *Applied Energy* 2014;115:57–64. <https://doi.org/10.1016/j.apenergy.2013.10.057>.
- [57] Lundholm K, Rogers JM, Haynes BS, Boström D, Nordin A. Fate of Cu, Cr, and As during the Combustion Stages of CCA-Treated Wood Fuel Particles. *Energy Fuels* 2008;22:1589–97. <https://doi.org/10.1021/ef700621y>.
- [58] Wasson SJ, Linak WP, Gullett BK, King CJ, Touati A, Huggins FE, et al. Emissions of chromium, copper, arsenic, and PCDDs/Fs from open burning of CCA-treated wood. *Environ Sci Technol* 2005;39:8865.
- [59] Kim J-Y, Oh S, Park Y-K. Overview of biochar production from preservative-treated wood with detailed analysis of biochar characteristics, heavy metals behaviors, and their ecotoxicity. *Journal of Hazardous Materials* 2020;384:121356. <https://doi.org/10.1016/j.jhazmat.2019.121356>.
- [60] Wei J, Guo Q, Ding L, Gong Y, Yu J, Yu G. Understanding the Effect of Different Biomass Ash Additions on Pyrolysis Product Distribution, Char Physicochemical Characteristics, and Char Gasification Reactivity of Bituminous Coal. *Energy Fuels* 2019;33:3068–76. <https://doi.org/10.1021/acs.energyfuels.9b00064>.
- [61] Li C, Hu X, Feng W, Wu B, Wu K. A supported solid base catalyst synthesized from green biomass ash for biodiesel production. *Energy Sources, Part A: Recovery, Utilization, and Environmental Effects* 2018;40:142–7. <https://doi.org/10.1080/15567036.2017.1405121>.
- [62] Qin Y, He Y, Ren W, Gao M, Wiltowski T. Catalytic effect of alkali metal in biomass ash on the gasification of coal char in CO₂. *J Therm Anal Calorim* 2020;139:3079–89. <https://doi.org/10.1007/s10973-019-08719-2>.
- [63] Yildiz G, Ronsse F, Venderbosch R, Duren R van, Kersten SRA, Prins W. Effect of biomass ash in catalytic fast pyrolysis of pine wood. *Applied Catalysis B: Environmental* 2015;168–169:203–11. <https://doi.org/10.1016/j.apcatb.2014.12.044>.
- [64] Ashok J, Das S, Yeo TY, Dewangan N, Kawi S. Incinerator bottom ash derived from municipal solid waste as a potential catalytic support for biomass tar reforming. *Waste Management* 2018;82:249–57. <https://doi.org/10.1016/j.wasman.2018.10.035>.
- [65] Loy ACM, Yusup S, Lam MK, Chin BLF, Shahbaz M, Yamamoto A, et al. The effect of industrial waste coal bottom ash as catalyst in catalytic pyrolysis of rice husk for syngas production. *Energy Conversion and Management* 2018;165:541–54. <https://doi.org/10.1016/j.enconman.2018.03.063>.
- [66] Nanda S, Dalai AK, Berruti F, Kozinski JA. Biochar as an Exceptional Bioresource for Energy, Agronomy, Carbon Sequestration, Activated Carbon and Specialty Materials. *Waste Biomass Valor* 2016;7:201–35. <https://doi.org/10.1007/s12649-015-9459-z>.
- [67] Lee J, Kim K-H, Kwon EE. Biochar as a Catalyst. *Renewable and Sustainable Energy Reviews* 2017;77:70–9. <https://doi.org/10.1016/j.rser.2017.04.002>.

Chapter 1

Materials and Methods

1.1. Introduction

As the interest for biocarbon catalysts was developed regarding rising concern related to current environmental and sanitary issues, this chapter will develop the techniques employed to prepare these catalysts. They are then to be tested in target applications, namely the deNO_x, RWGS and WGS. The choice of bioresource is vital as it determines the composition and characteristics of the resulting biocarbon. To overcome this and simulate phytoremediation and hyperaccumulation of metals, the bioresource was impregnated with nickel and iron. To monitor the evolution of the properties and how they affect the reactions, characterizations were performed. The equipment associated to each reaction was set-up and presented. Lastly, choice of parameters and WGS reaction were simulated.

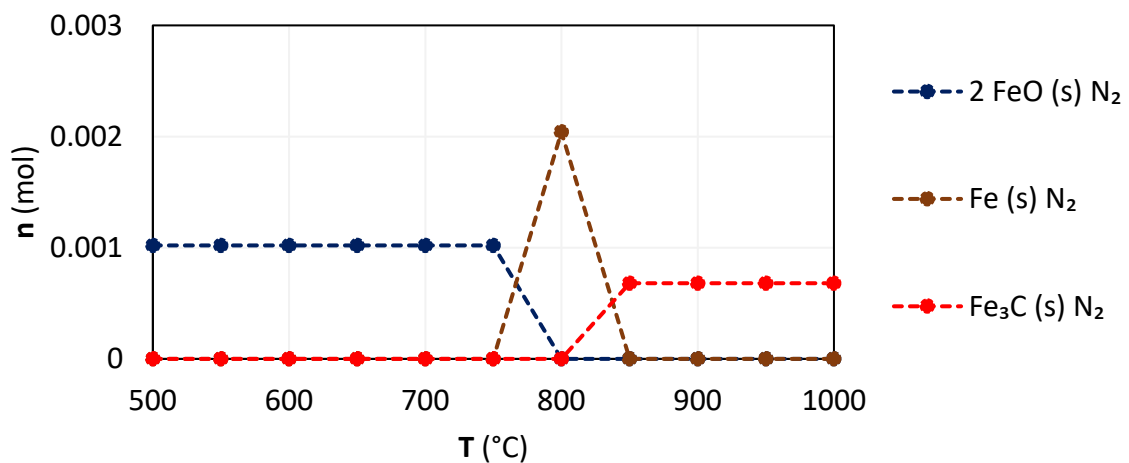
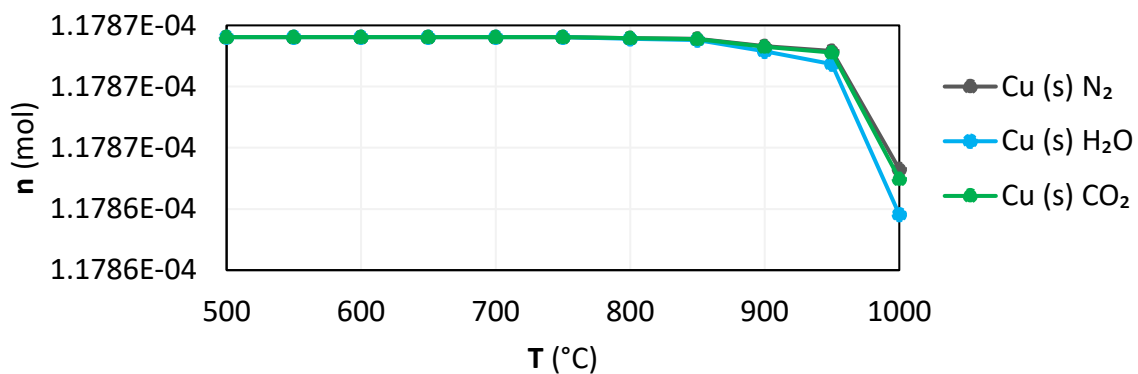
1.2. Preparation of catalysts

Fern and willow were selected as carbon bases for the catalysts. They also represent two different types of biomass: herbaceous and deciduous respectively and both having phytoremediation capacities [1]. Fern was collected from shrublands in Brittany and was provided by Eizhy [2]. Willow was from the south of France from the Mobile Flip program [3]. Once received, the biomass was treated by the company RAGT. Initially, they were dried on a heated holed drier at 30°C and air-blown for 1 day in order to have a relative humidity of less than 20%. They were then milled for specific sizes and then grinded (**Fig. 1.1**).



Fig. 1.1. 10 mm fern on the left, 6 mm willow on the right

Biocarbon was produced by pyrolysis under a flow rate of 1 L/min N_2 , with an increase in temperature from 25 to 800°C and a heating rate of 2°C/min, followed by 1-hour isotherm. Biocarbon operating conditions were determined based on results from literature and was complemented with characterizations and simulation. To determine the influence of the gaseous atmosphere and temperature, FactSage software was used to simulate the pyrolysis of biomass with known elemental composition and see how these elements associate at thermodynamic equilibrium according to these two parameters (**Fig. 1.2**). The atmosphere in which to perform pyrolysis was selected to be N_2 as this limited slight degradation of the biomass inherent metals, such as copper (Cu), due to volatilization but also the biocarbon structure. The pyrolysis temperature was selected to be 800°C, to limit the formation of iron (Fe) carbide which does not generally act as a catalyst but as a support and to avoid potential degradation of metallic nickel (Ni) [4–6]. These speciation of these last two metals, Fe and Ni, were the main interest of this thesis as they were selected as catalytic doping agents to produce the biocarbon catalysts.



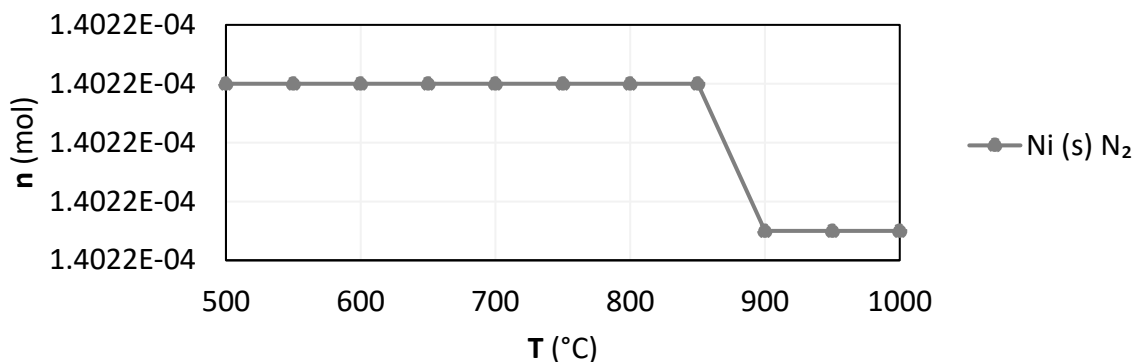


Fig. 1.2. Speciation of Fe, Ni and Cu at thermodynamic equilibrium depending on temperature and gaseous atmosphere of pyrolysis of fern simulated using FactSage

Thermogravimetric analysis (TGA) was performed in a Labsys evo device by Seteram to determine the impact of heating rate on the biomass degradation (Fig. 1.3). The variation between TGA at 2, 5 and 10°C/min had little impact on the mass loss of the biomass, so 2°C/min was retained as it is reported to develop catalytic properties, namely porosity, of the produced biocarbon [7].

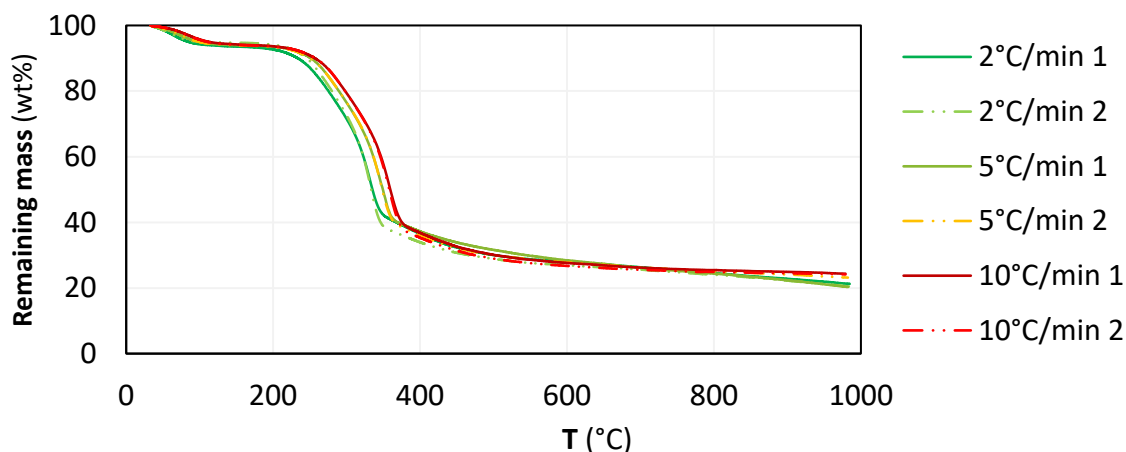


Fig. 1.3. TGA of willow biomass under N₂ with increase from 30 to 1000°C at 2, 5 and 10°C/min

The 1-hour isotherm was to guarantee repeatability of results, the relative standard deviation (RSD) being less than 5% for both biomass.

The device used to produce biocarbon is a carbolite VST 12/65/600 oven [8]. Biomass are deposited in a quartz crucible whose internal diameter is 4 cm with a height of 5 cm. This crucible's bottom piece slots onto a quartz tube which then elevates the sample through a quartz reactor to the isothermal region of the oven (Fig. 1.4). The heating rate and pyrolysis temperature is imposed by an external controller. The N₂ flow is manually fixed by adjusting an Aalborg rotameter.

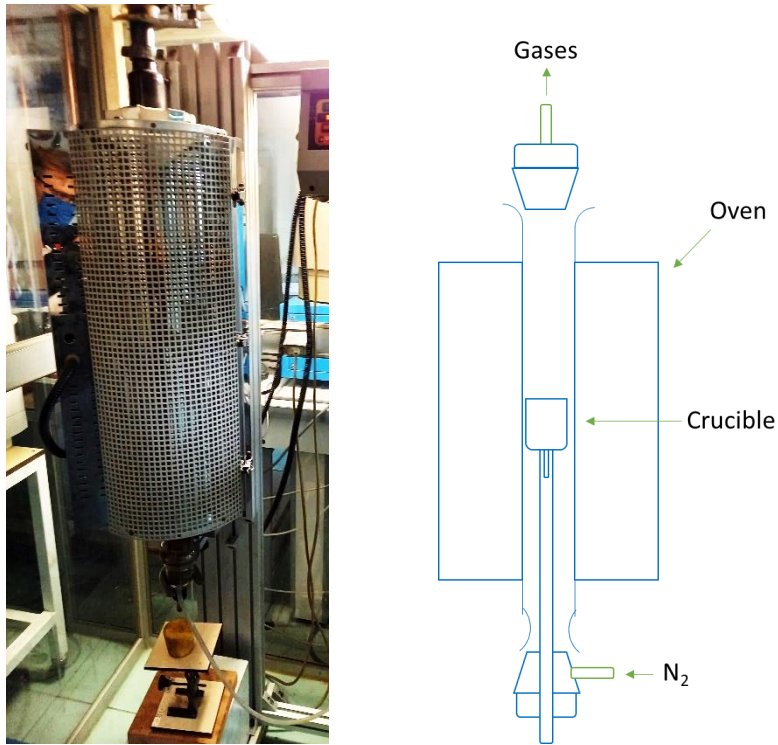


Fig. 1.4. Oven providing heat and N₂ for biocarbon production on the left, diagram of the setup on the right

Condensable and non-condensable gas production were not quantified. Solid mass loss was estimated via the difference in mass between the biomass introduced in the reactor and the biocarbon remaining after pyrolysis (Eq.1.1).

$$\text{Mass loss (wt\%)} = \frac{m_{\text{biomass}} - m_{\text{biocarbon}}}{m_{\text{biomass}}} \times 100 = 100 - \text{yield}_{\text{biocarbon}} \text{ (wt\%)} \quad \text{Eq.1.1}$$

Two biocarbon, one for each biomass, were produced in the previously determined conditions (Table 1.1).

Table 1.1. Unimpregnated biocarbon, names, pyrolysis conditions and mass loss

Biocarbon	Abbreviation	Pyrolysis conditions	Mass loss	
			Average (wt%)	RSD (%)
Unimpregnated fern biocarbon	RF	1 L/min, T _{amb} – 800°C, 2°C/min, 1-hour isotherm at 800°C	68.3	1.2
Unimpregnated willow biocarbon	RW	1 L/min, T _{amb} – 800°C, 2°C/min, 1-hour isotherm at 800°C	71.6	3.6

To imitate phytoremediation, the objective of Ni or Fe impregnation was to reach 30 mg of metal per g of biocarbon (highest content in Table 1.5, 1/3 mass loss to form biocarbon from biomass). Impregnation was optimized in terms of contact time, metal concentration in impregnation solution and biocarbon mass/solution volume ratio (Appendix A). Fern and willow samples were impregnated before and after pyrolysis with 98 wt% pure Ni nitrate hexahydrate (Ni(NO₃)₂·6H₂O) and Fe nitrate nonahydrate (Fe(NO₃)₃·9H₂O). The contact of biomass and metallic species was carried out in 1L of

water [9]. The contact of biocarbon was fulfilled in 100mL then at a higher volume (250 or 600mL), while maintaining biomass and nitrate to water ratio, to increase production. The impregnation before pyrolysis lasted 3 days, while impregnation after pyrolysis lasted on average 10 days. Following these impregnations, the material was filtered with filter paper and then dried for at least 24 hours, at 60°C for biomass to avoid risks of burning and 105°C for biocarbon. Biomass samples were then pyrolyzed following the same conditions as the unimpregnated biomass. From these preparations, eight additional batches were produced (Table 1.2). Metal content was determined via inductively coupled plasma optical emission spectroscopy (ICP-OES). These batches were selected as to reach as close as possible the phytoremediation objective (30 mg/g biocarbon or 3wt%).

Table 1.2. Impregnated biocarbon, names, impregnation conditions

Impregnated biocarbon	Name	Impregnation conditions				Metal content (wt%)
		t_{contact} (d)	m_{resource} (g)	m_{nitrate} (g)	V_{solution} (L)	
Fern biocarbon impregnated with Ni before pyrolysis	FNi-B	3	21.8	9.8	1	3.96
Fern biocarbon impregnated with Ni after pyrolysis	FNi-A	7	2.0	1.3	0.1	1.43
Fern biocarbon impregnated with Fe before pyrolysis	FFe-B	3	21.7	25.7	1	13.17
Fern biocarbon impregnated with Fe after pyrolysis	FFe-A	13	2.0	13.5	0.1	0.51
Willow biocarbon impregnated with Ni before pyrolysis	WNi-B	3	21.6	4.4	1	2.41
Willow biocarbon impregnated with Ni after pyrolysis	WNi-A	10	2.0	1.3	0.1	1.81
Willow biocarbon impregnated with Fe before pyrolysis	WFe-B	3	20.4	4.1	1	4.64
Willow biocarbon impregnated with Fe after pyrolysis	WFe-A	10	5.0	4.8	0.25	0.23

The produced biocarbon were crushed using a spice mill to reduce their particle size, in this instance to less than 125 μm (Fig. 1.5). Granulometry of biocarbon was obtained using a Retsch AS 200 vibratory sieve shaker with 50, 125, 250, 500 μm sieves at 40% amplitude (1.2 mm) for 1 hour.

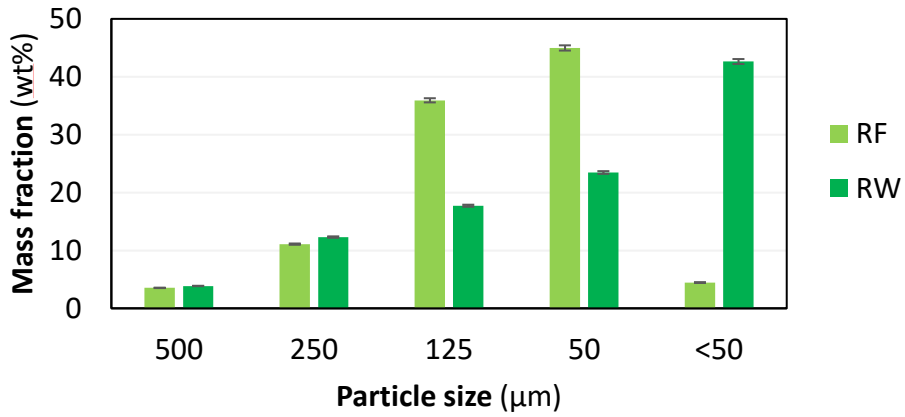


Fig. 1.5. Decreasing distribution of particle size of milled unimpregnated biocarbon

The produced biocarbon were considered stable up to 500°C (Fig. 1.6). This stability was estimated under N₂ by TGA. Biocarbon underwent a temperature increase from 30°C to 500°C at 2°C/min followed by a 24-hour isotherm at 500°C. The mass loss due to the increase to 500°C, total mass loss and mass loss due to the 24-hour isotherm were noted (Table 1.3). Mass loss during the isotherm is comparable to mass loss during heating, therefore the degradation of refractory organic C during 24h is as impactful as volatile release and therefore could attest to the stability of the biocarbon [10].

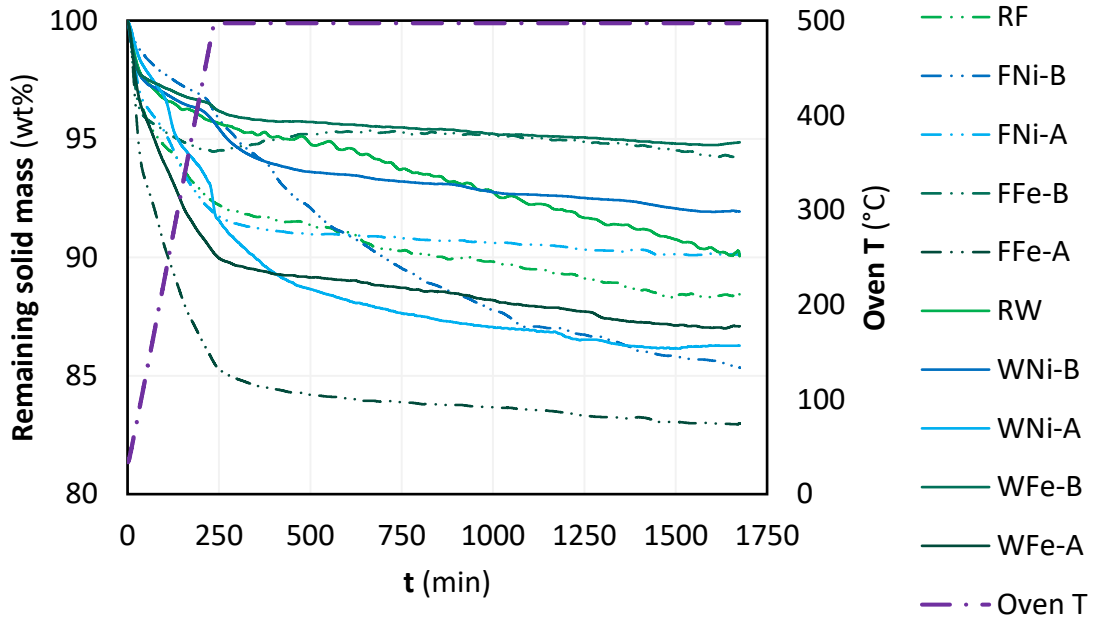


Fig. 1.6. Remaining solid mass by TGA of aforementioned biocarbon to observe 24h stability under N₂

Table 1.3. Mass losses of biocarbon due to increase to 500°C and 24-h isotherm

Biocarbon	Mass loss before isotherm (wt%)	Mass loss after isotherm (total, wt%)	24-hour mass loss (difference, wt%)
RF	7.66	11.57	3.92
FNi-B	3.78	14.64	10.86
FNi-A	8.10	9.88	1.79
FFe-B	5.53	5.77	0.24
FFe-A	14.41	17.02	2.62
RW	4.27	9.91	5.64
WNi-B	4.26	8.07	3.81
WNi-A	7.76	13.73	5.97
WFe-B	3.66	5.14	1.48
WFe-A	9.79	12.91	3.12

They were thereafter tested as biocarbon catalysts in applications where they would undergo little degradation because can be realized under 500°C. These applications are direct decomposition of nitrous oxides (NO_x), reverse and direct water-gas shift (RWGS and WGS respectively). The following sections will describe the methodology behind the characterizations to determine properties relevant to the catalytic capabilities of the biocarbon as well as the conditions of the applications in which these biocarbon catalysts were trialed.

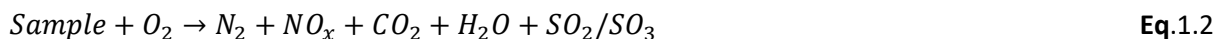
1.3. Characterization of catalysts

To determine the catalytic properties, the biocarbon were characterized before and after their use in deNO_x, RWGS and WGS. To oversee the composition in organic and inorganic species, ultimate analysis using CHNS and ICP-OES was performed. Proximate analysis of biocarbon determined moisture and ash content. Choice of pyrolysis parameters, stability of the carbon matrices, ash content and eventual desorption of gases was observed via TGA with differential scanning calorimetry (DSC) coupling. N₂ adsorption-desorption isotherms were used to characterize specific surface area and pore properties. Imagery techniques, scanning electron microscopy coupled with energy dispersive X-ray spectroscopy (SEM-EDX) and high-resolution transmission electron microscopy (HRTEM) brought to light information on structure and metal dispersion on the biocarbon. Temperature programmed desorption, oxidation or reduction (TPD, TPO or TPR) of NH₃, CO₂ and H₂ helped evaluate gas adsorption capabilities and surface groups. X-ray diffraction spectrometry (XRD) was used to identify phases of the main structured components of biocarbon.

1.3.1. Ultimate analysis: CHNS and ICP

The mass fractions of carbon (C), hydrogen (H), nitrogen (N) and sulfur (S), composing biocarbon, can be quantified by CHNS analysis. The device used is the Flash 2000. The CHNS analysis is carried out by

flash combustion under a dynamic flow of O₂ at 950°C. During this combustion, organic and inorganic CHNS components are converted into stable gaseous forms (**Fig. 2.1.2**).



Following this oxidation is an additional oxidation step and a reduction step to reduce the species of higher oxidation number to species detectable later (**Eq.1.3**). This also allows to retain excess O₂.



The elements are then separated by a gas chromatography (GC) column heated at 65°C using a He gas carrier. Finally, quantification of the four gases N₂, CO₂, H₂O and SO₂ is carried out using a thermal conductivity detector (TCD) and via standards methionine and BBOT following norms ISO16948 and ASTM D5291 [11]. O content was then determined by difference (**Eq.1.4**).

$$O \text{ (wt\%)} = 100 - C \text{ (wt\%)} - H \text{ (wt\%)} - N \text{ (wt\%)} - S \text{ (wt\%)} - \text{Ash content (wt\%)} \quad \text{Eq.1.4}$$

To perform CHNS analysis, 1-3 mg of biocarbon was introduced in a tin crucible and then introduced in the analyzer. The spatula used was wiped using ethanol or acetone so as to minimize error related to residual samples and 4 crucibles were measured to guarantee good repeatability of the analysis of these 10 biocarbon catalysts (Table 1.4). The RSD was generally between 0.03 to 10% and is generally higher as the value is low.

Table 1.4. Organic content (wt%) of biocarbon catalysts

Biocarbon	C	H	N	S
RF	72.78	0.93	1.47	<0.01
FNi-B	71.23	0.73	1.86	<0.01
FNi-A	75.72	1.14	1.65	<0.01
FFe-B	71.01	0.49	1.07	<0.01
FFe-A	70.98	1.24	2.28	<0.01
RW	86.62	0.96	0.82	<0.01
WNi-B	72.14	1.57	1.29	<0.01
WNi-A	81.64	1.09	1.03	<0.01
WFe-B	79.29	0.71	0.53	<0.01
WFe-A	76.33	1.35	1.59	<0.01

ICP-OES is an analytical technique for determining the inorganic elemental composition (alkali and alkaline earth metals/AAEM, transition metals, rare earth metals) of a sample. The device used is the Ultima 2. Liquid samples are transported via capillaries and a pump to an argon (Ar) plasma (ICP) where they are atomized and the different minerals are excited. The transition from this excited level to another level releases quantifiable energy of a wavelength specific to the element in question. These

wavelengths are in the near-visible spectra and are directed via mirrors towards a spectrophotometer (OES). This analysis is sequential meaning the elements are detected and quantified one after another. Intensity is therefore perceived depending on the concentration of the sample and a linear correlation can be established using standards of known concentration. Thereafter, unknown samples can be analyzed. Using this technique, content of sodium (Na), potassium (K), magnesium (Mg), calcium (Ca), manganese (Mn), Fe, cobalt (Co), Ni, Cu, aluminum (Al), zinc (Zn), cadmium (Cd), silica (Si) and phosphorus (P) in biocarbon was evaluated. The sensitivity for these elements is at most 1.5 µg/L [12].

Due to the size of capillaries, any solid part has to be dissolved via mineralization prior to the analysis. For this, 100 ± 10 mg of biocarbon is weighed and inserted in Teflon tubes. This is repeated thrice (average RSD < 10%). Then, acid is added using a plastic graduated pipette to the 3 samples: 1.5 mL of H₂O₂, 4 ml of HNO₃ and 0.5 mL of HF. The Teflon tubes are inserted in enclosed iron reactors. The samples are then heated in a Berghof DAB reactor to 220°C for 8 hours to ensure total mineralization of the sample. In case of non-mineralization of the sample, extra acid is added and the sample is heated longer. After mineralization, the liquid samples are diluted to 50mL using distilled water. Using values of mass and volume, the sensitivity is at most 1 µg/g. The inorganic content of the 10 studied biocarbon catalysts was quantified (Table 1.5).

Table 1.5. Inorganic content (µg/g) of biocarbon employed as catalysts

	RF	FNi-B	FNi-A	FFe-B	FFe-A	RW	WNi-B	WNi-A	WFe-B	WFe-A
Na	3822	<1	<1	1218	<1	245	<1	<1	<1	<1
K	19192	5134	4565	3976	6588	6660	2003	1860	1395	1859
Mg	2759	904	380	887	720	1968	745	1455	562	1049
Ca	9321	4446	7818	3436	8110	23393	7349	7117	1059	6862
Mn	68	<1	<1	73	<1	172	<1	<1	74	<1
Fe	263	<1	<1	131669	5098	279	<1	<1	46409	2276
Co	245	<1	31	311	<1	186	<1	<1	51	<1
Ni	1	39580	14282	49	<1	16	24075	18147	45	<1
Cu	<1	<1	<1	<1	<1	<1	<1	<1	82	<1
Al	172	742	<1	2877	43	81	456	489	127	3481
Zn	19	927	<1	21	<1	67	846	819	<1	822
Cd	<1	<1	<1	<1	<1	<1	<1	<1	21	<1
Si	17450	14040	20870	44151	31987	1058	401	1327	<1	2197
P	2257	1500	1207	3989	1203	3607	<1	2489	<1	300

1.3.2. Moisture and ash Content

Moisture content (MC) and ash content (AC) of unimpregnated biomass was realized following standards ISO18134 and ISO18122 [11]. To measure MC, 2 crucibles were tempered at 105°C then weighed empty (m_1). 1g ± 1mg of biomass was introduced in the crucible and then weighed (m_2). The

biomass was after dried under air at 105°C for 24h. The residual mass (m_3) was weighed. MC is therefore the ratio between water mass dried from the biomass and the initial mass of biomass (Eq.1.5). This was 7.1 wt% for willow and 8.4 wt% for fern. The MC for both biomass was also determined using the MJ33 moisture analyzer that dries quickly and follows the variation in mass of the sample. This was 8.0 wt% for willow and 10.0 wt% for fern. The values are comparable to the standard but are higher, caused by severer drying. Therefore, the moisture analyzer technique was applied to biocarbon.

$$MC (wt\%) = \frac{m_2 - m_3}{m_2 - m_1} \times 100 \quad \text{Eq.1.5}$$

To determine AC, 2 crucibles were also tempered according to the following temperature program and then weighed empty (m_1). $1g \pm 1mg$ of biomass was introduced in the crucible, then weighed (m_2), and put in a Heraeus K1252 muffle oven. The sample was heated from 25 to 280°C (250°C in crucible) at 5°C/min. It was maintained at this temperature for 1h and the temperature was then increased to 650°C (550°C in crucible) at 10°C/min, followed by a 2-hour isotherm at this temperature. The crucible was then removed and cooled for 5min on a heat resistant plate and cooled to room temperature in a desiccant at which the remaining mass was weighed (m_3). AC (wt%) is therefore the ratio between the burned biomass and the initial mass of biomass (Eq.1.6). AC of fern and willow biomass was 6.4 and 1.9 wt% (moisture free, mf) respectively. TGA was also performed following the same program to estimate AC while conserving mass of the sample. The remaining masses for both biomass using TGA were 14.4 wt% and 6.7 wt% respectively in biocarbon and therefore 4.8 wt% and 1.9 wt% in biomass considering the mass loss associated to both biomass pyrolysis (Table 1.1). As these values are slightly inferior the temperature program might be severe resulting in loss of inorganic mass. MC and AC for all 10 catalysts were noted (Table 1.6).

$$AC (wt\%, mf) = \frac{m_3 - m_1}{m_2 - m_1} \times 100 \times \frac{100}{100 - MC (wt\%)} \quad \text{Eq.1.6}$$

Table 1.6. MC and AC of biocarbon catalysts

Biocarbon catalyst	MC (wt%)	AC (wt%, mf)
RF	10.0	14.4
FNi-B	8.7	20.4
FNi-A	8.2	13.7
FFe-B	8.3	28.1
FFe-A	5.2	12.2
RW	8.0	6.7
WNi-B	8.7	10.1
WNi-A	8.0	7.4
WFe-B	6.2	16.7
WFe-A	8.0	5.7

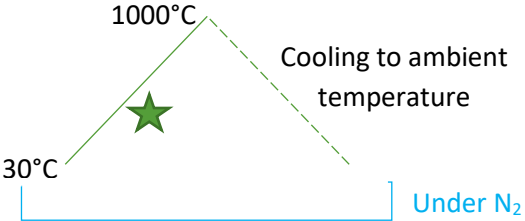
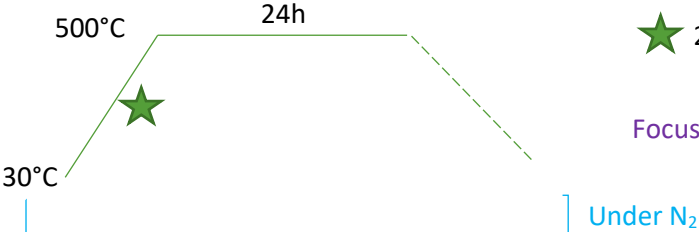
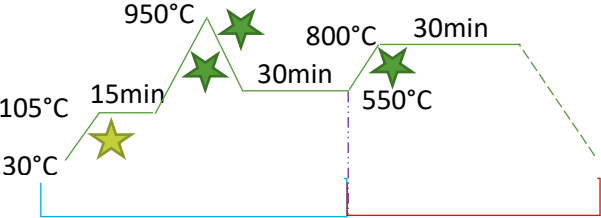
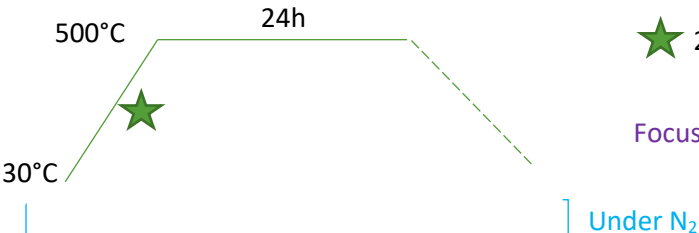
1.3.3. TGA-DSC: Thermal stability and regenerability

As previously mentioned, TGA was used to determine the choice of heating rate for the production of biocarbon (**Fig. 1.3**), in addition to guaranteeing stability of produced biocarbon catalysts (**Fig. 1.6**) and evaluating ash content of these biocarbon (Table 1.6).

The device used is the Labsys evo (Setaram). This device consists of a microbalance and a heating system with a precision of 0.01% and 1°C respectively. It is also coupled with a DSC with a 2% precision. The furnace heats the sample following a controlled temperature program, while the microbalance measures the mass variation during the analysis: when a mass variation occurs due to a transformation of the sample, a proportional variation in electric current is applied to a coil that maintains the microbalance at an equilibrium position. The intensity of the electric current variation is therefore used to deduce the corresponding mass variation. The sample is socketed via a crucible on a stick that contains a thermocouple. This technique makes it possible to obtain the numerical values of temperature and mass variation as a function of time. The DSC coupling enables simultaneous determination of the variation in heat flow rate by difference in temperature between the sample and a reference crucible. This variation in heat is associated with physicochemical or mechanical transformations such as water desorption or a change in crystal structure.

The first steps to realize TGA was identical: a weighed mass between 10 mg and 30 mg of sample was contained in a 100 µL Pt crucible that after underwent an unmeasured 20 min step at 30°C under 50 mL/min of N₂. The next step is the measured temperature program, varying depending on the objective of the analysis (Table 1.7). The last step was also unmeasured and permitted cooling of the TGA.

Table 1.7. Different TGA-DSC programs used in this work

Objective of TGA-DSC	Measured temperature program
Choice of heating rate for biocarbon production	 <p>1000°C 30°C Cooling to ambient temperature ★ 2, 5 or 10°C/min Under N₂</p>
Stability of biocarbon for use in applications	 <p>500°C 24h 30°C ★ 2°C/min Focus on TGA Under N₂</p>
Ash content in low mass samples	 <p>950°C 800°C 30min 550°C 30min 105°C 15min 30°C ★ 10°C/min ★ 20°C/min Under air</p>
Regenerability of biocarbon after use in application	 <p>500°C 24h 30°C ★ 2°C/min Focus on DSC Under N₂</p>

By looking at the temperatures of desorption of possible physisorbed molecules as well as the energy associated, using the DSC profile, regenerability of biocarbon spent by the applications can be inferred (Table 1.8). By using the program to test the stability of biocarbon, most physisorbed species should be desorbed. However, considering the energy associated to these molecules, chemisorption is possible and could lead to a reduction in active sites and therefore a reduction in activity when catalysts are reused.

Table 1.8. Temperature and energy of desorption of possible adsorbed molecules due to applications

Molecules	T (°C)	Energy (kJ/mol)	References
NO	212 ± 35	114	[13,14]
	527 (strong)	140	
N ₂ O	200	31	[15,16]
NO ₂	380	168	[14,17]
O ₂	200	134	[14]
	450±25	164	
H ₂	105±80	20	[18,19]
CO ₂	100±20	36	[20,21]
CO	333	100	[19,22,23]
CH ₄	285±15	16	[19,22,24]

1.3.4. Adsorption-desorption isotherms: specific surface area and pore type

The specific surface area and porous distribution of the samples can be determined by N₂ adsorption-desorption isotherms. The device used is the Tristar II 3020. The analysis technique is based on the physisorption of gases at low temperatures. An adsorbate (inert gas), in this case nitrogen, is injected isothermally in a determined and increasing quantity into a tube containing the biocarbon. At each stage, the amount of adsorbed gas is determined by volumetric techniques when the pressure of the adsorbate in the gas phase has reached equilibrium. The isothermal set of adsorbed quantities at equilibrium, measured for different pressure values is called the adsorption isotherm. This isotherm is a characteristic of the surface texture studied [11,25].

Before analyzing, the sample is dried, weighed and rid of gases from ambient and experimental atmosphere by heating at 110°C and vacuuming the sample to less than 100 mTorr, during 24h. To minimize interaction of He with the biocarbon surface, free space was calculated according to Micromeritics application notes 104 and 105 [26]. Empty tubes underwent an injection of N₂ at a relative pressure of 0.3 and warm and cold free spaces were measured by He injection. Using mass and true density of the samples, free spaces were then calculated taking in account the introduction of the sample (Eq.1.7 and 8). The calculated free spaces were entered on the computer and not measured for the analysis of the sample.

$$V_{warm,calculated} = V_{warm,measured} - \frac{m_{sample}}{\rho_{sample}} \times \frac{273.15 K}{T_{amb}} \quad \text{Eq.1.7}$$

$$V_{cold,calculated} = V_{cold,measured} - \frac{m_{sample}}{\rho_{sample}} \times \frac{273.15 K}{T_{bath}} \quad \text{Eq.1.8}$$

Samples at a room temperature of 293 K were then submerged in a liquid N₂ bath at 77 K. The isotherm was performed from relative pressures 0.025 to 0.993 and 0.993 to 0.427 for adsorption and desorption respectively. BET (Brunauer, Emmett and Teller) model was applied to at least 3 points under 0.3 relative pressure [11]. The Rouquerol transformation results in a pseudo-bell curve and BET can only be applied to points in the increasing part of the bell. The BET constant was positive and the correlation coefficient was superior to 0.999. The biocarbon were studied in triplicates as to guarantee repeatability of results. For the samples, the shape of the isotherm is comparable (Fig. 1.7).

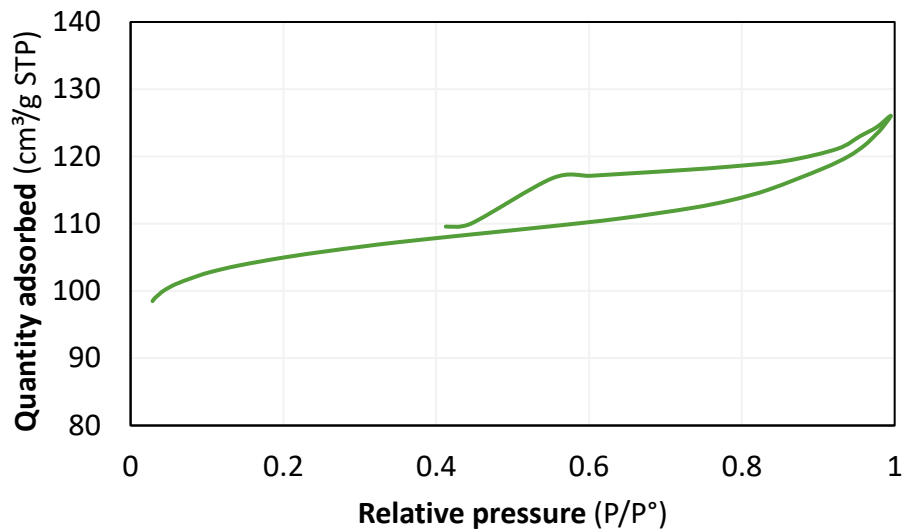


Fig. 1.7. Example of N₂ adsorption-desorption isotherm of one of the applied biocarbon

Isotherms were of type II, which is characteristic of nonporous or macroporous adsorbents [25]. Porous volume was therefore not estimated. However, for this type of pore, a hysteresis should not be possible. Here, it is a type H4, implying mesoporosity. This hysteresis might be related to cavitation and saturation pressure of the gas: biocarbon might deform under these conditions allowing for higher thresholds for N₂ adsorption and resulting in extra gas being released during desorption as the biocarbon retracts, ergo the hysteresis. Changing gases could allow for different saturation pressures and identify if this hysteresis is possible. It is also possible that these biocarbon present a combination of various types of porosity [11]. Finally, using microscopy could inform further on the type of porosity.

1.3.5. Microscopy: dispersion and phases of metals, structure and porosity of biocarbon surface

To observe the surface of the biocarbon locally, SEM is used. It functions by shooting electrons on the sample, scanning the selected zone and they are then redirected towards captors. The recollection of these electrons then forms an image that portrays the shape of the observed surface. Secondary electrons (ETD here) scrape the near surface of the biocarbon and topographic contrast is drawn: lighter means more electrons are deflected, whereas darker means the electrons are trapped. This is

the difference between hills and crevices such as pores. When detecting back-scattering electrons (ABS here) that are more energetic and seep deeper in the sample, chemical contrast is visible due to better dispersion of the electrons by heavier atoms. Lighter here means heavier and therefore metals of higher atomic number will be brighter. Also, comparable masses are difficult to differentiate therefore EDX spectroscopy is used to differentiate metals that are excited and release a specific X-ray spectrum [11]. The ESEM-FEG (type of canon) used for this work is a Thermo Fisher Quattro S under a high vacuum and with an accelerating voltage of 6 kV.

To work at a nanometric scale and go further in depth about porosity and metals, HRTEM is used [27,28]. The principle is similar to SEM but instead of detecting the electrons that are reflected by the surface, TEM captures the highly accelerated electrons that go through the sample and collide with its components. The equipment is a JEOL JEM-ARM200F Cold FEG probe Cs corrected coupled with EDS/EELS for better determination of the chemical nature of the structure.

1.3.6. TPX: Gas adsorption and surface groups

Temperature Programed (TPX) Desorption (X = D), Oxidation (X = O) and Reduction (X = R) are used to characterize the density and binding force of acid, basic and reduction sites respectively. A gas (NH_3 , CO_2 or H_2 respectively) is adsorbed at a low temperature and then they are desorbed as temperature increases, forming a peak. The position and surface area of the peaks indicate the strength and quantity of the sites. The device used is the Micromeritics Autochem 2920. TPD under He (exclusively) can be coupled with μGC to obtain additional information on the type of functional group knowing the desorbed gases released by the surface of the adsorbent and the temperature at which they desorbed [27–30].

The sample is first cleared under a flow of inert gas (He) at 40°C for 10 min followed by an isotherm at 110°C for 2h. Then, it is brought back to 50°C where the solid is then saturated with probe gases NH_3 , CO_2 , H_2 or He for 60 min then He is introduced for 2h. Probe gases are injected at a ratio with He of 5 %vol. μGC begins at this point and He continues to be injected at 50°C for 10 min before undergoing a programmed temperature rise to desorb the probe molecules. Temperature rises to 950°C and then is maintained for 2h. Desorption peaks are recorded during this program (**Fig. 1.8**). This protocol is similar for TPR but adjustments are made to the heating ramps and duration of isotherms (**Fig. 1.9**).

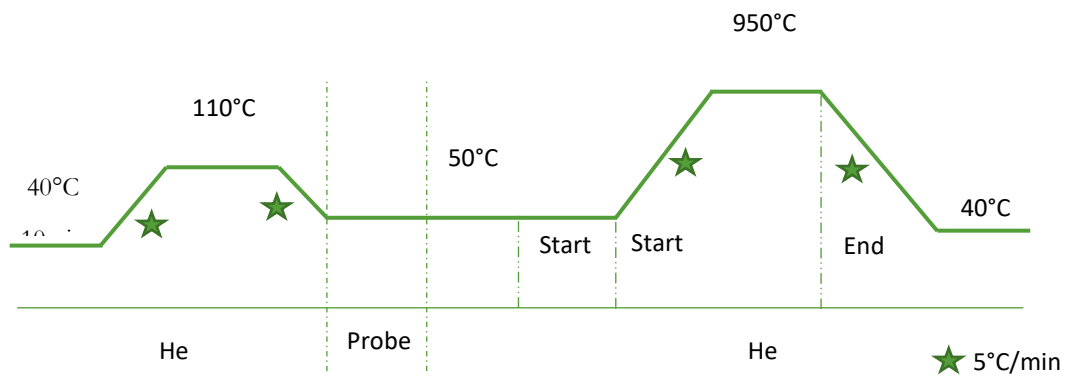


Fig. 1.8. TPD and TPO program

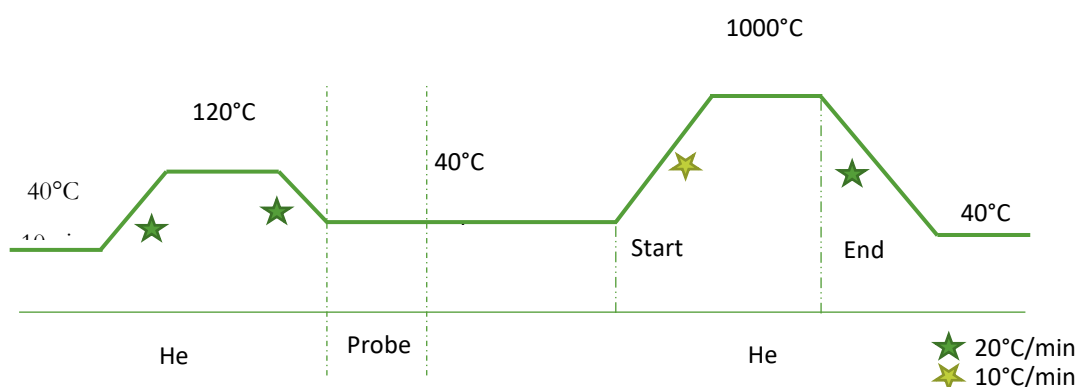


Fig. 1.9. TPR program

The TPX curves are thereafter represented as a signal from TPX directly or μGC (y) in function of time (t). Temperature can be associated to time using this program.

Deconvoluting the peaks analyzed in μGC can give further insight into the type of site. By correlating the temperature of desorption and the desorbed gas with data from literature, it is possible to identify and quantify the function group (Table 1.9).

Table 1.9. Desorption temperatures and gases associated to functional groups from literature [11,27–30]

Surface functional group	Temperature ranges (°C)		Desorbed gases
	Low	High	
Carboxyl	100	400	CO ₂ +CO
	200	300	CO ₂
	300	430	CO ₂
	400	550	CO ₂ +CO
Lactone	190	650	CO ₂
	600	750	CO ₂
	570	900	CO ₂
Peroxide	450	580	CO ₂
Anhydride	627		CO ₂ +CO
	350	450	CO
	540	640	CO
	350	627	CO ₂ +CO
Hydroxyl	570	670	CO
Phenol	580	710	CO
	690	800	CO
Ether	700		CO
	794	910	CO
Carbonyl + Quinone	800	900	CO
	700	980	CO
Quinone	830	950	CO
Pyrone	920	1023	CO

Peaks were deconvoluted using gaussian functions (Eq.1.9) from MagicPlot without imposing specified peak temperatures to obtain a fitted curve comparable to the experimental curve [28].

$$y = a \times e^{-\ln(2) \times \left(\frac{t-t_0}{dt}\right)^2} \quad \text{Eq.1.9}$$

Where a is the amplitude, dt the half width at half maximum (HWHM) and t₀ the time of the peak

Once fitted, the aforementioned parameters of the gauss peaks were extracted then their temporal ranges were estimated by adding or subtracting twice the standard deviation (σ) to the time of the peak (Eq.1.10). This range accounts for 95% of the area of the peak.

$$\sigma = \frac{dt}{\sqrt{2 \times \ln(2)}} \approx \frac{dt}{1.18} \quad \text{Eq.1.10}$$

Temperatures (T) associated to these times were deduced using a linear regression of the temperature program. The temperature ranges, smallest to biggest temperature (T_s to T_b) of the gaussian curves, were then correlated to literature and coverage of the peak in temperature range (low to high temperature, T_l to T_h) of the functions was estimated (Eq.1.11-13) to indicate the likelihood of each function being associated to the gaussian peak.

To define coverage, 6 case scenarios were considered. Two considered none coverage of the peak in the interval given by literature because the maximum between the T_s (Gauss) and the T_l (literature) was bigger than the minimum between T_b (Gauss) and T_l (literature) (Eq.1.11).

$$\max(T_s \text{ and } T_l) > \min(T_b \text{ and } T_h) \Rightarrow \text{coverage} = 0 \quad \text{Eq.1.11}$$

3 scenarios considered total or partial inclusion of the peak in the interval. Coverage was therefore defined as the ratio of the difference in the minimum between T_b (Gauss) and T_h (literature) with the maximum between T_s (Gauss) and T_l (literature), divided by the difference between T_h and T_l (Eq.1.12).

$$\text{coverage} = \frac{\min(T_b \text{ and } T_h) - \max(T_s \text{ and } T_l)}{T_h - T_l} \quad \text{Eq.1.12}$$

The last scenario considered the inclusion of the interval in the range of the peak. In this case, the coverage was indicated as probable but the choice was related to the presence of other likely functional groups. This case is likely for the groups were there is only one reported temperature (ether and anhydride).

A molar percentage of each peak was estimated by the ratio of the area of the given peak with the sum of the area of all peaks (Eq.1.13).

$$\text{Area of a gauss peak} = a \times dt \times \sqrt{\frac{\pi}{\ln(2)}} \quad \text{Eq.1.13}$$

1.3.7. XRD: main organic and inorganic speciation

During pyrolysis and the applications, mineral species can undergo changes in their chemical structure. The major species formed can be determined by XRD. A sample is exposed to X-rays that are diffracted, according to the Bragg angle 2θ , by this structure. The intensity of the diffracted ray is then measured by captors. The associated graph represents intensity in function of 2θ and using different components from databases based on organic and inorganic content of the sample, a curb can be fitted correspondingly. XRD is performed by the Philips PANalytical X'PERT PRO MDP diffractometer. The software used to extract data from the diffractogram is the PANalytical HighScore Plus. To identify the crystalline phases, the Crystallographic Open Database (COD) is used. 2θ spans 10 to 80° with a pace of 0.033° .

1.3.8. Summary

Various techniques were used to determine the biocarbon characteristics in the view of their utilization as catalysts. Indeed, the biocarbon catalysts were characterized in terms of organic element content (CHNS analysis) and inorganic element content (ICP-OES), proximate analysis and thermal stability

(TGA-DSC), surface area and surface chemical groups (BET and TPX), metal dispersion on the carbonaceous matrix (SEM and TEM), as well as the crystalline structure (XRD).

Once the efficiency of biocarbon is tested in the NO_x decomposition (deNO_x) and WGS experiments, they are again characterized according to these characterization techniques. By comparing these results with those obtained before experimentation, the factors influencing the reaction mechanisms are highlighted and related to the behavior of biocarbon.

1.4. Direct decomposition of NO_x

The biocarbon catalysts are tested for NO_x decomposition at laboratory scale, under atmospheric pressure. For this, a system consisting of a gas cylinder containing 1007 ppm NO in Ar, a rotameter, a fixed-bed reactor, three bubblers and gas analyzers is used (**Fig. 1.10**). The fixed-bed reactor consisted of a quartz tube (3.6 cm internal diameter, 85 cm long) arranged vertically in a Heraeus Ro 4/50 oven [30,31]. A thermocouple placed inside the reactor enabled the monitoring of the working temperature of the oven. Bubblers were used to trap impurities and moisture that may end up in the circuit. The first bubbler, filled with isopropanol and cooled by a thermostatic bath at 5°C, was used to trap soot, tars and other condensable gases that can form during treatments at 500°C. The other two bubblers, respectively filled with silica gel and empty, were used to trap residual moisture to prevent damage to the analytical devices. These trapped species were not quantified. The assembly of this experimental set-up was completely developed, installed and optimized during this thesis, and supposed a major experimental and analytical advance to support and enlarge the research activities of the RAPSODEE Research Center.

For the first campaign of results, a three-way valve sent gas either to a ThermoScientific 42 i-HL NO_x analyzer or to a 0.5 L sampling bag to further analyze gases in a 3000A micro gas chromatograph (μGC) [27,32].

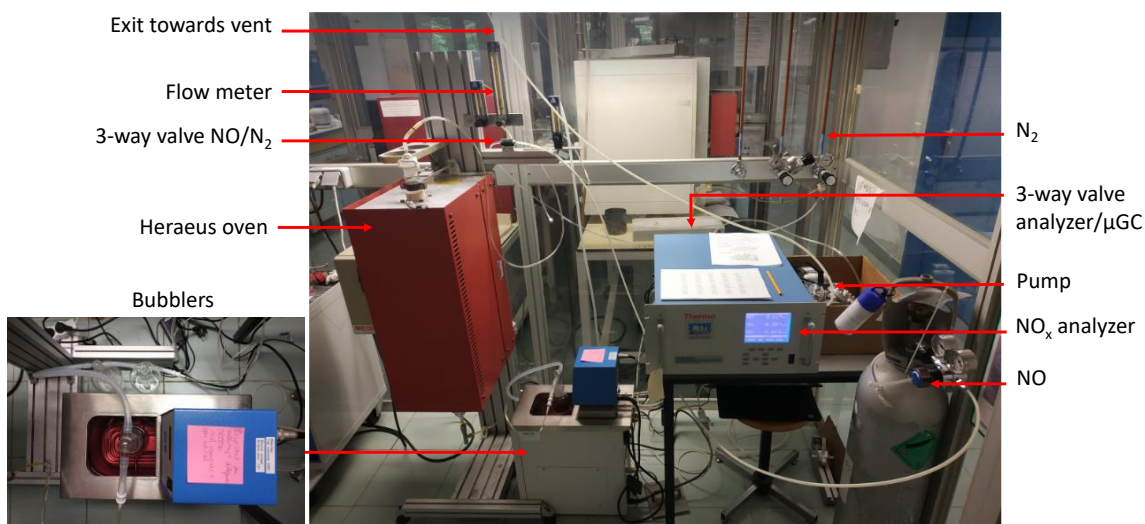
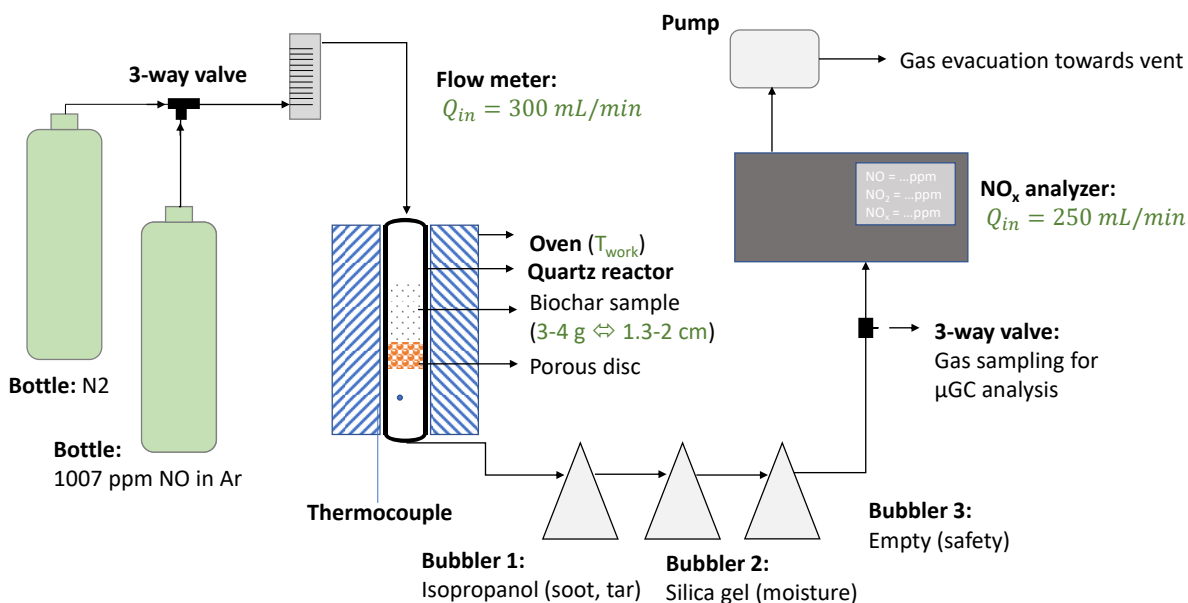


Fig. 1.10. Scheme and picture of the setup for deNO_x experiments, 1st campaign

In order to test the activity of biocarbon for deNO_x, 3 to 4 g (i.e. a bed height of 2 cm) was introduced in a quartz crucible (2.5 cm diameter, 10 cm long) with a porous bottom inside the quartz reactor on a porous disc [33]. Then, the biocarbon catalyst was heated to 140°C at 10°C/min under 300 mL/min of N₂ and this temperature was maintained for 15 min. This pretreatment eliminates traces of moisture and undesirable physisorbed compounds [34–36]. The working temperature, from ambient to 500°C, of the NO_x decomposition was thereafter set and temperature increases at 10°C/min. Once at this temperature, a flow rate of 300 mL/min of NO at a concentration of 1007 ppm with argon background was sent into the setup. This stage lasted 4 hours. Finally, the biocarbon underwent an uncontrolled cooling step under 300 mL/min of N₂. The rate was estimated at 1°C/min maximum. This protocol was repeated for samples of interest, with the NO_x treatment stage lasting 1h30. Blank tests where biocarbon was not introduced were also realized. These operating conditions were based on literature as well as the constraints of use of analytical devices [37]. The flow rate was conditioned by the NO_x

analyzer, which must receive a minimal input flow of 250 mL/min. However, the circuit induced a drop of 50 mL/min, value which was determined using a Restek ProFlow 6000 portable flow meter. The gas flow rate at the inlet of the circuit needed to therefore be set at 300 mL/min. Also, the NO_x analyzer can perceive a maximal value of 5000 ppm of NO_x, and is precise to less than 1 ppb.

The NO_x analyzer measures continuously concentrations of nitrogen oxide and dioxide (NO and NO₂) and NO_x as the sum of both. These measures are then averaged over 10 seconds and a value is saved every minute. This device (**Fig. 1.11**) functions by chemiluminescence. The reaction between NO and ozone (O₃) produces luminescent radiation with an intensity directly proportional to the concentration of NO (**Eq.1.14**).



A photomultiplier detects this luminescence and converts optical energy into electrical energy. NO₂ is thereafter converted to NO and then detected similarly. NO_x is calculated as a sum of both. This device has other protecting components such as desiccants, filters and pressure regulators.

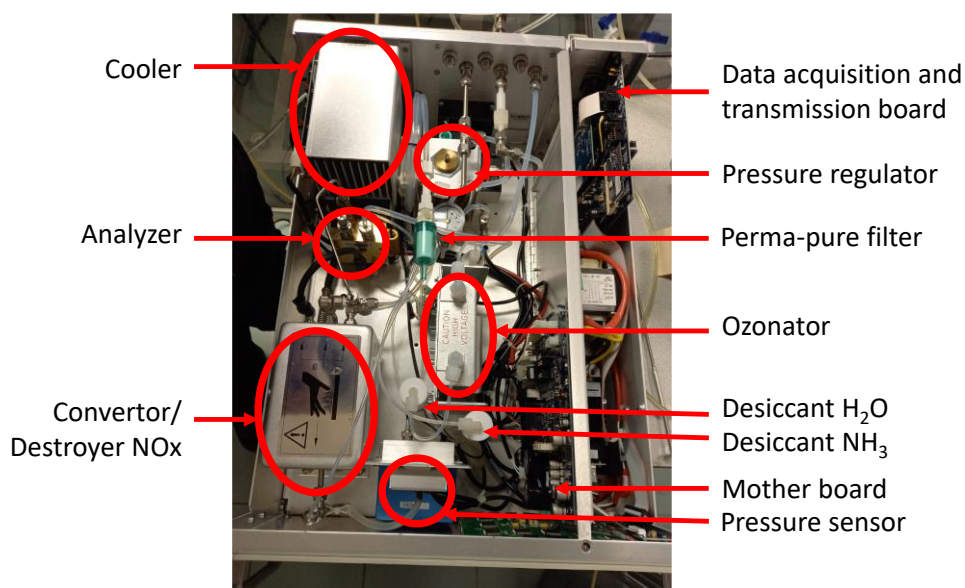


Fig. 1.11. Picture of the different components of the NO_x analyzer

As mentioned, part of the produced gases was diverted to a 0.5 L gas pocket using the three-way valve and then analyzed by an offline μGC. The gases were taken every 5 min for the first hour, then every 30 min for the remaining 3 hours. The time of an analysis is 200 seconds. During this time, gases are separated from lightest to heaviest components by 4 columns: MS5A, PPQ, PLOTU, OV1. For repeatability of the measure, the same pocket was sampled thrice. The μGC was calibrated up to 25 vol% H₂, 99.5 vol% N₂, 8 vol% O₂, 10 vol% CH₄, 25 vol% CO, 15 vol% CO₂ for the main gases and 0.5 vol% for C₂H₄, C₂H₆, C₃H₆, C₃H₈, C₄H₁₀. The vector gases were Ar and He. NO was also observed using the

bottle but the method and use by the μ GC was not adapted because a small peak is observed close to the residence time of CO_2 . In this experiment, only N_2 , O_2 , CO and CO_2 (and NO) were of interest in understanding the mechanism of reactions between biocarbon and NO_x .

Finally, the regeneration of biocarbon was studied. Above 400°C , the physisorbed species used and produced in the NO_x decomposition experiment were desorbed. Thus, the descent in temperature from 500°C to 400°C could act as an additional heat treatment to desorb these species: the sample is swept by a flow of 300 mL/min N_2 for 1h40. The effectiveness of this regeneration has been studied using the same TGA-DSC for the best samples (Table 1.7). The same temperature program as stability was employed with a focus on the DSC and a comparison with samples before NO_x treatment. Additionally, the efficiency of heat treatment to regenerate catalysts should increase with the rise in temperature [38]. However, the question of the stability of biocarbon arises. Indeed, biocarbon have an acceptable decomposition up to 500°C (Fig. 1.6). Beyond this temperature, biocarbon showed a significant mass loss due to its deterioration and modification with an increase in surface oxygen groups under the oxidative atmosphere or graphitic structures with the thermal treatment [29].

For the second campaign of results, a new μ GC (Agilent 990) was placed on-line before the NO_x analyzer due to its destructive nature and after the traps to avoid its degradation (Fig. 1.12).

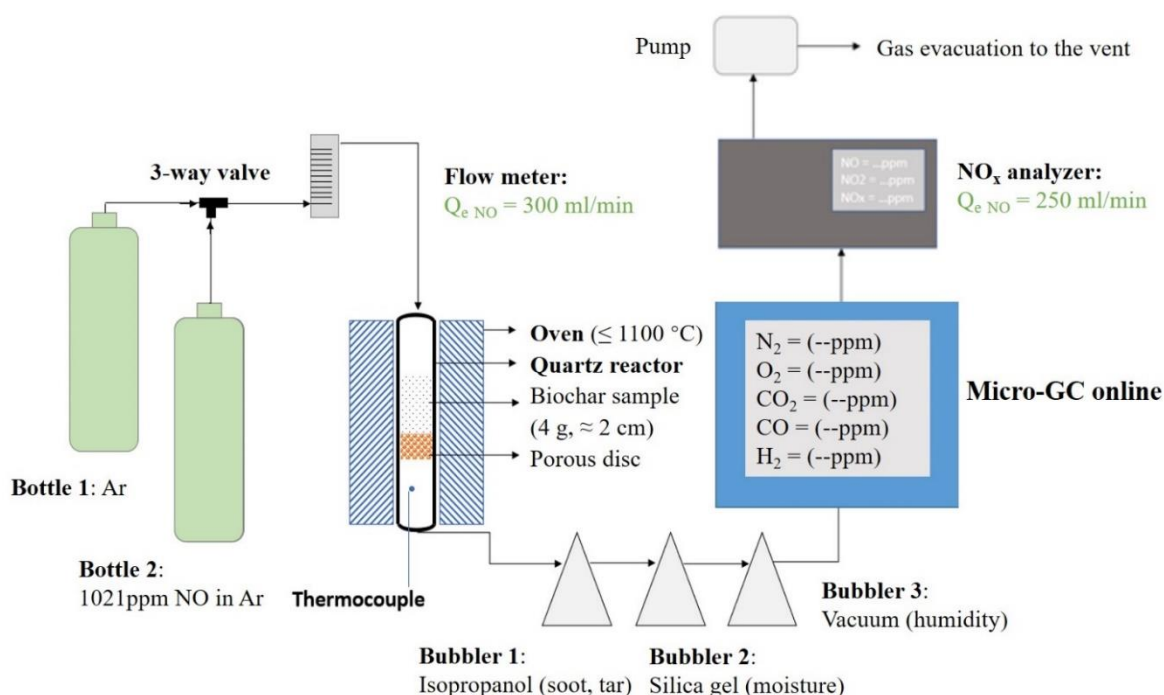




Fig. 1.12. Scheme and picture of the setup for deNO_x experiments, 2nd campaign

Similar conditions were used with little increase in flow rate to account for on-line μGC. In addition, gas was sampled once by μGC every 2.5 minutes. The on-line μGC was equipped with columns MS5A and PPU. This μGC was calibrated for H₂, N₂, O₂, CH₄, CO and CO₂. This change in configuration improved observation of the variations in gas reactants and products to go in depth in the mechanisms at play. The program was also changed (Fig. 1.13) to account for degradation of the biocarbon during the heating phase by sweeping with Ar during 30 min before and after the introduction of (1021 ppm) NO at operating temperature. The duration was also reduced to 1h.

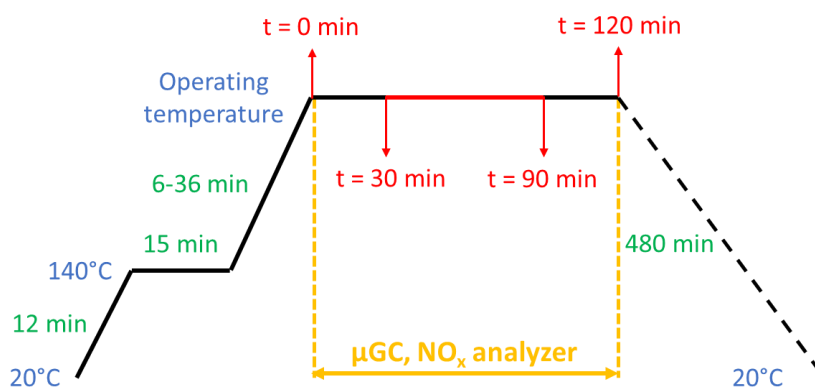


Fig. 1.13. New and optimized program for deNO_x

The evaluation of the performance of catalysts for deNO_x was not addressed in this chapter but shall be addressed later. The next section however will concern another application in which the catalysts were trialed: WGS and rWGS.

1.5. WGS and rWGS experiments

The biocarbon catalysts are secondly tested for WGS and rWGS at laboratory scale. The development, assembly and optimization of this experimental set-up was carried out during this thesis, and was recognized as an experimental set-up that contributes to reinforce and enlarge the research activities of the RAPSODEE Research Center. The biocarbon underwent an initial trial with a first setup to determine water production from rWGS and therefore the most active biocarbon (**Fig. 1.14**). Using a control box, specified flow rates of H₂, N₂, CH₄, CO₂, CO, Ar, O₂ from gas bottles (least pure: 99%) were mixed then sent towards a preheater whose temperature was also controlled and observed by the box. Water flow was controlled by a HPLC pump channeling distilled water from a semi-closed bottle to the mixer thereafter vaporized by the preheater. After preheating, the mix of gases was sent to the reactor: a ceramic tube (8 mm diameter, 25 cm long) enclosed in steel contained in a carbolite oven whose temperature was also controlled. A thermocouple was inserted in the ceramic tube to monitor the temperature at the center of the reactor and indicated on the control board. The produce gas was thereafter sent to a condenser whose temperature was indicated by the control box but controlled by a Fisherbrand Isotemp refrigerated bath circulator set at 5°C. Condensed gases such as water were collected by opening a valve and then weighed. Once cooled the gases passed by a second valve followed by a silica gel trap, adding a second manner of preventing subsequent analysis devices of being damaged by water and other condensable gases. Once the valve opened, 0.5 L sampling bags were quantified in μ GC analysis or the flow rate was observed by the portable flow meter. A back-pressure regulator was located after the sampling points and manually turned to adjust pressure. Pressure dropped when sampling due to this configuration. After the back-pressure regulator, the gases were sent to the vent from which flow rate could also be measured without disrupting activity of the catalysts.

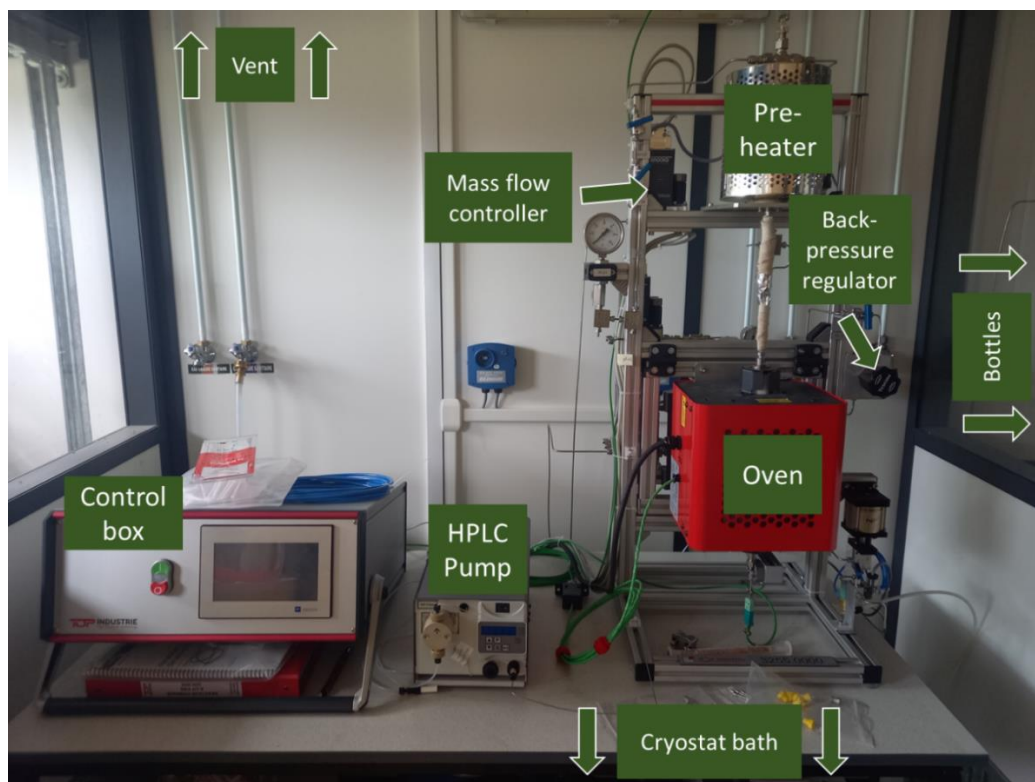
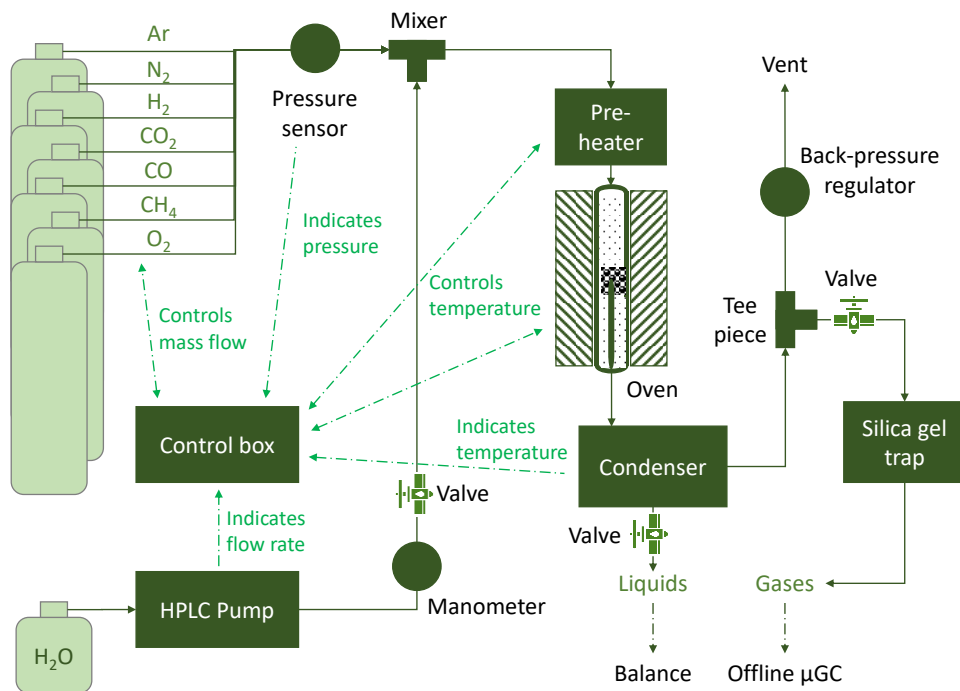


Fig. 1.14. Scheme and picture of the setup for RWGS and WGS experiments, 1st campaign

Biocarbon was introduced by inserting inert alumina (θ) up to the end of the thermocouple, then $1 \text{ g} \pm 10 \text{ mg}$ of biocarbon was mixed with $1 \text{ g} \pm 10 \text{ mg}$ of alumina to guarantee homogeneous temperature of the biocarbon and dissipate heat [28]. Alumina was then added again to enclose the sample and avoid keeping air in the reactor. The reactor was after heated under a flow of N_2 to 500°C at $8^\circ\text{C}/\text{min}$ where H_2 was added to reduce the catalyst under a volume ratio H_2/N_2 of 60%/40%. The temperature

was then reduced to 400°C at 1°C/min. At this temperature, an equimolar mix of 20 mL/min of H₂ and CO₂ was introduced, pressure was set at 3.0 ± 0.1 bar and the reaction begun. 400°C was selected as a high temperature to avoid degradation of the catalyst, to favorize at most the endothermic rWGS reaction and for possible future use as a high-temperature Fischer-Tropsch catalyst. The flow rate of reactive gases was selected to be in stoichiometric conditions and conditions of previous works on Fischer-Tropsch [28]. Pressure was raised to the highest possible for comparison with Fischer-Tropsch. 3 bar were the limit for the mass flow controllers. These conditions were maintained for 94h. This time was reduced if little to no evolution was observed. After reaction, the sample was cooled down to ambient temperature at 1°C/min using N₂.

During reaction, liquid and gas samples are taken every hour. Liquid is weighed and gas is analyzed thrice for repeatability. Due to the configuration of the setup, pressure dropped every time a liquid or gas sample was taken which could affect reactivity of the catalysts [39]. Nevertheless, during this first trial where all catalysts were tested, activity was identified based on water production. The μ GC employed is the same as for conversion of NO_x (3000A) and the same method was used. Liquid was weighed using a Sartorius balance precise to 1 mg and cumulated and total water mass were represented to facilitate the identification of the 2 most active catalysts for the following trial. The mass of the silica gel trap was weighed before and after analysis and was introduced to the results as an error: the trap could gain or lose mass depending on activity of the catalysts, duration of the reaction or heat in the cabin.

For the second campaign of results, the previous setup was changed (**Fig. 1.15**) including the μ GC (Agilent 990). The catalysts and additionally rust and Fe doped alumina were trialed in rWGS. The heating and gas programs were changed. Heating and cooling rates were 5 and 2.5°C/min respectively. The reactor was heated to 120°C under Ar and maintained for 1h to remove physisorbed molecules such as water. It was then heated to 500°C under a volume ratio H₂/Ar of 60%/40%. This step to reduce the catalyst was held for 2h and was followed by cooling to 180°C. Preheating was increased from 120 to 180°C at this step. At this temperature, the reactive gas mixture of 20, 60 and 150 mL/min for CO₂, H₂ and Ar respectively was introduced, with H₂ being in excess to force the reaction in the direction of products [40–42]. This temperature was maintained for 1h30 to observe stability of gas mixture by μ GC and no CO production was observed. This temperature was then increased to 400°C where the reaction takes place for at most 4 days, time being reduced as little to no evolution was observed. Gas was sampled every 20 minutes to maintain a frequency of 3 samples per hour. This also guaranteed that no gas could remain in μ GC. Pressure was adjusted to 3 bar as possible but was generally not fixed as a change in particle size due to milling resulted in flow resistance and increased

pressure. This however did not affect repeatability. A preheating of 180°C was chosen as result of an Aspen simulation and physical tests in WGS conditions.

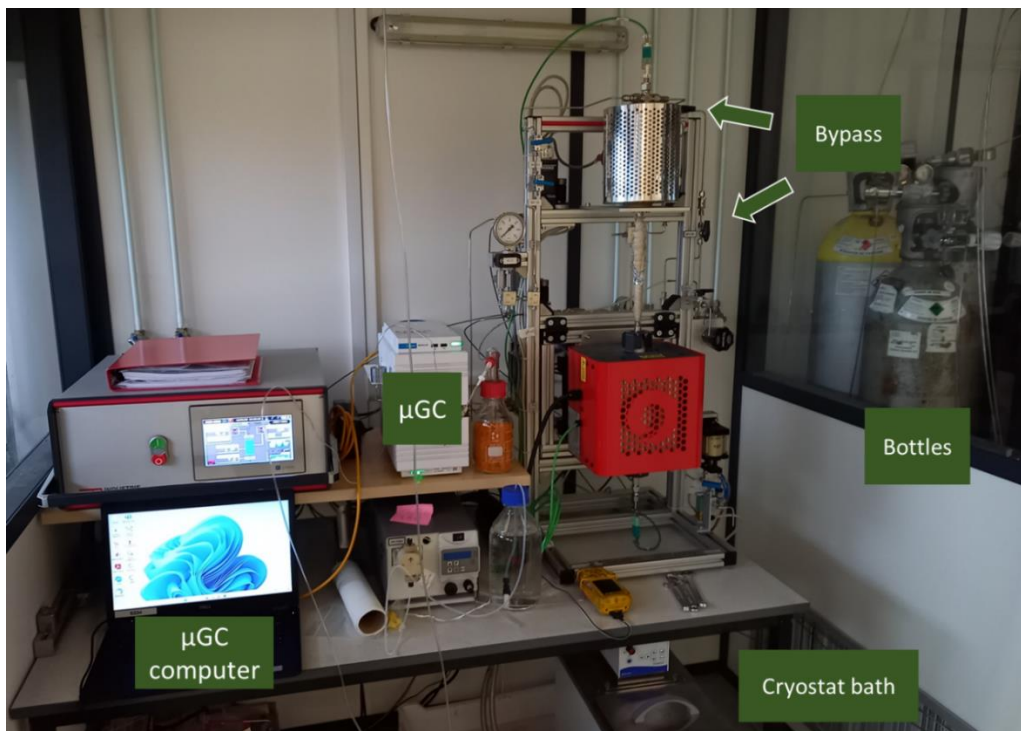
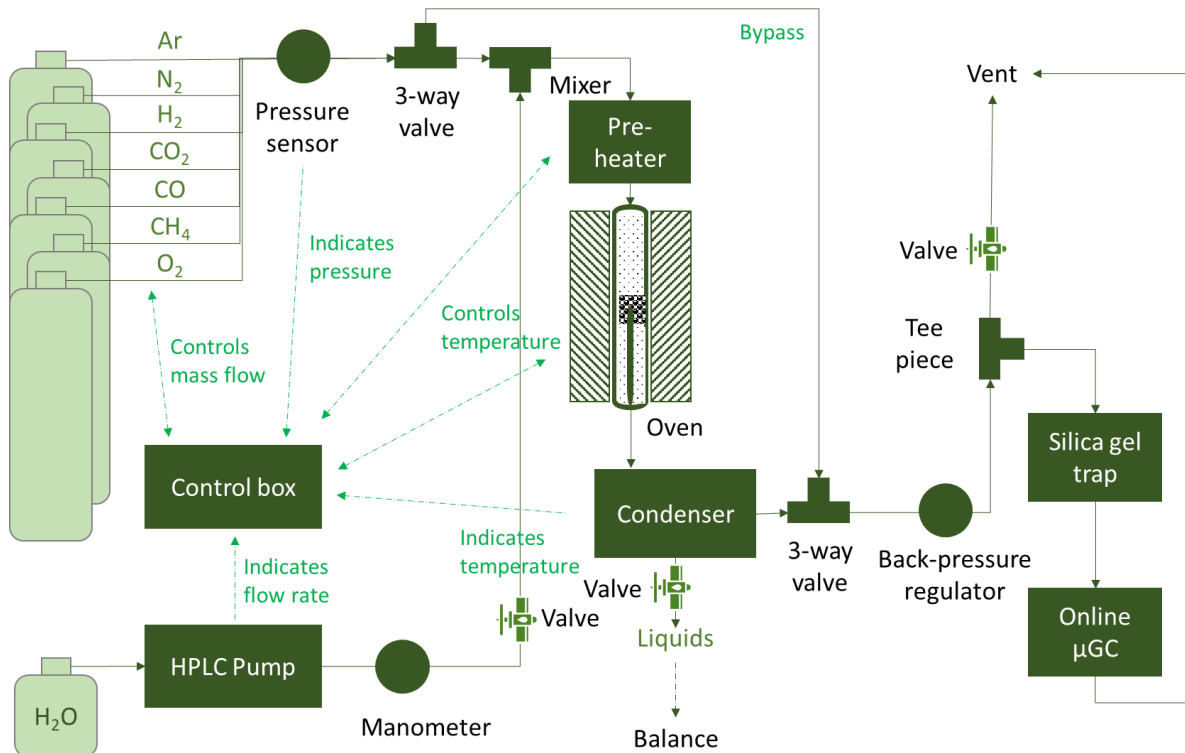


Fig. 1.15. Scheme and picture of the setup for RWGS and WGS experiments, 2nd campaign

Once active biocarbon were identified, the best (fern-based) catalysts were trialed in WGS and compared to their unimpregnated equivalent and the most active species between the rust and doped alumina. They were then repeated. Some conditions for WGS were changed: temperature was

increased from 180 to at least 280°C by 20°C steps every 1h30, and H₂ and CO₂ during stabilization of reactive gas mix, and later reaction, were replaced by 0.08 mL/min of distilled H₂O (5.5 excess) and 20 mL/min of CO [43–45]. For some catalysts, the steam excess was then varied from 1.4 to 20.7. Water mass via condensation and the trap was also only measured before reaction after the initial step at 120°C and after reaction. Total flow rate was also only measured at the beginning or the end of the reaction.

Biocarbon mixed with alumina after application were also tested for regenerability using TGA (Table 1.7). Between the cooling under inert gas after reaction and initial removal of physisorbed species at 120°C, impact of application should not be seen when catalysts are reused.

Like with deNO_x, the evaluation of the performance of catalysts for deNO_x was not addressed in this chapter but shall be addressed later, but the next section will present the methodology employed for simulating biomass pyrolysis, WGS preheating and its reaction.

1.6. Thermodynamic and process modelling

FactSage 6.3 was used to determine the speciation of metals as the pyrolysis temperature was increased or as the gaseous atmosphere was changed (**Fig. 1.2**). FactSage functions on the basis of the minimalization Gibbs free enthalpy [9,32]. Free molar enthalpy of a pure substance i in the phase α , $g^\alpha(T)$, corresponds to its chemical potential $\mu_i^{\circ\alpha}(T)$ and $g^\alpha(T) = h_i^{\circ\alpha}(T) - s_i^{\circ\alpha}(T) \cdot T$. This can be expressed as a function of molar standard enthalpy of formation (at 298 K), molar absolute standard entropy (at 298 K) and molar heat capacity (**Eq.1.15**).

$$\mu_i^{\circ\alpha}(T) = \Delta_f h_i^{\circ\alpha}(298) - s_i^{\circ\alpha}(298) \cdot T + \int_{298}^T c_{p_i}^{\alpha}(T) \cdot dT - T \cdot \int_{298}^T \frac{c_{p_i}^{\alpha}(T)}{T} \cdot dT \quad \text{Eq.1.15}$$

Once the free molar enthalpy is obtained, FactSage minimalizes free enthalpy and equates it to the sum of the products between the quantity of matter in phase α and the previously obtained molar free enthalpy (**Eq.1.16**).

$$\min(G^{tot}(T, P, N_i)) = \min(\sum_{\alpha} n^{\alpha} \cdot g^{\alpha}(T, P, x_i^{\alpha})) \quad \text{Eq.1.16}$$

The thermodynamic data used for these calculations are archived in databases and can be extrapolated if the temperature is out of range of reported values. The ones used here were FToxid (contains oxides), FTsalt (salts), FactPS (pure substances) and SGPS (complements FactPS), and were used in this order. In case an element exists in many databases, the retained data is that of the first database appearing in this order.

The studied sample was 1 kg of fern composed of 16 species (C, H, N, ...) [46]. Data was initialized at 500°C and simulated every 50°C from 500 to 1000°C. A constant flow of 65 mg every 50°C was

introduced by opening the system. This resulted in a total of 967 species that could be formed during the simulation (the limit was 1500 species).

To simulate WGS preheating and reaction in Aspen Plus V8.6, conventional H₂O, CO, CO₂, H₂, CH₄ and Ar were used from databanks PURE32, AQUEOUS, SOLIDS and INORGANIC. The Peng-Robinson method with Boston-Mathias (PR-BM) modification was used [47]. The objective of determining the temperature of the preheater was to limit possible introduction of liquid water into the reactor. A previous attempt at WGS resulted in transport of the catalyst throughout the reactor. For this, a mix of gases were supplied: 20mL/min of CO, 60mL/min of Ar and 1 mL/min of H₂O (to maximize risk), at 1 bar and 25°C. They were then preheated, possible heat loss between preheater and reactor was quantified. The percentage of vapor present in the outlet flow could then indicate the risk of introducing liquid water in the reactor. The result of this simulation is presented in the WGS chapter, but 180°C was selected as preheating temperature.

To simulate the WGS reaction, this previous model served as basis. To it was added a duplicator so as to simulate simultaneously the kinetics and the thermodynamics of WGS. Indeed, after each steam was added a reactor, plug flow and Gibbs respectively, and their own condenser (at 10°C). Thereafter, reactor temperature and steam excess were varied to observe their impact on the WGS reaction. The details of this simulation are also presented in the WGS chapter.

1.7. Conclusion

Fern and willow-based biocarbon catalysts were impregnated with Ni and Fe to test their potential catalytic activity in deNO_x, RWGS and WGS. To produce these catalysts, the biomass was pyrolyzed under a flow rate of 1 L/min N₂, with an increase in temperature from 25 to 800°C and a heating rate of 2°C/min, followed by 1-hour isotherm. This choice of conditions was based on characterizations and simulations complimented with literature. The biomass and biocarbon were impregnated with Ni and Fe salts in a water-based medium. The resulting impregnated biocarbon was then milled for homogeneity. They were also characterized through CHNS analysis, ICP-OES, TGA-DSC, BET, TPX, SEM, TEM and XRD to determine organic and inorganic element content, moisture and ash content, thermal stability, specific surface area, surface chemical groups and metal dispersion. These characterizations can help validate certain catalytic behaviors of the biocarbon catalysts as they were applied to deNO_x, RWGS and WGS reactions. The different steps to setting up these applications was presented and an optimal configuration was achieved. The development, assembly and optimization of these set-up was accomplished during this work and will be a basis for future work at the RAPSODEE Research Center. The modalities of simulated parameters and WGS was also conveyed.

The following chapters will address how these catalysts performed in relation to literature, simulated and thermodynamic data, the characterizations of these catalysts and how this affected their activity towards deNO_x, RWGS and WGS.

References

- [1] M. González Martínez, C. Dupont, S. Thiéry, X.-M. Meyer, C. Gourdon, Impact of biomass diversity on torrefaction: Study of solid conversion and volatile species formation through an innovative TGA-GC/MS apparatus, *Biomass and Bioenergy*. 119 (2018) 43–53. <https://doi.org/10.1016/j.biombioe.2018.09.002>.
- [2] Eizhy, EIZHY. (n.d.). <https://www.eizhy.fr/eizhy/> (accessed January 12, 2023).
- [3] M. González Martínez, Woody and agricultural biomass torrefaction : experimental study and modelling of solid conversion and volatile species release based on biomass extracted macromolecular components, *These de doctorat*, Toulouse, INPT, 2018. <https://www.theses.fr/2018INPT0091> (accessed January 12, 2023).
- [4] A. Kraupner, M. Antonietti, R. Palkovits, K. Schlicht, C. Giordano, Mesoporous Fe₃C sponges as magnetic supports and as heterogeneous catalyst, *Journal of Materials Chemistry*. 20 (2010) 6019–6022. <https://doi.org/10.1039/C0JM00774A>.
- [5] I. Vollmer, S. Ould-Chikh, A. Aguilar-Tapia, G. Li, E. Pidko, J.-L. Hazemann, F. Kapteijn, J. Gascon, Activity Descriptors Derived from Comparison of Mo and Fe as Active Metal for Methane Conversion to Aromatics, *J. Am. Chem. Soc.* 141 (2019) 18814–18824. <https://doi.org/10.1021/jacs.9b09710>.
- [6] J.H. Lee, H.-K. Lee, D.H. Chun, H. Choi, G.B. Rhim, M.H. Youn, H. Jeong, S.W. Kang, J.-I. Yang, H. Jung, C.S. Kim, J.C. Park, Phase-controlled synthesis of thermally stable nitrogen-doped carbon supported iron catalysts for highly efficient Fischer-Tropsch synthesis, *Nano Res.* 12 (2019) 2568–2575. <https://doi.org/10.1007/s12274-019-2487-4>.
- [7] S. Nanda, A.K. Dalai, F. Berruti, J.A. Kozinski, Biochar as an Exceptional Bioresource for Energy, Agronomy, Carbon Sequestration, Activated Carbon and Specialty Materials, *Waste Biomass Valor.* 7 (2016) 201–235. <https://doi.org/10.1007/s12649-015-9459-z>.
- [8] T. Béguerie, E. Weiss-Hortala, A. Nzihou, Calcium as an innovative and effective catalyst for the synthesis of graphene-like materials from cellulose, *Sci Rep.* 12 (2022) 21492. <https://doi.org/10.1038/s41598-022-25943-3>.
- [9] M. Said, L. Cassayre, J.-L. Dirion, X. Joulia, A. Nzihou, Effect of Nickel Impregnation on Wood Gasification Mechanism, *Waste Biomass Valor.* 8 (2017) 2843–2852. <https://doi.org/10.1007/s12649-017-9911-3>.
- [10] L. Leng, H. Huang, H. Li, J. Li, W. Zhou, Biochar stability assessment methods: A review, *Science of The Total Environment*. 647 (2019) 210–222. <https://doi.org/10.1016/j.scitotenv.2018.07.402>.
- [11] A. Nzihou, ed., *Handbook on Characterization of Biomass, Biowaste and Related By-products*, Springer International Publishing, 2020. <https://doi.org/10.1007/978-3-030-35020-8>.
- [12] ULTIMA 2 - HORIBA Scientific - PDF Catalogs | Technical Documentation | Brochure, (n.d.). <https://pdf.directindustry.com/pdf/horiba-scientific/ultima-2/25366-401301.html> (accessed March 9, 2023).
- [13] C.-B. Wang, J.-G. Chang, R.-C. Wu, C.-T. Yeh, Promotion effect of coating alumina supported palladium with sodium hydroxide on the catalytic conversion of nitric oxide, *Applied Catalysis B: Environmental*. 17 (1998) 51–62. [https://doi.org/10.1016/S0926-3373\(97\)00103-3](https://doi.org/10.1016/S0926-3373(97)00103-3).
- [14] J. Segner, W. Vielhaber, G. Ertl, Interaction of NO₂ with a Pt(111) Surface, *Israel Journal of Chemistry*. 22 (1982) 375–379. <https://doi.org/10.1002/ijch.198200067>.
- [15] D.A. Hoffman, J.B. Hudson, The adsorption and decomposition of N₂O on nickel (100), *Surface Science*. 180 (1987) 77–88. [https://doi.org/10.1016/0039-6028\(87\)90037-9](https://doi.org/10.1016/0039-6028(87)90037-9).
- [16] R. Sau, J.B. Hudson, The oxidation of carbidic monolayers on Ni(110), *Surface Science*. 102 (1981) 239–254. [https://doi.org/10.1016/0039-6028\(81\)90318-6](https://doi.org/10.1016/0039-6028(81)90318-6).
- [17] J. Despres, M. Koebel, O. Kröcher, M. Elsener, A. Wokaun, Adsorption and desorption of NO and NO₂ on Cu-ZSM-5, *Microporous and Mesoporous Materials*. 58 (2003) 175–183. [https://doi.org/10.1016/S1387-1811\(02\)00627-3](https://doi.org/10.1016/S1387-1811(02)00627-3).
- [18] G.E. Ioannatos, X.E. Verykios, H₂ storage on single- and multi-walled carbon nanotubes,

- International Journal of Hydrogen Energy. 35 (2010) 622–628. <https://doi.org/10.1016/j.ijhydene.2009.11.029>.
- [19] P. Ciambelli, V. Palma, A. Ruggiero, Low temperature catalytic steam reforming of ethanol. 2. Preliminary kinetic investigation of Pt/CeO₂ catalysts, *Applied Catalysis B: Environmental*. 96 (2010) 190–197. <https://doi.org/10.1016/j.apcatb.2010.02.019>.
- [20] X. Zhang, H. Liu, Z. Liang, R. Idem, P. Tontiwachwuthikul, M. Jaber Al-Marri, A. Benamor, Reducing energy consumption of CO₂ desorption in CO₂-loaded aqueous amine solution using Al₂O₃/HZSM-5 bifunctional catalysts, *Applied Energy*. 229 (2018) 562–576. <https://doi.org/10.1016/j.apenergy.2018.07.035>.
- [21] Y. Ji, C. Zhang, X.J. Zhang, P.F. Xie, C. Wu, L. Jiang, A high adsorption capacity bamboo biochar for CO₂ capture for low temperature heat utilization, *Separation and Purification Technology*. 293 (2022) 121131. <https://doi.org/10.1016/j.seppur.2022.121131>.
- [22] M.C. Leuenberger, M.F. Schibig, P. Nyfeler, Gas adsorption and desorption effects on cylinders and their importance for long-term gas records, *Atmospheric Measurement Techniques*. 8 (2015) 5289–5299. <https://doi.org/10.5194/amt-8-5289-2015>.
- [23] B.Q. Pham, V.H. Nguyen, T.N. Truong, Size dependence of graphene chemistry: A computational study on CO desorption reaction, *Carbon*. 101 (2016) 16–21. <https://doi.org/10.1016/j.carbon.2016.01.028>.
- [24] H. Xu, W. Chu, X. Huang, W. Sun, C. Jiang, Z. Liu, CO₂ adsorption-assisted CH₄ desorption on carbon models of coal surface: A DFT study, *Applied Surface Science*. 375 (2016) 196–206. <https://doi.org/10.1016/j.apsusc.2016.01.236>.
- [25] M. Thommes, K. Kaneko, A.V. Neimark, J.P. Olivier, F. Rodriguez-Reinoso, J. Rouquerol, K.S.W. Sing, Physisorption of gases, with special reference to the evaluation of surface area and pore size distribution (IUPAC Technical Report), *Pure and Applied Chemistry*. 87 (2015) 1051–1069. <https://doi.org/10.1515/pac-2014-1117>.
- [26] Library, Micromeritics. (n.d.). <https://www.micromeritics.com/resources/library/> (accessed March 13, 2023).
- [27] L.M.R. Millan, Steam gasification of tropical lignocellulosic agrowaste: impact of biomass characteristics on the gaseous and solid by-products, (n.d.) 208.
- [28] A.C. Ghogia, theses.fr – Amel cydric Ghogia, Développement de catalyseurs monolithiques structurés du type Co/C/mousse pour le procédé de synthèse Fischer-Tropsch, (n.d.). <http://www.theses.fr/s184711> (accessed October 18, 2021).
- [29] M. Ducouso, Gasification biochar reactivity toward methane cracking, phdthesis, Ecole des Mines d’Albi-Carmaux, 2015. <https://tel.archives-ouvertes.fr/tel-01411838> (accessed October 28, 2020).
- [30] M. Hervy, Valorisation de chars issus de pyrogazéification de biomasse pour la purification de syngas : lien entre propriétés physico-chimiques, procédé de fonctionnalisation et efficacité du traitement, These de doctorat, Ecole nationale des Mines d’Albi-Carmaux, 2016. <http://www.theses.fr/2016EMAC0013> (accessed June 15, 2021).
- [31] Z. Taheri, K. Nazari, A.A. Safekordi, N. Seyed-Matin, R. Ahmadi, N. Esmaeili, A. Tofigh, Oxygen permeation and oxidative coupling of methane in membrane reactor: A new facile synthesis method for selective perovskite catalyst, *Journal of Molecular Catalysis A: Chemical*. 286 (2008) 79–86. <https://doi.org/10.1016/j.molcata.2008.01.043>.
- [32] M. Said, Comportements et rôles des métaux lourds au cours de la pyro-gazéification de la biomasse : études expérimentales et thermodynamiques, phdthesis, Ecole des Mines d’Albi-Carmaux, 2016. <https://tel.archives-ouvertes.fr/tel-01541337> (accessed June 9, 2021).
- [33] S.A. Dastgheib, H. Salih, T. Ilangovan, J. Mock, NO Oxidation by Activated Carbon Catalysts: Impact of Carbon Characteristics, Pressure, and the Presence of Water, *ACS Omega*. 5 (2020) 21172–21180. <https://doi.org/10.1021/acsomega.0c02891>.
- [34] Dynamic Adsorption of Nitric Oxide (NO) in a Fixed-bed Reactor Using Rubber Seed Shell-derived Biochar, *Biointerface Res Appl Chem*. 12 (2021) 1638–1650.

- <https://doi.org/10.33263/BRIAC122.16381650>.
- [35] Z. Zhu, Z. Liu, S. Liu, H. Niu, Adsorption and reduction of NO over activated coke at low temperature, *Fuel*. 79 (2000) 651–658. [https://doi.org/10.1016/S0016-2361\(99\)00192-1](https://doi.org/10.1016/S0016-2361(99)00192-1).
- [36] J. Zawadzki, M. Wiśniewski, Adsorption and decomposition of NO on carbon and carbon-supported catalysts, *Carbon*. 40 (2002) 119–124. [https://doi.org/10.1016/S0008-6223\(01\)00081-1](https://doi.org/10.1016/S0008-6223(01)00081-1).
- [37] Arrêté du 2 février 1998 relatif aux prélèvements et à la consommation d'eau ainsi qu'aux émissions de toute nature des installations classées pour la protection de l'environnement soumises à autorisation - Légifrance, (n.d.). <https://www.legifrance.gouv.fr/loda/id/LEGITEXT000005625281/> (accessed January 17, 2023).
- [38] Z. Chen, Y. Peng, J. Chen, C. Wang, H. Yin, H. Wang, C. You, J. Li, Performance and Mechanism of Photocatalytic Toluene Degradation and Catalyst Regeneration by Thermal/UV Treatment, *Environ. Sci. Technol.* 54 (2020) 14465–14473. <https://doi.org/10.1021/acs.est.0c06048>.
- [39] S. Dzurzyk, E. Rezaei, Intensification of the Reverse Water Gas Shift Reaction by Water-Permeable Packed-Bed Membrane Reactors, *Ind. Eng. Chem. Res.* 59 (2020) 18907–18920. <https://doi.org/10.1021/acs.iecr.0c02213>.
- [40] S. Sengupta, A. Jha, P. Shende, R. Maskara, A.K. Das, Catalytic performance of Co and Ni doped Fe-based catalysts for the hydrogenation of CO₂ to CO via reverse water-gas shift reaction, *Journal of Environmental Chemical Engineering*. 7 (2019) 102911. <https://doi.org/10.1016/j.jece.2019.102911>.
- [41] M.R. Gogate, R.J. Davis, Comparative study of CO and CO₂ hydrogenation over supported Rh–Fe catalysts, *Catalysis Communications*. 11 (2010) 901–906. <https://doi.org/10.1016/j.catcom.2010.03.020>.
- [42] M.M. Barreiro, M. Maroño, J.M. Sánchez, Hydrogen permeation through a Pd-based membrane and RWGS conversion in H₂/CO₂, H₂/N₂/CO₂ and H₂/H₂O/CO₂ mixtures, *International Journal of Hydrogen Energy*. 39 (2014) 4710–4716. <https://doi.org/10.1016/j.ijhydene.2013.11.089>.
- [43] L. Gradisher, B. Dutcher, M. Fan, Catalytic hydrogen production from fossil fuels via the water gas shift reaction, *Applied Energy*. 139 (2015) 335–349. <https://doi.org/10.1016/j.apenergy.2014.10.080>.
- [44] H.M. Jang, K.B. Lee, H.S. Caram, S. Sircar, High-purity hydrogen production through sorption enhanced water gas shift reaction using K₂CO₃-promoted hydrotalcite, *Chemical Engineering Science*. 73 (2012) 431–438. <https://doi.org/10.1016/j.ces.2012.02.015>.
- [45] D.B. Bukur, B. Todic, N. Elbashir, Role of water-gas-shift reaction in Fischer–Tropsch synthesis on iron catalysts: A review, *Catalysis Today*. 275 (2016) 66–75. <https://doi.org/10.1016/j.cattod.2015.11.005>.
- [46] M. González Martínez, C. Dupont, D. da Silva Perez, L. Míguez-Rodríguez, M. Grateau, S. Thiéry, T. Tamminen, X.-M. Meyer, C. Gourdon, Assessing the suitability of recovering shrub biowaste involved in wildland fires in the South of Europe through torrefaction mobile units, *Journal of Environmental Management*. 236 (2019) 551–560. <https://doi.org/10.1016/j.jenvman.2019.02.019>.
- [47] L.P.R. Pala, Q. Wang, G. Kolb, V. Hessel, Steam gasification of biomass with subsequent syngas adjustment using shift reaction for syngas production: An Aspen Plus model, *Renewable Energy*. 101 (2017) 484–492. <https://doi.org/10.1016/j.renene.2016.08.069>.

Chapter 2

NO_x decomposition using nickel and iron-loaded biocarbon

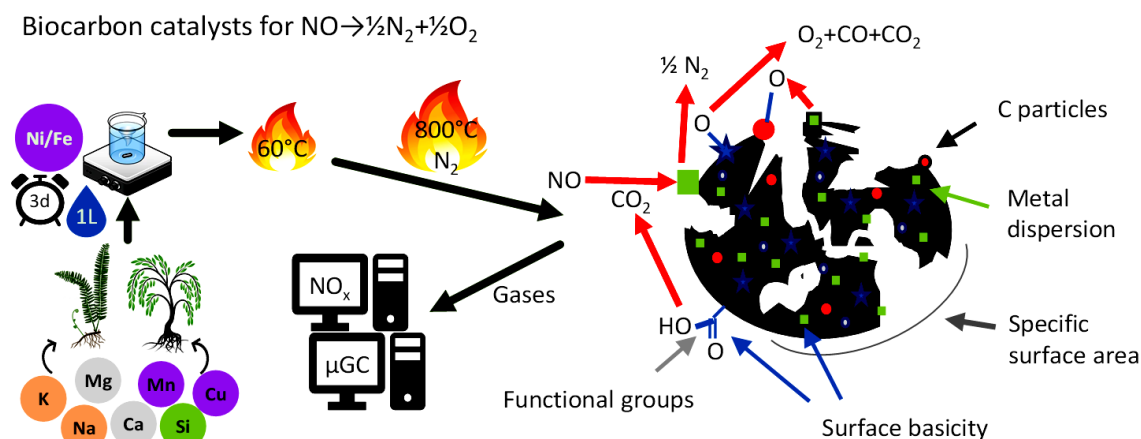
Highlights

- Ni- and Fe-loaded biocarbon performed suitably for NO decomposition.
- Biocarbon inherent metals (K, Ca, Na) showed catalytic ability to NO decomposition.
- Impregnation before pyrolysis enhanced biocarbon catalytic activity at 200 and 350°C.
- N₂ formation may indicate direct NO decomposition or NO catalytic reduction.

Abstract

Fern and willow impregnated with heavy metals (Ni/Fe) were pyrolyzed (800°C, N₂) to produce heavy metal-loaded biocarbon to be used as biocarbon catalysts for NO decomposition (deNO_x). The effects of reaction temperature (200, 350 and 500°C), type of biomass and impregnated metals were investigated on deNO_x performance using a specific on-line NO_x analyzer. Willow-based biocarbon impregnated with Fe (WFe) and Ni (WNI) achieved the highest deNO_x performance at 200°C (16.5 %) and 500°C (30.6 %) respectively. The composition and structure of biocarbon are crucial for the effective adsorption of NO and the dispersion of metal catalysts, which was evidenced by higher CO₂ adsorption (TPO), high specific surface area (419.1 m²/g for WNI), and highly dispersed small particles of Ni by SEM. Abundant inherent metals in fern allowed low temperature activity comparable to that of raw willow raw biocarbon. However, loaded metals were more active for deNO_x at higher temperatures. The main routes for deNO_x were direct decomposition of NO into N₂ and O₂, and catalytic reduction of NO on active sites producing N₂, CO and CO₂. On-line monitored H₂, CO and CO₂ production before and during reaction was linked to deNO_x and biocarbon decomposition mechanisms. Dispersed catalytic metals as well as NO adsorption and reactivity by biocarbon functional groups reflect the cost-effective and eco-friendly potential of biocarbon catalysts for deNO_x.

Graphical abstract



2.1. Introduction

As one of the major air pollutants, nitrogen oxides (NO_x) are responsible to the formation of acid rain, photochemical smog, the depletion of ozone and respiratory diseases, seriously affecting human health and the environment [1–3]. NO_x are mainly emitted from the combustion of fossil fuels and some fundamental industrial processes [4,5]. As nitrogen oxide (NO) takes up the majority of NO_x emissions (> 95%), its removal remains a growing global concern [2,5]. Currently, selective catalytic reduction (SCR) and three-way catalysts are widely used to decompose NO_x in fixed and mobile sources, respectively [6]. Even if SCR can achieve a NO_x decomposition (deNO_x) efficiency of 90 %, it requires ammonia as reducing agent and its leakage can cause secondary pollution [7,8]. Regarding commercial catalysts used in pipes of gasoline-engine vehicles, they contain expensive rare metals with considerable environmental impacts. Therefore, there is an urgent need to develop catalysts able to convert NO_x pollutants in an effective, sustainable and economic way.

2.1.1. NO decomposition mechanisms

The homogeneous decomposition of NO (**Eq.2.1**) is thermodynamically feasible with $\Delta G = -86.6 \text{ kJ/mol}$ at 100 °C [2]. However, the strong binding energy between N and O atom ($\sim 630.6 \text{ kJ mol}^{-1}$) results in a high activation energy ($\sim 335 \text{ kJ mol}^{-1}$) for this reaction [9]. Various catalysts have been proposed to bring down the activation energy of NO direct decomposition, from noble metals [10–12], simple metal oxides [13–15], rare-earth metal oxides [16,17], complex metal oxides [18–20] to zeolites [21,22] and graphene catalysts [23]. These catalysts suffer high prices (noble metals and rare-earth metal oxides), high reaction temperatures (noble metals) and low activity with the presence of oxygen (Cu-ZSM-5, perovskite-type oxides), which might impede their practical applications [2,24].



The high binding energy between N-O also complicates activation on catalytic surfaces compared to C-H, C-C and H-H bonds [25]. Therefore, the catalytic pathways for NO direct decomposition over different catalysts remain controversial with various mechanisms being proposed [2]. The widely accepted mechanism is that NO molecules adsorb on the active sites and are dissociated to form N₂ and O₂; the active sites are regenerated after the desorption of the produced N₂ and O₂ molecules. Nevertheless, the adsorption sequences of two NO molecules, the reaction intermediates, and the rate determining step (RDS) still remain controversial [2].

The Langmuir–Hinshelwood (L–H) model indicated that two NO molecules simultaneously adsorbed on the vacant active catalyst sites (Eq.2.2-5, represented as *) [26]. The chemical adsorption of NO is single-layered, occurring on free sites only with adsorbed molecules that do not interact with each other. Therefore, under this model the reaction of two adsorbed NO species is the RDS [26].



The Eley-Rideal (E-R, Eq.2.6-10) model supported the successive adsorption and the reaction between the firstly adsorbed NO species and NO molecule colliding from the gas phase [27]. In this mechanism, the reaction of a gas-phase NO molecule and adsorbed NO or an N-containing species such as a nitrate or nitrite ion or a dinitrosyl species on the catalyst surface is assumed to be the RDS [28].



2.1.2. Biocarbon for NO decomposition

Biomass, due to its low cost, availability and carbon neutral potential, is a promising raw material for the production of carbon-rich materials, which have been widely employed as catalysts and catalytic supports in various applications [29–31]. Biocarbon (or biochar) is an eco-friendly carbon-rich material produced through the torrefaction, pyrolysis or gasification of biomass, which has been given diverse applications including catalytic supports and catalysts [29,32,33].

Biocarbon has been found effective in deNO_x without the use of additional reducing agents such as ammonia [34]. To maximize the catalytic performance of biocarbon, activation and functionalization strategies are needed, including impregnation, physical and chemical activation as the most common methods [35]. Impregnation is a preferred choice as it incorporates active metallic species into the structure of the biocarbon by mixing biomass or biocarbon with metal precursors, which is the most direct way to imitate the contamination of metals. Active interfaces and binding sites are created during impregnation, which increases the active surface area and the total volume of pores [35].

2.1.2.1. Biocarbon structure

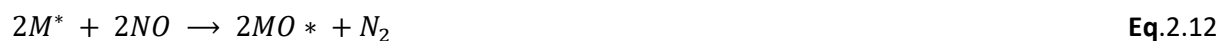
The high specific surface area, well-developed pore structure, and abundant surface functional groups of biocarbon make it competitive to current carbon-based catalytic supports [36–38]. Moreover, the intrinsic heteroatoms (e.g. N, O, S, P) and metallic compounds impregnated in the biocarbon add to the catalytic performance of biocarbon itself [29]. In addition, the surface characteristics of biocarbon can be controlled by further physical or chemical activation processes, allowing for the targeted design for various catalytic scenarios [29,38].

2.1.2.2. Biocarbon metallic elements

For the preparation of biocarbon as an effective biocarbon catalyst for deNO_x, the nature of biomass materials plays an important role. Hyperaccumulators, which absorb heavy metals through phytoextraction, and enrich themselves with heavy metals during their growth [39,40], are a pertinent resource for this application. According to the literature, after the pyrolysis of heavy metal-polluted biomass at 600°C, more than 98.5 wt% of heavy metals such as Ni, Zn, Cu and Co, are retained in the biocarbon [41–43]. These heavy metals, especially transition metals such as Ni, Fe and Cu, can act as excellent in-situ catalysts for deNO_x. This offers an environmentally friendly solution not only for deNO_x but for a wide range of applications including soil and water remediation.

Transition metals generally have strong redox ability because of their unique valence electron structure [44,45]. Among them, iron and nickel are widely available, cheap and, more importantly, iron

is not toxic. When the biocarbon is impregnated with Ni or Fe, NO will preferentially react with catalytic metals. NO will first be reduced by zerovalent Ni or Fe, forming N₂ or N₂O. The resulting metal oxides are then reduced by carbon, forming zerovalent metals again (Eq.2.11-13).



Where M is Ni or Fe, and x = 1 or 2 in case of CO or CO₂ being produced.

At temperature above 200°C, the addition of both Ni and Fe was found to significantly enhance deNO_x on carbon surface, while Ni has better performance than Fe [31]. Indeed, the redox property of the metals (Ni > Fe) seems decisive in their catalytic activity, especially at relatively high temperature [31]. In short, metal catalytic activity for deNO_x by carbon is the result of two factors, the tendency of the metal to be oxidized by NO and the easiness of the resulting metal oxide to be reduced by carbon [46,47]. During slow pyrolysis, the biomass is steadily decomposed into gaseous or solid products, which act as reducing agents for the reduction of high valence metal precursors (Ni²⁺/Fe³⁺) [48]. The formed metal nanoparticles are well dispersed inside the biocarbon due to the release of volatiles and could in turn catalyze the carbonization of biomass to improve biocarbon quality [48–50]. For the impregnation with Ni, the nickel ion is used in form of [Ni(H₂O)₆]²⁺, and is subsequently converted into Ni(OH)₂ and then into NiO during thermal treatment [51,52]. With carbon as a reductant, the metallic nickel can be generated via the reaction 2NiO + C → 2Ni + CO₂ [53,54]. Finally, the embedded metallic Ni nanoparticles induce highly active catalytic sites in regards to their dispersion and interaction with the carbon matrix [49,50,55]. Similarly, oxidized iron can be simultaneously reduced to zerovalent iron and other crystalline forms of iron during pyrolysis [56,57].

2.1.3. Objective of this study

In this study, fern (herbaceous) and willow (hardwood) impregnated with nickel (Ni) and iron (Fe) before pyrolysis were used to mimic a hyperaccumulative resource with short growth cycle and easy availability [58]. Biocarbon catalysts before and after deNO_x experiments were characterized in terms of their elemental and inorganic composition, specific surface area, surface functional groups, porosity and thermal behavior. The effects of reaction temperature, nature of biomass, impregnated metals on deNO_x performance were investigated and linked to the properties of the biocarbon catalyst.

2.2. Materials and methods

2.2.1. Preparation of biocarbon catalysts

Fern and willow were selected as raw materials for this study. As short rotation coppices, they present a fast growth and short cycle, which justified their interest in phytoremediation and rapid metal accumulation. For the large-scale production of biocarbon catalysts, availability and abundance of the bioresource in the territory needs to be considered for its selection. To simulate heavy metal content, impregnation of raw biomass with Ni or Fe nitrates ($\text{Ni}(\text{NO}_3)_2 \cdot 6\text{H}_2\text{O}$ and $\text{Fe}(\text{NO}_3)_3 \cdot 9\text{H}_2\text{O}$) was carried out. In a preliminary study, impregnation of biocarbon (after pyrolysis) resulted in a generally poorer deNO_x performance than impregnation of biomass (before pyrolysis, Table 2.1). This might be attributed to the anchored metals on the surface blocking the pores of biocarbon during post-impregnation, which resulted in the reduced surface porosity and surface area of biocarbon [32]. Therefore, in this study, only impregnation before pyrolysis was carried out to investigate further in the deNO_x mechanism with optimized experiment set-ups and processes.

Table 2.1. Steady state deNO_x ratio (X_{NO}) of different biocarbon catalysts, from a preliminary study

T (°C)	Biomass	Ni		Fe	
		Before pyrolysis	After pyrolysis	Before pyrolysis	After pyrolysis
X_{NO} (%)					
200	Fern	4.1	12.9	22.5	10.4
	Willow	16.4	7.4	19.0	10.4
500	Fern	33.8	23.1	32.7	25.2
	Willow	55.8	35.1	28.4	28.8

Wetness impregnation (WI) was applied to raw biomass. This method consists of the active metallic species incorporation into biocarbon structures via (in-situ) mixing of feedstock with metal precursors, forming active interfaces and binding sites [35,56]. For each round of impregnation, 20 g of biomass was submerged in 1 L aqueous solutions containing Fe or Ni nitrates, stirred for 3 days to reach optimal dispersion of metallic species [59]. The amount of Fe and Ni nitrates used are calculated based on the final goal of reaching a same quality of metal load in biocarbon (30 mg metal per g of biocarbon, Table 2.2). Three different Fe and Ni impregnation concentrations were used for fern (FFe*, FNi* and FNiFe were only tested at 500°C). Following the impregnation, the biomass was filtered and dried for 24 hours at 60°C [59].

Table 2.2. Mass of biomass and metal nitrates used for impregnation

Biocarbon	Name	Biomass	Metal	Biomass (g)	Metal nitrates (g)
Fern biocarbon impregnated with Ni before pyrolysis	FNi	Fern	Ni	21.8	9.8
Fern biocarbon highly impregnated with Ni before pyrolysis	FNi*	Fern	Ni	23.1	26.1
Fern biocarbon impregnated with Fe before pyrolysis	FFe	Fern	Fe	21.7	25.7
Fern biocarbon highly impregnated with Fe before pyrolysis	FFe*	Fern	Fe	21.9	55.4
Fern biocarbon impregnated with Ni and Fe before pyrolysis	FNiFe	Fern	Ni Fe	21.4	21.6 28.4
Willow biocarbon impregnated with Ni before pyrolysis	WNi	Willow	Ni	21.6	4.4
Willow biocarbon impregnated with Fe before pyrolysis	WFe	Willow	Fe	20.4	4.1

In this study, the impregnated biomass was pyrolyzed under 1 L/min N₂ from 25 to 800°C, at 2°C/min, followed by a 1h-isothermal step at 800°C. For each pyrolysis experiment, 9-10 g of biomass was placed into the crucible and the biocarbon generated was 2-3 g depending on the sample. This would give a proximate solid yield of 25 wt%. Unimpregnated fern biocarbon (RF) and willow biocarbon (RW) were prepared under the same pyrolysis conditions for comparison.

2.2.2. deNO_x experiments

The performance of prepared biocarbon catalysts in deNO_x was tested at laboratory scale. The experimental set-up (Fig. 2.1), conceived during this PhD work, consisted in a fixed-bed reactor followed by a cold trap system, an on-line μGC (Agilent 990) and an on-line NO_x analyzer (ThermoScientific, 42i-HL). The fixed-bed reactor consisted of a quartz tube with a porous disc in the isothermal area of the reactor, so the sample could be placed in a quartz crucible on it. The fixed-bed reactor was arranged vertically in a Heraeus furnace (D-6450 Hanau), able to work up to 1100°C. Cold traps were used to trap impurities and moisture that may end up in the circuit. The first cold trap, filled with isopropanol and cooled by a thermostatic bath, was used to trap soot and tars that can form during treatments at high temperatures (500°C). The other two traps, at room temperature, respectively filled with silica gel and empty, were used to trap residual moisture to prevent damage to the analytical devices. On-line μGC monitored the outlet gas composition (N₂, O₂, CO₂, CO and H₂) with an interval of 2.5 min. On-line NO_x analyzer monitored outlet NO and NO₂ concentration with an averaging time of 1 min.

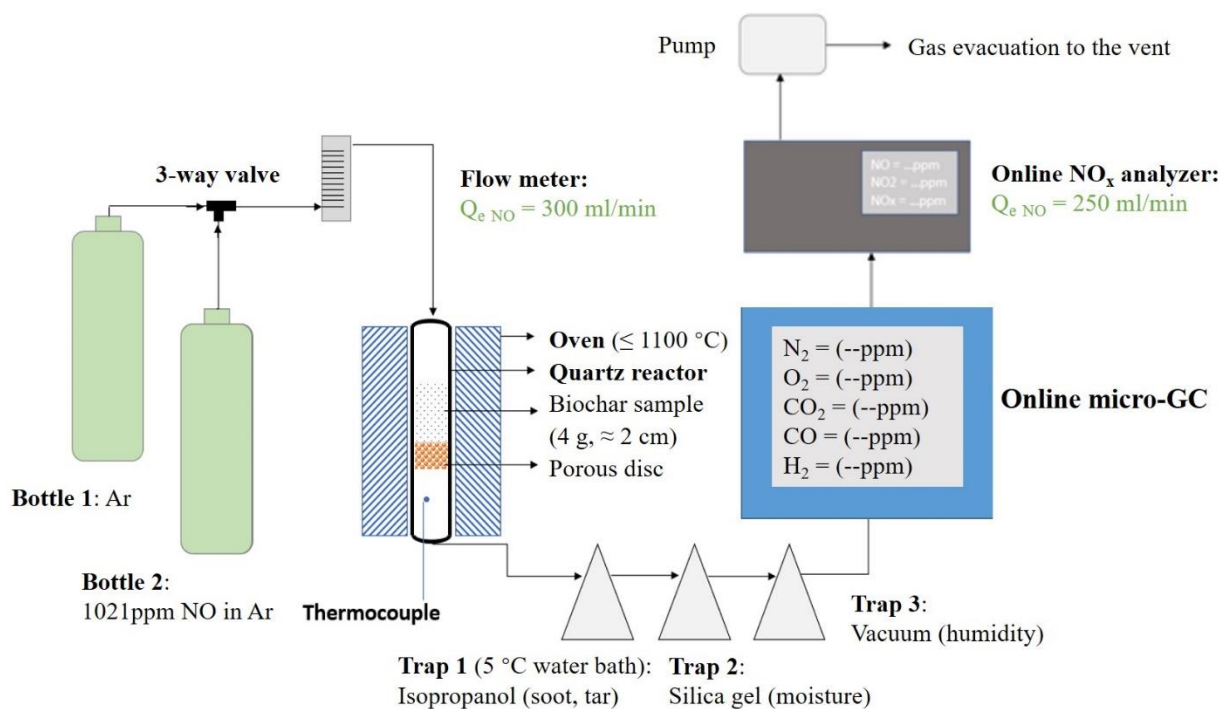


Fig. 2.1. Experiment set-up for testing deNO_x performance of biocarbon catalysts

4 g (i.e. a bed height of around 2 cm) of biocarbon catalyst were placed in a quartz crucible inside the quartz reactor [60]. The temperature of the oven was then raised to 140°C under constant argon (Ar) flow (300 mL/min, 1 atm) and kept for 15 min to eliminate traces of moisture and undesirable compounds [61–63]. After that, the temperature was raised to the experiment temperature (200, 350 or 500°C) with a heating rate of 10°C/min. The beginning of the experiment was considered when the isothermal step was reached the experiment temperature (set as t = 0 min, Fig. 2.2). During the first 30 min, CO, CO₂ and H₂ were released. This production was related to the thermal decomposition of the catalysts and was measured by the online μGC under Ar flow. At 30 min, the inlet gas was switched to a constant flow of 1021 ppm NO in Ar (300 mL/min, 1 atm). This concentration was chosen to simulate the high concentration of nitric oxide (600-1200 ppm) in exhaust gas [25]. The deNO_x performance was tested for 1 hour. Finally, the gas was switched again to Ar and kept for 30 minutes to observe the desorption phase. At the end of the experiment, the reactor was cooled down and the spent biocarbon catalyst was stored for characterization. Extended experiments were carried out for selected samples to evaluate the degradation of catalysts, with a longer exposure under NO flow (4 h).

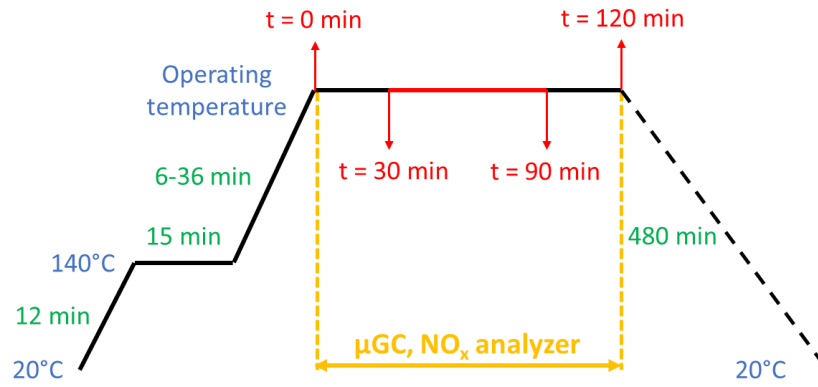


Fig. 2.2. Temperature program of the oven during one standard experiment

To compare the deNO_x performance, the deNO_x ratio was calculated as the percentage of NO being removed after contacting with biocarbon catalysts (Eq.2.14).

$$X_{NO} = \frac{C_{NO,in} - C_{NO,out}}{C_{NO,in}} \quad \text{Eq.2.14}$$

Where X_{NO} is the deNO_x ratio, $C_{NO,in}$ is the inlet NO concentration, $C_{NO,out}$ is the outlet NO concentration, which is the measured value on the NO_x analyzer. For $C_{NO,in}$, it is calculated with the average NO concentration of respective blank test.

Repetitions of experiments were conducted on selected samples, including FNi, WNi and WFe at 200°C. Their standard deviations of X_{NO} (Eq.2.14) are 0.02 %, 1.78 % and 0.83%, respectively.

2.2.3. Characterization techniques

Biocarbon catalysts were characterized in terms of organic element content (CHNS analysis, Flash 2000) and inorganic element content (ICP-OES, Ultima 2) before and after deNO_x experiments. The dispersion of metals on the carbonaceous matrix were characterized with SEM and TEM. The biocarbon thermal stability was determined with TGA-DSC (Setaram Labsys Evo 1600). The surface area and surface chemical groups were characterized by BET (Micromeritics Tristar II 3020) and TPD, TPR, TPO (Micromeritics Autochem 2920), respectively.

2.3. Results and discussion

2.3.1. Biocarbon characterization

2.3.1.1. Elemental composition

The biocarbon catalysts produced were characterized in terms of elemental composition before and after deNO_x experiments (Table 2.3). The results showed higher C content for willow-based than for fern-based catalysts, which was coherent with biomass composition (woody vs. herbaceous) [58,64].

Impregnation of both Ni and Fe resulted in slight to important changes in the organic composition of biocarbon. A slight increase of C content was generally observed after deNO_x experiments due to thermal decomposition, the total observed mass loss being around 5 to 10 %.

Table 2.3. CHNS elemental composition of biocarbon catalysts characterized before and after 500°C deNO_x experiments

Sample	deNO _x	C	H (wt%, moisture free)	N	S
RF	Before	72.78	0.93	1.47	<0.01
	After	70.92	1.00	1.52	<0.01
FNi	Before	71.23	0.73	1.86	<0.01
	After	72.78	0.83	1.57	<0.01
FNi*	Before	54.68	0.86	1.28	<0.01
	After	57.66	0.52	1.22	<0.01
FFe	Before	71.01	0.49	1.07	<0.01
	After	72.05	0.51	0.94	<0.01
FFe*	Before	52.43	0.47	0.74	<0.01
	After	53.36	0.38	0.71	<0.01
FNiFe	Before	66.99	0.84	1.15	<0.01
	After	72.28	0.52	1.16	<0.01
RW	Before	80.07	1.32	0.81	<0.01
	After	83.22	1.24	0.89	<0.01
WNI	Before	80.34	0.73	0.71	<0.01
	After	87.14	0.51	0.85	<0.01
WFe	Before	82.55	0.74	0.62	<0.01
	After	86.12	0.69	0.67	<0.01

The inorganic composition of biocarbon catalysts were based on ICP-OES analysis (Table 2.4). Raw biocarbon (RF and RW) had negligible content of Fe and Ni, while the impregnation brought the value above the thresholds of hyperaccumulation (> 3000 µg/g biocarbon, [65]). Both RF and RW biocarbon had high AAEM content: RF was especially rich in K and had high content of Na, Mg and Ca; while RW was especially rich in Ca and had high content of K. Impregnation with Ni and Fe salts resulted in the leaching of inherent AAEM, which might reduce catalytic performance. Alkali/alkaline-earth metal (AAEM) ions have been proved to be effective in promoting the deNO_x activity for many simple metal oxides [2]. They play multiple roles including increasing the surface area, creating basic sites to promote NO adsorption, facilitating the desorption of O₂ and forming active sites, leading to enhanced activity [2]. Therefore, AAEM can be seen as inherent metals that may present a catalytic activity for deNO_x. Si content is very high in fern biocarbon, compared to the relatively small content in willow biocarbon, which is caused by the nature of biomass. Si is an inhibitor for deNO_x. It can deactivate the inherent K by forming silicate in pores and encapsulates active sites, which reduces the accessibility to

active sites, thus reducing catalytic activity [66]. Additionally, the increase in Ni and Fe content helps catalyze pyrolysis and dilutes the organic content by increasing inorganic mass [67]. Both could explain the decrease in organic content (Table 2.3) and the decrease seems more important as inorganic content is high (FFe* and FNi* compared to RF).

Table 2.4. Inorganic composition of biocarbon catalysts before deNO_x experiments

Sample	Fe	Ni	K	Na	Mg	Ca	Si
($\mu\text{g/g}$ biocarbon)							
RF	263	1	19192	3822	2759	9321	17450
FNi	556	86204	930	621	605	4242	23342
FNi*	641	379582	12244	1996	1825	8098	22281
FFe	131669	49	3976	1218	887	3436	44151
FFe*	641730	69	8641	1605	1754	7525	35709
FNiFe	103030	80800	3619	904	1055	4708	45653
RW	279	16	6660	245	1958	23393	1058
WNi	< 1	24075	2003	< 1	745	7349	401
WFe	46409	45	1395	< 1	562	1059	< 1

2.3.1.2. Surface characterization

The biocarbon catalysts were characterized in terms of specific surface area and porosity type through BET analysis under N₂. Furthermore, the surface chemical groups were analyzed through temperature programmed desorption (TPD, NH₃), oxidation (TPO, CO₂) and reduction (TPR, H₂) (Table 2.5).

The quantity of chemical surface groups and specific surface area are lower for RF biocarbon than for RW biocarbon. Lower specific surface of RF biocarbon (8.8 m²/g) could be due to lower volatile matter content resulting in less porosity generated during pyrolysis, and this is coherent with herbaceous type biomass data from the literature [64,68,69]. Impregnation impacts little the chemical adsorption, as the total adsorption of three gases (NH₃, CO₂ and H₂) are similar as long as the biocarbon composition remains the same. However, biocarbon impregnated with both Ni and Fe showed higher specific surface area (> 150 m²/g) than raw biocarbon (< 50 m²/g), which was also observed in previous studies [70]. This increase could be attributed to the intensifying volatile release during pyrolysis, resulting in the formation of internal porous structure, while the presence of Ni and Fe (Table 2.4) catalyzes this process [71,72]. Introduction of metals onto the biocarbon could lead to a blocking of pores that reduces access to surface area and adsorption sites for gas (Table 2.5, FFe*) [73]. Indeed, a loss of pores induces a decrease in surface area. If increased, then porosity is developed and can reflect better access to adsorption sites and could result in higher adsorbed gases. This increase due to impregnation is however not as noticeable as the difference in adsorption between bioresource. This means that the surface groups that the biocarbon develops during pyrolysis could have a higher impact on the

adsorption of gases than the presence of metals. Therefore, the combination of highly dispersed active sites that perform deNO_x and the omnipresence of NO adsorption sites provided by the surrounding biocarbon could possibly result in high performance.

Table 2.5. Surface chemical groups and specific surface area of biocarbon catalysts before deNO_x

Sample	TPD-NH ₃		TPD-CO ₂		TPD-H ₂		Specific surface area (m ² /g)
	Total adsorption (mmol/g)	T _{max} (°C)	Total adsorption (mmol/g)	T _{max} (°C)	Total adsorption (mmol/g)	T _{max} (°C)	
RF	0.779	913	12.003	915	2.545	993	8.8
FNi	1.480	912	16.207	920	2.921	986	151.6
FNi*	0.645	939	8.975	934	1.684	999	187.5
FFe	0.553	951	8.258	905	0.158	981	309.6
FFe*	0.485	956	6.360	940	1.657	990	259.4
FNiFe	1.088	923	15.980	924	0.994	1000	367.9
RW	1.460	889	23.288	907	1.501	999	42.4
WNi	1.968	949	25.458	914	0.282	988	419.1
WFe	1.249	960	27.773	935	2.108	985	384.2

Imagery of the catalysts was also performed through SEM (Fig. 2.3). Dispersion of metals was observable for willow biocarbon but not for fern biocarbon due to the higher metal content and their lack of discernible feature (dots of Ni). This lack of distinctive structure could be indicative of agglomerated metals and could explain lesser activity and gas adsorption capabilities on behalf of the fern biocarbon (Table 2.5). However, fern biocarbon possesses higher inorganic content (Table 2.4) which could be beneficial to deNO_x. It was also possible to see some exposed inherent metals that constitute the structure of willow and is associated with wood bark [74]. It was also noted that some metals may be covered by a sheet of carbon that could result in loss of active sites (Fig. 2.4). This sheet could have been formed during pyrolysis and deposited on the reactive metals, and could induce loss in reactive sites and gas adsorption capabilities without losing specific surface area [75]. This could also be a possible source of C for selective reduction of NO or a reduction source for oxidized metals (Eq.2.13) [76].

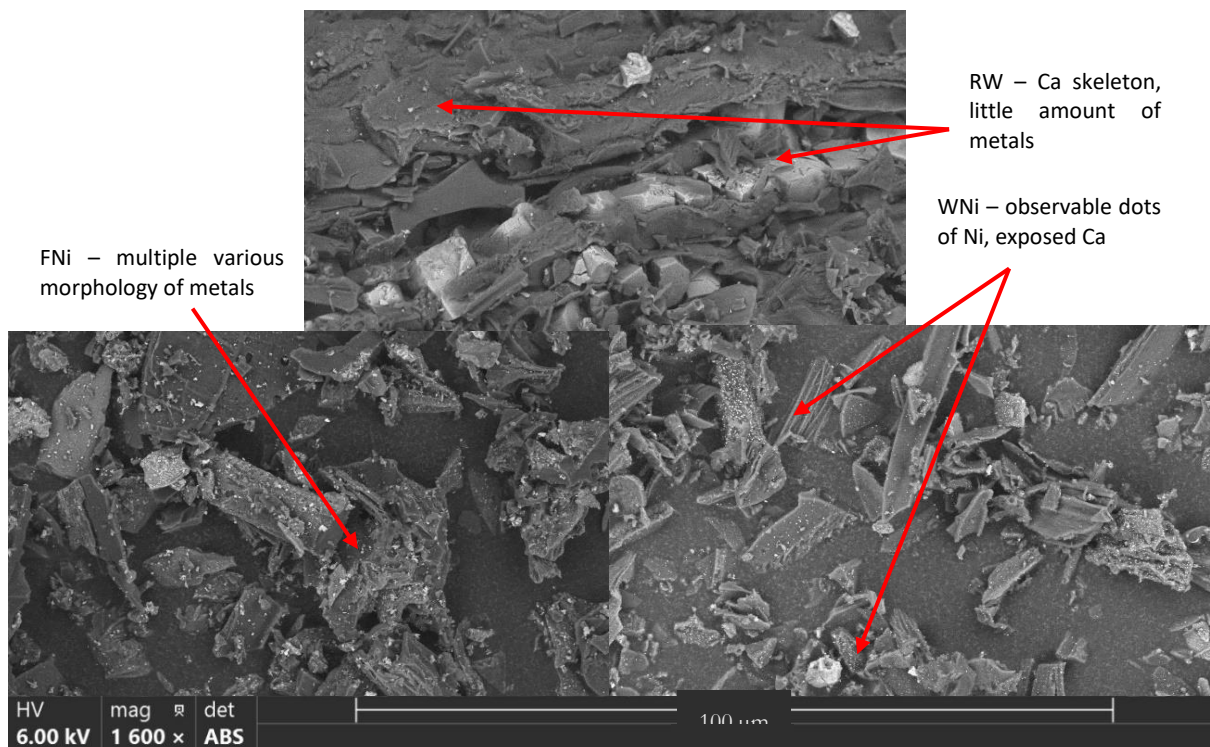


Fig. 2.3. SEM imagery of different biocarbon catalysts (RW, FNi and WNi biocarbon)

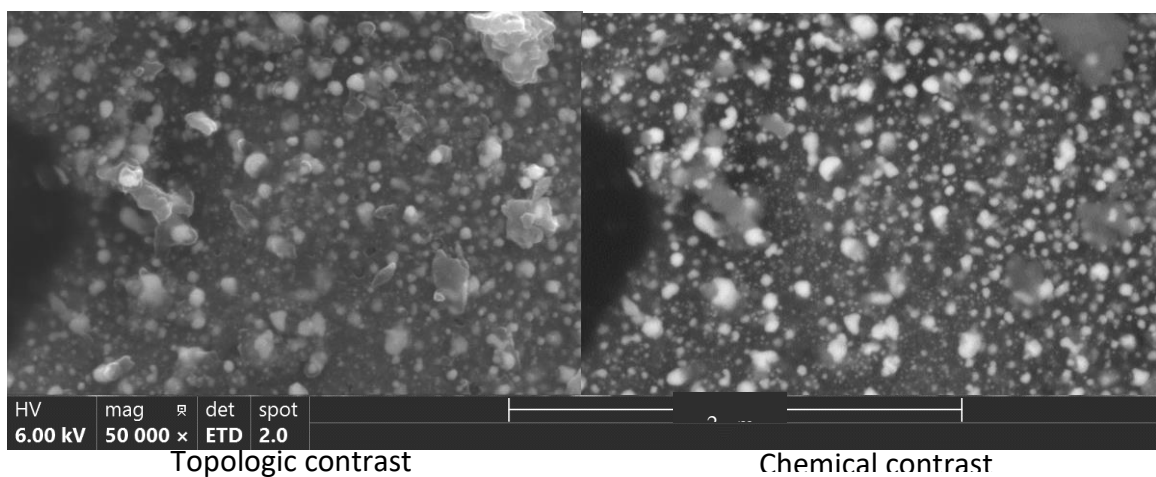


Fig. 2.4. SEM imagery of FNi biocarbon showing encapsulation of metals

2.3.2. deNO_x experiments

2.3.2.1. deNO_x performance, NO analysis

The concentration of NO and NO₂ was analyzed on-line every minute (in ppm). No significant production of NO₂ was observed during the experiments conducted. Therefore, only X_{NO} was calculated and averaged in 15 min (**Fig. 2.5**), which indicated the overall deNO_x performance of different biocarbon catalysts. For all the samples, X_{NO} did not significantly change after 50 min and became almost stable after 75 min. Therefore, the averaging X_{NO} from 75 to 90 min was defined as the steady state X_{NO} (Table 2.6).

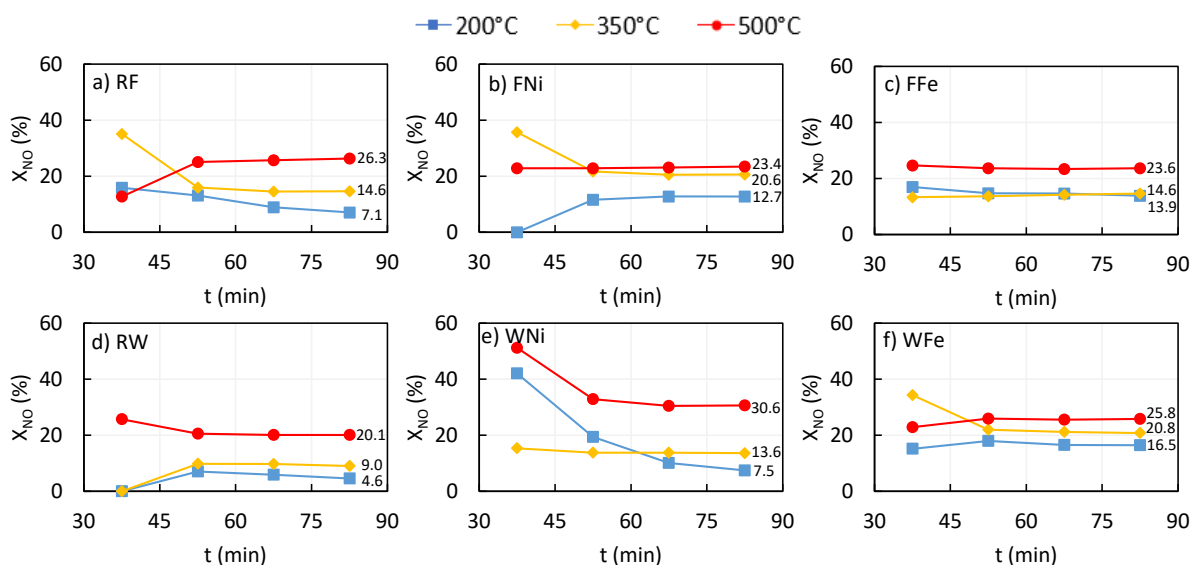


Fig. 2.5. NO removal ratio X_{NO} of different biocarbon catalysts (RF, FNi, FFe, RW, WNi, WFe) under 1021 ppm NO/Air

Table 2.6. Steady state X_{NO} (averaging from $t = 75$ to 90 min)

T (°C)	RF	FNi	FFe	RW	WNi	WFe
	X_{NO} (%)					
200	7.1	12.7	13.9	4.6	7.5	16.5
350	14.6	20.6	14.6	9.0	13.6	20.8
500	26.3	23.4	23.6	20.1	30.6	25.8

2.3.2.1.a. Effects of temperature

Higher temperature has shown promoting effects on the deNO_x performance for all the samples (Fig. 2.5). The raw biocarbon (RF and RW, Fig. 2.5a and d) were not fully activated at 200 and 350°C and had very limited deNO_x effects. Rising temperature to 500°C significantly enhanced their catalytic activity, as the activation energy needed for the inherent metals was achieved. However, impregnated biocarbon presented a higher X_{NO} with increasing temperature, which should be related to the presence of Fe and Ni (Table 2.4). This was also shown for WNi (Fig. 2.5e), except that its performance at 500°C was the highest ($X_{NO} = 30.6\%$). For FNi (Fig. 2.5b), the performance was close between 350 and 500°C, both significantly higher than that at 200°C. This indicated a lower activation temperature for this catalyst for a similar efficiency. This could be related to the high CO₂ adsorption capabilities of willow biocarbon (Table 2.5) that are related to the capacity to adsorb NO. This adsorption by the surface of the biocarbon means more NO is in contact of active sites and this higher quantity should result in more frequent reaction with NO and therefore higher X_{NO} . For WFe (Fig. 2.5f), X_{NO} was already high at 200°C and steadily increased, almost linearly, with temperature, which indicated a wider range of temperature for the use of this catalyst. For FFe (Fig. 2.5c), similar X_{NO} was achieved at both 200 and 350°C, both remarkably lower than that at 500°C. This indicated a higher activation temperature for

FFe. Therefore, the high presence of other metals such as AAEM in fern biocarbon did not therefore contribute to diminishing energy barriers and could even be inhibiting at higher temperatures, but the gas adsorbing capabilities of willow biocarbon could contribute to its higher performance. Nevertheless, temperature did increase the deNO_x performance of all biocarbon catalysts.

2.3.2.1.b. Effects of biomass

The nature of the biomass was an important factor that could influence the effectiveness of the biocarbon catalyst. Indeed, the composition of the initial biomass determined the composition and structure of the biocarbon formed, favorable or not to the NO adsorption and deNO_x. In addition, the effectiveness of impregnation may also depend on biomass characteristics. At both 200 and 350°C, fern biocarbon achieved obviously higher deNO_x performance than their respective willow biocarbon (the only exception is FFe vs. WFe). This was directly relevant to the difference in the inherent metal content of fern and willow, especially K, Na and Mg (Table 2.4). RF, for example, was significantly better than RW from 200 to 500°C, which best reflected the influence of biomass and its inherent metals as there was no tangible interference from the impregnated metals. Furthermore, the higher presence of carbon from willow biocarbon (Table 2.3) could interfere with the small amount of potential active sites (**Fig. 2.4**). When impregnated however, the capacity to adsorb higher quantities of NO by the willow-based biocarbon catalysts (Table 2.5) is highly beneficial to their deNO_x performance.

2.3.2.1.c. Effects of impregnated metals

The effects of impregnated metals were also important. First of all, impregnation successfully enhanced the performance of the biocarbon catalysts at least at both 200 and 350°C, as a result of more catalysts available for the adsorption and decomposition. Remarkable examples were FFe at 200°C (**Fig. 2.5c**), and WFe at 200 and 350°C (**Fig. 2.5f**), which at least doubled X_{NO} compared with respective raw biocarbon (Table 2.6). According to literature, the deNO_x efficiency of Ni-impregnated and Fe-impregnated active carbon were similar at 300°C and both significantly higher than that of raw active carbon [46]. This also agrees with the fact that metal-loaded carbons show high activity due to the dissociative NO chemisorption [77]. In this study, the performance was not always positively correlated to the metal amount because during pyrolysis the impregnated metals could be coated with carbon or aggregated and were therefore not accessible by NO. For example, FNi and FFe (**Fig. 2.5b** and **c**) were both high in their loaded metal content (Table 2.4), but their performance at 500°C was worse than the raw biocarbon (RF, **Fig. 2.5a**). This was the result of poor availability of metals after pyrolysis at high temperature. For WNi and WFe (**Fig. 2.5e** and **f**), though the loaded metal content was not so high, their performance was better (Table 2.6).

To investigate the synergistic effects of Ni and Fe, a bimetallic impregnation was carried out to produce a fern-based biocarbon catalysts containing both Ni and Fe (FNI_{Fe}). The deNO_x performance of this sample was compared to that of fern biocarbon (FFe and FNI, Fig. 2.6). None of the samples achieved better performance than raw biocarbon (RF) at 500°C. FNI and FFe were close in steady stage X_{NO} (23.4 % vs. 23.6 %), which were both better than the bimetallic sample, FNI_{Fe} (Fig. 2.6). Therefore, a synergistic effect of Ni and Fe was not found.

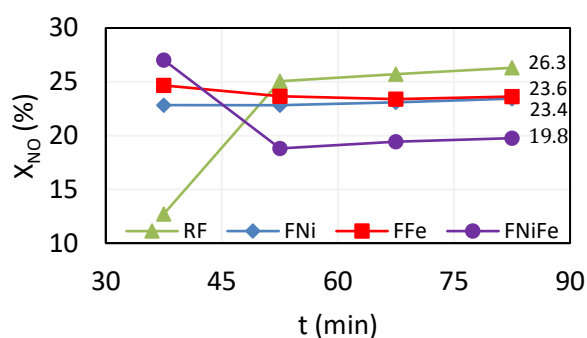


Fig. 2.6. X_{NO} of fern biocarbon at 500°C

2.3.2.1.d. Effects of metal content

It was revealed above that not only the kind of impregnated metals but also the loaded metals content on biocarbon has significant influence on the deNO_x performance of biocarbon catalysts. Therefore, the behavior of fern-based catalysts with different Ni and Fe content were tested in deNO_x experiments at 200°C (FFe*, Fig. 2.7, left) and 500°C (FNI* and FFe*, Fig. 2.7).

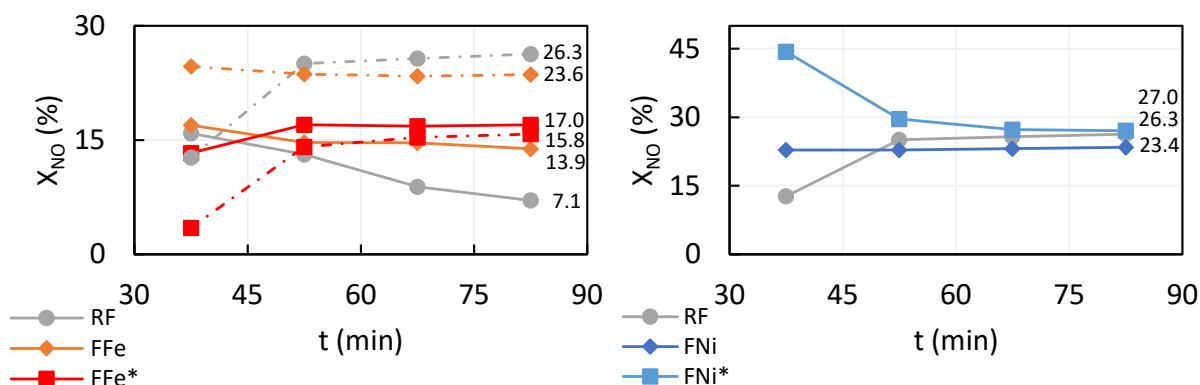


Fig. 2.7. X_{NO} of fern-based biocarbon catalyst impregnated with higher Fe content and used in deNO_x at 200 and 500°C (left), and impregnated with higher Ni content and used in deNO_x at 500°C (right)

For FFe, the effects of additional metal content were different at 200 and 500°C (Fig. 2.7, left). At 200°C, FFe* (with 64.17 wt% Fe) performed slightly better than FFe (with 13.17 wt% Fe), both significantly better than RF. Therefore, a positive correlation could be expected between impregnated Fe content (≤ 64 wt%) and the deNO_x performance at 200°C. At 500°C, however, highest values of metal content drastically reduced the performance of biocarbon. This indicated the metal blocking of biocarbon pore

structure (Table 2.5) happened mainly at higher temperature. Therefore, consideration of optimal metal content might be different depending on the temperature of emission sources.

In the case of Ni-based catalysts, the steady state X_{NO} of FNi was enhanced from 23.4% to 27.0% at 500°C when the Ni content was increased from 8.62 wt% (FNi) to 37.96 wt% (FNi*, Fig. 2.7, right). This made its performance slightly better than that of RF. In an industrial application, it needs to be evaluated if the improvement achieved justifies the higher metal cost.

2.3.2.1.e. Catalyst deactivation

Extended deNO_x experiments were conducted to evaluate the catalyst deactivation, as well as their thermal stability (Fig. 2.8, Table 2.7).

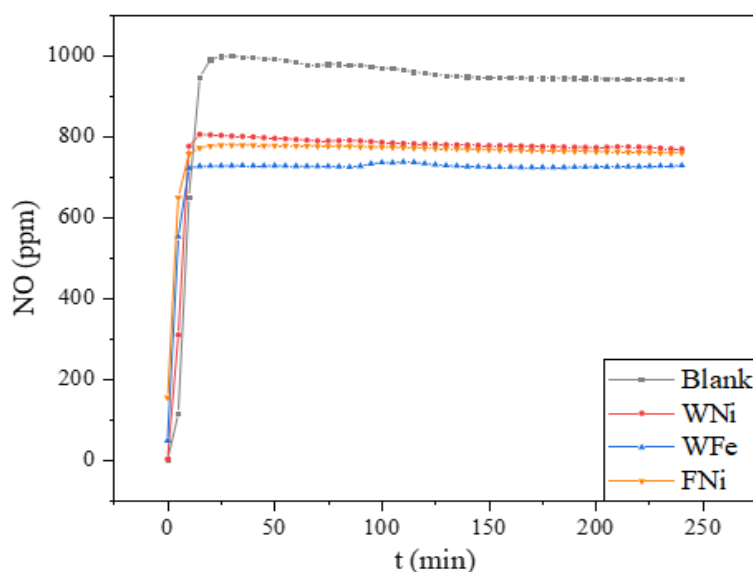


Fig. 2.8. NO concentration curves of selected biocarbon catalysts (WNi, WFe, FNi and blank test) during 500°C deNO_x experiments for extended time (4h), under 1021 ppm NO/Ar

Table 2.7. Mass loss of biocarbon catalysts after standard deNO_x experiments (1h)

T (°C)	RF	FNi	Mass loss (wt%, moisture free)			
			FFe	RW	WNi	WFe
200	8.6	3.6	3.2	5.9	5.0	3.4
350	6.3	2.8	3.4	7.7	7.6	4.7
500	9.9	4.6	2.1	7.2	4.8	7.2

Within the experimental conditions considered, no significant deactivation of catalysts was observed even in extended deNO_x experiments (Fig. 2.9), as the NO concentration remained stable after initial transitional stage (15 min), indicating constant deNO_x. Therefore, stability could be expected for the biocarbon catalysts. In terms of mass loss (Table 2.7), the impregnated biocarbon seemed to be better with most of them losing less than 5 wt% after 1h deNO_x experiments. The raw biocarbon, however, had a mass loss of 5 to 10 wt%. The mass loss, to be noted, was not entirely from the reaction with NO,

as the biocarbon could lose surface functional groups and release CO and CO₂ during the heating stage [66,78–81]. This could be possibly linked to catalyzed pyrolysis that, in addition to reducing organic content (more O and H, Table 2.3), could stabilize the carbon matrix [82].

2.3.2.2. deNO_x performance, N₂ analysis

Due to the input and replacement of reactor containing biocarbon catalysts at the beginning of each deNO_x experiment, air background is inevitable throughout the experiment. The time needed for gas replacement from gas bottles to μGC analyzer was estimated as 15 min considering the total volume of gas channel. Therefore, the background N₂ concentration was calculated by averaging the measured N₂ concentration from t = 30 to 45 min (before the inlet NO gas completely replaced Ar). Then the N₂ concentrations were normalized according to this standard to represent the N₂ produced during the test (Eq.2.15).

$$C_{N_2,nor} = C_{N_2} - C_{N_2,BG} \quad \text{Eq.2.15}$$

Where $C_{N_2,nor}$ is the normalized N₂ concentration, C_{N_2} is the measured N₂ concentration (15 min average) and $C_{N_2,BG}$ is the background N₂ concentration.

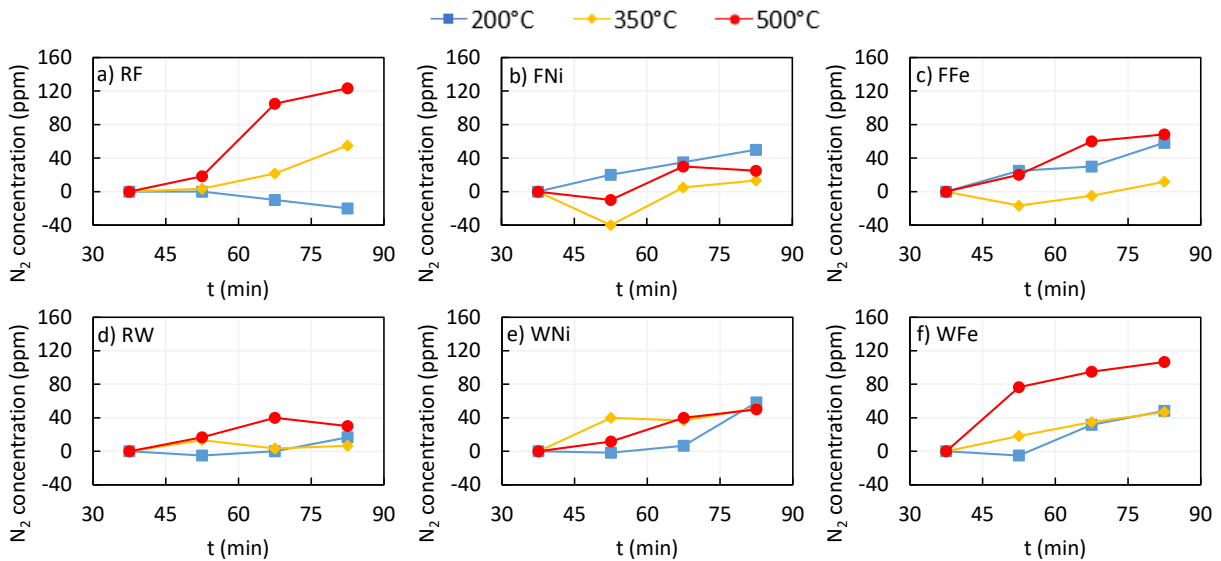


Fig. 2.9. Normalized N₂ concentration of different biocarbon catalysts (RF, FNi, FFe, RW, WNi, WFe), under 1021 ppm NO/Ar

The normalized N₂ concentration $C_{N_2,nor}$ can be seen as the indicator of direct decomposition reaction of NO (Fig. 2.9). In most cases, $C_{N_2,nor}$ was positive during NO phase. Even for those with initial negative values, the curves started to rise after. These indicated that NO is decomposed into N₂ either through direct decomposition or through catalytic reduction (Eq.2.10-12). For RF, the catalyzing performance was enhanced with the increase of temperature, resulting in its higher X_{NO} at higher temperature (Table 2.6). Also, RF performed better than RW, which was related to their difference in inherent metal contents (Table 2.4). FNi and FFe achieved highest decomposition performance at

200°C, in contrary to WNi and FFe. This caused their higher X_{NO} , while the NO removed by WNi and WFe was mostly through adsorption at this temperature. With the increase of temperature, both FNi and FFe showed a trend of catalyst deactivation, which should be due to the inhibiting effects of their higher Si content (Table 2.4), while these did not happen to the respective willow-based biocarbon catalysts (WNi and WFe).

2.3.2.3. Other gases

Selective reduction with biocarbon will lead to the formation of N_2 , CO and CO_2 [31], which was also observed in the experiments. This is a side reaction that can cause the degradation of biocarbon.

From the results, the CO_2 evolution followed similar trends among samples (Fig. 2.10). CO_2 concentration was very high at the beginning and decreased sharply up to 30 min (under Ar). This may be explained by the oxygen groups on biocarbon surface releasing large amounts of CO_2 (Table 2.3). It is fair to assume that the peak of CO_2 should be during the temperature rising stage ($t < 0$). In addition, this process was significantly influenced by temperature, as biocarbon released significantly more CO_2 from 350°C than at 200°C, which indicated a threshold between 200 to 350°C. When Ar is switched to NO, CO_2 concentration kept at a low value and steadily decreased. The reasons behind this should be a combination of residue oxygen groups releasing CO_2 and the reduction of NO by biocarbon producing CO_2 . This showed that raw biocarbon released more CO_2 than impregnated biocarbon, which corresponded to their higher mass loss (Table 2.7). This may be an indicator of the supposedly better regenerability of impregnated biocarbon.

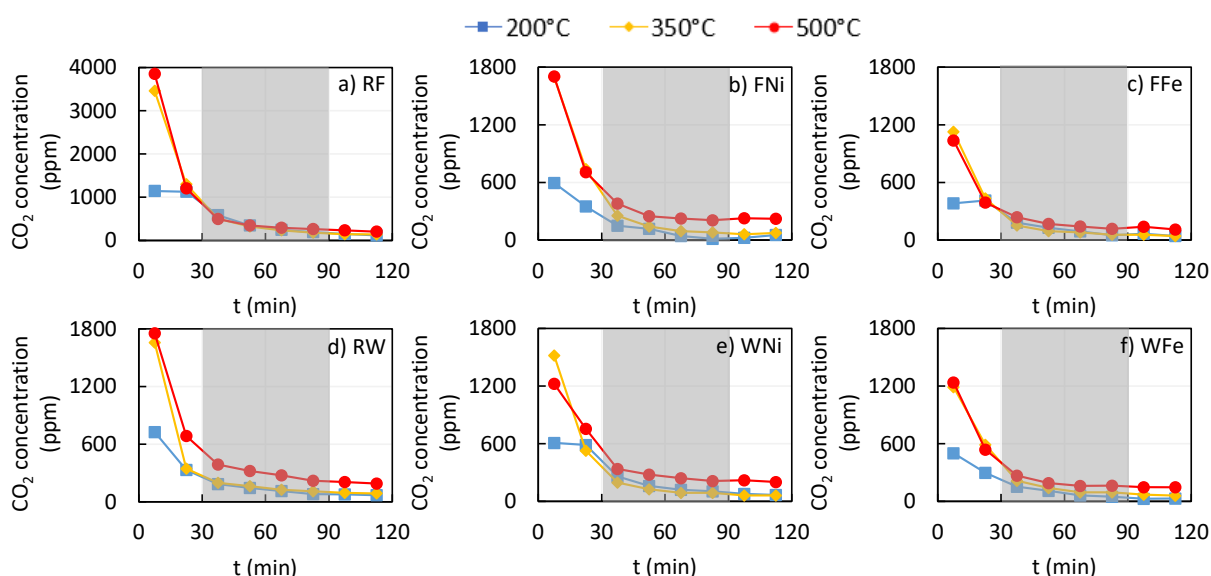


Fig. 2.10. CO_2 concentration of different biocarbon catalysts (RF, FNi, FFe, RW, WNi, WFe), blank area: Ar; shadow area: 1021 ppm NO/Ar

Regarding to the CO concentration, there was no CO release at 200°C and negligible release at 350°C, therefore only the evolution of CO concentration at 500°C is presented (Fig. 2.11). Compared to CO_2 ,

the quantity of CO released was much smaller, indicating CO₂ as the major product of selective reduction reaction. Unlike for CO₂, the impregnated biocarbon released more CO than the raw biocarbon.

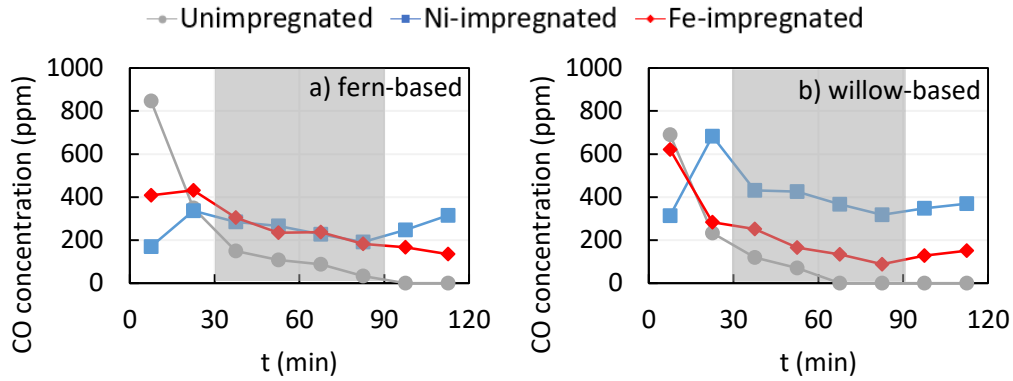


Fig. 2.11. CO concentration of different biocarbon catalysts during 500°C deNO_x experiments (a: fern biocarbon; b: willow biocarbon), blank area: Ar; shadow area: 1021 ppm NO/Ar

H₂ release was not observed at 200°C, so, only the evolution of H₂ concentration at 350 and 500°C was presented (Fig. 2.12). H₂ release was not so significant at 350°C and was mostly during the Ar phase. At 500°C, willow biocarbon released more H₂ than respective fern biocarbon. At both temperatures, almost no H₂ release was found for raw biocarbon.

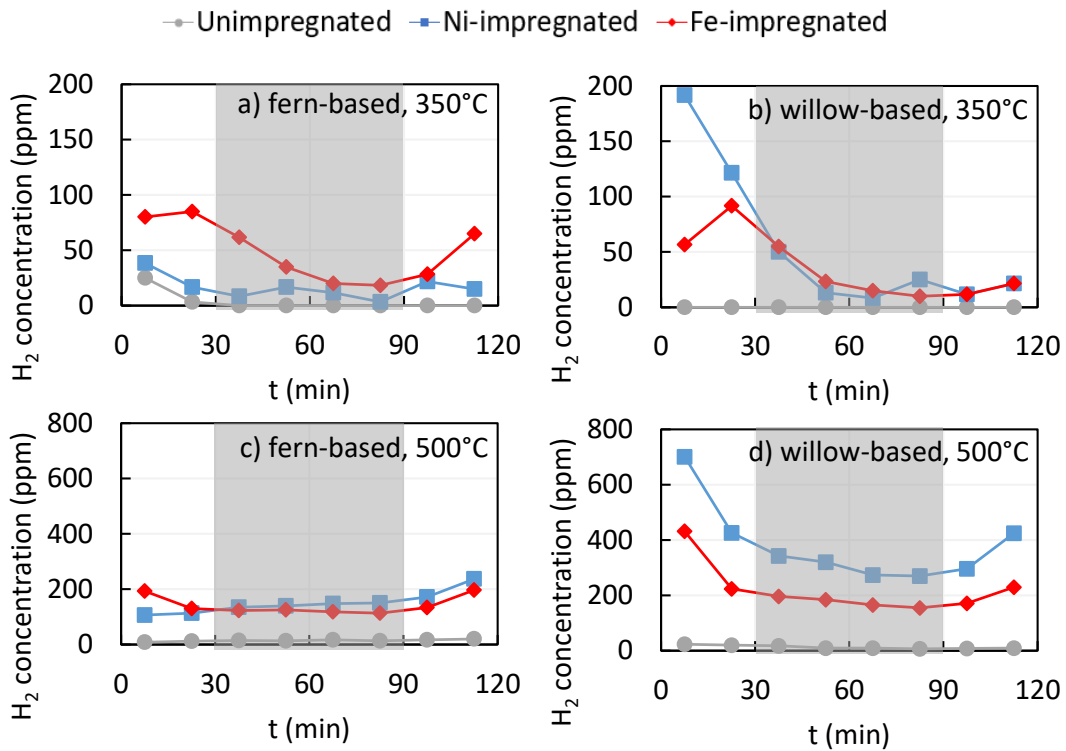


Fig. 2.12. H₂ concentration of different biocarbon catalysts during 350 and 500°C deNO_x experiments (a: fern biocarbon at 350°C; b: willow biocarbon at 350°C; c: fern biocarbon at 500°C; d: willow biocarbon at 500°C), blank area: Ar; shadow area: 1021 ppm NO/Ar

Based on results discussed in this chapter, a graphical illustration of reported mechanisms for deNO_x was represented (Fig. 2.13) with the associated equations (Eq.2.16-28). In this work, the metal-based mechanism is likely, with C provided by the biocarbon directly.

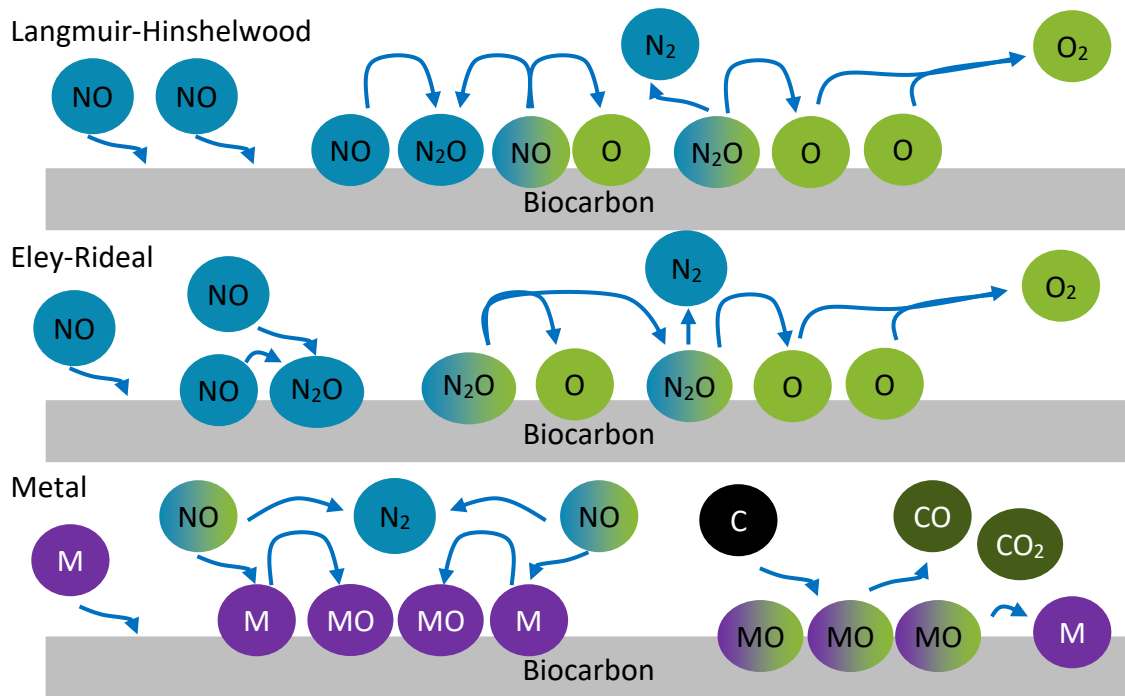


Fig. 2.13. Graphical representation of deNO_x mechanism

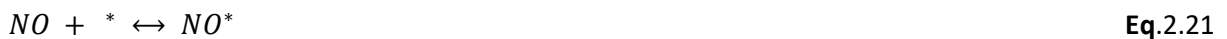
Global reaction for direct decomposition of NO:



Langmuir-Hinshelwood mechanism:

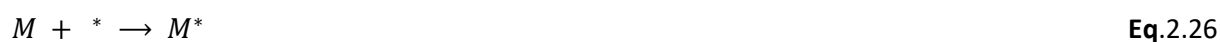


Eley-Rideal mechanism:





deNO_x reaction over metal:



2.4. Conclusions

Lignocellulosic fern and willow impregnated with heavy metals (Ni/Fe) were pyrolyzed (800°C, N₂) to produce biocarbon catalysts, which showed promising performances in NO decomposition (deNO_x) at 200, 350 and 500°C. Generally, higher temperatures showed better performances but a strict linear correlation was not observed. At 200 and 350°C, adsorption of NO on biocarbon surface was facilitated by the high specific surface area of impregnated biocarbon (151.6 to 419.1 m²/g), compared to that of raw biocarbon (< 50 m²/g). This resulted in a remarkable enhancement of deNO_x performance at this temperature range. At 500°C, adsorption and decomposition were competing in the deNO_x mechanism, and the inherent metals from raw biocarbon seemed to play an important part. As a result, the effects of impregnated metals were less positive or even negative at this temperature, except for WNi, which achieved a remarkably high deNO_x ratio of 30.6% (10.5% higher than RW). Fern biocarbon achieved higher deNO_x performance than the respective willow biocarbon at both 200 and 350°C, mostly due to their higher content of inherent metals (K, Na) that could facilitate activity from loaded metals (Ni or Fe). At 500°C, willow biocarbon could outperform their fern counterparts as the loaded metals could be activated and benefit from the high NO adsorption of the biocarbon. Increasing the metal content generally slightly enhanced their performance in deNO_x at 200°C, but not significantly at 500°C, and could justify use of a metal-poor biocarbon. No significant synergistic effects were found with fern biocarbon impregnated with both Ni and Fe.

A production of N₂ was observed during deNO_x experiments under NO flow, suggesting that the direct decomposition of NO was the main reaction, facilitated by higher temperature for most catalysts. The release of CO₂ observed under both Ar and NO flow was mostly from the surface chemical groups on biocarbon surface and peaked at the temperature rising stage (under Ar). The selective reduction of NO with biocarbon also contributed slightly to this release and was a side reaction. CO and H₂ was detected in smaller quantities. The impregnated biocarbon released less gas (CO₂, CO and H₂) than raw biocarbon, resulting in lower mass loss after deNO_x, and suggested better stability and regenerability.

Further work will be carried out to study the influence of activating the biocarbon catalysts and use of a real gaseous effluent containing nitrogen oxides. Furthermore, potential regeneration routes will be explored to facilitate the upscaling in the use of these biocarbon catalysts.

References

- [1] Feng K, Hu Y, Cao T. Mechanism of Fuel Gas Denitration on the KOH-Activated Biochar Surface. *J Phys Chem A* 2022;126:296–305. <https://doi.org/10.1021/acs.jpca.1c09518>.
- [2] Xie P, Ji W, Li Y, Zhang C. NO direct decomposition: progress, challenges and opportunities. *Catal Sci Technol* 2021;11:374–91. <https://doi.org/10.1039/D0CY02041A>.
- [3] Li N, Wang Y, Cui S, Jin X. Experimental and Kinetic Investigation on NO Reduction by Rice Husk Char and Catalytically with CO. *Applied Sciences* 2020;10:6715. <https://doi.org/10.3390/app10196715>.
- [4] Chen L, Liu L, Zhao Y, Zhao Y, Sun R, Sun S, et al. Char structural evolution characteristics and its correlation with reactivity during the heterogeneous NO reduction in a micro fluidized bed reaction analyzer: The influence of reaction atmosphere. *Fuel* 2021;303:121173. <https://doi.org/10.1016/j.fuel.2021.121173>.
- [5] Deng W, Tao C, Cobb K, Zhou H, Su Y, Ruan R. Catalytic oxidation of NO at ambient temperature over the chars from pyrolysis of sewage sludge. *Chemosphere* 2020;251:126429. <https://doi.org/10.1016/j.chemosphere.2020.126429>.
- [6] Roy S, Hegde MS, Madras G. Catalysis for NOx abatement. *Applied Energy* 2009;86:2283–97. <https://doi.org/10.1016/j.apenergy.2009.03.022>.
- [7] Cheng X, Cheng Y, Wang Z, Ma C. Comparative study of coal based catalysts for NO adsorption and NO reduction by CO. *Fuel* 2018;214:230–41. <https://doi.org/10.1016/j.fuel.2017.11.009>.
- [8] Wang L, Cheng X, Wang Z, Ma C, Qin Y. Investigation on Fe-Co binary metal oxides supported on activated semi-coke for NO reduction by CO. *Applied Catalysis B: Environmental* 2017;201:636–51. <https://doi.org/10.1016/j.apcatb.2016.08.021>.
- [9] Sun Q, Wang Z, Wang D, Hong Z, Zhou M, Li X. A review on the catalytic decomposition of NO to N₂ and O₂: catalysts and processes. *Catal Sci Technol* 2018;8:4563–75. <https://doi.org/10.1039/C8CY01114A>.
- [10] Ogata A, Obuchi A, Mizuno K, Ohi A, Aoyama H, Ohuchi H. Enhancement effect of Mg²⁺ ion on direct nitric oxide decomposition over supported palladium catalysts. *Applied Catalysis* 1990;65:L11–5. [https://doi.org/10.1016/S0166-9834\(00\)81582-1](https://doi.org/10.1016/S0166-9834(00)81582-1).
- [11] Green TE, Hinshelwood CN. CCXXIV.—The catalytic decomposition of nitric oxide at the surface of platinum. *J Chem Soc* 1926;129:1709–13. <https://doi.org/10.1039/JR9262901709>.
- [12] Gervasini A, Carniti P, Ragaini V. Studies of direct decomposition and reduction of nitrogen oxide with ethylene by supported noble metal catalysts. *Applied Catalysis B: Environmental* 1999;22:201–13. [https://doi.org/10.1016/S0926-3373\(99\)00053-3](https://doi.org/10.1016/S0926-3373(99)00053-3).
- [13] Fraser JM, Daniels F. The Heterogeneous Decomposition of Nitric Oxide with Oxide Catalysts. *J Phys Chem* 1958;62:215–9. <https://doi.org/10.1021/j150560a017>.
- [14] Shelef M, Otto K, Gandhi H. The heterogeneous decomposition of nitric oxide on supported catalysts. *Atmospheric Environment* (1967) 1969;3:107–22. [https://doi.org/10.1016/0004-6981\(69\)90002-X](https://doi.org/10.1016/0004-6981(69)90002-X).
- [15] Xie S, Mestl G, Rosynek MP, Lunsford JH. Decomposition of Nitric Oxide over Barium Oxide Supported on Magnesium Oxide. 1. Catalytic Results and in Situ Raman Spectroscopic Evidence for a Barium–Nitro Intermediate. *J Am Chem Soc* 1997;119:10186–91. <https://doi.org/10.1021/ja970809k>.
- [16] Imanaka N, Masui T, Masaki H. Direct Decomposition of Nitric Oxide over C-Type Cubic (Gd_{1-x-y}Y_xBay)₂O_{3-y} Solid Solutions. *Advanced Materials* 2007;19:3660–3. <https://doi.org/10.1002/adma.200602323>.
- [17] Tsujimoto S, Yasuda K, Masui T, Imanaka N. Effects of Tb and Ba introduction on the reaction mechanism of direct NO decomposition over C-type cubic rare earth oxides based on Y₂O₃. *Catal Sci Technol* 2013;3:1928–36. <https://doi.org/10.1039/C3CY20746C>.
- [18] Teraoka Y, Fukuda H, Kagawa S. Catalytic Activity of Perovskite-Type Oxides for the Direct Decomposition of Nitrogen Monoxide. *Chem Lett* 1990;19:1–4. <https://doi.org/10.1246/cl.1990.1>.

- [19] Fang S, Takagaki A, Watanabe M, Ishihara T. The direct decomposition of NO into N₂ and O₂ over copper doped Ba₃Y₄O₉. *Catal Sci Technol* 2020;10:2513–22. <https://doi.org/10.1039/D0CY00194E>.
- [20] Xie P, Yong X, Wei M, Li Y, Zhang C. High Performance Catalysts BaCoO₃–CeO₂ Prepared by the One-Pot Method for NO Direct Decomposition. *ChemCatChem* 2020;12:4297–303. <https://doi.org/10.1002/cctc.202000701>.
- [21] Kagawa S, Yoko-o S, Iwamoto M. Activity of copper(II)-exchanged Y-type zeolites in the catalytic decomposition of nitrogen monoxide. *Journal of the Chemical Society, Chemical Communications* 1978;0:1058–9. <https://doi.org/10.1039/C39780001058>.
- [22] Iwamoto M, Furukawa H, Mine Y, Uemura F, Mikuriya S, Kagawa S. Copper(II) ion-exchanged ZSM-5 zeolites as highly active catalysts for direct and continuous decomposition of nitrogen monoxide. *J Chem Soc, Chem Commun* 1986:1272–3. <https://doi.org/10.1039/C39860001272>.
- [23] Wang Y, Shen Y, Zhou Y, Xue Z, Xi Z, Zhu S. Heteroatom-Doped Graphene for Efficient NO Decomposition by Metal-Free Catalysis. *ACS Appl Mater Interfaces* 2018;10:36202–10. <https://doi.org/10.1021/acsami.8b09503>.
- [24] Imanaka N, Masui T. Advances in direct NO_x decomposition catalysts. *Applied Catalysis A: General* 2012;431–432:1–8. <https://doi.org/10.1016/j.apcata.2012.02.047>.
- [25] Garin F. Mechanism of NO_x decomposition. *Applied Catalysis A: General* 2001;222:183–219. [https://doi.org/10.1016/S0926-860X\(01\)00827-4](https://doi.org/10.1016/S0926-860X(01)00827-4).
- [26] Vannice MA, Walters AB, Zhang X. The Kinetics of NO_x Decomposition and NO Reduction by CH₄overLa₂O₃and Sr/La₂O₃. *Journal of Catalysis* 1996;159:119–26. <https://doi.org/10.1006/jcat.1996.0071>.
- [27] Pancharatnam S, Lim KJ, Mason DM. The decomposition of nitric oxide on a heated platinum wire. *Chemical Engineering Science* 1975;30:781–7. [https://doi.org/10.1016/0009-2509\(75\)80042-X](https://doi.org/10.1016/0009-2509(75)80042-X).
- [28] Xie S, Rosynek MP, Lunsford JH. Catalytic Reactions of NO over 0–7 mol% Ba/MgO Catalysts: I. The Direct Decomposition of NO. *Journal of Catalysis* 1999;188:24–31. <https://doi.org/10.1006/jcat.1999.2648>.
- [29] Lee J, Kim K-H, Kwon EE. Biochar as a Catalyst. *Renewable and Sustainable Energy Reviews* 2017;77:70–9. <https://doi.org/10.1016/j.rser.2017.04.002>.
- [30] Liu X, Dai L. Carbon-based metal-free catalysts. *Nat Rev Mater* 2016;1:1–12. <https://doi.org/10.1038/natrevmats.2016.64>.
- [31] Shu Y, Zhang F, Wang F, Wang H. Catalytic reduction of NO_x by biomass-derived activated carbon supported metals. *Chinese Journal of Chemical Engineering* 2018;26:2077–83. <https://doi.org/10.1016/j.cjche.2018.04.019>.
- [32] Younis S, Kim K-H. Recent Advances in Biochar-based Catalysts: Air Purification and Opportunities for Industrial Upscaling. *Asian Journal of Atmospheric Environment* 2022;16:104–20. <https://doi.org/10.5572/ajae.2022.117>.
- [33] Bolan N, Hoang SA, Beiyuan J, Gupta S, Hou D, Karakoti A, et al. Multifunctional applications of biochar beyond carbon storage. *International Materials Reviews* 2022;67:150–200. <https://doi.org/10.1080/09506608.2021.1922047>.
- [34] Wu XY, Song Q, Zhao HB, Zhang ZH, Yao Q. Kinetic Modeling of Inherent Mineral Catalyzed NO Reduction by Biomass Char. *Environ Sci Technol* 2014;48:4184–90. <https://doi.org/10.1021/es405521k>.
- [35] Do Minh T, Song J, Deb A, Cha L, Srivastava V, Sillanpää M. Biochar based catalysts for the abatement of emerging pollutants: A review. *Chemical Engineering Journal* 2020;394:124856. <https://doi.org/10.1016/j.cej.2020.124856>.
- [36] Yin Y, Zhang J, Sheng C. Effect of pyrolysis temperature on the char micro-structure and reactivity of NO reduction. *Korean J Chem Eng* 2009;26:895–901. <https://doi.org/10.1007/s11814-009-0150-6>.
- [37] Garijo EG, Jensen AD, Glarborg P. Kinetic Study of NO Reduction over Biomass Char under Dynamic Conditions. *Energy Fuels* 2003;17:1429–36. <https://doi.org/10.1021/ef020276n>.

- [38] Jung S, Park Y-K, Kwon EE. Strategic use of biochar for CO₂ capture and sequestration. *Journal of CO₂ Utilization* 2019;32:128–39. <https://doi.org/10.1016/j.jcou.2019.04.012>.
- [39] Suzaki PYR, Munaro MT, Triques CC, Kleinübing SJ, Klen MRF, de Matos Jorge LM, et al. Biosorption of binary heavy metal systems: Phenomenological mathematical modeling. *Chemical Engineering Journal* 2017;313:364–73. <https://doi.org/10.1016/j.cej.2016.12.082>.
- [40] Liu W-J, Li W-W, Jiang H, Yu H-Q. Fates of Chemical Elements in Biomass during Its Pyrolysis. *Chem Rev* 2017;117:6367–98. <https://doi.org/10.1021/acs.chemrev.6b00647>.
- [41] Koppolu L, Agblevor FA, Clements LD. Pyrolysis as a technique for separating heavy metals from hyperaccumulators. Part II: Lab-scale pyrolysis of synthetic hyperaccumulator biomass. *Biomass and Bioenergy* 2003;25:651–63. [https://doi.org/10.1016/S0961-9534\(03\)00057-6](https://doi.org/10.1016/S0961-9534(03)00057-6).
- [42] Koppolu L, Prasad R, Davis Clements L. Pyrolysis as a technique for separating heavy metals from hyperaccumulators. Part III: pilot-scale pyrolysis of synthetic hyperaccumulator biomass. *Biomass and Bioenergy* 2004;26:463–72. <https://doi.org/10.1016/j.biombioe.2003.08.010>.
- [43] Koppolu L, Clements LD. Pyrolysis as a technique for separating heavy metals from hyperaccumulators. Part I: Preparation of synthetic hyperaccumulator biomass. *Biomass and Bioenergy* 2003;24:69–79. [https://doi.org/10.1016/S0961-9534\(02\)00074-0](https://doi.org/10.1016/S0961-9534(02)00074-0).
- [44] Li X, Wang H, Shao G, Wang G, Lu L. Low temperature reduction of NO by activated carbons impregnated with Fe based catalysts. *International Journal of Hydrogen Energy* 2019;44:25265–75. <https://doi.org/10.1016/j.ijhydene.2019.04.008>.
- [45] Cheng X, Zhang X, Zhang M, Sun P, Wang Z, Ma C. A simulated rotary reactor for NO_x reduction by carbon monoxide over Fe/ZSM-5 catalysts. *Chemical Engineering Journal* 2017;307:24–40. <https://doi.org/10.1016/j.cej.2016.08.076>.
- [46] Illán-Gómez MJ, Raymundo-Piñero E, García-García A, Linares-Solano A, Salinas-Martínez de Lecea C. Catalytic NO_x reduction by carbon supporting metals. *Applied Catalysis B: Environmental* 1999;20:267–75. [https://doi.org/10.1016/S0926-3373\(98\)00119-2](https://doi.org/10.1016/S0926-3373(98)00119-2).
- [47] Zhao Z, Li W, Qiu J, Li B. Catalytic effect of Na–Fe on NO–char reaction and NO emission during coal char combustion 2002:6.
- [48] Liu W-J, Jiang H, Yu H-Q. Development of Biochar-Based Functional Materials: Toward a Sustainable Platform Carbon Material. *Chem Rev* 2015;115:12251–85. <https://doi.org/10.1021/acs.chemrev.5b00195>.
- [49] Richardson Y, Blin J, Volle G, Motuzas J, Julbe A. In situ generation of Ni metal nanoparticles as catalyst for H₂-rich syngas production from biomass gasification. *Applied Catalysis A: General* 2010;382:220–30. <https://doi.org/10.1016/j.apcata.2010.04.047>.
- [50] Richardson Y, Motuzas J, Julbe A, Volle G, Blin J. Catalytic Investigation of in Situ Generated Ni Metal Nanoparticles for Tar Conversion during Biomass Pyrolysis. *J Phys Chem C* 2013;117:23812–31. <https://doi.org/10.1021/jp408191p>.
- [51] Cao J-P, Liu T-L, Ren J, Zhao X-Y, Wu Y, Wang J-X, et al. Preparation and characterization of nickel loaded on resin char as tar reforming catalyst for biomass gasification. *Journal of Analytical and Applied Pyrolysis* 2017;127:82–90. <https://doi.org/10.1016/j.jaap.2017.08.020>.
- [52] Sharma A, Nakagawa H, Miura K. Uniform dispersion of Ni nano particles in a carbon based catalyst for increasing catalytic activity for CH₄ and H₂ production by hydrothermal gasification. *Fuel* 2006;85:2396–401. <https://doi.org/10.1016/j.fuel.2006.04.007>.
- [53] Chen X, Ma X, Peng X, Chen L, Lu X, Tian Y. Effect of synthesis temperature on catalytic activity and coke resistance of Ni/bio-char during CO₂ reforming of tar. *International Journal of Hydrogen Energy* 2021;46:27543–54. <https://doi.org/10.1016/j.ijhydene.2021.06.011>.
- [54] Anto S, Sudhakar MP, Shan Ahamed T, Samuel MS, Mathimani T, Brindhadevi K, et al. Activation strategies for biochar to use as an efficient catalyst in various applications. *Fuel* 2021;285:119205. <https://doi.org/10.1016/j.fuel.2020.119205>.
- [55] Cheng F, Li X. Preparation and Application of Biochar-Based Catalysts for Biofuel Production. *Catalysts* 2018;8:346. <https://doi.org/10.3390/catal8090346>.

- [56] Lawrinenko M, Wang Z, Horton R, Mendivelso-Perez D, Smith EA, Webster TE, et al. Macroporous Carbon Supported Zerovalent Iron for Remediation of Trichloroethylene. *ACS Sustainable Chem Eng* 2017;5:1586–93. <https://doi.org/10.1021/acssuschemeng.6b02375>.
- [57] Lawrinenko M, Laird DA, van Leeuwen JH. Sustainable Pyrolytic Production of Zerovalent Iron. *ACS Sustainable Chem Eng* 2017;5:767–73. <https://doi.org/10.1021/acssuschemeng.6b02105>.
- [58] González Martínez M, Dupont C, da Silva Perez D, Míguez-Rodríguez L, Grateau M, Thiéry S, et al. Assessing the suitability of recovering shrub biowaste involved in wildland fires in the South of Europe through torrefaction mobile units. *Journal of Environmental Management* 2019;236:551–60. <https://doi.org/10.1016/j.jenvman.2019.02.019>.
- [59] Said M. Comportements et rôles des métaux lourds au cours de la pyro-gazéification de la biomasse : études expérimentales et thermodynamiques. phdthesis. Ecole des Mines d'Albi-Carmaux, 2016.
- [60] Dastgheib SA, Salih H, Ilangovan T, Mock J. NO Oxidation by Activated Carbon Catalysts: Impact of Carbon Characteristics, Pressure, and the Presence of Water. *ACS Omega* 2020;5:21172–80. <https://doi.org/10.1021/acsomega.0c02891>.
- [61] Anthonysamy SI, Lahijani P, Mohammadi M, Mohamed A. Dynamic Adsorption of Nitric Oxide (NO) in a Fixed-bed Reactor Using Rubber Seed Shell-derived Biochar. *Biointerface Research in Applied Chemistry* 2021;12:1638–50. <https://doi.org/10.33263/BRIAC122.16381650>.
- [62] Zhu Z, Liu Z, Liu S, Niu H. Adsorption and reduction of NO over activated coke at low temperature. *Fuel* 2000;79:651–8. [https://doi.org/10.1016/S0016-2361\(99\)00192-1](https://doi.org/10.1016/S0016-2361(99)00192-1).
- [63] Zawadzki J, Wiśniewski M. Adsorption and decomposition of NO on carbon and carbon-supported catalysts. *Carbon* 2002;40:119–24. [https://doi.org/10.1016/S0008-6223\(01\)00081-1](https://doi.org/10.1016/S0008-6223(01)00081-1).
- [64] Vassilev SV, Baxter D, Andersen LK, Vassileva CG. An overview of the chemical composition of biomass. *Fuel* 2010;89:913–33. <https://doi.org/10.1016/j.fuel.2009.10.022>.
- [65] Reeves RD, Baker AJM, Jaffré T, Erskine PD, Echevarria G, Ent A van der. A global database for plants that hyperaccumulate metal and metalloid trace elements. *The New Phytologist* 2018;218:407–11.
- [66] Hervy M. Valorisation de chars issus de pyrogazéification de biomasse pour la purification de syngas : lien entre propriétés physico-chimiques, procédé de fonctionnalisation et efficacité du traitement. These de doctorat. Ecole nationale des Mines d'Albi-Carmaux, 2016.
- [67] Leng E, Guo Y, Chen J, Liu S, E J, Xue Y. A comprehensive review on lignin pyrolysis: Mechanism, modeling and the effects of inherent metals in biomass. *Fuel* 2022;309:122102. <https://doi.org/10.1016/j.fuel.2021.122102>.
- [68] González Martínez M, Dupont C, Meyer XM, Gourdon C. Woody and agricultural biomass diversity in torrefaction: A complete study in solid conversion and volatiles formation on TGA-GCMS. *Biochar: Production, Characterization and Applications* 2017.
- [69] Mukherjee A, Zimmerman AR, Harris W. Surface chemistry variations among a series of laboratory-produced biochars. *Geoderma* 2011;163:247–55. <https://doi.org/10.1016/j.geoderma.2011.04.021>.
- [70] Zeng K, Li R, Minh DP, Weiss-Hortala E, Nzihou A, Zhong D, et al. Characterization of char generated from solar pyrolysis of heavy metal contaminated biomass. *Energy* 2020;206:118128. <https://doi.org/10.1016/j.energy.2020.118128>.
- [71] Li R, Huang H, Wang JJ, Liang W, Gao P, Zhang Z, et al. Conversion of Cu(II)-polluted biomass into an environmentally benign Cu nanoparticles-embedded biochar composite and its potential use on cyanobacteria inhibition. *Journal of Cleaner Production* 2019;216:25–32. <https://doi.org/10.1016/j.jclepro.2019.01.186>.
- [72] Xia S, Li K, Xiao H, Cai N, Dong Z, Xu C, et al. Pyrolysis of Chinese chestnut shells: Effects of temperature and Fe presence on product composition. *Bioresource Technology* 2019;287:121444. <https://doi.org/10.1016/j.biortech.2019.121444>.

- [73] Akhil D, Lakshmi D, Kartik A, Vo D-VN, Arun J, Gopinath KP. Production, characterization, activation and environmental applications of engineered biochar: a review. *Environ Chem Lett* 2021;19:2261–97. <https://doi.org/10.1007/s10311-020-01167-7>.
- [74] Hanger BC. The movement of calcium in plants. *Communications in Soil Science and Plant Analysis* 1979;10:171–93. <https://doi.org/10.1080/00103627909366887>.
- [75] Feng D, Zhang Y, Zhao Y, Sun S, Gao J. Improvement and maintenance of biochar catalytic activity for in-situ biomass tar reforming during pyrolysis and H₂O/CO₂ gasification. *Fuel Processing Technology* 2018;172:106–14. <https://doi.org/10.1016/j.fuproc.2017.12.011>.
- [76] Gholami Z, Luo G, Gholami F, Yang F. Recent advances in selective catalytic reduction of NO_x by carbon monoxide for flue gas cleaning process: a review. *Catalysis Reviews* 2021;63:68–119. <https://doi.org/10.1080/01614940.2020.1753972>.
- [77] Mehandjiev D, Bekyarova E, Khristova M. Study of Ni-Impregnated Active Carbon. *Journal of Colloid and Interface Science* 1997;192:440–6. <https://doi.org/10.1006/jcis.1997.4901>.
- [78] Nzihou A, editor. *Handbook on Characterization of Biomass, Biowaste and Related By-products*. Springer International Publishing; 2020. <https://doi.org/10.1007/978-3-030-35020-8>.
- [79] Millan LMR. *Steam gasification of tropical lignocellulosic agrowaste: impact of biomass characteristics on the gaseous and solid by-products* n.d.:208.
- [80] Ghogia AC. *theses.fr – Amel cydric Ghogia, Développement de catalyseurs monolithiques structurés du type Co/C/mousse pour le procédé de synthèse Fischer-Tropsch* n.d. <http://www.theses.fr/s184711> (accessed October 18, 2021).
- [81] Ducousso M. *Gasification biochar reactivity toward methane cracking*. phdthesis. Ecole des Mines d’Albi-Carmaux, 2015.
- [82] Jeon J, Park JH, Wi S, Yang S, Ok YS, Kim S. Characterization of biocomposite using coconut oil impregnated biochar as latent heat storage insulation. *Chemosphere* 2019;236:124269. <https://doi.org/10.1016/j.chemosphere.2019.06.239>.

Chapter 3

Nickel and iron-doped biocarbon catalysts for reverse water-gas shift

Some elements of this chapter have been used in Graul, T., Gonzalez Martinez, M., & Nzihou, A. (2024), Nickel and Iron-Doped Biocarbon Catalysts for Reverse Water-Gas Shift Reaction, *ChemCatChem*, e202301398, under DOI 10.1002/cctc.202301398.

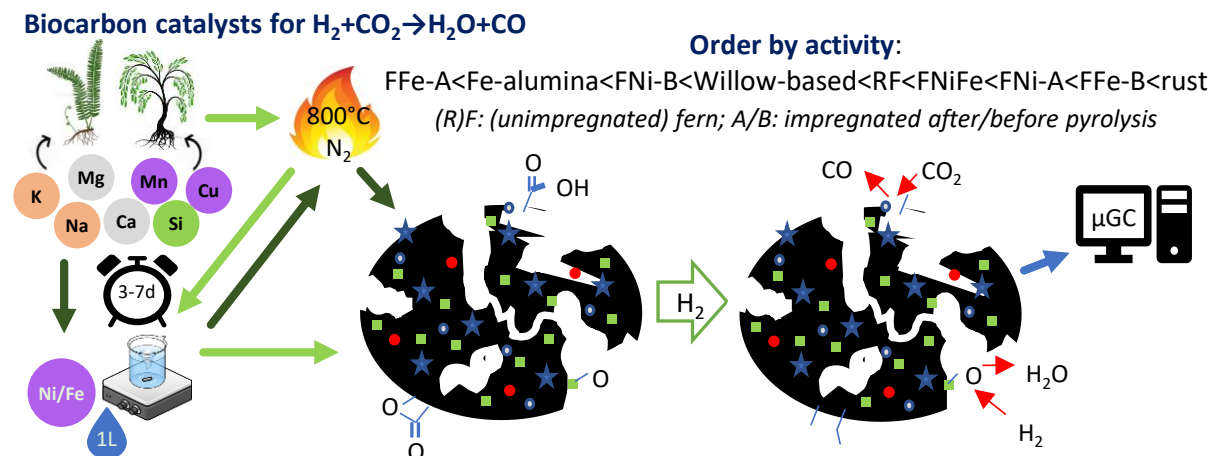
Highlights

- Biocarbon catalysts could be a relevant substitute for commercial catalysts.
- Biocarbon catalysts allowed high selectivity and conversion of RWGS at 400°C.
- Doping improved catalyst performance and stability in RWGS.
- Ni- and Fe-doped biocarbon catalyst reduction might inhibit CO₂ and H₂ conversion.
- Long-term use did not affect Fe-biocarbon catalyst performance.

Abstract

This work was focused on producing biocarbon catalysts for reverse water-gas shift reaction (RWGS). They were produced from pyrolyzed fern and willow impregnated with iron (Fe) and nickel (Ni) nitrates. They were tested in a fixed-bed reactor for RWGS at 400°C with a H₂/CO₂ ratio of 3. They showed high selectivity towards CO (>84%) and fair conversion (<17%) compared to both reference catalysts, rust (81%, 30%, respectively) and Fe-impregnated alumina (100%, 8%). These values are related to thermodynamic equilibrium calculations (100%, 35%). They were also stable as no sintering nor fouling were observed even at a long residence time (288h). The presence of inherent metals in biomass could provide sites to adsorb reactive gases and improve their transformation by dispersing electrons, which effectively reduces energy barriers for adsorption and dissociation by other active sites. K, Mg and Ca present in fern biocarbon catalysts may be responsible of their higher performances compared to willow catalysts, despite this, they have less CO₂ uptake and less specific surface area. The pre-reduction step of oxygen functional groups from biocarbon catalysts could produce electron deficient sites that may facilitate CO₂ uptake and activation. The best biocarbon catalyst was fern-based biocarbon impregnated with Ni after pyrolysis, as it benefitted from the synergetic effect of the inherent metals combined to O vacancies and strong metal-carbon interactions.

Graphical abstract



3.1. Introduction

Greenhouse gas emissions are the main cause of current global warming. This accounts for climate damages including destructive storms, severe droughts and quicker wildfires, among others, which results in an increasing devastating of humanity's livelihood. To limit Earth's warming, the 2015 Paris Agreement engaged the 193 signatory nations to reduce greenhouse gas emissions namely carbon dioxide (CO_2) [1]. Consumption of CO_2 via chemical (ex. thermal conversion) or biologic pathways (ex. photosynthesis) or restriction of its production by optimizing CO_2 producing processes are means to limit its emission. Therefore, biomass and biowaste valorization into hydrogen (H_2), biofuels and other products may play a significant role in reaching this objective, due to the carbon neutrality and high availability of these bioresources.

Thermochemical conversion processes of bioresources to produce syngas, containing H_2 , tar and biocarbon typically require high temperatures (between 500 to 1000°C) and the use of catalysts allows lower operating temperatures and energy saving. Fischer-Tropsch synthesis (FTS) however allows the production of synthetic fuel from synthetic gas composed of mainly carbon monoxide (CO) and H_2 at milder conditions. This process, operating from 180 to 400°C and around 20 bar, requires noble or transition metal-based catalysts, including iron (Fe) and nickel (Ni) [2,3]. Reverse Water-Gas Shift (RWGS) is implied in FTS reactions by reversibly converting CO_2 and H_2 into CO and H_2O (Eq.3.1). This reaction requires similar catalysts to those of FTS and higher temperatures due to its endothermicity ($\Delta H_{298}^0 = 42.1 \text{ kJ/mol}$) [4].



Eq.3.1

Commercial catalysts, generally made of noble metals, have a high environmental impact because of the metal extraction processes that are energetic and intensive in solvent, and also metal scarcity [5–

7]. These metals can be sourced more sustainably through plant phytoextraction and could then be transformed into catalysts [8,9]. To overcome this burden, in this work, we aim at producing catalysts from pyrolyzed metal-loaded bioresources and test them in RWGS. The characterization of the produced catalysts before and after the reaction have been performed.

3.1.1. Pyrolysis for biocarbon production

Slow pyrolysis is a thermochemical process occurring at temperatures ranging from 400 to 900°C, at a heating rate of 1 to 100°C/min and under an inert atmosphere. This transformation results in the production of biochar (biocarbon), tar and gaseous products whose proportions and properties are highly dependent on the operating conditions, mainly temperature and heating rate.

Higher temperature results in a decreased biocarbon yield due to its transformation into gaseous products. This decrease is less important as temperature increases due to a more ordered structure in biocarbon [10]. Above 800°C, tar content is lower and biocarbon is further converted but the risk of metal sintering increased [11]. Slow heating rates (<25°C/min) limit volatilization of biocarbon but tars are not eliminated due to possible formation of more stable tars. Operating conditions can also influence the development of the biocarbon properties [12,13]. Biocarbon produced above 500°C had increased C-C bond content at the expense of O and H. Alkaline content is also increased at higher temperatures resulting in improved surface basicity. These conditions also induce biocarbon with enhanced specific surface area and pore volume [14]. Pyrolysis temperature is positively correlated with pH, fixed C content, biocarbon stability, and ash content and negatively correlated with biocarbon yield, O and H mass fractions, and the number of surface functional groups [15].

Higher heating rates corresponding to fast or flash pyrolysis (>900°C/min) can however result in bigger porosity (macropores) with a more open structure, which provides better access to active sites [10]. Alkaline metals are better retained when the heating rate is low (6-60°C/min) [14]. Higher heating rates (100°C/min) lead to biocarbon with higher reactivity, that also had a higher pore volume, consisting mainly of meso- and macropores, whereas at lower heating rates (1-50°C/min), the pore volume was lower as structures mainly consisted of micropores [16,17].

With long steam residence time (>2s), biocarbon and tar yields decrease due to devolatilization. This results in the formation of meso and macropores in the biocarbon, which results in a better accessibility of the active sites [10]. Longer residence time (10-100min) favors tar conversion, increasing biocarbon yield [14].

The type of reactor can also affect product distribution as it limits or amplifies the contact of gas and heat with the feedstock. The batch reactor strength and weakness are its ability to contain the

feedstock and products, meaning there is no possible displacement of equilibrium. Furthermore, biomass conversion in this type of reactor is limited by the partial pressure of formed gases. As a result, deactivating agents such as coke are not removed during the reaction and could potentially foul catalysts. The semi-batch reactor allows for introduction and removal of products and is reported to facilitate the removal of oils of up to 90%. This removal could contribute to the displacement of equilibrium and improve formation of tar and gas products [18]. Fixed and fluidized bed strengthened biomass conversion and multistage reactions due to their compacity. This results in an enhanced production of gases and liquids, as well as a downstream conversion of liquids to gas. Because of their compacity, less catalyst is required. Heat and mass transfer are improved through fluidization but residence time is diminished so liquids are less likely to be converted into gases and a tar yield of at most 87 wt% was reported [18]. Conical sprouted bed reactor facilitates fluid conversion and inhibits adhesion of biomass and biomass products to reactor walls, which can limit conversion. It also limits the residence time of the feedstock and results in a higher tar production compared to that of gas. This type of reactor is less effective at higher temperatures which can result in unfavored conversion if the products are non-adhesive and limits degradation of solids and liquids to gas. Microwave assisted reactors benefit from quicker heating and could result in improved tar yields reaching 84 wt% [18,19]. With similar biocarbon production reported at 35-36 wt%, fixed, fluidized and conical sprouted bed reactors resulted in tar yields of 46.6, 50.0 and 58.2 wt% respectively and gas yields of 17.7, 14.6 and 5.9 wt%. Tar yields for fixed beds were reported to vary between 35 and 55 wt%, for rotary and screw kilns, this is approximately 40 wt%, for fluidized beds it is higher than 50 wt% and the highest is conical reactors at 60 wt% [20].

The product distribution is also affected by the initial feedstock. Indeed, it is reported that cellulose content is related higher production of liquid (anhydrosugars) and lesser solid, hemicellulose to gas and liquid (water, phenol, ketones) and lignin to biocarbon and liquid (phenol) [21]. The production of volatile gases (condensable and non-condensable), and inversely the degradation of the solid, are caused by a stronger breakdown of these macromolecules, so a harder to decompose lignin for instance would result in less gas and more solid production [21,22]. This could explain why cellulose and hemicellulose rich biomass species such as herbaceous plants tend to suffer severer mass loss than lignin-rich woody biomass [23]. It is also possible that this diversity does not affect biocarbon production but only the distribution of volatile gases [24].

Biocarbon production yield is higher in pyrolysis under N_2 , compared to steam gasification [10]. To better promote tar removal and biocarbon conversion, O_2 can be added. CO_2 can also contribute to tar reduction and coke conversion [11]. Furthermore, CO_2 tends to develop bigger pores in biocarbon, with diameters ranging from 2 to 50 μm , while pores developed under steam range from 10 to 20 μm .

CO₂-formed biocarbon is more reactive in pyrogasification and its volatilization is facilitated, leading to reduced biocarbon yield and reduced C content. With steam, biocarbon surface was less damaged and metal concentration in biocarbon tended to be higher with steam or steam-CO₂ [16,17].

While studying Alkaline and Alkaline-Earth Metals (AAEM) on biocarbon during gasification, it was found that the catalytic properties of K and Ca were improved under steam rather than CO₂ since during gasification, they migrated to the surface of the biocarbon while rearranging its structure and this migration was facilitated by the impact of steam on the porous structure. Therefore, active sites were rendered more accessible with reduced C content and K and Ca were more exposed to perform catalysis [25].

Experimental conditions can determine the distribution of the products of pyrolysis and consequently influence their properties. To produce a biocarbon-based catalyst, carbon should be little converted to maintain a stable structure in which metals are dispersed. The biocarbon however also needs to develop high specific area, porosity and accessible metals that may require volatilization and consumption of this carbon. This can be achieved through the use of high temperatures, slow heating rates and high residence times in fixed or fluidized bed reactors. These operating conditions minimize biocarbon consumption while allowing time for volatiles to release to form pores and expose catalytic metals. The choice of the feedstock to form the catalyst then depends on the application as inherent metal content can determine the activity of the biocarbon catalyst. In the next section, the effect of these metallic elements on thermochemical conversion and more precisely RWGS will be assessed.

3.1.2. The effect of inorganic elements in RWGS

The presence of inorganic elements on biomass can have a catalytic or inhibiting effect in thermochemical conversion processes, such as pyrogasification and FTS. This includes direct and reverse WGS, but also the pyrolysis process for the biocarbon catalyst production. The effect of these inorganic elements is close for reactions involved in thermochemical conversion happening under close operating conditions, such as temperature and reaction atmosphere which are the most influencing parameters. In this section, the inorganic elements with a catalytic or inhibiting effect, as well as their synergetic effect, in thermochemical conversion processes have been analyzed in detail, with a special focus on RWGS. Commercial catalysts loaded with the metals identified as catalytically active for direct and reverse WGS were reported and reviewed. The objective is to identify the metals contained and doped on biocarbon catalysts and determine how they impact direct and reverse WGS.

3.1.2.1. Alkali metals

Alkaline oxides and salts were used for tar reduction by reforming above 600°C or low temperature

hydrolysis (<170°C) [26,27]. Alkali promoters K, Na in combination with reducible (oxide) supports TiO₂ and CeO₂ assists in forming selectively CO in RWGS. These two, in addition to Rb and Cs, promote the activity of RWGS catalysts by transferring electrons facilitating activation and reaction of CO₂ [7].

Lithium carbonate (Li₂CO₃) has been shown to be effective for gasification and hydrogen production by improving conversion of organic content from biomass (C, H, O) [28]. An increase in hydrogen production from 14.5 vol% in syngas to 27.7 vol% in presence of LiCl was noticed [29].

Sodium ion (Na⁺) participated in catalytic pyrolysis by lowering bio-oil yields and increasing gas yields with little variation to biocarbon yield [30]. Na₂CO₃ catalyzed gas production, including H₂ and increased the gasification rate during pyrolysis and gasification. It also helped degrade the cellular structure often obtained during pyrolysis. It contributed to reduce coke deposit [28,29,31]. The presence of NaCl was reported to contribute to a slight increase in hydrogen production from 14.5 to 16.2 vol% in gas [29].

Potassium ion (K⁺) participated in catalytic pyrolysis by participating in reducing the energy barriers of formation of small molecules such as formic acid [30]. K₂CO₃ improved H₂ production, namely by catalyzing WGS. Its addition also increased the pyrogasification rate up to 31.1 times its initial value and the hydrogen production increased from 42.7 to 52.8 vol% while reducing coke deposition and tar formation. It also helped degrade the cellular structure during pyrolysis [13,28,29,31]. K₂Ca(CO₃)₂ would be active for gasification [28]. An increase in hydrogen content in gas from 14.5 to 15.7 vol% or 30 to 55 vol% in presence of KCl was reported. It also influenced pyrogasification by reforming tar (reduction in tar yield by 2/3rd) and could shift the equilibrium of WGS by increasing CO₂ adsorption but too much loading of KCl decreased CO₂ adsorption. The loading also results in a decrease of CO/H₂ from 1.8 to 0.7 [29,32,33].

Rubidium and **Cesium** carbonate (Rb₂CO₃ and Cs₂CO₃) would be effective for gasification increasing hydrogen production due to decreasing activation energy and electronegativity resulting in improved electron transfer mechanisms [28]. Rb can promote catalysts of RWGS by modifying the electronic structure and reducing energy barriers resulting in better conversion of CO₂ to CO [7].

3.1.2.2. Alkaline-earth metals

The presence of alkaline-earth oxides was reported to limit coke deposits that could hinder catalytic activity [29].

Magnesium oxide (MgO) was reported to promote syngas production by improving CO₂ adsorption, allowing for further gases to be produced, and reduce tar by reducing temperatures for cracking [32,34]. MgCO₃ was used for tar cracking where the adsorption of produced CO₂ was facilitated by the

pore volume created by the metal resulting in a shift in equilibrium [34]. MgCl_2 improved H_2 production by catalyzing WGS due to its electronic properties [28].

Calcium. In the case of the HyPr-RING (Hydrogen Production by Reaction Integrated Novel Gasification), calcium carbonate and oxide (CaCO_3 and CaO) played a catalytic role in WGS. HyPr-RING is a two-cycle reaction where hydrocarbons are degraded to H_2 , CO , steam (H_2O) and CO_2 . Then these calcium species perform WGS at 650°C , generating H_2 and CO_2 from CO and H_2O while shifting equilibrium towards products by extracting CO_2 by a cycle between different calcium species [26]. CaO could have a catalytic role on cracking tar due to increased contact time allowing for further conversion. It was also reported for syngas production due to its ability to absorb CO_2 and was shown to double H_2 production when compared to non-catalytic processes. Others reported an increase in gas production from 38 to 41.3 wt% and a hydrogen concentration in gas from 47 to 53 vol% with a CaO loading from 10 to 40 wt%, attributed to catalyzing WGS [26,32,34,35]. CaCO_3 were used for tar cracking and reduce coke deposition by providing oxygen for combustion. It could catalyze H_2 production at high temperatures without sintering and while retaining its dispersion (750°C for oxide formation and 1200°C for metal mobility) [29,34]. Additionally, hydroxyapatite (calcium-based) supports have been studied in length in the RAPSODEE research center (theses of Thanh Son Phan and Bruna Rêgo de Vasconcelos, [36,37]).

3.1.2.3. Transition metals

Iron, chromium, molybdenum and tungsten carbonyls ($\text{Fe}(\text{CO})_5$, $\text{Cr}(\text{CO})_6$, $\text{Mo}(\text{CO})_6$, $\text{W}(\text{CO})_6$) favored reactions occurring in gaseous phases that consume H_2 . This was attributed to the formation of clusters with strong electronic properties [28]. This is owed to the attraction of electrons towards O and the proximity between metals in a cluster who during reaction disperse electrons then gather electrons provided by reactive gases to form the product gases [38,39].

Manganese (Mn) formed nanoparticles that could contribute to H_2 production due to high dispersion. Gas production of biomass pyrolysis was reported to increase from 14 to 19 wt% when Mn was ionically introduced into biomass, and tar production decreased by 10 wt% [30].

Iron. At 350 to 500°C , iron-chromium oxide ($\text{Fe}_2\text{O}_3\text{-Cr}_2\text{O}_3$) was used for WGS and Cr oxide could have a catalytic effect during pyrolysis due to its ability to switch from oxidized to reduced states that enables adsorption of CO and H_2O and further increases gas production [26,40]. The catalytic activity for hydrogen production when using dolomites as a catalyst could be associated to an increasing content in Fe_2O_3 . The difference in gas yield and hydrogen content in gas was 20% and 4 vol% respectively between the dolomite with the highest Fe content and the lowest [29]. Fe formed nanoparticles that

could increase H₂ production and contribute to methane reforming due to high dispersion [30,41,42]. Fe on hydroxyapatite support did not have much effect during steam, methane and CO₂ reforming but this was attributed to a lack of prereduction and co-promotion with other metals as prereduction could the formation of an active metallic phase, amplified by electron exchange with co-promoters, and provide extra sites for gas adsorption by the support. Fe took part in tar elimination from pyrolysis of eucalyptus wood by reducing its fraction by 8 wt% [28,30,37,43]. Fe-Co reduced tar fraction from 30 to nearly 0 wt% [43,44]. Introduction of Fe(NO₃)₃ during pyrogasification of cellulose doubled hydrogen content (from 1 to 2 %vol) that was attributed to WGS production and a decrease by 50% in CH₄ content was related to reforming [30,45]. Fe oxides promoted by Pt, Cu, Ag, Ba, K, Cr and supported with Cr₂O₃, CeO₂-ZrO₂, MnO are common catalysts of industrial (>350°C) WGS and RWGS reactions with magnetite (Fe₃O₄) being the active phase and at lower temperatures this is Cu-Zn/Al₂O₃. Fe supported on γ-Al₂O₃ and promoted by K resulted in increased rates (1.5 times due to support and 3 times more with addition of K) of CO formation during RWGS at 500°C with at least 99% selectivity [46,47]. Fe₃C formed during RWGS could have catalytic properties due to the distribution of electrons towards C that facilitates adsorption and reaction of CO₂ and H₂ on Fe sites [47–50].

Cobalt. Cobalt oxide (CoO) contributed to WGS catalysis due to presence of agglomerated particles that allowed better adsorption of H₂O [51,52]. Co forms nanoparticles that could contribute to H₂ production and methane reforming thanks to high dispersion, reducibility and basicity that allows improved CO₂ adsorption and coke removal [30,42,53]. The influence of Co on hydroxyapatite support, on steam, CO₂, methane reforming, and H₂ production was attributed to its high dispersion but also requires promoters to lessen energy barriers. Co also facilitates dispersion of promoters such as Ni [28,37,42,43,53]. Co, Ni-Co and Fe-Co also took part in tar elimination by providing highly dispersed active sites [43]. Co⁰ nanoparticles are active in RWGS and methanation but on different sites (oxidized and metallic sites respectively) as particle size and dispersion affect the ability of the active sites to adsorb and react with CO₂ and H₂ [7,54].

Nickel. The combination of Ni and Al oxides is effective to catalyze H₂ production. Without catalyst, H₂ production by steam reforming of acetic acid was close to 0 but in presence of the catalyst this could lead to 0.14 g H₂ per g of acetic acid (65 mol% H₂ in gas containing also CO and CO₂). H₂ yield doubled by pyrogasification of mixed biomass/plastic feedstock [55,56]. Ni formed nanoparticles that could contribute to H₂ production through biomass gasification by increasing gasification rates at least 120-fold (0.04 to 4.8 %/hour), and by reducing temperatures for complete carbon conversion by 100°C. The activity of Ni⁰ nanoparticles was associated to its ability to lessen energy required to cleave C-C and C-H bonds and to adsorb O molecules. Well dispersed Ni⁰ provided sufficient active sites to allow adsorption of gasifying agents H₂O, O₂ and CO₂ and reaction resulting in H₂-rich and tar-free syngas.

The facilitated electronic interactions also enable steam and methane reforming and WGS which can be selectively induced by promoting elements such as tin (Ni-Sn). It also improved tar reforming by decreasing its yield by 2-14 wt% [13,30,41,57,58]. H₂ quantities increased in presence of reduced Ni-Al alloy at 750-800°C under inert atmosphere. This was attributed to lower binding energy of CO that enabled increased activity for reforming due to high availability of active sites [26]. Ni on oxide and hydroxyapatite supports took part in WGS, steam, CO₂ and methane reforming and globally catalyzed H₂ production due to enabling H transfer reactions related to reduced energy barriers, improved electron dispersion and reducibility. Ni was also mentioned for tar and coke reduction due to surface basicity that resulted in better adsorption and reaction [13,26–29,37,42,43,53]. Ni(NO₃)₂ reduced tar production by 7.5 wt%, increased biocarbon production by 2.5 wt%, and double H₂ production during cellulose pyrogasification [30]. Ni₂P(001) could catalyze WGS due to its structure that eases scission of O bonds enabled by strong interactions between P and O [57]. The performance of Ni in RWGS could be related to its surface energy resulting in better activity as it increases [7,59].

Copper. At 200 to 250°C, CuO-ZnO was used for WGS due to its reducibility that enables adsorption and reaction of CO and H₂O [26]. Reduced CuO contributed to WGS catalysis due to strong binding of O and CO that in turn maximize CO₂ and H₂ production. With reduced ceria (Ce), this results in oxygen vacancies with improved H₂O dissociation capabilities. With the right conditions such as pre-reduction and optimized Cu-Ce distribution, conversion can rise from 25 to 80% (equilibrium value) [60,61]. Cu⁰ nanoparticles could contribute to H₂ production by increasing gas yields from biomass pyrolysis by 4 wt% and decreasing tar yields by 9 wt%. Cu⁰ was suggested for WGS catalysis because of high dispersion and little permanent binding of molecules involved in the reaction due to lower electronic interactions than Ni, despite the impact on H₂ production rate being low. With a reducible support, the activity of Cu⁰ can increase due to electron transfers and better adsorption and activation of CO and H₂O [30,57,62]. Cu on hydroxyapatite support was not reported to be active for steam reforming, methane reforming, and H₂ production catalysis despite being highly dispersed as small particles (<200nm) [37]. Cu promoted by K₂O and supported SiO₂ converted CO₂ increasingly from 1.8% to 12.8% with a rise from 500°C to 600°C and K loading from 0 to 1.9 wt% [46,63]. Cu could reach conversions close to equilibrium (80%) in RWGS due to high surface energy and low CO₂ and H₂ adsorption energies. Its reactivity is also related to its facility in switching from an oxidized state to a reduced state [7,64].

Molybdenum. Mo could promote catalytic metals in RWGS by improving their activity, selectivity and dispersion and the transfer of electrons [7,65,66].

Ruthenium. Well dispersed ruthenium nanoparticles (Ru⁰) took part in methane reforming with conversion of CH₄ and CO₂ nearing 95% [42,67]. Ru was mentioned for tar reduction but showed poorer

yields than Pt, Pd and Ni (6% more) [26,68]. Ru^o were effective for RWGS especially when supported on CeO₂ since it helps drive CO selectivity towards 97% at 230°C but CO₂ conversion was adjusted to be less than 5% (equilibrium is 14%) [7,69].

Rhodium. The CH₄ and CO₂ reaction rates for methane reforming were double for rhodium (Rh) than Ru and CO₂ was slightly more consumed resulting in a slight favoring of RWGS [4,70,71].

Palladium. Palladium (Pd) was mentioned for tar reduction with yields as low as 2 wt% [26,68]. The performance of Pd in RWGS, as with Ni, could also be related to its surface energy [7,47,72].

Silver. Silver could promote a conversion of 10% at 700°C in RWGS that could be hindered by low surface energy. A 10% conversion could also be attained at 800°C in the absence of catalysts so there is a slight catalytic effect and promotion could be necessary to better its electronic properties [7].

Platinum. Well dispersed platinum (Pt^o) nanoparticles took part in methane reforming with CH₄ conversion reaching 75% at 800°C [42,73]. Pt was mentioned for tar reduction reaching 50% C conversion at 800°C [26,74]. Pt supported by CeO₂ could reach near equilibrium CO₂ conversion (45%) at 450°C in RWGS while maintaining CO selectivity above 98% [7,75].

Gold. Gold (Au) supported on Al₂O₃ and TiO₂ were highly catalytic of WGS and RWGS. Its conversion in RWGS varied between 0% at 250°C and 40% at 450°C (nearly equilibrium) depending on the support (Ti>Al) and gas flow rate (decreased conversion) [7,76].

3.1.2.4. Lanthanides

Cerium. Cerium (Ce) formed nanoparticles that could contribute to H₂ production by facilitating adsorption and activation of O and other electronegative molecules due to its strong electronic properties, but it is not too active and is generally used as a support [30,77].

3.1.2.5. Post-transition metals

Aluminum. At 350 to 500°C, Fe₂O₃-Al₂O₃ was used for WGS. Al is generally used as a support as its reduced state allows for improved O molecule uptake which is beneficial for WGS (CO, H₂O) and RWGS (CO₂) [26]. The combination of Ni and Al oxides was effective to catalyze H₂ production, doubling H₂ yield from pyrogasification of mixed biomass/plastic feedstock [55,56].

Zinc. Zn and Zn on hydroxyapatite support do not seem to have a stand-alone effect on reforming reactions, but when co-catalyzed with Cu for example, (methanol) conversion can reach 97-100% [30,37,78]. ZnCl₂ improved H₂ production by catalyzing WGS and it increased H₂ yield by approximately 20% [28,29,31,79]. ZnO contributed to the activity of Cu in RWGS due to electron transfer and adsorption and reaction of H₂ to facilitate formation of intermediate species forming ultimately CO [7].

3.1.2.6. Metalloids and nonmetals

Carbon. Carbon (C) can be in many forms in pyrogasification, from the carbon matrix of biocarbon to the formation of inhibiting species such as coke and tar. Coke inhibited catalysts by creating deposits on their surface, thereby reducing the number of active sites that are accessible to gasifying agents [29]. To counteract coke production, a light flow of air or O₂ can be introduced, which will combust it as it is formed [27]. Furthermore, combustion heat generated by consuming coke feeds endothermic reactions. Tar deposit may corrode and deactivate catalysts [13]. The increase in air to biomass ratio, temperature and the reduction in steam quantities limits the formation of tar. Reforming of tar is favored by the high temperature and the presence of catalysts. However, the presence of CO could also restrict the decomposition of tar [29].

Silicon and phosphorus. Si and P both have a similar effect. By comparing reactivities of different biomass, it was shown that species with the least silicon and phosphorus were more reactive [80]. They deactivate K by forming silicates and phosphates. In addition, these silicates and phosphates would be formed in pores, encapsulating them, reducing accessibility to active sites and thereafter reducing catalytic activity [43]. Despite this, Ni₂P(001) could catalyze WGS due to maintaining access to the catalytic site and P reinforced the electronic properties of Ni [57].

Sulfur. Sulfur (S) and hydrogen sulfide (H₂S) poison catalysts by forming stable species such as sulfides and sulfates. They chemisorb on active sites and sometimes block pores. This limits the regeneration of catalysts in addition to reducing the catalytic effect of the active sites. At the cost of H₂, it is possible to maintain sulfur as H₂S. Like with coke, O₂ could maintain sulfur in form of sulfur dioxide (SO₂) [81]. Sulfur species are known to be corrosive [82]. Steam could also have the same effect as H₂ and O₂ [43].

Chlorine. Chlorine (Cl) and hydrochloric acid (HCl) are often associated to the corrosion of equipment and catalysts. They are also related to the volatilization of metals, namely alkaline and alkaline earth-metals, and therefore the vaporization of catalytic species [13,82]. However, some salts containing Cl are reported to have a catalytic effect. An increase in hydrogen production in presence of KCl, LiCl, NaCl and ZnCl₂ was noted. The reactivity increased least with KCl and most with ZnCl₂ [29]. The role KCl played during pyrolysis by reforming tar, and in WGS, was mentioned [32,33]. MgCl₂ improved H₂ production by catalyzing WGS [28]. ZnCl₂ was suggested as a catalyst for H₂ production because it increased H₂ yield by approximately 20%. It also catalyzed WGS [28,31,79].

3.1.2.7. Synergies between inorganic elements

Synergy is the interaction between two metals that leads to benefic catalytic effects. This can be caused by one metal absorbing CO₂, another H₂, and the facilitation of the reaction between these molecules

thanks to the closer proximity of active sites (less than 1 nm). This can also be related to the prevention of the deactivation of one metal by sintering thanks to the presence of another metal, or a stronger uptake of the reactive species [7,83,84].

Fe does not show a strong catalytic activity on its own and is generally promoted by AAEM namely K, Mg and Na or co-catalysts such as Ni, Cu and Co, more active species [46,49,85,86]. Fe allows strong CO₂ adsorption through strong electron exchange and O vacancies that accept CO₂ electrons (Lewis base). Fe and Ni can be supported by Al₂O₃, SiO₂, CrO₂. These supports and the promoters prevent sintering, coking and other deactivation phenomena, through transformation of the active phase, while improving reactant adsorption thanks to O vacancies. These promoters and supports can also adjust selectivity towards a specific product, CO for RWGS, by weak adsorption and fast removal because of limited electron availability [4,7,46,47,66,87]. Ni favors CO and CH₄ formation so promotion and support can be necessary for its selectivity [4,59,77,88]. Fast CO desorption with low H₂ adsorption could also unlock access to active sites for CO₂, increasing catalytic performance. Promoters can help reducing the energy necessary for adsorption and desorption in addition to providing further adsorption sites [4,7,47,66]. Biocarbon can act as a potent support allowing strong metal-surface interaction and increased O vacancies related to the bond between metal and carbon that furthers electron transfer, and the reduction of O functional groups respectively [89,90]. The dispersion of the metal active sites and the adsorption of gases are also affected because of this bond and are linked to the porous structure of biocarbon (site availability) and heterogenous surface sites (different electron density) [91,92]. The aforementioned effect of the inorganic elements during pyrogasification reactions and their synergy was summarized (Table 3.1).

Table 3.1. Inorganic species and their role (inhibition or catalysis) in pyrogasification and RWGS

AAEM		Transition, post-transition and lanthanide	Metalloid/Nonmetal
Alkaline	Alkaline-earth		
$\text{Li}_2\text{CO}_3/\text{LiCl}$			C (coke and tar)
$\text{Na}^+/\text{Na}_2\text{CO}_3/\text{NaCl}/\text{Na pr.}$	$\text{MgO}/\text{MgCO}_3/\text{MgCl}_2$	$\text{Fe}_2\text{O}_3\text{-Al}_2\text{O}_3/\text{Ni-Al oxide}/\text{Ni-Al}/\text{Al}_2\text{O}_3\text{ sup.}$	$\text{SiO}_2\text{ phosphate}/\text{Ni}_2\text{P}/\text{SiO}_2\text{ sup.}$ $\text{H}_2\text{S}/\text{sulfide}/\text{sulfate}/\text{SO}_2$ $\text{Cl}/\text{HCl}/\text{LiCl}/\text{NaCl}/\text{KCl}/\text{MgCl}_2/\text{ZnCl}_2$
$\text{K}^+/\text{K}_2\text{CO}_3/\text{K}_2\text{Ca}(\text{CO}_3)_2/\text{KCl}/\text{K pr.}$	$\text{CaCO}_3/\text{CaO}/\text{Ca}^{2+}/\text{K}_2\text{Ca}(\text{CO}_3)_2$	$\text{Fe}_2\text{O}_3\text{-Cr}_2\text{O}_3/\text{Fe}_2\text{O}_3\text{-Al}_2\text{O}_3/\text{CoO}/\text{Ni-Al oxide}/\text{CuO- ZnO}/\text{Zn}^\circ/\text{Zn}/\text{ZnCl}_2/\text{Cu-Zn}/\text{ZnO sup.}$ $\text{TiO}_2\text{ sup.}/\text{Cr oxide}/\text{Cr pr.}/\text{Cr}_2\text{O}_3\text{ sup.}$ $\text{Mn}^\circ/\text{Mn}^{2+}/\text{MnO sup.}$ $\text{Fe}(\text{CO})_5/(\alpha\text{-})/\text{Fe}_2\text{O}_3/\text{Fe}^\circ/\text{Fe}/\text{Fe-Co}/\text{Fe}(\text{NO}_3)_3/\text{Fe}/\text{Fe oxide}/\text{Fe}_3\text{C}$ $\text{Co}^\circ/\text{Co}/\text{Ni-Co}/\text{Fe-Co}/\text{Co oxide}/\text{Ni-Al}/\text{Ni-Sn}/\text{Ni}/\text{Ni}(\text{NO}_3)_2/\text{Ni}_2\text{P}/\text{Ni}$ $\text{Cu}^\circ/\text{Cu}/\text{Cu pr.}/\text{Cu}/\text{Cu oxide}$	
$\text{Rb}_2\text{CO}_3/\text{Rb pr.}$		$\text{ZrO}_2\text{-CeO}_2\text{ sup.}/\text{Mo}(\text{CO})_6/\text{Mo pr.}$ $\text{Ru}^\circ/\text{Ru}/\text{Ru}^\circ$ Rh Pd/Pd $\text{Ag pr.}/\text{Ag}$	Ni-Sn
$\text{Cs}_2\text{CO}_3/\text{Cs pr.}$	Ba pr.	$\text{Ce}^\circ/\text{ZrO}_2\text{-CeO}_2\text{ sup.}/\text{CeO}_2\text{ sup.}$ $\text{W}(\text{CO})_6$ $\text{Pt}^\circ/\text{Pt}/\text{Pt pr.}/\text{Pt}$ Au	
Legend sup.: support pr.: promoter	Reforming catalyst WGS/RWGS ¹ catalyst Pyrolysis and production of H ₂ (WGS, reforming or production of H ₂ not detailed)	Pyrolysis catalyst H ₂ production catalyst	Generally inhibiting Inhibiting/little effect

1: Underlined = RWGS

3.2. Materials and methods

3.2.1. Preparation and utilization of the biocarbon catalysts

3.2.1.1. Production of biocarbon catalysts

Fern and willow were selected as raw bioresources because of their ability to cumulate heavy metals from soil in phytoremediation, and for their availability. Willow was harvested in the South of France in 2015. Fern corresponds to shrublands mainly composed of fern harvested in Brittany (France) in 2019.

To mimic heavy metal content in phytoremediation and to obtain a biocarbon catalyst with a controlled metal content, both biomass and resulting biocarbon were impregnated. A 98 wt% pure Ni nitrate ($\text{Ni}(\text{NO}_3)_2 \cdot 6 \text{H}_2\text{O}$) and Fe nitrate ($\text{Fe}(\text{NO}_3)_3 \cdot 9 \text{H}_2\text{O}$) solutions containing traces of other metal elements including Co, Cu, Zn and Si, were used for this aim. For biocarbon catalysts preparation, biomass was pyrolyzed under 1 L/min nitrogen (N_2) from 25°C to 800°C, at 2°C/min, followed by an isothermal step at 800°C for an hour. Gibbs free energy minimization via FactSage software was used to simulate metal partitioning during biomass pyrolysis and select the optimal pyrolysis temperature (500 to 1000°C, every 50°C). Fe partitioning was shown to be dependent on pyrolysis temperature: under 750°C FeO was formed, at 800°C metallic Fe was formed and above this temperature Fe_3C was the main species formed. In the case of Ni, the main species was metallic Ni but a slight volatilization (< 1 wt%) of the content was noted above 850°C. 800°C was therefore selected as biomass pyrolysis temperature to avoid volatilization or transformation of catalytic metal species.

In a second step, impregnation was carried out to reach a metal load of 30 mg per g of biocarbon. Wetness impregnation (WI) was applied to biomass: 20 g of biomass was submerged in different 1 L aqueous solutions containing Fe or Ni nitrates, stirred for 3 days and then dried for 1 day at 60°C [6]. WI based on insipient WI (IWI) was applied to biocarbon: wettable volume and amount of nitrate to attain a fixed percentage of metal in biocarbon helped determine a concentration of nitrate to thereafter be replicated in 100 mL of water for 2 g of biocarbon [3]. The solutions were stirred for varying amounts and time and then dried for 1 day at 60-105°C (Table 3.2). Unimpregnated fern biocarbon (RF) and willow biocarbon (RW) were prepared in the same conditions of pyrolysis for comparison.

Table 3.2. Biocarbon catalysts, names, impregnation conditions and metal content in biocarbon

Biocarbon catalyst	Abbreviation	Impregnation conditions			Metal content (wt% in BC)
		Raw material	Impregnation method	Impregnated metal	
Fern biocarbon impregnated with Ni before pyrolysis	FNi-B	Fern	Before pyrolysis (WI of BM)	Ni	3.96
Fern biocarbon impregnated with Ni after pyrolysis	FNi-A	Fern	After pyrolysis (WI of BC)	Ni	1.43
Fern biocarbon impregnated with Fe before pyrolysis	FFe-B	Fern	Before pyrolysis	Fe	13.17
Fern biocarbon impregnated with Fe after pyrolysis	FFe-A	Fern	After pyrolysis	Fe	0.51
Fern biocarbon impregnated with Fe & Ni before pyrolysis	FNiFe	Fern	Before pyrolysis	Fe Ni	10.30 8.08
Willow biocarbon impregnated with Ni before pyrolysis	WNi-B	Willow	Before pyrolysis	Ni	2.41
Willow biocarbon impregnated with Ni after pyrolysis	WNi-A	Willow	After pyrolysis	Ni	1.81
Willow biocarbon impregnated with Fe before pyrolysis	WFe-B	Willow	Before pyrolysis	Fe	4.64
Willow biocarbon impregnated with Fe after pyrolysis	WFe-A	Willow	After pyrolysis	Fe	0.23

3.2.1.2. Utilization of biocarbon catalysts in RWGS

Biocarbon catalysts were then tested for RWGS reaction in a fixed bed reactor (Top Industries (France), 8 mm diameter, 25 cm long, Fig. 3.1). The reactor was filled with the catalyst and an inert bed of alumina ($\theta\text{-Al}_2\text{O}_3$, [93]), which steadied the catalysts position in the isothermal area of the reactor [2,3]. Moisture was removed before reaction by flowing Ar at 120°C for 1h and samples were then pre-reduced under 60/40 vol% H₂/Ar at 500°C for 2h. RWGS was carried out at 400°C, for at least 3 bar during a maximum of 72h. Some variation in pressure (3 bar increase) was observed between repetitions but the results were little affected (low deviation). Gas flows used were 60 mL/min of H₂, 20 mL/min of CO₂, and 150 mL/min of Ar. All gases were preheated at 120°C before being introduced in the reactor. Dried permanent gases (CO, CO₂, H₂, CH₄) were analyzed by online $\mu\text{-GC/TCD}$ (Agilent 990) connected after the reactor [4].

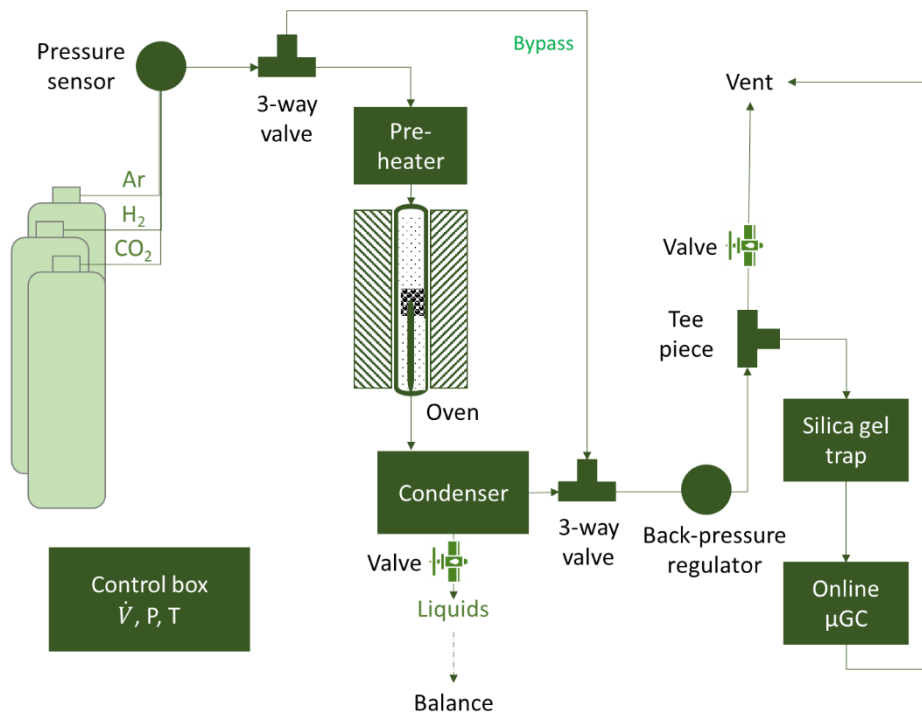


Fig. 3.1. Set-up for the Reverse Water-Gas Shift (RWGS) experiments

To compare experimental results, equilibrium of RWGS was calculated only considering the species involved in the reaction at the conditions of the reaction. These conditions were 400°C and initially 20 mL/min CO₂ and 60 mL/min H₂. Equilibrium values were determined using the expression of equilibrium constant according to concentrations of reactive and produced gases at equilibrium, and reported values for the WGS equilibrium constant (Eq.3.2, $K_{eq,WGS} = 11.74$) [94].

$$K_{eq,RWGS} = \frac{[CO]_{eq}[H_2O]_{eq}}{[CO_2]_{eq}[H_2]_{eq}} = \frac{1}{K_{eq,WGS}} \quad \text{Eq.3.2}$$

Following these calculations, the flow rates at equilibrium of the reactive and produced gases are 52.94 mL/min of H₂, 12.94 mL/min of CO₂, 7.06 mL/min of CO and 7.06 mL/min of H₂O. Ar flow rate remains unchanged. This results in a conversion rate of CO₂ to CO of 35% at equilibrium.

Biocarbon catalysts were characterized in terms of organic elements content (CHNS analysis, Flash 2000), inorganic elements content (ICP-AES, Ultima 2) and their dispersion on the carbonaceous matrix (SEM, Thermo Fischer Quattro S; HRTEM, JEOL JEM-ARM200F), thermal stability (TGA-DSC, Labsys Evo 1600), surface area (BET, N₂, Tristar II 3020), textural properties and surface chemical groups (TPD, TPR, TPO, Micromeritics Autochem 2920; XRD, PANalytical X'PERT PRO MDP). The changes in the structure of the biocarbon catalyst were analyzed before and after the chemical reaction.

3.2.2. Performance of the biocarbon catalysts

The performance of the biocarbon catalysts was evaluated by the mean of selectivity and conversion rate. Selectivity (S) allows to compare produced molecules and identify, in this case, if CO₂ forms preferentially CO or CH₄. Therefore, selectivity was defined as the ratio of the molar or volumetric flow (\dot{V}) of the target carbon gases produced compared to the sum of all carbon gases produced through the reaction (Eq.3.3 and 4).

$$S_{CO} = \frac{\dot{V}_{CO}}{\dot{V}_{CO} + \dot{V}_{CH_4}} \quad \text{Eq.3.3}$$

$$S_{CH_4} = 1 - S_{CO} \quad \text{Eq.3.4}$$

Conversion rate of the limiting gas CO₂ represents consumption of this gas to form products. A higher conversion represents a higher activity from the biocarbon catalyst. Conversion (X) was therefore defined as the ratio between the consumed amount of CO₂, calculated by the difference of inlet and outlet flowrate, divided by the inlet flow rate of the respective gas (Eq.3.5).

$$X_{CO_2} = \frac{\dot{V}_{inlet,CO_2} - \dot{V}_{outlet,CO_2}}{\dot{V}_{inlet,CO_2}} \quad \text{Eq.3.5}$$

3.3. Experimental results

In this section, the results obtained for the catalysts in RWGS are presented and discussed.

3.3.1. Performance of the biocarbon catalysts for RWGS

The performance of the catalysts was evaluated through CO selectivity and CO₂ conversion comparing type of bioresource (fern (Fig. 3.2) and willow (Fig. 3.3)), type of impregnation (before and after pyrolysis), and type of metal impregnated (Fe and Ni). The results are summarized in terms of the concentration of the reactive (H₂ and CO₂) and the product gases (CO and CH₄), the selectivity towards CO and CH₄ and the CO₂ conversion. This allows the comparison of the catalytic activity between biocarbon catalysts, reference catalysts and equilibrium conditions (Table 3.3).

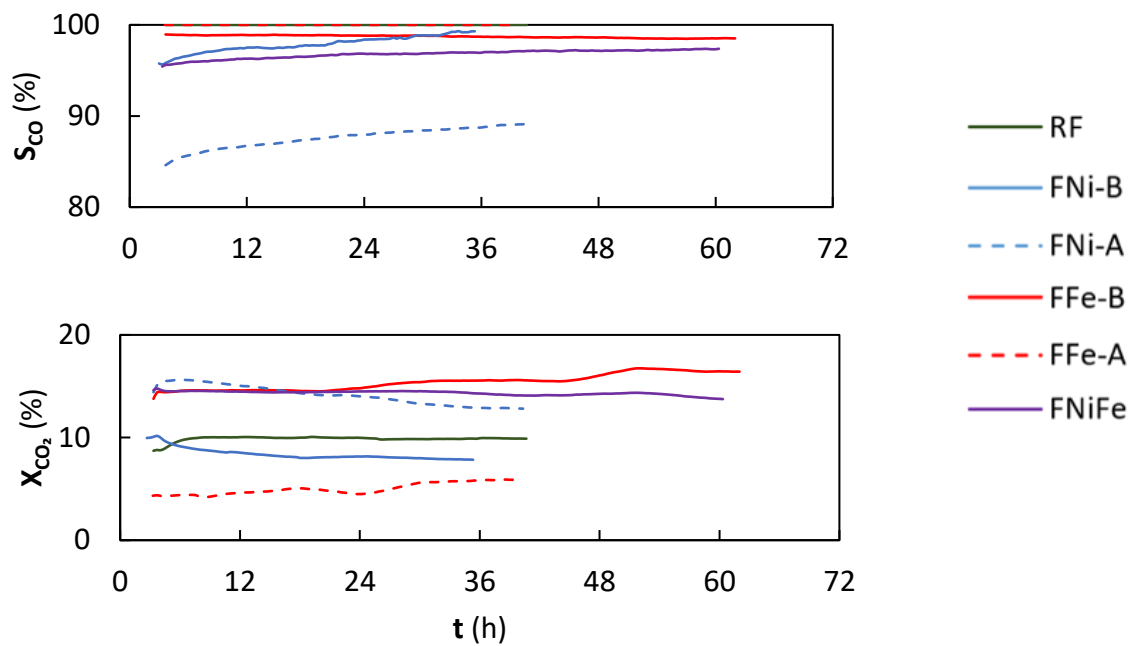


Fig. 3.2. Selectivity in CO (top) and conversion of CO₂ (bottom) of fern biocarbon catalysts tested in RWGS at 400°C

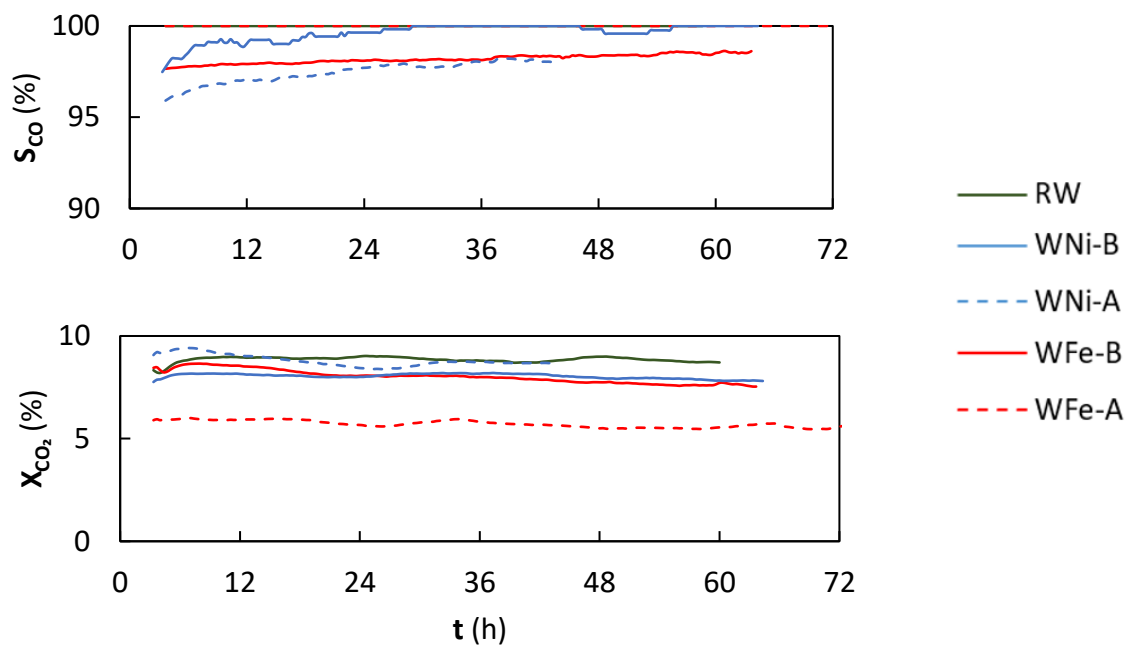


Fig. 3.3. Selectivity in CO (top) and conversion of CO₂ (bottom) of willow biocarbon catalysts tested in RWGS at 400°C

Table 3.3. Summary of averaged concentrations, selectivity and conversion for the trialed catalysts

				Concentration of gases (vol%)				Conversion	Selectivity (%)	
				H ₂	CO ₂	CO	CH ₄	X _{CO₂} (%)	S _{CO}	S _{CH₄}
Biocarbon and reference catalysts		Initial composition		26.1	8.7	-	-	-	-	-
		RWGS equilibrium		23.0	5.6	3.1	-	35.0	100	0
Sample	Biomass	Metal	Impregnation before/after pyrolysis	Concentration of gases (vol%)				Conversion	Selectivity (%)	
				H ₂	CO ₂	CO	CH ₄	X _{CO₂} (%)	S _{CO}	S _{CH₄}
RF	fern	-	-	21.9	7.4	0.1	<0.0	10.0	100	0
FNi-B	fern	Ni	before	21.8	7.4	0.2	<0.0	8.5	97.8	2.2
FNi-A	fern	Ni	after	21.2	6.7	0.8	0.1	15.5	88.3	11.7
FFe-B	fern	Fe	before	21.1	6.8	0.9	<0.0	16.1	98.0	2.0
FFe-A	fern	Fe	after	21.8	7.5	0.1	<0.0	5.0	100	0
FNiFe	fern	Fe,Ni	before	21.1	6.9	0.6	<0.0	14.3	96.7	3.3
RW	willow	-	-	21.9	7.4	0.1	<0.0	9.1	100	0
WNI-B	willow	Ni	before	21.7	7.5	0.1	<0.0	8.0	99.4	0.6
WNI-A	willow	Ni	after	21.8	7.5	0.2	<0.0	8.8	97.4	2.6
WFe-B	willow	Fe	before	21.8	7.2	0.2	<0.0	9.2	98.2	1.8
WFe-A	willow	Fe	after	21.9	7.5	0.1	<0.0	5.7	100	0
FNi-A no red	fern	Ni	after	21.0	6.7	0.9	0.1	17.2	94.4	5.6
FFe-B long	fern	Fe	before	21.0	6.7	0.9	<0.0	17.1	97.5	2.5
Rust	-	Fe	-	18.9	5.5	1.8	0.4	29.6	81.0	19.0
Fe doped alumina	-	Fe	-	21.5	7.3	0.3	<0.0	7.6	100	0

Values for CO (and other gases) concentration are in a comparable range to equilibrium concentration (3.1 vol%, Table 3.3). The values may appear as low, due to the Ar dilution, but remain above μ GC detection limit (0.001 vol%). The most active biocarbon catalysts were tested twice, the maximum relative standard deviation obtained was 5.5%.

The catalysts present a high selectivity towards CO, which is reflected by the low CH₄ production. This is especially relevant compared to the rust (88-100% versus 81%), which is usually taken as a reference. It should be noted that selectivity towards CO is high (>80%) for all catalysts and in these operating conditions despite the fact that CH₄ is formed thermodynamically [4,95,96]. Reported commercial catalysts can reach selectivity close to 100% but the promoting effect of other metals, such as K, is necessary [46,47]. Some biocarbon catalysts shown conversion rates lower than that of Fe-doped alumina, while others are more performant (at most 17.2% compared to 7.6%). Their performance is however inferior to rust (29.6%) or other reported catalysts (near equilibrium, in this case 35%) [97]. On another hand, the performance of the biocarbon catalysts was stable as no loss in conversion was observed during the 288h on stream, whereas commercial catalysts are deactivated by sintering and C fouling before 120h [7,46,47].

3.3.1.1. Type of bioresource

The type of bioresource proved to have an effect on RWGS, as fern catalysts showed a higher CO₂ conversion at the cost of CO selectivity (Table 3.3, Fig. 3.2 and 3). This behavior may be explained by

the higher inherent content of metals in fern, obtained through ICP-AES analysis (Table 4). According to the elemental composition for unimpregnated biocarbon, total inorganic content and composition are coherent with reported fern and willow. Slight differences observed could be due to the origin of the biomass (soil, species, age, ...) [98–103]. Impregnated biocarbon content is higher than that reported for phytoremediation and hyperaccumulation plants to clearly show the effect of Ni and Fe as catalysts in RWGS [104–110]. Nevertheless, it can be noted that AAEM were leached due to impregnation but Ni or Fe content increased and could be comparable to thresholds for hyperaccumulation (3000 µg/g biocarbon, [110]). The content of some heavy metals such as Zn could increase with impregnation due to their introduction in the impregnation medium as impurities of the Fe and Ni nitrates.

3.3.1.2. Inorganic elements

The results showed that fern-based biocarbon catalysts converts better the reactive gases of RWGS (Table 3.3). This difference in performance compared to the willow biocarbon could be firstly explained by inorganic elements (Table 3.4). AAEM in fern biocarbon could facilitate reducibility and stability of active metals by lowering energy barriers and preventing their transformation and sintering. The synergy of these metals could limit the uptake of H₂ therefore preventing hydrogenation of CO, in addition to allotting more sites for an increased CO production [111–114]. They can also result in higher CO₂ reactivity and better activation from fern biocarbon catalysts. This could be explained by a better electronic transfer and an increase in reactive sites.

Table 3.4. Inorganic composition (µg/g biocarbon) of willow and fern biocarbon catalysts before RWGS

	RF	FNi-B	FNi-A	FFe-B	FFe-A	FNiFe	RW	WNi-B	WNi-A	WFe-B	WFe-A
Na	3822	<1	<1	1218	<1	904	245	<1	<1	<1	<1
K	19192	5134	4565	3976	6588	3619	6660	2003	1860	1395	1859
Mg	2759	904	380	887	720	1055	1968	745	1455	562	1049
Ca	9321	4446	7818	3436	8110	4708	23393	7349	7117	1059	6862
Mn	68	<1	<1	73	<1	186	172	<1	<1	74	<1
Fe	263	<1	<1	131669	5098	103030	279	<1	<1	46409	2276
Co	245	<1	31	311	<1	750	186	<1	<1	51	<1
Ni	1	39580	14282	49	<1	80800	16	24075	18147	45	<1
Cu	<1	<1	<1	<1	<1	1	<1	<1	<1	82	<1
Al	172	742	<1	2877	43	1448	81	456	489	127	3481
Zn	19	927	<1	21	<1	311	67	846	819	<1	822
Cd	<1	<1	<1	<1	<1	1	<1	<1	<1	21	<1
Si	17450	14040	20870	44151	31987	45653	1058	401	1327	<1	2197
P	2257	1500	1207	3989	1203	4473	3607	<1	2489	<1	300

The multitude of metals inherent to fern biocarbon (RF) was also observable by HRTEM (Fig. 3.4). Some elements such as Mg, K and Cl are highly dispersed on the carbon surface, others such as Ca and Si are more agglomerated with a particle size reaching 27 nm. Similarly, dispersed O, which indicates O

groups related to the carbon surface or O containing metal speciation, seems denser in areas where Si and Ca are located. These results agree with XRD characterizations (Fig. 3.5), which show that Si is in an oxidized state. However, these metals seem covered by a carbon layer without a structured morphology, meaning that the active sites might not be accessible for RWGS activity.

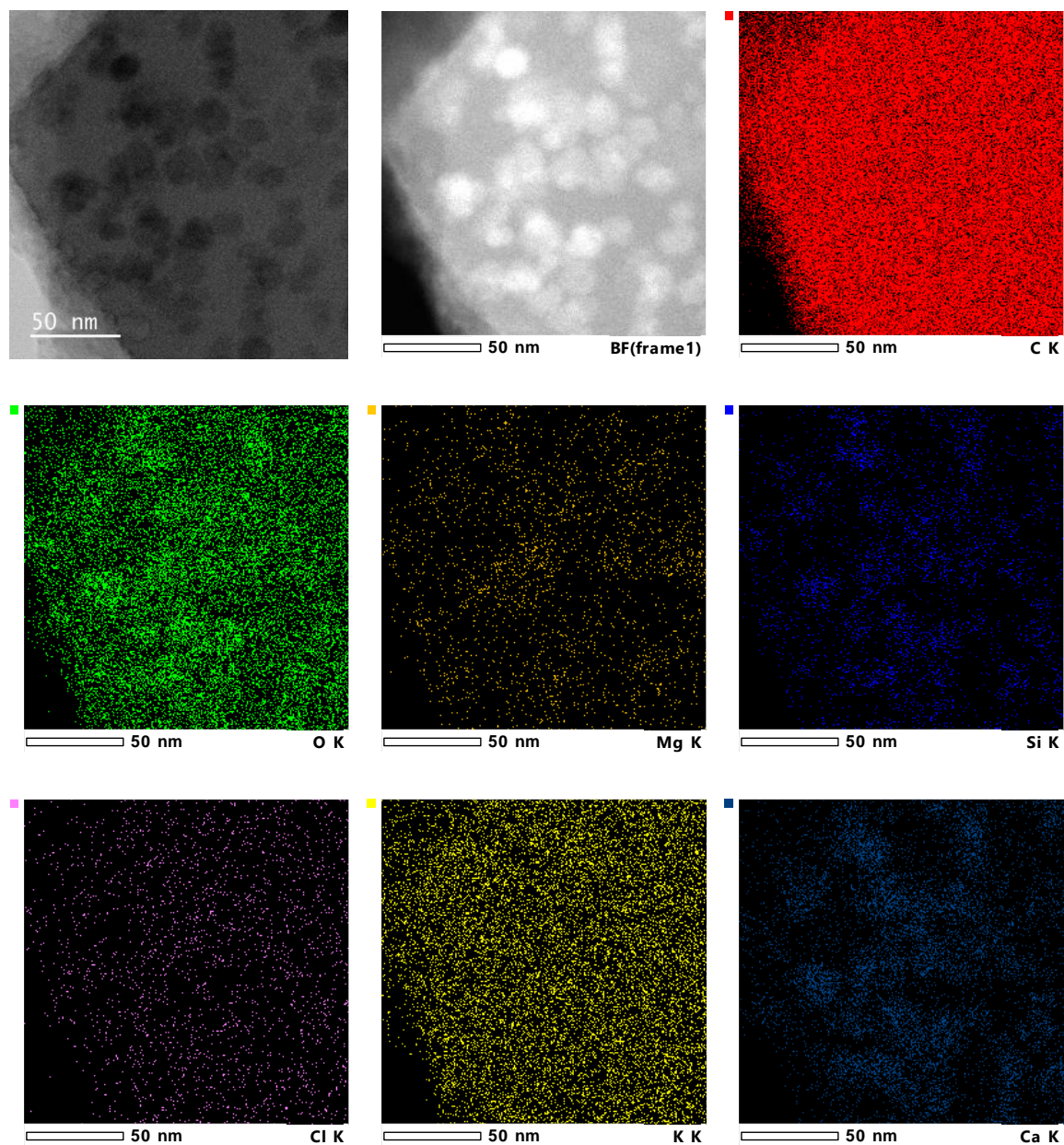


Fig. 3.4. HRTEM images of unimpregnated fern biocarbon (RF) before its use in RWGS

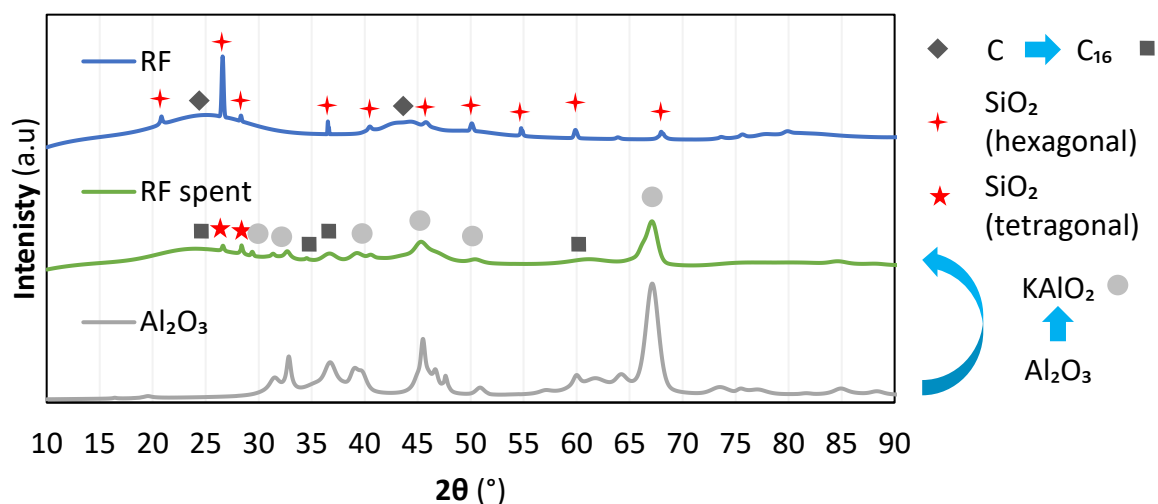


Fig. 3.5. XRD diffractogram of unimpregnated fern biocarbon (RF) not spent and spent by RWGS (and Al₂O₃)

The high activity of the fern biocarbon impregnated with Ni after pyrolysis (FNI-A) could be linked to dispersion of Ni. Varying sizes of particles were observed, reaching hundreds of nanometers. They could possibly be in an oxidized state before reaction that once reduced results in O deprived sites that could facilitate the capture of O from CO₂ (Fig. 3.6). As Ni was deposited on the surface of the biocarbon, it is possible that they were easily accessible, which may explain the enhanced activity of this catalyst.

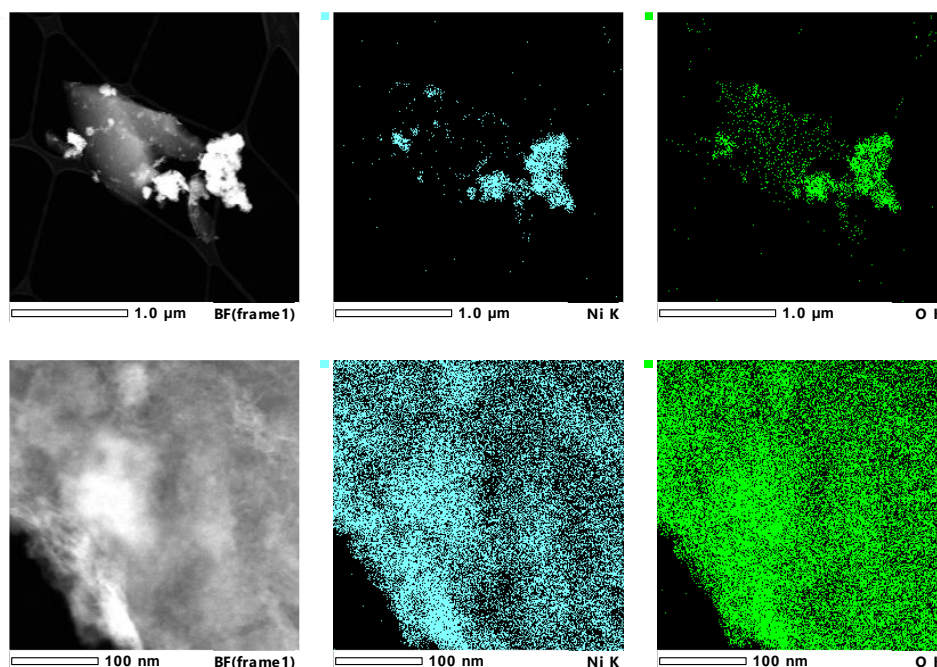


Fig. 3.6. HRTEM images of fern biocarbon impregnated with Ni after pyrolysis (FNI-A) before its use in RWGS

This variety in particle size also stands out with fern biocarbon impregnated with Fe before pyrolysis (FFe-B), as big as 56 nm, and in a possible oxidized state (Fig. 3.7). The addition of Fe could however

create an ordered state of carbon (graphitization) and an external shell composed of Fe and C surrounding an Fe dense structure [115,116]. This could induce an increase in specific surface area, and improve electric and thermal conductivities [117].

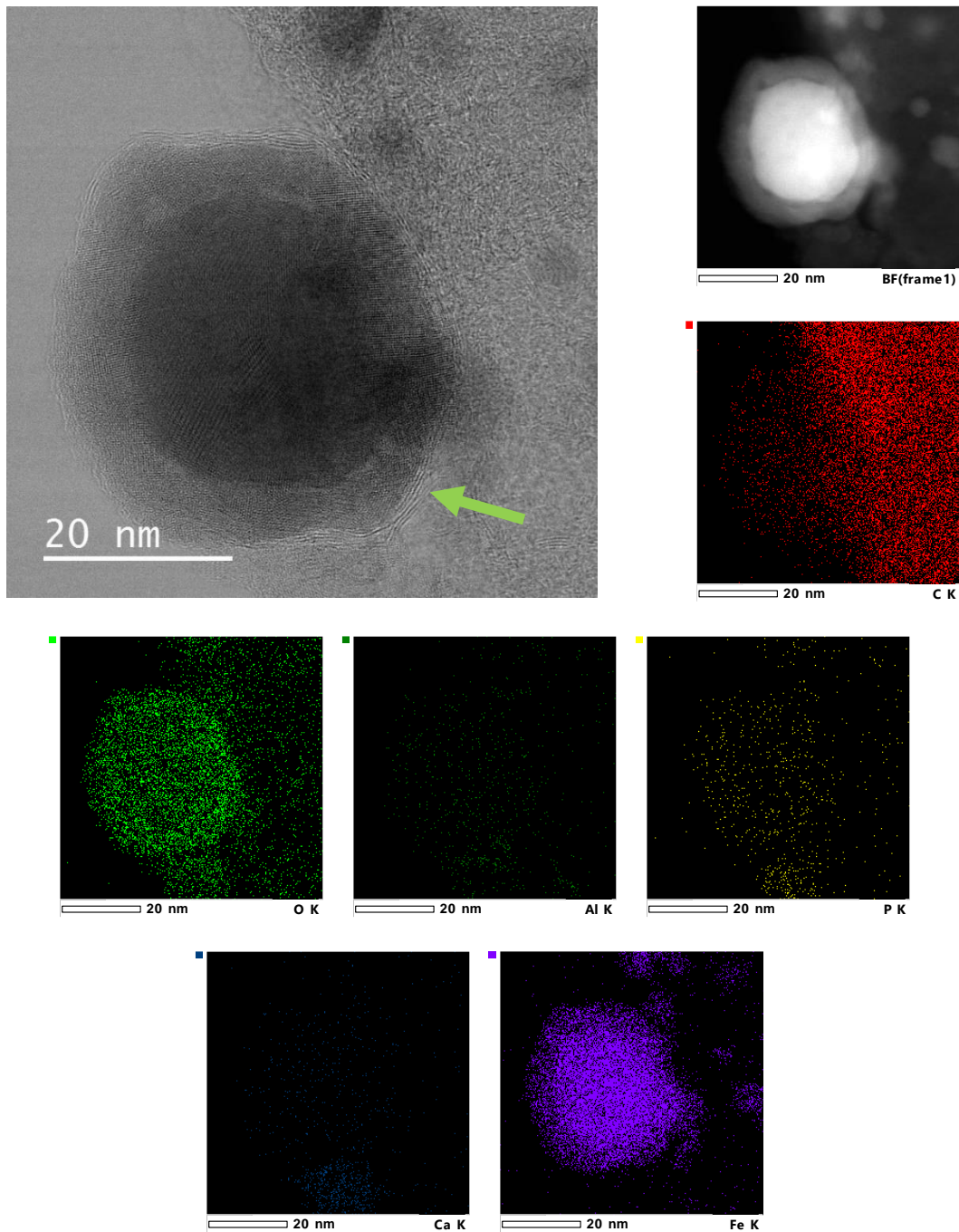


Fig. 3.7. HRTEM images of fern biocarbon impregnated with Fe before pyrolysis (FFe-B) before its use in RWGS

3.3.1.3. Surface properties and functional groups

The type (acid, basic, reduction sites) and force (value of maximal temperature) of surface chemical functions were measured through temperature programmed desorption (TPD, NH_3), oxidation (TPO, CO_2) and reduction (TPR, H_2 , Table 3.5). The total amount of adsorbed probe gases, corresponding to

the sum of the area of peaks from TPX (X = D, O, R), and the specific surface area, obtained via BET measurements under N₂, were indicated (Table 3.5).

The values for the total quantity of adsorbed NH₃, CO₂, H₂ and the specific surface area were found to be inferior for fern-based biocarbon catalysts than for willow-based. This contrasts to the higher metal content of fern biocarbon catalysts. Therefore, fern-based biocarbon should possess a higher and stronger surface basicity in relation to this higher metal content. This would enable more CO₂ adsorption and higher desorption temperature. Given the adsorptive nature of the unimpregnated biocarbon, surface functional groups could be responsible for a higher and stronger uptake of gases compared to the metals [118–120]. This could explain why willow-based biocarbon having better gas adsorptive properties does not result in better RWGS performance as it lacks the synergetic effect provided by other metals (Table 3.4). Lower specific surface area could be due to lower volatile matter content resulting in less porosity formed during pyrolysis, which is coherent with the literature results for herbaceous biomass such as fern [100,121]. Impregnation seems to impact little the chemical adsorption. This could be explained by the impregnation of metals Fe or Ni on the biomass or biocarbon compensated by AAEM leached by the impregnating medium. Additionally, a decrease in adsorption is possible if the impregnating metals block porosity and should result in an equal loss of specific surface area. In this case, the specific surface area increases with impregnation. In the case of impregnation before pyrolysis, this increase could be related to the development of pores during catalyzed pyrolysis or due to opening of enclosed pores during impregnation after pyrolysis [122,123]. In certain cases, it is possible that the presence of Fe in the initial biomass favors the graphitization of carbon, as it was evidenced by HRTEM (**Fig. 3.7**). This creates porosity, which could explain the high specific surface for these catalysts. According to the results, the specific surface area seems decorrelated from the gas adsorption. There is a slight effect of pore blocking or opening that could affect specific surface area but does not impact the availability of the functional groups. This could be again related to the biocarbon functional groups being responsible for the gas adsorption and therefore a modification in surface area barely modifies the gas adsorption because of the omnipresence of the functional groups. This however affects the activity of the catalysts as a severe loss in surface area (a collapse of porosity) induces a loss in availability of active sites and in turn results in (Fe) doped biocarbon catalysts even lesser active than undoped ones (Table 3.3).

Table 3.5. Chemical surface groups versus specific surface area of the biocarbon catalysts, before RWGS

Sample	TPD-NH ₃		TPD-CO ₂		TPD-H ₂		Specific surface area (m ² /g)
	Total adsorption (mmol/g)	T _{max} (°C)	Total adsorption (mmol/g)	T _{max} (°C)	Total adsorption (mmol/g)	T _{max} (°C)	
RF	0.779	913	12.003	915	2.545	993	8.8
FNi-B	1.480	912	16.207	920	2.921	986	151.6
FNi-A	0.847	945	11.956	923	1.673	989	100.0
FFe-B	0.553	951	8.258	905	0.158	981	309.6
FFe-A	0.840	951	10.918	956	2.617	981	27.4
FNiFe	1.088	923	15.980	924	0.994	1000	367.9
RW	1.460	889	23.288	907	1.501	999	42.4
WNI-B	1.968	949	25.458	914	0.282	988	419.1
WNI-A	1.548	930	26.260	915	2.922	986	336.4
WFe-B	1.249	960	27.773	935	2.108	985	384.2
WFe-A	1.255	940	14.810	960	1.393	982	9.2

In the case of willow biocarbon catalysts, the catalytic activity seems independent to the impregnation method (before or after pyrolysis) or the metal (Fe or Ni, **Fig. 3.2**). Stronger differences could be observed for fern biocarbon catalysts (**Fig. 3.3**) and the best results were obtained for fern biocarbon impregnated with Fe before pyrolysis (FFe-B), impregnated with Ni after pyrolysis (FNi-A) and impregnated with Fe and Ni before pyrolysis (FNiFe). This could be related to the high dispersion of highly active sites of small particle size in combination with inherent metals (ex. K) and O vacancies that could be observed by HRTEM (**Fig. 3.4** and 6). They enhance reactivity and facilitate adsorption and transformation of CO₂ and H₂ [124–126].

The nature of the O surface functional groups of biocarbon catalysts can be evidenced by TPD coupled with μ GC. An inert gas (He) is used to transport gases produced and desorbed by the biocarbon. This analysis provides insights on the type of functional group knowing the desorbed gases released (CO or CO₂ here) by the surface of the adsorbent and the temperature at which they desorbed [43,119,127,128]. Deconvoluting the peaks detected in μ GC can inform about the type of site. By correlating the temperature of desorption and the desorbed gas with data from literature, it is possible to identify and quantify the functional group (Table 3.6). Once reduced, these O functional groups create O vacancies which are involved electron transfer in RWGS.

Table 3.6. Desorption temperatures and gases associated to functional groups from literature [43,119,127–129]

Surface functional group	Temperature ranges (°C)		Desorbed gases
	[Low	; High]	
Carboxyl	[100	; 400]	CO ₂ +CO
	[200	; 300]	CO ₂
	[300	; 430]	CO ₂
	[400	; 550]	CO ₂ +CO
Lactone	[190	; 650]	CO ₂
	[600	; 750]	CO ₂
	[570	; 900]	CO ₂
Peroxide	[450	; 580]	CO ₂
Anhydride	[350	; 450]	CO ₂ +CO
	[540	; 640]	CO
	[350	; 627]	CO
	[350	; 627]	CO ₂ +CO
Hydroxyl	[570	; 670]	CO
Phenol	[580	; 710]	CO
	[690	; 800]	CO
Ether	[794	; 910]	CO
	[794	; 910]	CO
Carbonyl + Quinone	[800	; 900]	CO
	[700	; 980]	CO
Quinone	[830	; 950]	CO
Pyrone	[920	; 1023]	CO

In the case of fern biocarbon impregnated with Fe and Ni before pyrolysis (FNiFe), only CO₂ was released (Fig. 3.8). By deconvoluting the CO₂ production of this catalyst before its use in RWGS (Fig. 3.8, left), the 4 Gauss curbs were attributed to carboxylic and lactone functions of increasing strengths (higher peak temperatures). While carboxylic groups are amphoteric, lactone groups are strictly basic. This contradicts the fact that biocarbon adsorbed more CO₂ than NH₃ without reduction (Table 3.5), as CO₂ is also basic. When reduced, these functional groups were deprived of O and will attract O containing species such as CO₂. Since here the RWGS reaction involved a step of pre-reduction and exposure to H₂, the lack of O surface functions after reaction was expected as no CO was produced and very little CO₂ (Fig. 3.8, right). The presence of these groups and that of inherent metals in the biomass allows a better activation and adsorption of the reactants due to stronger electronic properties. This also facilitates the desorption of the products and a better H spillover, which helps in separating H₂ and CO₂ in order to form H₂O and CO [125,130,131].

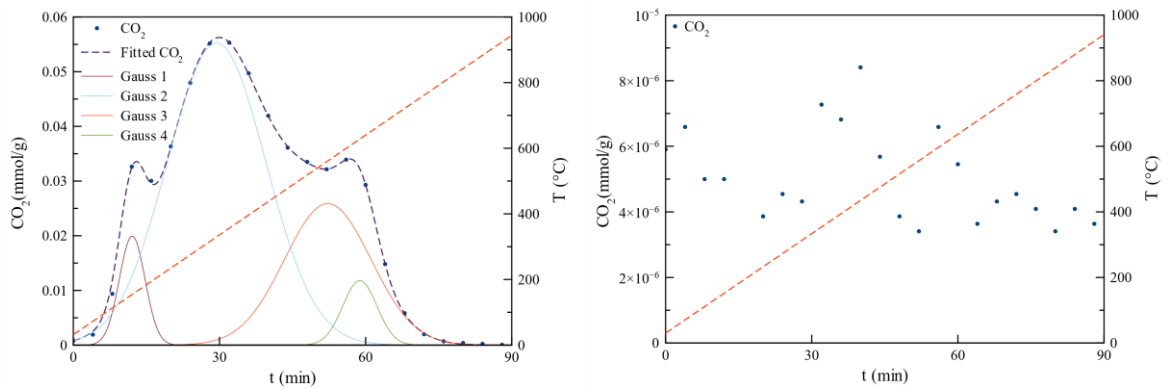


Fig. 3.8. CO₂ desorbed while increasing temperature of FNiFe before RWGS (left) and after RWGS (right)

The presence of iron carbides (Fe₃C) was detected for FFe-B by XRD, and could be related to the biocarbon graphitization (Fig. 3.7). Fe₃C contributes as well to improved H₂ and CO₂ activation and dissociation due to the difference in electronegativity, in relation to the developed thermal and electric conductivities, facilitating the acceptance of electrons by Fe (Fig. 3.9) [48,49,95]. The alumina mixed with the biocarbon catalyst is also functionalized by reaction with the K naturally present in fern (Fig. 3.9 and 10). By attrition, fern-based biocarbon loses K on its surface, diminishing the potential additional CO₂ adsorption and reaction related to its synergy with Fe active sites [128]. It should also be noted the difficulty to reduce this alumina as it conserves an oxidized state and should therefore contribute little to the RWGS reaction that involves a change of state [97].

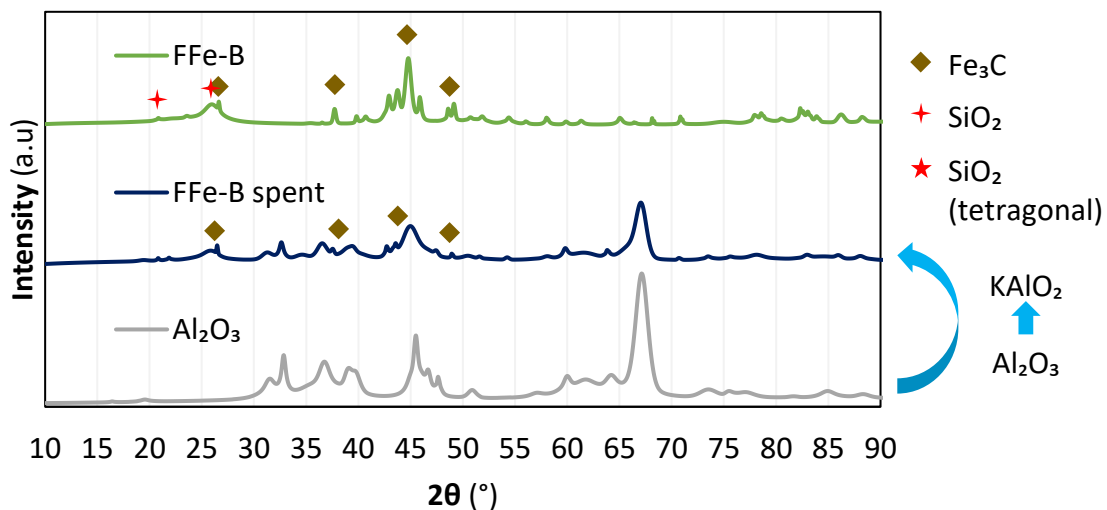


Fig. 3.9. XRD diffractogram of FFe-B not spent and spent by RWGS (and Al₂O₃)

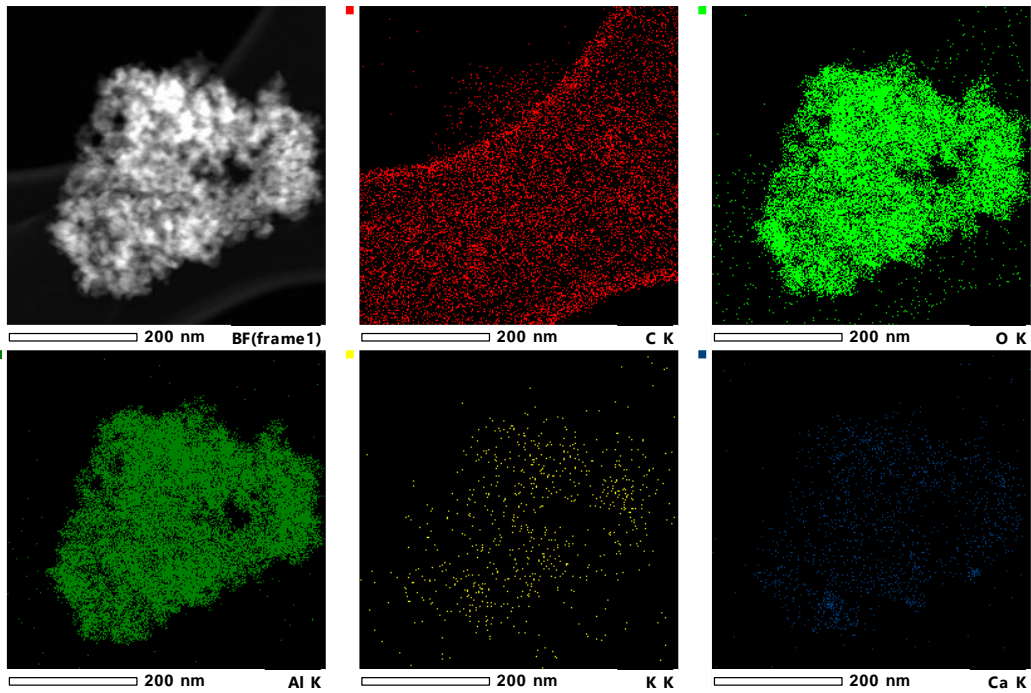


Fig. 3.10. HRTEM images of alumina after RWGS with RF, loss of metals on alumina

3.3.2. Comparison with other catalysts

Rust (Fe_2O_3) and Fe doped alumina ($\text{Fe-Al}_2\text{O}_3$) were tested under the same conditions as the biocarbon catalysts for comparison (Table 3.3, Fig. 3.11). Furthermore, the effect of the duration of the experiment was investigated by testing the fern catalyst impregnated with Fe before pyrolysis (FFe-B long) during 288 hours (Fig. 3.11, time divided by 6). Finally, the effect of the reduction was assessed through the use of the fern catalyst impregnated with Ni after pyrolysis (FNI-A no red) without reduction before reaction.

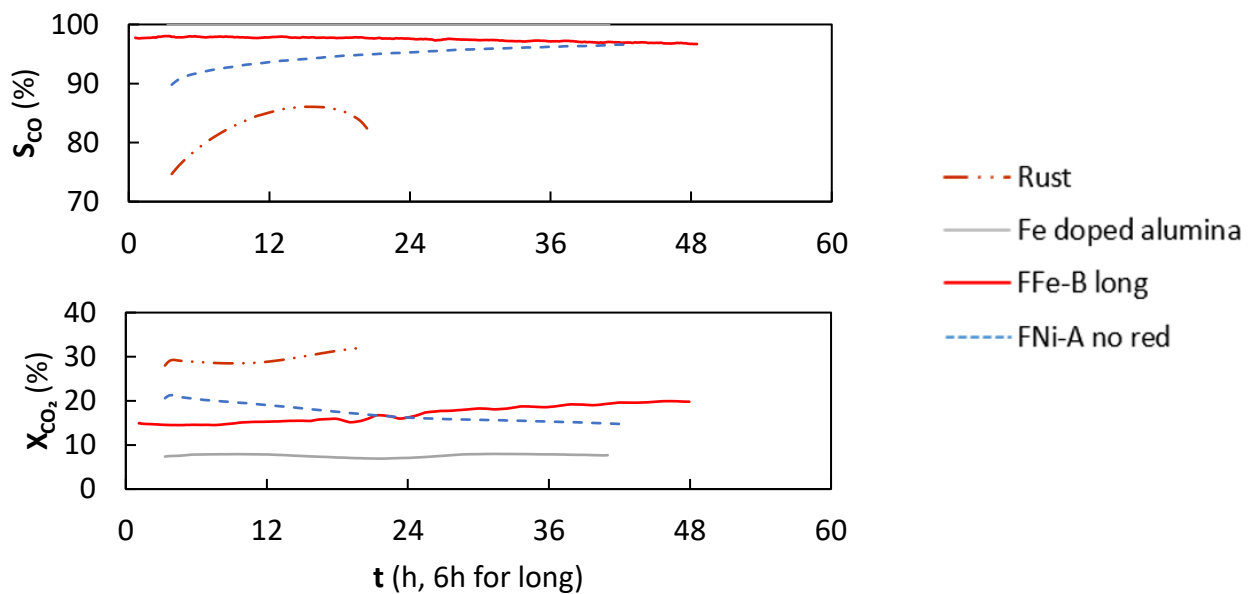


Fig. 3.11. Selectivity in CO (top) and conversion of CO_2 (bottom) of reference and biocarbon catalysts tested in RWGS at 400°C , with test of the effects of the duration and the reduction on the biocarbon catalysts

3.3.2.1. Rust and Fe-doped alumina

The catalytic activity of rust decreased with the production of CO, but then increased with the increasing production of CH₄. This first step of deactivation has been reported and attributed to the formation of Fe carbides [46,132]. During the experiment, the rust captured C up to 9.45 wt%. The presence of C and reducing atmosphere such as H₂ render the formation of Fe₃C possible (**Fig. 3.12**) and, despite being an active phase (Table 3.1), its formation in-situ induces loss of active sites by preventing access to the reacting gases. This could explain the higher presence of C and the shell-like structure of Fe observed in HRTEM of rust after RWGS (**Fig. 3.13**). This Fe ends up encapsulated by lowly structured C, that could result in the formation of Fe₃C, so Fe becomes unavailable for reaction.

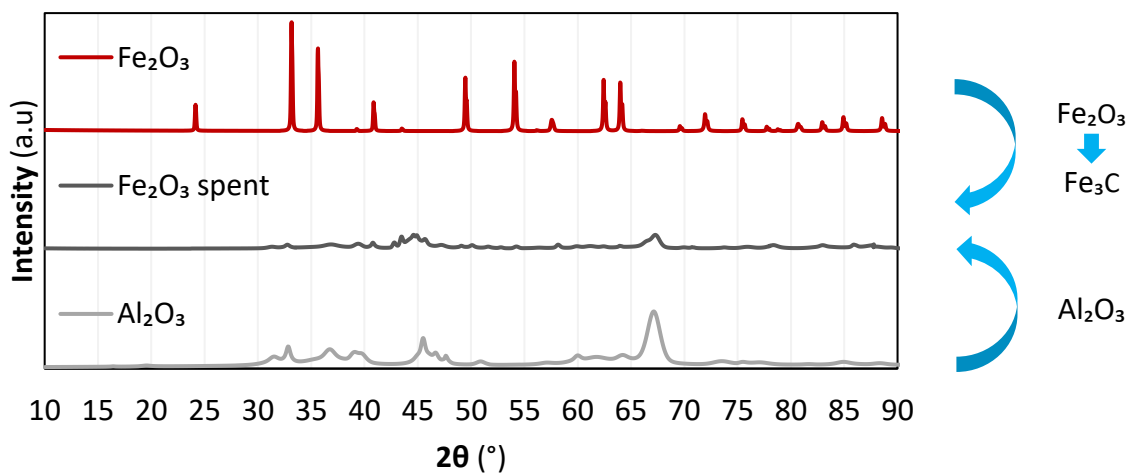


Fig. 3.12. XRD diffractogram of rust not spent and spent by RWGS (and Al₂O₃)

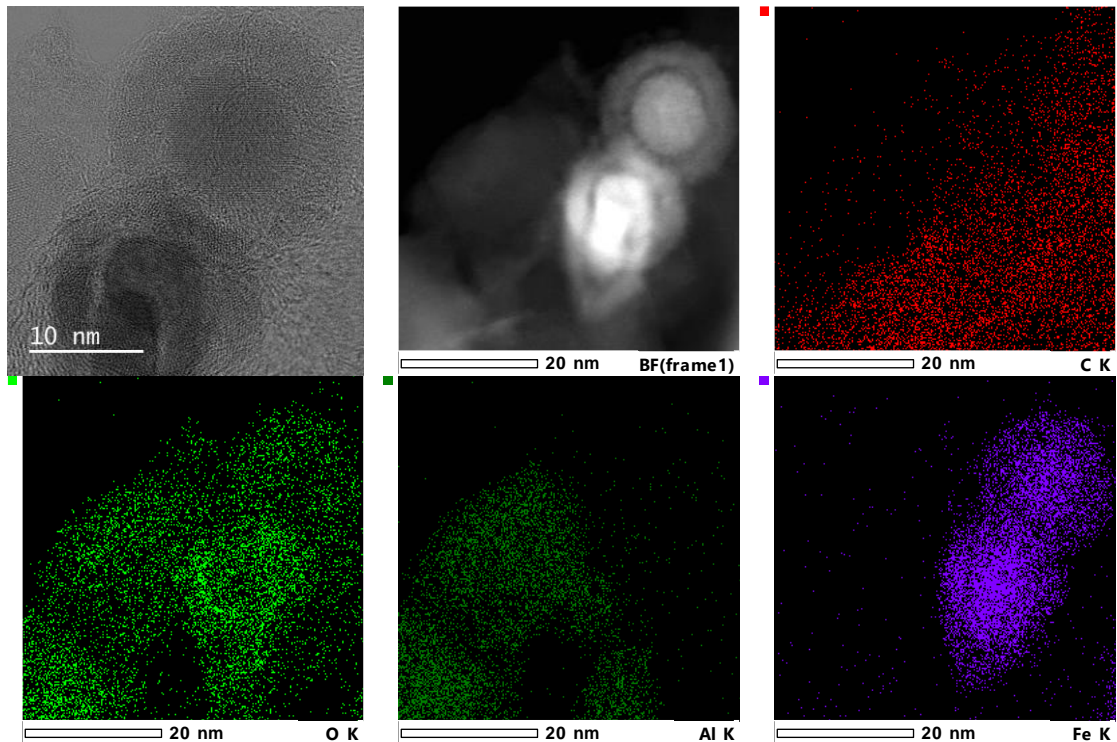


Fig. 3.13. HRTEM images of rust after RWGS

3.3.2.2. Influence of the pre-reduction stage

FNi-A was one of the best biocarbon catalysts in RWGS experiments and could have been in an oxidized state before RWGS (Fig. 3.6) compared to FFe-B that was in a partially reduced state (Fig. 3.7 and 9). The oxidized state of Ni was however not evidenced by XRD as no peaks related to Ni were identified (Fig. 3.14), possibly due to low crystalline content of Ni in the biocarbon that is inherently rich in other metals, namely Si, and further diluted by the presence of alumina after RWGS. The use of FNi-A without pre-reduction resulted in slightly better conversion and selectivity. This behavior may be due to a slight agglomeration of Ni⁰ when the catalyst is pre-reduced [91,133–135]. Likewise, the catalyst not having absorbed H₂ is favorable to immediately react with CO₂, whose absorption is more important than that of H₂ (Table 3.5). This is an important step for RWGS reaction, as it prevents further hydrogenation that may form CH₄ [124,136,137].

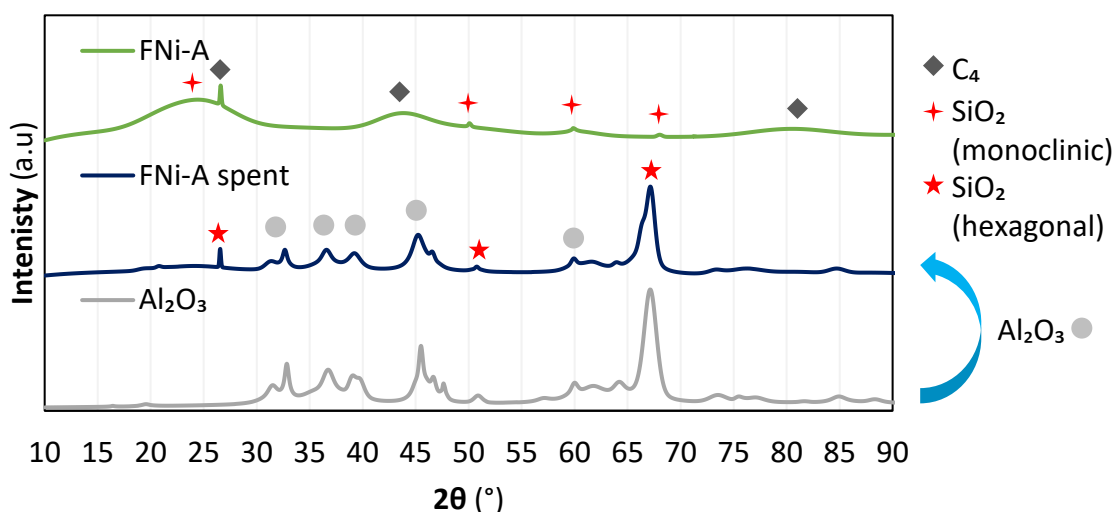


Fig. 3.14. XRD diffractogram of FNi-A not spent and spent by RWGS (and Al₂O₃)

3.3.2.3. Influence of a long residence time

Fern biocarbon impregnated with Fe before pyrolysis (FFe-B) was tested for 288h to investigate Fe deactivation. The biocarbon catalyst resulted in better conversion with little impact on selectivity. Fe catalysts can be deactivated via high temperature sintering or fouling by C deposition resulting also in loss of active sites [4,7,48,87]. In this case, no loss in activity was observed because of the presence of the active Fe₃C phase that, together with the mild operating conditions, prevents meaningful sintering (Fig. 3.11). Indeed, no significant difference in particle size was observed (less than 56 nm), and the slight constant increase in conversion observed over time could be related to better accessibility of the metals as the biocarbon is further graphitized by Fe (Fig. 3.15).

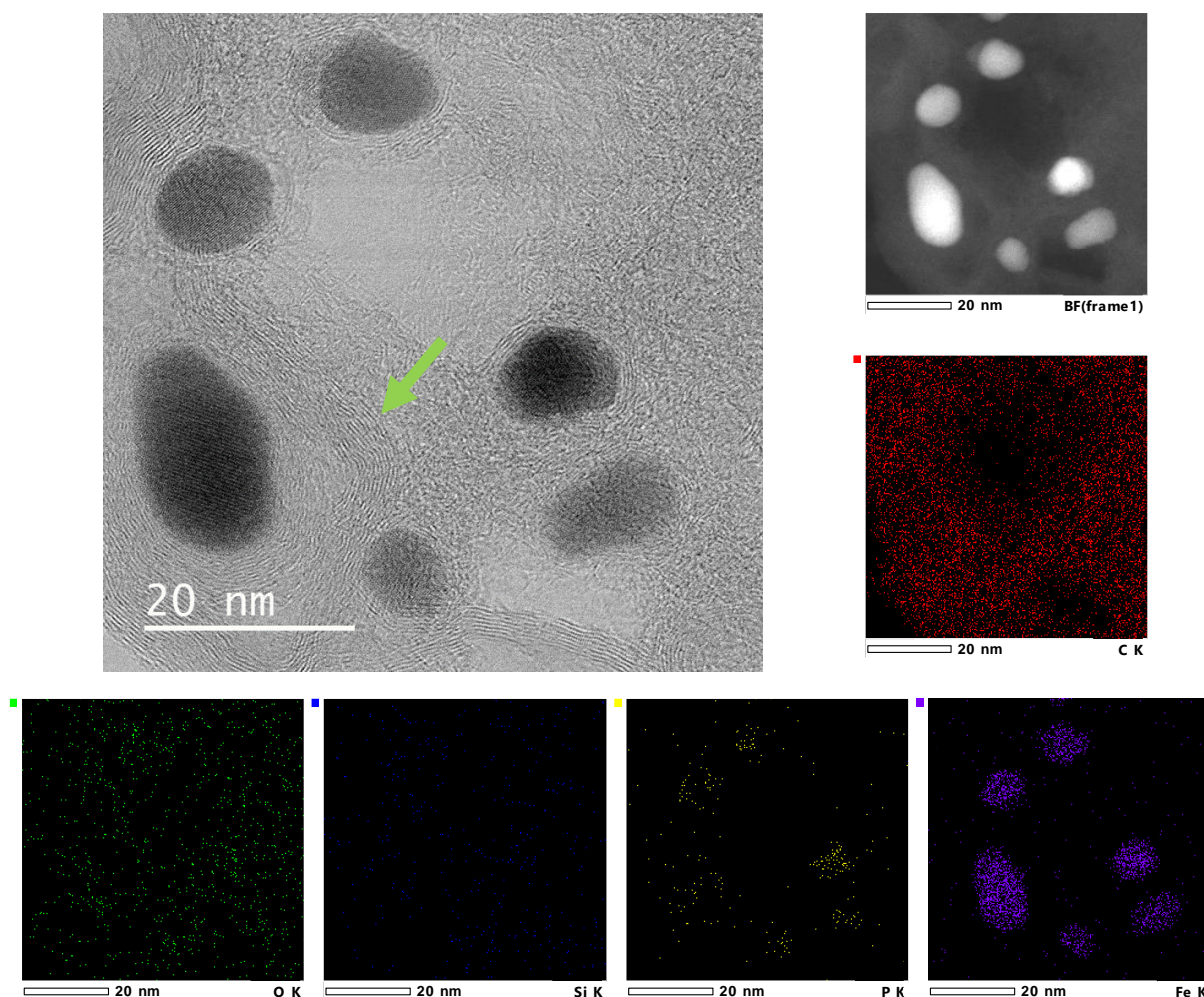


Fig. 3.15. HRTEM images of fern biocarbon impregnated with Fe before pyrolysis (FFe-B) after RWGS

3.4. Conclusion and perspectives

Biocarbon catalysts from fern and willow were produced, characterized and tested for RWGS reaction at 400°C and a ratio H_2/CO_2 of 3. These catalysts exhibited a strong ability to retain significant amounts of Fe and Ni after the impregnation process, while they also contain additional inherent metals. As a result, the synergistic effect of these metals could enhance the electronic properties of the active sites and facilitate the adsorption and dissociation of CO_2 and H_2 . The combination of these properties allowed fern to outperform willow-based biocarbon catalysts in RWGS. The surface functional groups and metals such as AAEM in addition to Fe or Ni have resulted in O vacancies after reduction that could increase catalytic performance due to better CO_2 adsorption and activation. Depending on the impregnation, the introduction of metals on the structure of the biocarbon could affect availability and activity of these sites by blocking access or by creating additional sites for better electron exchange. This could result in catalysts with high performances, such as FNi-A, FFe-B and FNiFe. Moreover, the biocarbon catalysts exhibited promising stability in the reaction conditions by maintaining conversion and selectivity for at least 72h, while Fe_2O_3 suffered severe C fouling. Complementary analytical

techniques could contribute in elucidating the role and influence of the structure and metal bonding of biocarbon catalysts in the high activity observed. This could be achieved by the modification of the catalyst structure through changing the operating conditions such as pre-reduction but also by activating and stabilizing the biocarbon through high temperature H₂O activation. This would allow use of the catalysts at higher temperatures, favoring RWGS while maintaining high selectivity. Additionally, future work should test catalysts performance in downstream reactions such as biofuel production by Fischer-Tropsch synthesis, CAMERE methanol synthesis, biogas reforming or conversion of pollutants in gaseous effluents. Finally, testing various inherently metal-rich biocarbon catalysts could help elucidate their high potential for RWGS.

References

- [1] Nations U. The Paris Agreement. United Nations n.d. <https://www.un.org/en/climatechange/paris-agreement> (accessed May 3, 2023).
- [2] Ghogia AC, Machado BF, Cayez S, Nzihou A, Serp P, Soulantica K, et al. Beyond confinement effects in Fischer-Tropsch Co/CNT catalysts. *Journal of Catalysis* 2021;397:156–71. <https://doi.org/10.1016/j.jcat.2021.03.027>.
- [3] Munirathinam R, Pham Minh D, Nzihou A. Effect of the Support and Its Surface Modifications in Cobalt-Based Fischer–Tropsch Synthesis. *Ind Eng Chem Res* 2018;57:16137–61. <https://doi.org/10.1021/acs.iecr.8b03850>.
- [4] Yang L. CO₂ conversion via reverse water-gas shift using multicomponent catalysts - University of Surrey. University of Surrey, 2021.
- [5] Lambert M, Leven BA, Green RM. New Methods of Cleaning Up Heavy Metal in Soils and Water. ENVIRONMENTAL SCIENCE AND TECHNOLOGY BRIEFS FOR CITIZENS n.d.:3.
- [6] Said M, Cassayre L, Dirion J-L, Joulia X, Nzihou A. Effect of Nickel Impregnation on Wood Gasification Mechanism. *Waste Biomass Valor* 2017;8:2843–52. <https://doi.org/10.1007/s12649-017-9911-3>.
- [7] Pahija E, Panaritis C, Gusarov S, Shadbahr J, Bensebaa F, Patience G, et al. Experimental and Computational Synergistic Design of Cu and Fe Catalysts for the Reverse Water–Gas Shift: A Review. *ACS Catal* 2022;12:6887–905. <https://doi.org/10.1021/acscatal.2c01099>.
- [8] Dastyar W, Raheem A, He J, Zhao M. Biofuel Production Using Thermochemical Conversion of Heavy Metal-Contaminated Biomass (HMCB) Harvested from Phytoextraction Process. *Chemical Engineering Journal* 2019;358:759–85. <https://doi.org/10.1016/j.cej.2018.08.111>.
- [9] Lee J, Kim K-H, Kwon EE. Biochar as a Catalyst. *Renewable and Sustainable Energy Reviews* 2017;77:70–9. <https://doi.org/10.1016/j.rser.2017.04.002>.
- [10] Di Blasi C. Combustion and gasification rates of lignocellulosic chars. *Progress in Energy and Combustion Science* 2009;35:121–40. <https://doi.org/10.1016/j.pecs.2008.08.001>.
- [11] Devi L, Ptasiński KJ, Janssen FJJG. A review of the primary measures for tar elimination in biomass gasification processes. *Biomass and Bioenergy* 2003;24:125–40. [https://doi.org/10.1016/S0961-9534\(02\)00102-2](https://doi.org/10.1016/S0961-9534(02)00102-2).
- [12] Sajjadi B, Chen W-Y, Egiebor N. A comprehensive review on physical activation of biochar for energy and environmental applications. *Reviews in Chemical Engineering* 2018;35. <https://doi.org/10.1515/revce-2017-0113>.
- [13] Said M. Comportements et rôles des métaux lourds au cours de la pyro-gazéification de la biomasse : études expérimentales et thermodynamiques. phdthesis. Ecole des Mines d’Albi-Carmaux, 2016.
- [14] Nanda S, Dalai AK, Berruti F, Kozinski JA. Biochar as an Exceptional Bioresource for Energy, Agronomy, Carbon Sequestration, Activated Carbon and Specialty Materials. *Waste Biomass Valor* 2016;7:201–35. <https://doi.org/10.1007/s12649-015-9459-z>.
- [15] Cheng F, Li X. Preparation and Application of Biochar-Based Catalysts for Biofuel Production. *Catalysts* 2018;8:346. <https://doi.org/10.3390/catal8090346>.
- [16] Butterman HC, Castaldi MJ. CO₂ as a Carbon Neutral Fuel Source via Enhanced Biomass Gasification. *Environ Sci Technol* 2009;43:9030–7. <https://doi.org/10.1021/es901509n>.
- [17] Guizani C, Jeguirim M, Gadiou R, Escudero Sanz FJ, Salvador S. Biomass char gasification by H₂O, CO₂ and their mixture: Evolution of chemical, textural and structural properties of the chars. *Energy* 2016;112:133–45. <https://doi.org/10.1016/j.energy.2016.06.065>.
- [18] Sekar M, Ponnusamy VK, Pugazhendhi A, Nižetić S, Praveenkumar TR. Production and utilization of pyrolysis oil from solid plastic wastes: A review on pyrolysis process and influence of reactors design. *Journal of Environmental Management* 2022;302:114046. <https://doi.org/10.1016/j.jenvman.2021.114046>.
- [19] Barr MR, Volpe R, Kandiyoti R. Influence of Reactor Design on Product Distributions from Biomass Pyrolysis. *ACS Sustainable Chem Eng* 2019;7:13734–45. <https://doi.org/10.1021/acssuschemeng.9b01368>.
- [20] Mkhize NM, Danon B, Alvarez J, Lopez G, Amutio M, Bilbao J, et al. Influence of reactor and condensation system design on tyre pyrolysis products yields. *Journal of Analytical and Applied Pyrolysis* 2019;143:104683. <https://doi.org/10.1016/j.jaap.2019.104683>.

- [21] Hlavsová A, Corsaro A, Raclavská H, Vallová S, Juchelková D. The effect of feedstock composition and taxonomy on the products distribution from pyrolysis of nine herbaceous plants. *Fuel Processing Technology* 2016;144:27–36. <https://doi.org/10.1016/j.fuproc.2015.11.022>.
- [22] Crombie K, Mašek O, Sohi SP, Brownsort P, Cross A. The effect of pyrolysis conditions on biochar stability as determined by three methods. *GCB Bioenergy* 2013;5:122–31. <https://doi.org/10.1111/gcbb.12030>.
- [23] González Martínez M, Dupont C, Thiéry S, Meyer X-M, Gourdon C. Impact of biomass diversity on torrefaction: Study of solid conversion and volatile species formation through an innovative TGA-GC/MS apparatus. *Biomass and Bioenergy* 2018;119:43–53. <https://doi.org/10.1016/j.biombioe.2018.09.002>.
- [24] Ronsse F, van Hecke S, Dickinson D, Prins W. Production and characterization of slow pyrolysis biochar: influence of feedstock type and pyrolysis conditions. *GCB Bioenergy* 2013;5:104–15. <https://doi.org/10.1111/gcbb.12018>.
- [25] Feng D, Zhao Y, Zhang Y, Xu H, Zhang L, Sun S. Catalytic mechanism of ion-exchanging alkali and alkaline earth metallic species on biochar reactivity during CO₂/H₂O gasification. *Fuel* 2018;212:523–32. <https://doi.org/10.1016/j.fuel.2017.10.045>.
- [26] Tanksale A, Beltramini JN, Lu GM. A review of catalytic hydrogen production processes from biomass. *Renewable and Sustainable Energy Reviews* 2010;14:166–82. <https://doi.org/10.1016/j.rser.2009.08.010>.
- [27] Bulushev DA, Ross JRH. Catalysis for conversion of biomass to fuels via pyrolysis and gasification: A review. *Catalysis Today* 2011;171:1–13. <https://doi.org/10.1016/j.cattod.2011.02.005>.
- [28] Nzihou A, Stanmore B, Sharrock P. A review of catalysts for the gasification of biomass char, with some reference to coal. *Energy* 2013;58:305–17. <https://doi.org/10.1016/j.energy.2013.05.057>.
- [29] Sutton D, Kelleher B, Ross JRH. Review of literature on catalysts for biomass gasification. *Fuel Processing Technology* 2001;73:155–73. [https://doi.org/10.1016/S0378-3820\(01\)00208-9](https://doi.org/10.1016/S0378-3820(01)00208-9).
- [30] Nzihou A, Stanmore B, Lyczko N, Minh DP. The catalytic effect of inherent and adsorbed metals on the fast/flash pyrolysis of biomass: A review. *Energy* 2019;170:326–37. <https://doi.org/10.1016/j.energy.2018.12.174>.
- [31] Demirbaş A. Gaseous products from biomass by pyrolysis and gasification: effects of catalyst on hydrogen yield. *Energy Conversion and Management* 2002;43:897–909. [https://doi.org/10.1016/S0196-8904\(01\)00080-2](https://doi.org/10.1016/S0196-8904(01)00080-2).
- [32] Yang H, Wang D, Li B, Zeng Z, Qu L, Zhang W, et al. Effects of potassium salts loading on calcium oxide on the hydrogen production from pyrolysis-gasification of biomass. *Bioresource Technology* 2018;249:744–50. <https://doi.org/10.1016/j.biortech.2017.10.083>.
- [33] Jiang L, Liu C, Hu S, Wang Y, Xu K, Su S, et al. Catalytic behaviors of alkali metal salt involved in homogeneous volatile and heterogeneous char reforming in steam gasification of cellulose. *Energy Conversion and Management* 2018;158:147–55. <https://doi.org/10.1016/j.enconman.2017.12.069>.
- [34] Klinghoffer N. Utilization of Char from Biomass Gasification in Catalytic Applications. Columbia University, 2013. <https://doi.org/10.7916/D86TOV1Z>.
- [35] Chen G, Andries J, Spliethoff H. Catalytic pyrolysis of biomass for hydrogen rich fuel gas production. *Energy Conversion and Management* 2003;44:2289–96. [https://doi.org/10.1016/S0196-8904\(02\)00254-6](https://doi.org/10.1016/S0196-8904(02)00254-6).
- [36] Son Phan T. Development, characterization and evaluation of a catalyst in the reforming of biogas for the production of green hydrogen. Phdthesis. Ecole des Mines d'Albi-Carmaux, 2020.
- [37] Vasconcelos BR de. Phosphates-based catalysts for synthetic gas (syngas) production using CO₂ and CH₄. phdthesis. Ecole des Mines d'Albi-Carmaux, 2016.
- [38] Dyson PJ. Catalysis by low oxidation state transition metal (carbonyl) clusters. *Coordination Chemistry Reviews* 2004;248:2443–58. <https://doi.org/10.1016/j.ccr.2004.04.002>.
- [39] Wu Z, Shen J, Li C, Zhang C, Feng K, Wang Z, et al. Mo₂TiC₂ MXene-Supported Ru Clusters for Efficient Photothermal Reverse Water–Gas Shift. *ACS Nano* 2023;17:1550–9. <https://doi.org/10.1021/acsnano.2c10707>.
- [40] Lei Y, Cant NW, Trimm DL. The origin of rhodium promotion of Fe₃O₄–Cr₂O₃ catalysts for the high-temperature water–gas shift reaction. *Journal of Catalysis* 2006;239:227–36. <https://doi.org/10.1016/j.jcat.2006.01.033>.

- [41] Shen Y. Chars as carbonaceous adsorbents/catalysts for tar elimination during biomass pyrolysis or gasification. *Renewable and Sustainable Energy Reviews* 2015;43:281–95. <https://doi.org/10.1016/j.rser.2014.11.061>.
- [42] Rego de Vasconcelos B, Pham Minh D, Martins E, Germeau A, Sharrock P, Nzihou A. Highly-efficient hydroxyapatite-supported nickel catalysts for dry reforming of methane. *International Journal of Hydrogen Energy* 2020;45:18502–18. <https://doi.org/10.1016/j.ijhydene.2019.08.068>.
- [43] Hervy M. Valorisation de chars issus de pyrogazéification de biomasse pour la purification de syngas : lien entre propriétés physico-chimiques, procédé de fonctionnalisation et efficacité du traitement. Thèse de doctorat. Ecole nationale des Mines d'Albi-Carmaux, 2016.
- [44] Wang L, Hisada Y, Koike M, Li D, Watanabe H, Nakagawa Y, et al. Catalyst property of Co–Fe alloy particles in the steam reforming of biomass tar and toluene. *Applied Catalysis B: Environmental* 2012;121–122:95–104. <https://doi.org/10.1016/j.apcatb.2012.03.025>.
- [45] Collard F-X, Bensakhria A, Drobek M, Volle G, Blin J. Influence of impregnated iron and nickel on the pyrolysis of cellulose. *Biomass and Bioenergy* 2015;80:52–62. <https://doi.org/10.1016/j.biombioe.2015.04.032>.
- [46] A. Loiland J, J. Wulfers M, S. Marinkovic N, F. Lobo R. Fe/ γ -Al₂O₃ and Fe–K/ γ -Al₂O₃ as reverse water-gas shift catalysts. *Catalysis Science & Technology* 2016;6:5267–79. <https://doi.org/10.1039/C5CY02111A>.
- [47] Chou C-Y, Loiland JA, Lobo RF. Reverse Water-Gas Shift Iron Catalyst Derived from Magnetite. *Catalysts* 2019;9:773. <https://doi.org/10.3390/catal9090773>.
- [48] Liu Y, Murthy PR, Zhang X, Wang H, Shi C. Phase transformation of iron oxide to carbide and Fe₃C as an active center for the RWGS reaction. *New J Chem* 2021;45:22444–9. <https://doi.org/10.1039/D1NJ04120G>.
- [49] Zhang Q, Pastor-Pérez L, Wang Q, Ramirez Reina T. Conversion of CO₂ to added value products via rWGS using Fe-promoted catalysts: Carbide, metallic Fe or a mixture? *Journal of Energy Chemistry* 2022;66:635–46. <https://doi.org/10.1016/j.jechem.2021.09.015>.
- [50] Kim DH, Han SW, Yoon HS, Kim YD. Reverse water gas shift reaction catalyzed by Fe nanoparticles with high catalytic activity and stability. *Journal of Industrial and Engineering Chemistry* 2015;23:67–71. <https://doi.org/10.1016/j.jiec.2014.07.043>.
- [51] Ghogia AC, Cayez S, Machado BF, Nzihou A, Serp P, Soulantica K, et al. Hydrogen Spillover in the Fischer-Tropsch Synthesis on Carbon-supported Cobalt Catalysts. *ChemCatChem* 2020;12:1117–28. <https://doi.org/10.1002/cctc.201901934>.
- [52] de la Osa AR, De Lucas A, Valverde JL, Romero A, Monteagudo I, Coca P, et al. Influence of alkali promoters on synthetic diesel production over Co catalyst. *Catalysis Today* 2011;167:96–106. <https://doi.org/10.1016/j.cattod.2010.11.064>.
- [53] Minh DP, Siang TJ, VO D-VN, Phan TS, Ridart C, Nzihou A, et al. Hydrogen production from biogas reforming: an overview of steam reforming, dry reforming, dual reforming, and tri-reforming of methane. In: Azzaro-Pantel C, editor. *Hydrogen supply chains : design, deployment and operation*, Elsevier; 2018, p. 111–66. <https://doi.org/10.1016/B978-0-12-811197-0.00004-X>.
- [54] Garbarino G, Cavattoni T, Riani P, Busca G. Support effects in metal catalysis: a study of the behavior of unsupported and silica-supported cobalt catalysts in the hydrogenation of CO₂ at atmospheric pressure. *Catalysis Today* 2020;345:213–9. <https://doi.org/10.1016/j.cattod.2019.10.016>.
- [55] Alvarez J, Kumagai S, Wu C, Yoshioka T, Bilbao J, Olazar M, et al. Hydrogen production from biomass and plastic mixtures by pyrolysis-gasification. *International Journal of Hydrogen Energy* 2014;39:10883–91. <https://doi.org/10.1016/j.ijhydene.2014.04.189>.
- [56] Bimbela F, Oliva M, Ruiz J, García L, Arauzo J. Hydrogen production by catalytic steam reforming of acetic acid, a model compound of biomass pyrolysis liquids. *Journal of Analytical and Applied Pyrolysis* 2007;79:112–20. <https://doi.org/10.1016/j.jaap.2006.11.006>.
- [57] Liu P, Rodriguez JA, Takahashi Y, Nakamura K. Water–gas-shift reaction on a Ni₂P(001) catalyst: Formation of oxy-phosphides and highly active reaction sites. *Journal of Catalysis* 2009;262:294–303. <https://doi.org/10.1016/j.jcat.2009.01.006>.
- [58] Marsh H, Adair RR. Catalytic gasification of doped carbon—a kinetic study. *Carbon* 1975;13:327–32. [https://doi.org/10.1016/0008-6223\(75\)90038-X](https://doi.org/10.1016/0008-6223(75)90038-X).

- [59] Benzinger W, Daymo E, Hettel M, Maier L, Antinori C, Pfeifer P, et al. Reverse water gas shift (RWGS) over Ni – Spatially-resolved measurements and simulations. *Chemical Engineering Journal* 2019;362:430–41. <https://doi.org/10.1016/j.cej.2019.01.038>.
- [60] Lang C, Sécordel X, Kiennemann A, Courson C. Water gas shift catalysts for hydrogen production from biomass steam gasification. *Fuel Processing Technology* 2017;156:246–52. <https://doi.org/10.1016/j.fuproc.2016.09.004>.
- [61] Schumacher N, Boisen A, Dahl S, Gokhale AA, Kandoi S, Grabow LC, et al. Trends in low-temperature water–gas shift reactivity on transition metals. *Journal of Catalysis* 2005;229:265–75. <https://doi.org/10.1016/j.jcat.2004.10.025>.
- [62] Lang C, Sécordel X, Courson C. Copper-Based Water Gas Shift Catalysts for Hydrogen Rich Syngas Production from Biomass Steam Gasification. *Energy Fuels* 2017;31:12932–41. <https://doi.org/10.1021/acs.energyfuels.7b01765>.
- [63] Chen C-S, Cheng W-H, Lin S-S. Study of reverse water gas shift reaction by TPD, TPR and CO₂ hydrogenation over potassium-promoted Cu/SiO₂ catalyst. *Applied Catalysis A: General* 2003;238:55–67. [https://doi.org/10.1016/S0926-860X\(02\)00221-1](https://doi.org/10.1016/S0926-860X(02)00221-1).
- [64] Choi S, Sang B-I, Hong J, Yoon KJ, Son J-W, Lee J-H, et al. Catalytic behavior of metal catalysts in high-temperature RWGS reaction: In-situ FT-IR experiments and first-principles calculations. *Sci Rep* 2017;7:41207. <https://doi.org/10.1038/srep41207>.
- [65] Yang L, Pastor-Pérez L, Villora-Pico JJ, Gu S, Sepúlveda-Escribano A, Reina TR. CO₂ valorisation via reverse water-gas shift reaction using promoted Fe/CeO₂-Al₂O₃ catalysts: Showcasing the potential of advanced catalysts to explore new processes design. *Applied Catalysis A: General* 2020;593:117442. <https://doi.org/10.1016/j.apcata.2020.117442>.
- [66] Kharaji AG, Shariati A, Takassi MA. A Novel γ -Alumina Supported Fe-Mo Bimetallic Catalyst for Reverse Water Gas Shift Reaction. *Chinese Journal of Chemical Engineering* 2013;21:1007–14. [https://doi.org/10.1016/S1004-9541\(13\)60573-X](https://doi.org/10.1016/S1004-9541(13)60573-X).
- [67] Das S, Shah M, Gupta RK, Bordoloi A. Enhanced dry methane reforming over Ru decorated mesoporous silica and its kinetic study. *Journal of CO₂ Utilization* 2019;29:240–53. <https://doi.org/10.1016/j.jcou.2018.12.016>.
- [68] Tomishige K, Asadullah M, Kunimori K. Syngas production by biomass gasification using Rh/CeO₂/SiO₂ catalysts and fluidized bed reactor. *Catalysis Today* 2004;89:389–403. <https://doi.org/10.1016/j.cattod.2004.01.002>.
- [69] Aitbekova A, Wu L, Wrasman CJ, Boubnov A, Hoffman AS, Goodman ED, et al. Low-Temperature Restructuring of CeO₂-Supported Ru Nanoparticles Determines Selectivity in CO₂ Catalytic Reduction. *J Am Chem Soc* 2018;140:13736–45. <https://doi.org/10.1021/jacs.8b07615>.
- [70] Doherty F, Goldsmith BR. Rhodium Single-Atom Catalysts on Titania for Reverse Water Gas Shift Reaction Explored by First Principles Mechanistic Analysis and Compared to Nanoclusters. *ChemCatChem* 2021;13:3155–64. <https://doi.org/10.1002/cctc.202100292>.
- [71] Djinić P, Črnivec IGO, Batista J, Levec J, Pintar A. Catalytic syngas production from greenhouse gasses: Performance comparison of Ru-Al₂O₃ and Rh-CeO₂ catalysts. *Chemical Engineering and Processing: Process Intensification* 2011;50:1054–62. <https://doi.org/10.1016/j.cep.2011.05.018>.
- [72] Pettigrew DJ, Trimm DL, Cant NW. The effects of rare earth oxides on the reverse water-gas shift reaction on palladium/alumina. *Catal Lett* 1994;28:313–9. <https://doi.org/10.1007/BF00806061>.
- [73] Ruiz JAC, Passos FB, Bueno JMC, Souza-Aguiar EF, Mattos LV, Noronha FB. Syngas production by autothermal reforming of methane on supported platinum catalysts. *Applied Catalysis A: General* 2008;334:259–67. <https://doi.org/10.1016/j.apcata.2007.10.011>.
- [74] Furusawa T, Saito K, Kori Y, Miura Y, Sato M, Suzuki N. Steam reforming of naphthalene/benzene with various types of Pt- and Ni-based catalysts for hydrogen production. *Fuel* 2013;103:111–21. <https://doi.org/10.1016/j.fuel.2011.09.026>.
- [75] Zhao Z, Wang M, Ma P, Zheng Y, Chen J, Li H, et al. Atomically dispersed Pt/CeO₂ catalyst with superior CO selectivity in reverse water gas shift reaction. *Applied Catalysis B: Environmental* 2021;291:120101. <https://doi.org/10.1016/j.apcatb.2021.120101>.
- [76] Bobadilla LF, Santos JL, Ivanova S, Odriozola JA, Urakawa A. Unravelling the Role of Oxygen Vacancies in the Mechanism of the Reverse Water–Gas Shift Reaction by Operando DRIFTS and Ultraviolet–Visible Spectroscopy. *ACS Catal* 2018;8:7455–67. <https://doi.org/10.1021/acscatal.8b02121>.

- [77] Sun F, Yan C, Wang Z, Guo C, Huang S. Ni/Ce–Zr–O catalyst for high CO₂ conversion during reverse water gas shift reaction (RWGS). *International Journal of Hydrogen Energy* 2015;40:15985–93. <https://doi.org/10.1016/j.ijhydene.2015.10.004>.
- [78] Sá S, Silva H, Brandão L, Sousa JM, Mendes A. Catalysts for methanol steam reforming—A review. *Applied Catalysis B: Environmental* 2010;99:43–57. <https://doi.org/10.1016/j.apcatb.2010.06.015>.
- [79] González JF, Román S, Bragado D, Calderón M. Investigation on the reactions influencing biomass air and air/steam gasification for hydrogen production. *Fuel Processing Technology* 2008;89:764–72. <https://doi.org/10.1016/j.fuproc.2008.01.011>.
- [80] Dupont C, Jacob S, Marrakchy KO, Hognon C, Grateau M, Labalette F, et al. How inorganic elements of biomass influence char steam gasification kinetics. *Energy* 2016;109:430–5. <https://doi.org/10.1016/j.energy.2016.04.094>.
- [81] Chen X, Jiang J, Yan F, Li K, Tian S, Gao Y, et al. Dry Reforming of Model Biogas on a Ni/SiO₂ Catalyst: Overall Performance and Mechanisms of Sulfur Poisoning and Regeneration. *ACS Sustainable Chem Eng* 2017;5:10248–57. <https://doi.org/10.1021/acssuschemeng.7b02251>.
- [82] Da Silva Perez D. DC. Characterisation of the most representative agricultural and forestry biomasses in France for gasification n.d. http://publications.cirad.fr/une_notice.php?dk=576525 (accessed June 15, 2021).
- [83] Shen C, Bao Q, Xue W, Sun K, Zhang Z, Jia X, et al. Synergistic effect of the metal-support interaction and interfacial oxygen vacancy for CO₂ hydrogenation to methanol over Ni/In₂O₃ catalyst: A theoretical study. *Journal of Energy Chemistry* 2022;65:623–9. <https://doi.org/10.1016/j.jechem.2021.06.039>.
- [84] Das S, Sengupta M, Patel J, Bordoloi A. A study of the synergy between support surface properties and catalyst deactivation for CO₂ reforming over supported Ni nanoparticles. *Applied Catalysis A: General* 2017;545:113–26. <https://doi.org/10.1016/j.apcata.2017.07.044>.
- [85] Yang L, Pastor-Pérez L, Villora-Pico JJ, Sepúlveda-Escribano A, Tian F, Zhu M, et al. Highly Active and Selective Multicomponent Fe–Cu/CeO₂–Al₂O₃ Catalysts for CO₂ Upgrading via RWGS: Impact of Fe/Cu Ratio. *ACS Sustainable Chem Eng* 2021;9:12155–66. <https://doi.org/10.1021/acssuschemeng.1c03551>.
- [86] Zhang Z, Huang G, Tang X, Yin H, Kang J, Zhang Q, et al. Zn and Na promoted Fe catalysts for sustainable production of high-valued olefins by CO₂ hydrogenation. *Fuel* 2022;309:122105. <https://doi.org/10.1016/j.fuel.2021.122105>.
- [87] Sai Prasad PS, Bae JW, Jun K-W, Lee K-W. Fischer–Tropsch Synthesis by Carbon Dioxide Hydrogenation on Fe-Based Catalysts. *Catal Surv Asia* 2008;12:170–83. <https://doi.org/10.1007/s10563-008-9049-1>.
- [88] Deng L, Ai X, Xie F, Zhou G. Efficient Ni-based catalysts for low-temperature reverse water-gas shift (RWGS) reaction. *Chemistry – An Asian Journal* 2021;16:949–58. <https://doi.org/10.1002/asia.202100100>.
- [89] Di Stasi C, Renda S, Greco G, González B, Palma V, Manyà JJ. Wheat-Straw-Derived Activated Biochar as a Renewable Support of Ni–CeO₂ Catalysts for CO₂ Methanation. *Sustainability* 2021;13:8939. <https://doi.org/10.3390/su13168939>.
- [90] Santos JL, Bobadilla LF, Centeno MA, Odriozola JA. Operando DRIFTS-MS Study of WGS and rWGS Reaction on Biochar-Based Pt Catalysts: The Promotional Effect of Na. *C* 2018;4:47. <https://doi.org/10.3390/c4030047>.
- [91] Wang Y, Shao Y, Zhang L, Zhang S, Wang Y, Xiang J, et al. Co-presence of hydrophilic and hydrophobic sites in Ni/biochar catalyst for enhancing the hydrogenation activity. *Fuel* 2021;293:120426. <https://doi.org/10.1016/j.fuel.2021.120426>.
- [92] Wang X, Liu Y, Zhu L, Li Y, Wang K, Qiu K, et al. Biomass derived N-doped biochar as efficient catalyst supports for CO₂ methanation. *Journal of CO₂ Utilization* 2019;34:733–41. <https://doi.org/10.1016/j.jcou.2019.09.003>.
- [93] Lee JS, Kim HS, Park N-K, Lee TJ, Kang M. Low temperature synthesis of α -alumina from aluminum hydroxide hydrothermally synthesized using $[\text{Al}(\text{C}_2\text{O}_4)_x(\text{OH})_y]$ complexes. *Chemical Engineering Journal* 2013;230:351–60. <https://doi.org/10.1016/j.cej.2013.06.099>.
- [94] J BSR, Loganathan M, Shantha MS. A Review of the Water Gas Shift Reaction Kinetics. *International Journal of Chemical Reactor Engineering* 2010;8. <https://doi.org/10.2202/1542-6580.2238>.
- [95] Su X, Yang X, Zhao B, Huang Y. Designing of highly selective and high-temperature durable RWGS heterogeneous catalysts: recent advances and the future directions. *Journal of Energy Chemistry* 2017;26:854–67. <https://doi.org/10.1016/j.jechem.2017.07.006>.

- [96] Kaiser P, Unde RB, Kern C, Jess A. Production of Liquid Hydrocarbons with CO₂ as Carbon Source based on Reverse Water-Gas Shift and Fischer-Tropsch Synthesis. *Chemie Ingenieur Technik* 2013;85:489–99. <https://doi.org/10.1002/cite.201200179>.
- [97] A. Daza Y, N. Kuhn J. CO₂ conversion by reverse water gas shift catalysis: comparison of catalysts, mechanisms and their consequences for CO₂ conversion to liquid fuels. *RSC Advances* 2016;6:49675–91. <https://doi.org/10.1039/C6RA05414E>.
- [98] Mai NT, Nguyen NH, Tsubota T, Shinogi Y, Dultz S, Nguyen MN. Fern *Dicranopteris linearis*-derived biochars: Adjusting surface properties by direct processing of the silica phase. *Colloids and Surfaces A: Physicochemical and Engineering Aspects* 2019;583:123937. <https://doi.org/10.1016/j.colsurfa.2019.123937>.
- [99] Hyväluoma J, Hannula M, Arstila K, Wang H, Kulju S, Rasa K. Effects of pyrolysis temperature on the hydrologically relevant porosity of willow biochar. *Journal of Analytical and Applied Pyrolysis* 2018;134:446–53. <https://doi.org/10.1016/j.jaap.2018.07.011>.
- [100] González Martínez M, Dupont C, da Silva Perez D, Míguez-Rodríguez L, Grateau M, Thiéry S, et al. Assessing the suitability of recovering shrub biowaste involved in wildland fires in the South of Europe through torrefaction mobile units. *Journal of Environmental Management* 2019;236:551–60. <https://doi.org/10.1016/j.jenvman.2019.02.019>.
- [101] Trinh TK, Tsubota T, Takahashi S, Mai NT, Nguyen MN, Nguyen NH. Carbonization and H₃PO₄ activation of fern *Dicranopteris linearis* and electrochemical properties for electric double layer capacitor electrode. *Sci Rep* 2020;10:19974. <https://doi.org/10.1038/s41598-020-77099-7>.
- [102] Siatecka A, Różyło K, Ok YS, Oleszczuk P. Biochars ages differently depending on the feedstock used for their production: Willow- versus sewage sludge-derived biochars. *Science of The Total Environment* 2021;789:147458. <https://doi.org/10.1016/j.scitotenv.2021.147458>.
- [103] Vassilev SV, Baxter D, Andersen LK, Vassileva CG, Morgan TJ. An overview of the organic and inorganic phase composition of biomass. *Fuel* 2012;94:1–33. <https://doi.org/10.1016/j.fuel.2011.09.030>.
- [104] Zhaol FJ, Dunham SJ, McGrath SP. Arsenic Hyperaccumulation by Different Fern Species. *The New Phytologist* 2002;156:27–31.
- [105] Akomolafe G, Dedeké, S.A S. TOLERANCE MECHANISMS IN PTERIDOPHYTES (FERNS) AND THEIR USE AS REMEDIATORS OF HEAVY METAL CONTAMINATED SITES, 2013.
- [106] Keller C, Ludwig C, Davoli F, Wochele J. Thermal Treatment of Metal-Enriched Biomass Produced from Heavy Metal Phytoextraction. *Environ Sci Technol* 2005;39:3359–67. <https://doi.org/10.1021/es0484101>.
- [107] Korzeniowska J, Stanislawski-Glubiak E. Phytoremediation potential of *Phalaris arundinacea*, *Salix viminalis* and *Zea mays* for nickel-contaminated soils. *Int J Environ Sci Technol* 2019;16:1999–2008. <https://doi.org/10.1007/s13762-018-1823-7>.
- [108] Meers E, Vandecasteele B, Ruttens A, Vangronsveld J, Tack FMG. Potential of five willow species (*Salix* spp.) for phytoextraction of heavy metals. *Environmental and Experimental Botany* 2007;60:57–68. <https://doi.org/10.1016/j.envexpbot.2006.06.008>.
- [109] Wani KA, Sofi ZM, Malik JA, Wani JA. Phytoremediation of Heavy Metals Using *Salix* (Willows). In: Bhat RA, Hakeem KR, Dervash MA, editors. *Bioremediation and Biotechnology, Vol 2: Degradation of Pesticides and Heavy Metals*, Cham: Springer International Publishing; 2020, p. 161–74. https://doi.org/10.1007/978-3-030-40333-1_9.
- [110] A global database for plants that hyperaccumulate metal and metalloid trace elements - Reeves - 2018 - *New Phytologist* - Wiley Online Library n.d. <https://nph.onlinelibrary.wiley.com/doi/full/10.1111/nph.14907> (accessed October 26, 2020).
- [111] Chen X, Chen Y, Song C, Ji P, Wang N, Wang W, et al. Recent Advances in Supported Metal Catalysts and Oxide Catalysts for the Reverse Water-Gas Shift Reaction. *Frontiers in Chemistry* 2020;8. <https://doi.org/10.3389/fchem.2020.00709>.
- [112] Luk HT, Mondelli C, Mitchell S, Siol S, Stewart JA, Curulla Ferré D, et al. Role of Carbonaceous Supports and Potassium Promoter on Higher Alcohols Synthesis over Copper–Iron Catalysts. *ACS Catal* 2018;8:9604–18. <https://doi.org/10.1021/acscatal.8b02714>.
- [113] Xu J, Gong X, Hu R, Liu Z, Liu Z. Highly active K-promoted Cu/β-Mo₂C catalysts for reverse water gas shift reaction: Effect of potassium. *Molecular Catalysis* 2021;516:111954. <https://doi.org/10.1016/j.mcat.2021.111954>.

- [114] Yang X, Su X, Chen X, Duan H, Liang B, Liu Q, et al. Promotion effects of potassium on the activity and selectivity of Pt/zeolite catalysts for reverse water gas shift reaction. *Applied Catalysis B: Environmental* 2017;216:95–105. <https://doi.org/10.1016/j.apcatb.2017.05.067>.
- [115] Béguerie T, Weiss-Hortala E, Nzihou A. Calcium as an innovative and effective catalyst for the synthesis of graphene-like materials from cellulose. *Sci Rep* 2022;12:21492. <https://doi.org/10.1038/s41598-022-25943-3>.
- [116] Ghogia AC, Romero Millán LM, White CE, Nzihou A. Synthesis and Growth of Green Graphene from Biochar Revealed by Magnetic Properties of Iron Catalyst. *ChemSusChem* 2023;16:e202201864. <https://doi.org/10.1002/cssc.202201864>.
- [117] N. Guskos, E.A. Anagnostakis, V. Likodimos, T. Bodziony, J. Typek, M. Maryniak, U. Narkiewicz, I. Kucharewicz, S. Waplak, Ferromagnetic resonance and ac conductivity of a polymer composite of Fe₃O₄ and Fe₃C nanoparticles dispersed in a graphite matrix, *Journal of Applied Physics*. 97 (2004) 024304. <https://doi.org/10.1063/1.1836855>.
- [118] Xiong J, Xu J, Zhou M, Zhao W, Chen C, Wang M, et al. Quantitative Characterization of the Site Density and the Charged State of Functional Groups on Biochar. *ACS Sustainable Chem Eng* 2021;9:2600–8. <https://doi.org/10.1021/acssuschemeng.0c09051>.
- [119] Ghogia AC. theses.fr – Amel cydric Ghogia, Développement de catalyseurs monolithiques structurés du type Co/C/mousse pour le procédé de synthèse Fischer-Tropsch n.d. <http://www.theses.fr/s184711> (accessed October 18, 2021).
- [120] Ducouso M. Gasification biochar reactivity toward methane cracking n.d.:283.
- [121] Vassilev SV, Baxter D, Andersen LK, Vassileva CG. An overview of the chemical composition of biomass. *Fuel* 2010;89:913–33. <https://doi.org/10.1016/j.fuel.2009.10.022>.
- [122] Xia S, Li K, Xiao H, Cai N, Dong Z, xu C, et al. Pyrolysis of Chinese chestnut shells: Effects of temperature and Fe presence on product composition. *Bioresource Technology* 2019;287:121444. <https://doi.org/10.1016/j.biortech.2019.121444>.
- [123] Yung MM, Starace AK, Mukarakate C, Crow AM, Leshnov MA, Magrini KA. Biomass Catalytic Pyrolysis on Ni/ZSM-5: Effects of Nickel Pretreatment and Loading. *Energy Fuels* 2016;30:5259–68. <https://doi.org/10.1021/acs.energyfuels.6b00239>.
- [124] Zhang J, Yang Y, Liu J, Xiong B. Mechanistic understanding of CO₂ hydrogenation to methane over Ni/CeO₂ catalyst. *Applied Surface Science* 2021;558:149866. <https://doi.org/10.1016/j.apsusc.2021.149866>.
- [125] Wang L, Liu H, Liu Y, Chen Y, Yang S. Influence of preparation method on performance of Ni-CeO₂ catalysts for reverse water-gas shift reaction. *Journal of Rare Earths* 2013;31:559–64. [https://doi.org/10.1016/S1002-0721\(12\)60320-2](https://doi.org/10.1016/S1002-0721(12)60320-2).
- [126] Tarifa P, González-Castaño M, Cazaña F, Monzón A, Arellano-García H. Development of one-pot Cu/cellulose derived carbon catalysts for RWGS reaction. *Fuel* 2022;319:123707. <https://doi.org/10.1016/j.fuel.2022.123707>.
- [127] Millan LMR. Steam gasification of tropical lignocellulosic agrowaste: impact of biomass characteristics on the gaseous and solid by-products n.d.:208.
- [128] Ducouso M. Gasification biochar reactivity toward methane cracking. phdthesis. Ecole des Mines d'Albi-Carmaux, 2015.
- [129] Nzihou A, editor. Handbook on Characterization of Biomass, Biowaste and Related By-products. Springer International Publishing; 2020. <https://doi.org/10.1007/978-3-030-35020-8>.
- [130] Gioria EG. Colloidal nanoparticles for the rational design of (multi)metallic heterogeneous catalysts 2022.
- [131] Chen Z, Liang L, Yuan H, Liu H, Wu P, Fu M, et al. Reciprocal regulation between support defects and strong metal-support interactions for highly efficient reverse water gas shift reaction over Pt/TiO₂ nanosheets catalysts. *Applied Catalysis B: Environmental* 2021;298:120507. <https://doi.org/10.1016/j.apcatb.2021.120507>.
- [132] Lee S-C, Kim J-S, Shin WC, Choi M-J, Chung S-J. Catalyst deactivation during hydrogenation of carbon dioxide: Effect of catalyst position in the packed bed reactor. *Journal of Molecular Catalysis A: Chemical* 2009;301:98–105. <https://doi.org/10.1016/j.molcata.2008.11.016>.

- [133] Le MC, Van KL, Nguyen THT, Nguyen NH. The Impact of Ce-Zr Addition on Nickel Dispersion and Catalytic Behavior for CO₂ Methanation of Ni/AC Catalyst at Low Temperature. *Journal of Chemistry* 2017;2017:e4361056. <https://doi.org/10.1155/2017/4361056>.
- [134] Feng K, Tian J, Guo M, Wang Y, Wang S, Wu Z, et al. Experimentally unveiling the origin of tunable selectivity for CO₂ hydrogenation over Ni-based catalysts. *Applied Catalysis B: Environmental* 2021;292:120191. <https://doi.org/10.1016/j.apcatb.2021.120191>.
- [135] Gioria E, Ingale P, Pohl F, d'Alnoncourt RN, Thomas A, Rosowski F. Boosting the performance of Ni/Al₂O₃ for the reverse water gas shift reaction through formation of CuNi nanoalloys. *Catalysis Science & Technology* 2022;12:474–87. <https://doi.org/10.1039/D1CY01585K>.
- [136] Hernandez Lalinde JA, Roongruangsree P, Ilsemann J, Bäumer M, Kopyscinski J. CO₂ methanation and reverse water gas shift reaction. Kinetic study based on in situ spatially-resolved measurements. *Chemical Engineering Journal* 2020;390:124629. <https://doi.org/10.1016/j.cej.2020.124629>.
- [137] Gao Z, Meng Y, Shen H, Xie B, Ni Z, Xia S. Theoretical study on low temperature reverse water gas shift (RWGS) mechanism on monatomic transition metal M doped C₂N catalyst (M=Cu, Co, Fe). *Molecular Catalysis* 2021;516:111992. <https://doi.org/10.1016/j.mcat.2021.111992>.

Chapter 4

Nickel and iron biocarbon catalysts for water-gas shift reaction

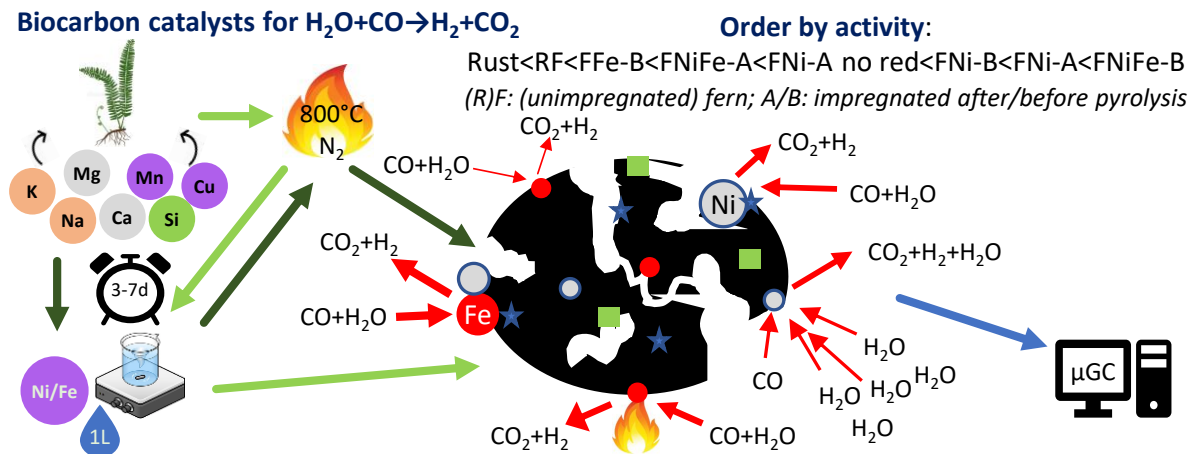
Highlights

- Biocarbon catalysts were more active than rust for water gas shift reaction (WGS).
- Ni-biocarbon catalysts were more active than Fe-biocarbon catalysts for WGS.
- WGS was kinetically driven and enhanced with increased temperature and steam.
- Biocarbon catalyst reduction could enhance catalyst performance in WGS.

Abstract

Biocarbon catalysts were prepared from pyrolyzed fern impregnated with iron (Fe) and nickel (Ni), to then be tested for water-gas shift (WGS) reaction. They were studied in a fixed-bed reactor from 180°C to 400°C with variable steam to carbon monoxide (CO) ratio (1.4 to 20.7). CO conversion for most catalysts was below 10% and was favored by increasing temperature and steam partial pressure, which may indicate that the reaction is kinetically driven. Ni-biocarbon catalysts were more active for WGS than their Fe counterparts. This was related to their activity at lower temperatures in accordance to their reducibility and the presence of promoting metals such as K, which improved electronic properties. The selectivity of all catalysts was generally above 95%, regardless the operating conditions, reflecting the predominance of WGS over methanation. Fern biocarbon impregnated with Ni and Fe before pyrolysis was the most performant with 10.3% CO conversion and 99.7% WGS selectivity at 280°C. While in other studies rust showed conversion around 10% at 300°C, in our case it showed the poorest performances at 6.9% at 280°C, attributed to its lack of catalytic effect. Catalysts activation energy and kinetic constant versus rust were determined with the most active species reaching high values (up to 92.1 kJ/mol and 2.2×10^8) for both constants, comparable to literature (up to 130 kJ/mol and 5.8×10^{10}). The combination of low temperature activity provided by Ni in coordination with the catalytic effect provided by Fe and the fern-inherent metals was reflected in the high WGS performance by the fern-based biocarbon impregnated with Ni and Fe before pyrolysis and its associated kinetic parameters (59.5 kJ/mol and 5.6×10^5).

Graphical abstract



4.1. Introduction

Human-caused climate change is worsening and results in scarcer food and water availability, deteriorated health and well-being, severer and more frequent damage to infrastructure and ecosystems. This change is a result of green-house gas (GHG) emissions namely carbon dioxide (CO₂) and their mitigation can help minimize present and future impacts.

The production of low-emission hydrogen (H₂) and H₂ derivatives through biomass and biowaste valorization could mitigate the use of fossils fuels in GHG intensive sectors [1]. H₂ can be produced via thermochemical conversion (500 to 1000°C, inert atmosphere). Water-gas shift (WGS) reaction is involved in thermochemical conversion pathways and allows increasing the hydrogen conversion from syngas thanks to steam ((H₂O)_v) (180 – 500°C, Eq.4.1).



Thermochemical conversion reactions can be catalyzed using noble or transition metal-based catalysts including iron (Fe) and nickel (Ni). This reduces reaction temperature, production processes cost and lowers H₂ production costs while favoring its accessibility [2–4]. This includes low temperature WGS, which is an exothermic reaction ($\Delta H_{298}^0 = -41.2 \text{ kJ/mol}$) kinetically restricted due to energy barriers that can be lowered through catalysis [5–7]. These thermochemical conversion processes are complex and imply many competitive reactions resulting in the production of unwanted byproducts such as CH₄ whose formation (methanation, Eq.4.2) rivals CO₂ formation by WGS.



The metal extraction for commercial catalyst production has a high environmental impact due to energy and solvent intensive processes that emit GHG. This is worsened for noble metals, that are

costlier due to scarcity but more active as catalysts [8–11]. To minimize the impact of this extraction, catalysts are being derived from inherently rich or loaded in metal bioresources [12]. However, the complex and heterogeneous structure of bioresources needs to be carefully understood to lead to a performant catalytic material. The objective of this work is therefore to produce, characterize and test biocarbon catalysts from bioresources loaded with heavy metals whose catalytic activity was identified for WGS.

4.1.1. Operating conditions for WGS and their impact

In addition to the choice of catalysts, operating conditions such as temperature, pressure, gas hourly space velocity (GHSV), contact time, steam/carbon ratio (S/C) and reactor configuration impact WGS and are discussed in this section.

4.1.1.1. Catalysts & kinetic parameters

As for thermochemical conversion, catalysts identified for WGS are mostly noble, transition and post-transition metal-based (Table 4.1). Alkaline and alkaline-earth metals can be used as promoters, together with the catalytic metals, while metalloids and lanthanide metals are used as supports. These promoters and supports improve the low temperature activity of catalysts, favored by the exothermicity of WGS reaction.

Table 4.1. Inorganic species and their role (inhibition or catalysis) in pyrogasification and RWGS, from Chapter 3

AAEM		Transition, post-transition and lanthanide	Metalloid/Nonmetal
Alkaline	Alkaline-earth		
Li_2CO_3 / LiCl			C (coke and tar)
Na^+ / Na_2CO_3 / NaCl / Na pr.	MgO / MgCO_3 / <u>MgCl_2</u>	<u>Fe_2O_3</u> - <u>Al_2O_3</u> / Ni-Al oxide/ Ni-Al / Al_2O_3 sup.	Cl/HCl / LiCl / NaCl / KCl / <u>MgCl_2</u> / ZnCl_2
K^+ / K_2CO_3 / $\text{K}_2\text{Ca}(\text{CO}_3)_2$ / KCl / K pr.	CaCO_3 / $\text{CaO}/\text{Ca}^{2+}$ / $\text{K}_2\text{Ca}(\text{CO}_3)_2$	<u>Fe_2O_3</u> - <u>Cr_2O_3</u> / <u>Fe_2O_3</u> - <u>Al_2O_3</u> / $\text{Fe}(\text{CO})_5$ / Co° / Co / Ni-Co / Fe-Co / Co / $\text{Ni}(\text{NO}_3)_2$ / <u>Ni_2P</u> / Ni Fe oxide / Fe_3C	CuO - <u>ZnO</u> / <u>CuO</u> / Zn° / Zn / Cu° / ZnCl_2 / Cu / <u>Cu-Zn</u> / Cu pr. ZnO sup. Cu oxide
Rb_2CO_3 / Rb pr.		ZrO_2 - CeO_2 sup. $\text{Mo}(\text{CO})_6$ / Mo pr. $\text{Ru}^\circ/\text{Ru}$ / Ru° Rh Pd/Pd Ag pr. / Ag	Ni-Sn
Cs_2CO_3 / Cs pr.	Ba pr.	Ce° / ZrO_2 - CeO_2 sup./ CeO_2 sup. $\text{W}(\text{CO})_6$ $\text{Pt}^\circ/\text{Pt}$ / $\text{Pt pr.}/\text{Pt}$ Au	
Legend sup.: support pr.: promoter	Reforming catalyst <u>WGS/RWGS¹ catalyst</u> Pyrolysis and production of H ₂ (WGS, reforming or production of H ₂ not detailed)	Pyrolysis catalyst H ₂ production catalyst	Generally inhibiting Inhibiting/little effect

1: Underlined = WGS

The kinetic impact of the catalyst can be expressed through the determination of the reaction rate based on theoretical calculations (Langmuir-Hinshelwood, power law, etc.) validated through experimental data (Table 4.2).

Table 4.2. Expression of reaction rates (mol g⁻¹ s⁻¹) for WGS with associated parameters and references

Expression and parameters	Ref.
$-r_{CO} = \frac{dX_{CO}}{d(W/F_{CO}^0)}$	[13,14]
<p>X_{co}: CO conversion; W: catalyst mass (g); F_{co}⁰: initial CO molar flow rate (mol/h)</p>	
$r = \frac{kK_{CO}K_{H_2O} \left([CO][H_2O] - \frac{[CO_2][H_2]}{K} \right)}{\left(1 + K_{CO}[CO] + K_{H_2O}[H_2O] + K_{CO_2}[CO_2] + K_{H_2}[H_2] \right)^2}$ $r = \frac{k[H_2O]}{1 + K \frac{[H_2O]}{[H_2]}}$ $r = \frac{k \left([CO][H_2O] - \frac{[CO_2][H_2]}{K} \right)}{1 + K_{CO}[CO] + K_{H_2O}[H_2O] + K_{CO_2}[CO_2] + K_{H_2}[H_2]}$ $r = \frac{k_1 k_2 \left([CO][H_2O] - \frac{[CO_2][H_2]}{K} \right)}{k_1[CO] + k_2[H_2O] + k_{-1}[CO_2] + k_{-2}[H_2]}$ $r = kP_{CO}^a P_{H_2O}^b P_{CO_2}^c P_{H_2}^d$	[13,15]
<p>a = [-0.24;1.10]; b = [-0.32;1.90]; c = [-0.90;0.85]; d = [-0.90;0]; E_a = [75;129] kJ/mol Fe-based catalysts</p>	
$r_i = k \left(P_{CO} P_{H_2O} - \frac{1}{e^{\frac{4577.8}{T} - 4.33}} P_{CO_2} P_{H_2} \right)$	[16]
<p>k₀ = 5.06 x 10⁷ mol m⁻³ bar⁻² s⁻¹; E_a = 49.8 kJ mol⁻¹; Pt/Ce-Al</p>	
$-r_{CO} = k \frac{P_{CO} P_{H_2O}^{0.1}}{P_{CO_2}^{0.3} P_{H_2}^{0.15}} \left(1 - \frac{1}{K_p} \frac{P_{H_2} P_{CO_2}}{P_{CO} P_{H_2O}} \right)$	[17]
<p>k₀ = 1.85 x 10⁻⁹ mol m⁻¹ s⁻¹ Pa⁻ⁿ; E_a = 13.5 kJ mol⁻¹; Pd-Cu-Ni/Ni</p>	
$r_i = \pm k_{WGS} P_{CO}^a P_{H_2O}^b (P_{CO_2} P_{H_2})^c \left(1 - \frac{P_{H_2} P_{CO_2}}{K_{eq} p_{CO} p_{H_2O}} \right) \rho_{cat}$	[18,19]
<p>k_{WGS} = 1.11 x e^{-62100/8.314T} mol kPa^{-0.444} g_{cat}⁻¹ s⁻¹ a = 0.38 ; b = -0.10 ; c = 0.082 ; ρ_{cat} : density of catalyst ln(K_{eq}) = 5693.3/T + 1.077 ln(T) + 5.44x10⁻⁴T - 1.125x10⁻⁷T² - 49.710 T⁻² - 13.148</p>	
$r = 1.85 \times 10^{-5} e^{12.88 - \frac{1855.5}{T}} p_{CO} p_{H_2O} \left(1 - \frac{p_{H_2} p_{CO_2}}{K_2 p_{CO} p_{H_2O}} \right)$	[20]
<p>K₂ = 1.77 x 10⁵ e^{-88680/(8.314T)}</p>	
$r_{WGS} = \frac{k_{WGS}^* K_{OH}^* \frac{p_{CO} p_{H_2O}}{p_{H_2}^{1/2}} \left(1 - \left(\frac{p_{H_2} p_{CO_2}}{K_{WGS}^{eq} p_{CO} p_{H_2O}} \right) \right) C_{S1}^{T^2}}{\left(1 + K_{CH_3O}^* \frac{p_{CH_3OH}}{p_{H_2}^{1/2}} + K_{HCOO}^* p_{CO_2} p_{H_2}^{1/2} + K_{OH}^* \frac{p_{H_2O}}{p_{H_2}^{1/2}} \right)^2}$	[20]
<p>k_{WGS}[*] = 5.9 x 10¹³ e^{87600/(8.314T)} m² s⁻¹ mol⁻¹; K_{OH}[*] = exp(-44.5/ 8.314+20000/ 8.314T) bar^{-0.5} ; C_{S1}^T = [21]; K_{CH3O}[*] = exp(-41.8/ 8.314+20000/ 8.314T) bar^{-0.5} ; K_{HCOO}[*] = exp(-179.2/ 8.314-100000/ 8.314T) bar^{-0.5}</p>	

The kinetic constants (k) are obtained by Arrhenius type equations (**Eq.4.3**). They are defined by their preexponential factor (A or k_0 , unit depends on reaction order) and the activation energy (E or E_a , kJ or kcal/mol) [17,22]. Based on this equation, rate and thereafter conversion of CO are increased by diminishing E_a or increasing k_0 , being all kinetic parameters impacted by the temperature.

$$k = k_0 \times e^{-\frac{E_a}{RT}} \quad \text{Eq.4.3}$$

The use of catalysts directly impacts the kinetic parameters of the reaction rate expressions. Noble metals such as Pt with supports Al_2O_3 , TiO_2 , CeO_2 , $\text{CeO}_2\text{-Al}_2\text{O}_3$, $\text{CeO}_2\text{-TiO}_2$ could reduce E_a from 21.8 (91.2 kJ/mol, Ce/Al) to 15.7 kcal/mol (65.7 kJ/mol, Ti) but could drop CO consumption rate from 21.1 (Ce/Ti) to $0.4 \mu\text{mol s}^{-1} \text{g}^{-1}$ (Al) [23]. Pt/ CeO_2 could also result in an E_a of 78.4 kJ/mol (18.7 kcal/mol) and k_0 of 1.4×10^6 . For other Pt catalysts promoted by Re or supported by Ce, Al, Zr, V or La, E_a could range from 39 to 91 kJ/mol [24,25].

Non-noble catalysts such as Ni catalysts supported by MgAl, Mg, Al and CaAl could catalyze WGS with E_a ranging 67 to 186 kJ/mol and k_0 ranging 5.4×10^4 to 4.3×10^{12} . Side reactions methanation and steam methane reforming can be catalyzed simultaneously with E_a ranging from 33 to 244 kJ/mol and k_0 from 5.5×10^3 to 1.2×10^{16} for both reactions [25]. Over CuO/ $\text{ZnO}/\text{Al}_2\text{O}_3$ and depending on the equation used to calculate initial rates, E_a can range from 28.5 to 92.9 kJ/mol and k_0 from 2.6×10^4 to 5.8×10^{10} [13].

A wide range of kinetic parameters can be found regarding Cu, Fe, Ru, Ni, Rh, Pd and Pt-based catalysts. This includes values between 0.5 to 130 kJ/mol for activation energy and between 5.4×10^{-7} to 1.5×10^{10} for the pre-exponential factor [13,15,27]. This variability in values obtained for these kinetic parameters stems from aforementioned promotion and support effects that decrease E_a but can also prevent the sintering of metal phases that could result in CO and H_2O reactivity loss. Additionally, different catalysts react different with the gases and adopt specific reaction mechanisms (associative, redox, Langmuir-Hinshelwood) that take in account their active sites and result in different methods to determine kinetic parameters [15,27,28]. A high density of dispersed active sites could be quite beneficial for WGS and result in faster kinetics at lower temperatures as the smaller active sites do not require as much energy to activate [15,29,30]. These mechanisms could involve a redox couple of a same metal that undergoes a switch from the oxidant to the reductant and inversely, which can be facilitated also through promotion [15,31]. Including possible reducible active phases, the speciation can determine WGS reactivity as a covalent bond could be less polarized and sources of electrons than ionic bonds. Additionally, the engaged orbitals could limit the direction of reaction of gases, especially for clusters that have less electron back-donation. As they can not densely engage electrons, this

weakens its gas activation and consequently kinetic capabilities [15,28,29]. Other sources of uncertainty were attributed to gas impurities, mass-diffusion limitations and the type of reactor related to pressure gradients that locally affect kinetics and inhibit or poison WGS and active sites [15,27,31].

Promoting Fe_2O_3 with Cu allows reaching similar conversions to unpromoted Fe_2O_3 but at much lower temperatures, for example 70% at 200°C instead of 400°C [14]. Therefore, catalysts impact the kinetic parameters, as well as the operating conditions which in turn affect the WGS reaction.

4.1.1.2. Temperature

The temperature influences WGS by providing energy necessary to the activity of catalysts and the activation of carbon monoxide (CO) and steam. Based on thermodynamics and equilibrium principles, an increase in temperature should decrease the conversion of the reaction due to exothermicity, but this increase promotes reaction kinetics by increasing the kinetic constant (Eq.4.3).

Some examples from literature show that, when WGS is kinetically driven, catalysts require high temperatures to convert CO and this conversion increases to 20% at 280-300°C where it shoots up to at least 80% above 320°C and where the reaction becomes limited by thermodynamics [32]. An increase in temperature from 180 to 340°C resulted in an increase of CO conversion from 5 to 90%. However, according to thermodynamic equilibrium, a drop is observed at 280°C over Pt/CeFeAl, while the increase was constant for Au/CeFeAl, Au/TiO₂, Au/TiCe₆O₂ and Au/TiCe₁₅O₂ [22,33]. Conversion increased from 10 to 80% from 350 to 550°C with Fe-based catalysts whose activity was ascribed to electron hopping between Fe²⁺ and Fe³⁺ sites facilitated by increasing temperature to reach reduction points for Fe that can be reduced by promotion with Cr, Mn, Co, Ni, Cu, Zn, Ce [34]. At temperatures reaching 700°C, the previously high conversion of CO at 90% at 300°C drops to 30% [35]. A maximal conversion of 98% around 300°C was noted when the temperature varied between 250 and 400°C. A compromise is therefore required to achieve maximal conversion [24].

Other factors complementary to the operating temperature can influence WGS. For instance, when heating from 220°C to 350°C, the conversion of CO on a catalytic medium could spike from 0 to 100%, more or less faster depending on the catalytic medium. In addition, catalytic supports can reduce temperature gradients if they are highly conductive, resulting in lower temperature drops that could reduce conversion [16]. This decrease was shown to be less important with smaller reactor sizes (less than 10°C for less than 10 cm) [17], which points out the importance of considering heat transfer limitations at larger scale. In the case of a WGS feed gas containing CO₂ and H₂, in addition to the reactive gases CO and steam, the conversion was restrained due to difficulty in displacing the

equilibrium caused by the presence of the WGS products. This conversion could increase from 30% to 70%, from 140°C to 200°C [36].

4.1.1.3. Pressure

On the thermodynamic stand-point, pressure should not influence the equilibrium of the reaction, according to Le Chatelier's principle (2 moles of reactive gas for 2 moles of produced gas). The rate of production and consumption can be influenced by partial pressure of gases and therefore by total pressure (Table 4.2).

An increase in pressure from 3 to 6 bar can result in an increase in CO conversion of 10%. This increase could be explained by the permeation and therefore removal of product gases (especially H₂) from the reaction chamber that shifts equilibrium towards products. This permeation is favored by high pressures and high temperatures [20].

4.1.1.4. Gas hourly space velocity and contact time

Gas hourly space velocity (GHSV) and contact time have similar functions: providing sufficient time to allow the gases to react with the active sites of the catalyst. These two parameters are however inverted with more GHSV resulting in less contact time and less conversion of the reactant gases. Longer contact time could however result in further downstream reactions such as methanation affecting selectivity towards WGS. Additionally, low GHSV and prolonged contact, similar to high pressure and temperature, facilitate permeation of reactive gases from the reactive chamber since it allows more time for gases to permeate.

An increase in GHSV from 1275.5 h⁻¹ to 10841.5 h⁻¹ reduced CO conversion from 100% to 5% depending on operating conditions [16]. With another type of reactor, an increase from 2000 to 8000 h⁻¹ could drop conversion from 99 to 83% [20,22]. With other reactor types this decrease was less than 4% when increasing GHSV from 5000 to 17000 h⁻¹ [22].

With a contact time above 0.4 s, CO conversion can increase from 0 to 80% where it seems to stabilize. CH₄ seems to increase proportionally with contact time [37]. GHSV is affected by change in inlet gas flow rate. Therefore, increasing steam to increase the steam to carbon ratio (S/C) can increase GHSV, unless the inert gas flow rate is decreased accordingly.

4.1.1.5. Steam/carbon ratio

The presence of a reactant in excess, expressed as S/C, could result in better conversion due to displacing equilibrium towards products according to equilibrium principles. Steam content but also CO can be varied to modify this ratio.

An increase in S/C from 3.25 to 5.41 could result in an increase of CO conversion from 90 to 95% but might require favorable conditions, for example more reactor length and less GHSV [17]. An increase in S/CO at maintained GHSV from 5 to 20 could increase the conversion from 50 to 98% but the increase is slow above 10 [24]. The impact of S/C is even more noticeable at higher temperatures where CO conversion decreases to 80% instead of 45% at 900°C when this ratio is at 7 instead of equimolar [38]. Excessive steam could however lead to thermal deactivation above 250°C [36].

An increase of S/CO from 1 to 3 over a Pt/La₂O₃-SiO₂ catalyst at 400°C improved conversion from 30 to 50%. By removing H₂, resulting in a displacement of the equilibrium, this conversion can increase from 80 to 97% with an increase in S/CO from 1 to 4 [22]. In the case of another reactor, conversion can increase from 20% to 98% when increasing S/C from 0.2 to 3 but maximal H₂ yield is at 1 and increasing S/C decreases maximal WGS reaction rate [39].

In the case of a WGS reactor following a steam methane reformer, this increase in conversion could vary from 60 to 95% with an increase in S/C from 1.5 to 3.5 [20]. In cases of WGS reactors following biomass (B/carbon based) gasification, the increase in S/B from 0.1 to 2 boosts the CO conversion from 25% to 90% [35]. An increase in CO molar fraction from 0.01 to 0.1 resulted in a decrease of CO conversion from 100% to 30% [16]. From these examples, we can see the importance of the inherent characteristics of the reactors on WGS.

4.1.1.6. Reactor configuration

The choice of reactor and its configuration can significantly impact the reaction. Using selective and reactive membranes can facilitate the removal of produce gases such as H₂ (permeance through porosity) or CO₂ (chemisorption) while catalyzing WGS [22]. The dimensions of the reactor including the volume of the bed of the catalyst could result in better distribution of the reactive gases and improved contact time. This contact can be further improved if the feed gas is counter-current to a sweep gas outside of the porous membrane.

A conversion of 20% higher with a tubular membrane type reactor was observed than with a plate-type catalytic reactor [22]. When the reaction is thermodynamically driven, external factors such as outer cooling, with the lack of isolation, can contribute to increasing the conversion of WGS [20].

The use of a permeating membrane to remove H₂ allows displacing the equilibrium of WGS towards H₂ production, and CO conversion can reach 97% at 450°C [22]. Pressure can influence this permeation. The use of a membrane specifically for permeation could also allow an increase of CO conversion from 70 to 97% from 10 to 14.4 bar [23,27]. The membrane can also play a catalytic role if catalysts are integrated into it or if composed of a reactive and microporous metal. This scenario was reported with

a Pd membrane reactor with Fe or Pt based catalysts, where conversion can reach up to 98% at 450°C (above equilibrium) with removal of H₂ of up to 92%. Additionally, the presence of CO₂ in feed gases induces faster deactivation so its removal could help in maintaining the activity. However, the conversion of CO over 50mg of Au/CeZrO₄ in plug flow microreactor heated from 140 to 200°C could increase from 30 to 90% with CO₂ removal while decreasing the deactivation 23 times [36]. A combination of reactive membranes that remove H₂ and directing the gases produced by WGS to chambers that purify CO₂ such as pressure swing absorbers or CO₂ chemisorbers before reintegrating them into the reactor (looping) could amplify even further the reaction towards the production of these two gases due to their removal. This effect could be additionally improved by the reduction of temperature caused by this displacement of equilibrium and the catalytic properties of the membrane with complementary catalysts [39]. The distribution of the catalyst is especially important with membranes with a best configuration being before and aside the membrane to allow initial conversion then filtration of the gases with simultaneous conversion: the catalyst needs to occupy space where the reactant gases pass to allow sufficient time to react (and permeate via the membrane) [22].

Conversion increased from 16 to 98% with increasing reactor length from 1 to 5 cm [20]. With a 9 mm diameter tubular reactor, conversion can increase from 0 to 90% at a reactor length of 60 cm [18]. For adiabatic reactors, conversion can reach 95% above 10 cm of reactor length [40]. Only 2 cm of a reactive solid and thermally conductive foam (Pt/Ce impregnated on Al foam) was needed to reach close to 100% CO conversion. In worse conditions, this conversion does not surpass 30% with 8 cm of this foam [16].

Depending on operating conditions, counter-current flow (feed gas flow opposite to membrane sweep gas) can result up to a 25% increase in CO conversion compared to co-current flow. On the other hand, reactor length and relatively sweeping surface, can improve the conversion from less than 20% under 0.5 m to 90% at 2 m [17]. This shows that WGS is highly influenced by the reactor configuration and characteristics, which determine if thermal or chemical limitations impact the reaction.

4.1.1.7. Summary of the impact of operating conditions on WGS

The selected operating conditions either enhance or hinder the performance of the WGS reaction (Table 4.3). In this work, we chose to observe the impact of the catalyst, temperature, S/C when possible, and indirectly GHSV.

The choice of the catalyst can determine the activity of WGS at low temperatures with high performance being related to minimal E_a and maximal k₀. These values can span 0.45 to 244 kJ/mol and 5.4 x 10⁻⁷ to 1.2 x 10¹⁶ respectively. Temperature helps driving kinetics, favored by temperature as

opposed to thermodynamics, and requires compromise when thermodynamic equilibrium is reached. High pressure improves gas permeation, removing H_2 and CO_2 and driving the reaction towards an additional production of these two gases to compensate their loss. More contact time between active sites and reactant gases results from reduced GHSV and could cause byproducts formation, such as CH_4 . S/C also requires compromise as increasing it can improve conversion but can also deactivate and deteriorate catalytic systems. Its increase can also affect H_2 yield and reaction rate. The activity of catalysts in WGS is also affected by the reactor configuration where equilibrium can be displaced through use of membranes or adsorbers that remove selectively H_2 and CO_2 produced by WGS or use of isolation (change in temperature). Additionally, a better contact of gas with catalyst can be achieved by increasing bed length or inverting the flow of gases (counter-current). Finally, the performance of the catalysts is highly dependent on the type of reactor relative to its ability to promote WGS.

Table 4.3. Summary of the influence and impact of operating conditions on WGS

Global parameters	Operating conditions	Influence and impact of conditions on WGS
Metals	Catalysts: Mg, Fe, Ni, Co, Cu, Ru, Rh, Pd, Ag, Pt, Au	<ul style="list-style-type: none"> • Reduces need for temperature, lowers H₂ production costs • Could catalyze side reactions producing CH₄ at expense of CO • E_a = [0.5;186] kJ/mol • k₀ = [1.9 x 10⁻⁹;4.3 x 10¹²] unit dependent on kinetic rate law
	Promoters/co-catalysts: Na, K, Cr, Cu, Rb, Mo, Ag, Cs, Ba, Pt, Re	<ul style="list-style-type: none"> • Helps catalyst be active at low temperatures
	Supports: Al, Si, Ti, Cr, Mn, Zn, Zr, Ce, V, La, Mg, Ca	<ul style="list-style-type: none"> • Reduces E_a, temperature gradients (conductive), prevents sintering
	Global	<ul style="list-style-type: none"> • High variation in kinetic parameters related to synergy between metals, their mechanistic behaviour, the density, dispersion, particle size and reducibility of active metals, and their interaction with the reactive gases depending on their electronic structure
Temperature		<ul style="list-style-type: none"> • Provides energy for activation of chemicals and molecules • Improves WGS kinetics but inhibits thermodynamic equilibrium (exothermic) • Facilitates change of electronic state of metals but could sinter
Gas feed	Presence of CO ₂ and H ₂	<ul style="list-style-type: none"> • Inhibits WGS by presence of the products of the reaction • Deactivates catalysts faster
Pressure		<ul style="list-style-type: none"> • Theoretically no influence (Le Chatelier's principle) • Can influence kinetic rates • Facilitates gas (mainly H₂) permeation shifting equilibrium
GHSV and contact time		<ul style="list-style-type: none"> • Affects duration of contact and reaction between gases and active sites (negatively for GHSV) • Facilitates permeation when contact is long • Can prevent access to thermodynamic equilibrium if contact is insufficient
S/C		<ul style="list-style-type: none"> • Displaces equilibrium by excess of one reactant • Deactivates catalyst in high excess
Reactor configuration	Type and accessories	<ul style="list-style-type: none"> • Tubular membrane converts better than plate-type reactor • Lack of insulation can improve WGS • Can prevent access to thermodynamic equilibrium if configuration does not allow sufficient contact
	Product gas removal	<ul style="list-style-type: none"> • Permeation membrane to remove H₂ and CO₂ absorbers (pressure swing): displaces equilibrium and catalyzes when catalytic (improved by configuration) • Lateral inert gas flow: improves contact if counter-current
	Reactor length	<ul style="list-style-type: none"> • Allows more contact between reactive gases and catalyst • Can prevent access to thermodynamic equilibrium if too short

4.2. Materials and methods

4.2.1. Preparation and utilization of the biocarbon catalysts

In a first approach, fern and willow were selected as raw bioresources known for the ability to cumulate heavy metals from soil by phytoremediation. Willow was harvested in the South of France in 2015. Fern corresponds to shrublands mainly composed of fern harvested in Brittany (France) in 2019.

To mimic heavy metal content in phytoremediation, both biomass and resulting biocarbon were impregnated with Ni and Fe nitrate ($\text{Ni}(\text{NO}_3)_2 \cdot 6 \text{H}_2\text{O}$ and $\text{Fe}(\text{NO}_3)_3 \cdot 9 \text{H}_2\text{O}$) to reach a metal load of 30 mg per g of biocarbon. As a result, we obtained biocarbon catalysts impregnated before and after pyrolysis. Biocarbon was produced by raw (RF and RW for fern and willow) or impregnated biomass pyrolysis under 1 L/min nitrogen (N_2) from 25°C to 800°C, at 2°C/min, followed by an isothermal step at 800°C for an hour. Wetness impregnation (WI) was applied to raw biomass: 20 g of biomass was submerged in different 1 L aqueous solutions containing Fe or Ni nitrates, stirred for 3 days and then dried for 1 day at 60°C [9]. WI based on insipient WI (IWI) was applied to biocarbon: wettable volume and amount of nitrate to attain a fixed percentage of metal in biocarbon helped determine a concentration of nitrate to thereafter be replicated in 100 mL of water for 2 g of biocarbon [41]. The solutions were stirred for varying amounts and time and then dried for 1 day at 60-105°C. The final nickel and iron content of the biocarbon catalysts was measured by ICP-OES (Table 4.4).

Table 4.4. Biocarbon catalysts, names, impregnation conditions and metal content in biocarbon

Biocarbon catalyst	Abbreviation	Impregnation conditions			Metal content (wt% in BC)
		Raw material	Impregnation method	Impregnated metal	
Fern biocarbon impregnated with Fe before pyrolysis	FFe-B	Fern	Before pyrolysis (WI of BM)	Fe	13.17
Fern biocarbon impregnated with Ni before pyrolysis	FNi-B	Fern	Before pyrolysis	Ni	3.96
Fern biocarbon impregnated with Ni after pyrolysis	FNi-A	Fern	After pyrolysis (WI of BC)	Ni	1.43
Fern biocarbon impregnated with Fe & Ni before pyrolysis	FNiFe	Fern	Before pyrolysis	Ni Fe	8.08 10.30
Fern biocarbon impregnated with Fe & Ni after pyrolysis	FNiFe-A	Fern	After pyrolysis	Ni Fe	0.36 0.76

Biocarbon catalysts were then tested for WGS reaction in a fixed bed reactor (Top Industries (France), 8 mm diameter, 25 cm long, **Fig. 4.1**). The reactor was filled with the catalyst and an inert bed of alumina ($\theta\text{-Al}_2\text{O}_3$, [42]), which allowed fixed catalyst position in the isothermal area of the reactor [41,43]. Moisture was removed before reaction by flowing argon (Ar) at 120°C for 1h and samples were then pre-reduced under 60%/40% H_2/Ar at 500°C for 2h. WGS was operated from 180°C by intervals of 20°C approximately every 1h30, at 3.0 ± 0.2 bar relative. Flows used were 20 mL/min of CO, 150 mL/min of Ar and 0.08 mL/min of liquid distilled water. This corresponds to a ratio S/C of 5.5 and GHSV of 30744 h^{-1} . In some experiments, water flow rate was additionally varied at 0.02, 0.04 and 0.30 mL/min resulting in S/C of 1.4, 2.8 and 20.7 and GHSV of 21686, 24705 and 63959 h^{-1} respectively. Both gases and water were preheated at 180°C before being introduced in the reactor. Dried permanent gases (CO , CO_2 , H_2 , CH_4) were analyzed every 5 minutes (30 minutes during the night) by online $\mu\text{-GC/TCD}$ (Agilent 990) connected after the reactor [44].

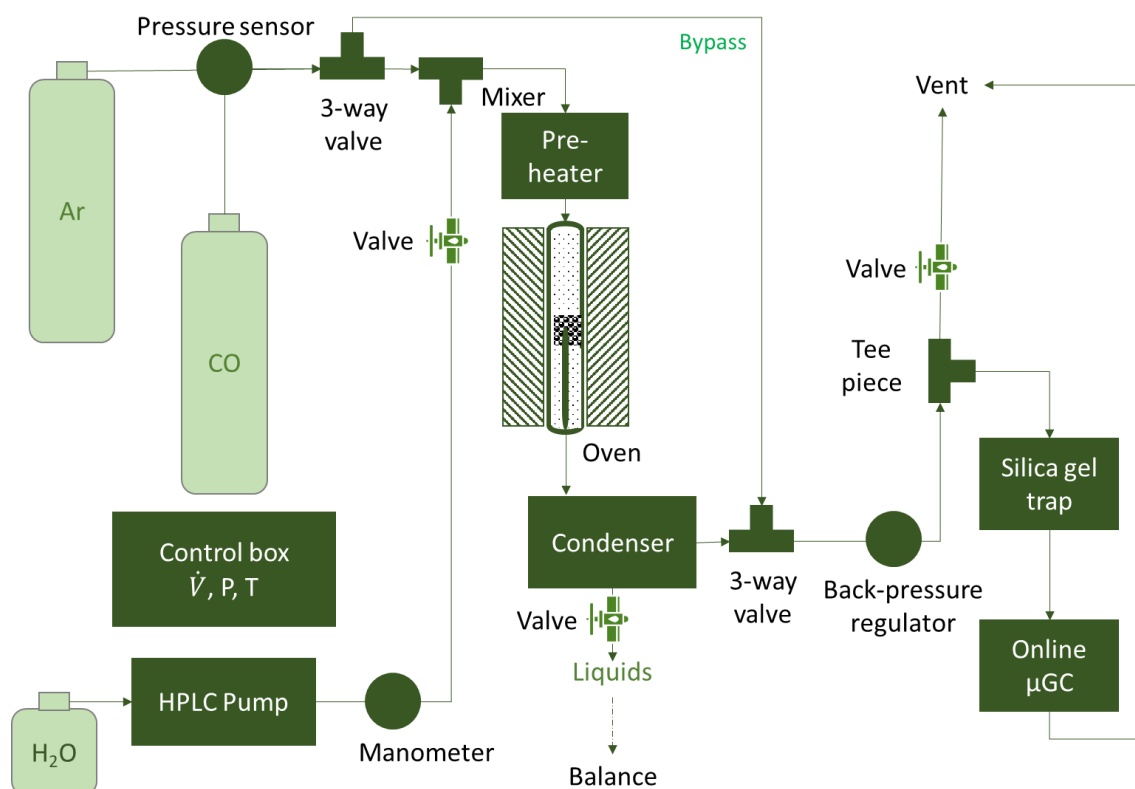


Fig. 4.1. Set-up for the Water-Gas Shift (WGS) experiments

Biocarbon catalysts were characterized in terms of organic element content (CHNS analysis), inorganic element content (ICP-AES) and its dispersion on the carbonaceous matrix (SEM, TEM), thermal stability (TGA-DSC), surface area (BET, N_2), textural properties and surface chemical groups (TPD, TPR, TPO, XRD). The changes in the structure of the biocarbon catalyst were analyzed before the chemical reaction.

4.2.2. Performance of the biocarbon catalysts

The performance of the biocarbon catalysts was estimated in terms of selectivity and conversion. Selectivity (S) allows to compare produced molecules and identify, in this case, if CO forms preferentially the main product CO₂ or the byproduct CH₄. Therefore, selectivity was defined as the ratio of the molar or volumetric flow (\dot{V}) of the target carbon gases produced compared to the sum of all carbon gases produced through the reaction (Eq.4.4 and 5).

$$S_{CO_2} = \frac{\dot{V}_{CO_2}}{\dot{V}_{CO_2} + \dot{V}_{CH_4}} \quad \text{Eq.4.4}$$

$$S_{CH_4} = 1 - S_{CO_2} \quad \text{Eq.4.5}$$

The conversion of the limiting gas represents the CO consumption to form products. A higher conversion represents a higher activity from the biocarbon catalyst. Conversion (X) was therefore defined as the ratio between the consumed amount of CO, calculated by the difference of inlet and outlet flowrate, divided by the inlet flow rate of the respective gas (Eq.4.6).

$$X_{CO} = \frac{\dot{V}_{inlet,CO} - \dot{V}_{outlet,CO}}{\dot{V}_{inlet,CO}} \quad \text{Eq.4.6}$$

The rate of CO₂ production (r_{CO_2}) was determined according to the variation in CO₂ concentration multiplied by the total flow rate divided by the mass of catalyst, therefore it represents the flow of CO₂ produced over the catalyst (Eq.4.7) [14].

$$r_{CO_2} = \frac{\Delta CO_2 \dot{V}_{total}}{m_{catalyst}} \quad \text{Eq.4.7}$$

4.3. Biocarbon-catalyzed WGS results: simulation, test and impact of variation of temperature and water partial pressure

4.3.1. Kinetic and thermodynamic simulations of WGS reaction conditions

In this section, the set-up for WGS and the selected operating conditions are optimized thanks to kinetic and thermodynamic simulations carried out on Aspen Plus. Initially, the preheating process was simulated to determine the required preheating temperature to limit condensation of water before the reactor, as too much liquid water could transport the catalyst downstream the oven. Based on this simulation, the WGS process was added and oven temperature and inlet water flow (liquid) was varied to determine their impact on WGS. The reaction was simulated kinetically and thermodynamically in

experimental conditions to carry out the experiments in representative conditions, in addition to defining the limits of our study.

4.3.1.1. *Setting gases preheating temperature prior WGS reactor*

First of all, gas preheating temperature prior their introduction in the WGS reactor was assessed. This parameter was chosen based on Aspen Plus simulations in order to limit the condensation of steam before the reactor that could cause transport of the catalyst downstream the oven. The impact of the pressure was also tested. The reaction atmosphere (argon), as well as reactive and produced gases were introduced as conventional components and the Peng Robinson – Boston Mathias (PR-BM) thermodynamic method was selected [45].

The Aspen flowsheet was defined by three blocks: a mixer and 2 heat exchangers. The 1st heat exchanger acts as the pre-heating temperature. It simultaneously defines the pressure before reaching the following blocks which are dependent on this pressure. The pressure of the experimental device is fixed by a back-pressure regulator located after the condenser that helps liquify condensable gases from the reactor and this regulator fixes the pressure preceding it (**Fig. 4.1**). The 2nd exchanger represents the heat loss before entering the reactor (**Fig. 4.2**). The heat loss (Q_{loss}) was quantified by convective exchange of the exterior of the tubing (28 cm long, 14 mm diameter) between the pre-heater and the reactor with ambient temperature (T_{amb} : 21°C). A thermocouple was used to estimate the temperature of the exterior of the tube (T_{tube}) at varying sections: 80°C for 2 cm, close to ambient for the rest of the tube. To account for overheating, possible loss of isolation around the tube and generally to overestimate the loss, half of the tube was considered at 80°C. The convective heat transfer coefficient (h) was selected as 10 W m⁻² K⁻¹ (average value for natural convection) [46]. The heat loss in these conditions was estimated at 3.93 W (**Eq.4.8**). Additionally, this worst-case scenario considered a liquid water flow rate of 1 mL/min. This liquid water is then vaporized in the pre-heating stage before being introduced in the reactor as steam.

$$Q_{loss} = h \times S \times (T_{tube} - T_{amb}) \quad \text{Eq.4.8}$$

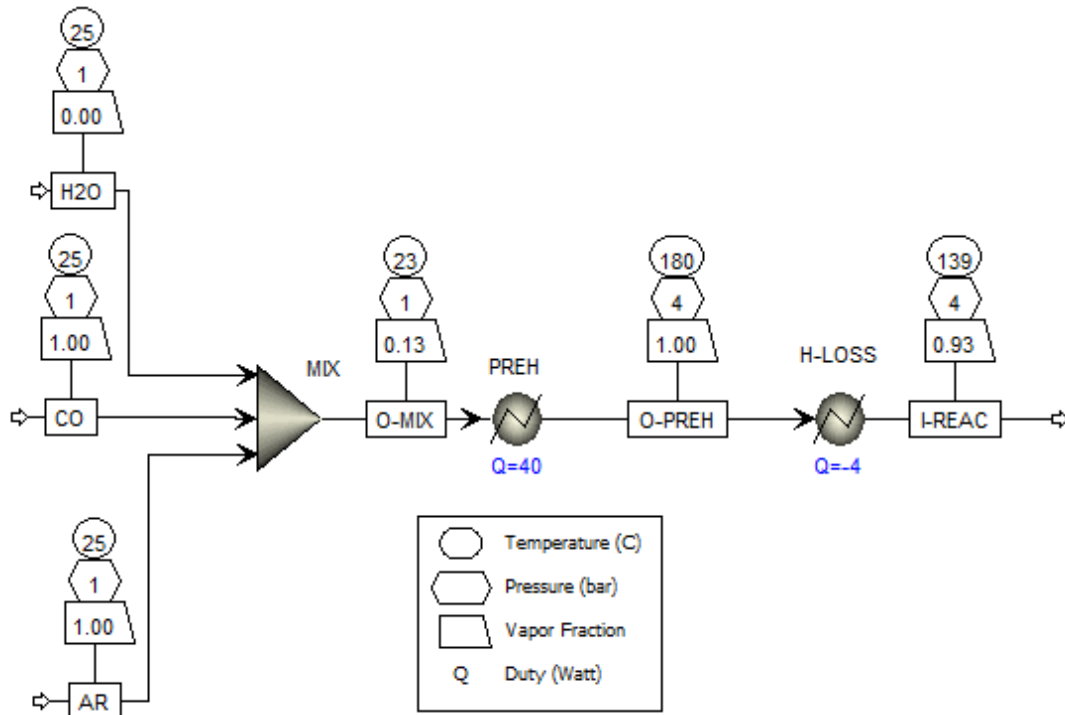


Fig. 4.2. Aspen Plus flowsheet for simulation of pre-heating temperature

A sensitivity analysis was performed on the temperature (100-200°C every 10°C) and the pressure (0-3 bar every bar, relative) of the pre-heater block to observe the rate of vaporization of liquids (Fig. 4.3). Under 140°C, the inlet stream to the reactor is mostly liquid. Therefore 180°C was selected for pre-heating to have a safe interval to account for possible increase in pressure and possible drops in temperature. This is what happens for example when significantly increasing water flow to guarantee its delivery to the reactor.

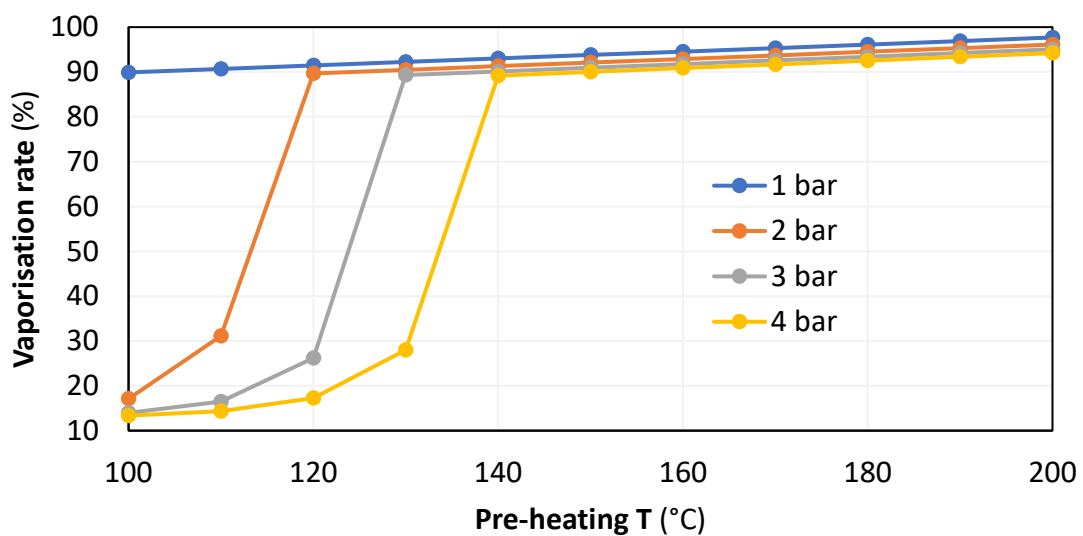


Fig. 4.3. Impact of pre-heating temperature and pressure on vaporization rate before entering reactor

4.3.1.2. Kinetic and thermodynamic simulations of the WGS reaction

Following this preestablished flowsheet, the WGS reaction was simultaneously assessed in 2 scenarios: kinetic-driven conditions using a plug flow reactor and thermodynamic-driven conditions using a Gibbs reactor followed by a condenser at 10°C (**Fig. 4.4**). Conditions for pre-heating were established as 0.58 W, corresponding to the estimated heat loss (2 cm of the tube at 80°C), and 3 bar of relative pressure, as with experimental WGS. The plug flow reactor represents the stoichiometric conversion according to reaction kinetics. The Gibbs reactor calculates the composition at thermodynamic equilibrium of outlet gas based on the minimization of Gibbs energy of the selected components at specified temperature (varied) and pressure (isobaric) [3,9].

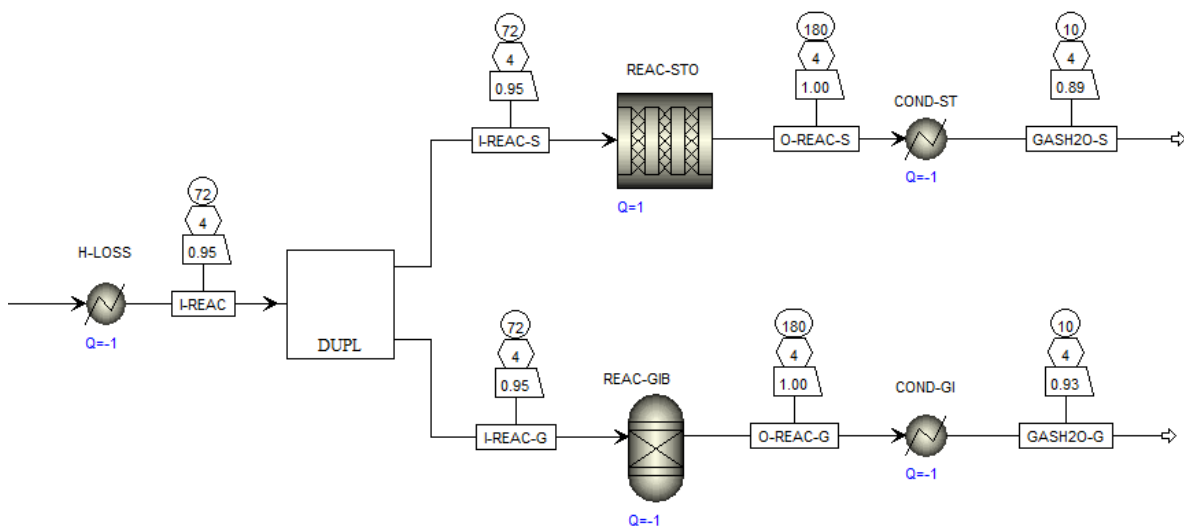


Fig. 4.4. Addition of WGS reactors to preheating flowsheet

The plug flow reactor block contains a specified reactor temperature (varied), dimensions set at 6 cm of length (estimate of catalyst bed length) and 8 mm of diameter, and a set of power law reactions (Table 4.2, 2nd line, last r expression) to represent WGS and RWGS, and to introduce formation and consumption of CH₄ via methanation (MET) and steam methane reforming (SMR) respectively (Eq.4.2,9 and 10) [19,20]. They were characterized by a specific set of parameters from the Arrhenius equation (Eq.4.3, Table 4.5). For WGS, both constants are low relative to previously reported values (Table 4.2) and could result in similar results due to the compensative effect of both constants. The other reactions (RWGS, MET, SMR) have however more elevated constants which could result in them being less active in WGS conditions. SMR could be the most active due to lowest activation energy and highest kinetic constant of the 3 and RWGS being the least active inversely.



Table 4.5. Set of parameters to kinetically simulate WGS process [25,45,47-51]

Reaction	k_0 (rate dependent unit)	E_a (kJ/mol)
WGS	5.4×10^4	67.1
RWGS	6.4×10^6	326.4
MET	2.8×10^{15}	243.9
SMR	1.2×10^{16}	240.1

A sensitivity analysis was performed on steam excess (S/C) and on the temperature of the selected reactor (T) to observe their influence on conversion, selectivity and outlet gas composition. S/C was observed from 1.4 to 20.7, with an increasing step of 1.4. T was varied from 180°C (pre-heating temperature) to 400°C (high temperature WGS) every 20°C.

For the plug flow reactor, conversion, selectivity and generally gas composition were unaffected by increasing temperature. Conversion increased initially from 1.5% to 3.3% from (S/C=) 1.4 to 8.4 then dropped to 2.7% at 0.30 mL/min (Fig. 4.5). The increase in S/C results in less water being vaporized when reaching the reactor which may cause the conversion drop since the reactor cannot provide enough energy to produce steam while maintaining the reaction. With this given set of kinetic parameters, only WGS and RWGS are dominant resulting in a CO₂ selectivity of 100%. The experimental gas composition takes in account the Ar as an inert sweeping gas and does not consider the composition of water as it is condensed before arriving at the μ GC, so to imitate this and facilitate further comparison, the simulated results were corrected by accounting for presence of Ar and adding it to the mix of reactive and produced gases, and by removing water content. The resulting simulated gas composition follows the same trend as conversion (Fig. 4.6).

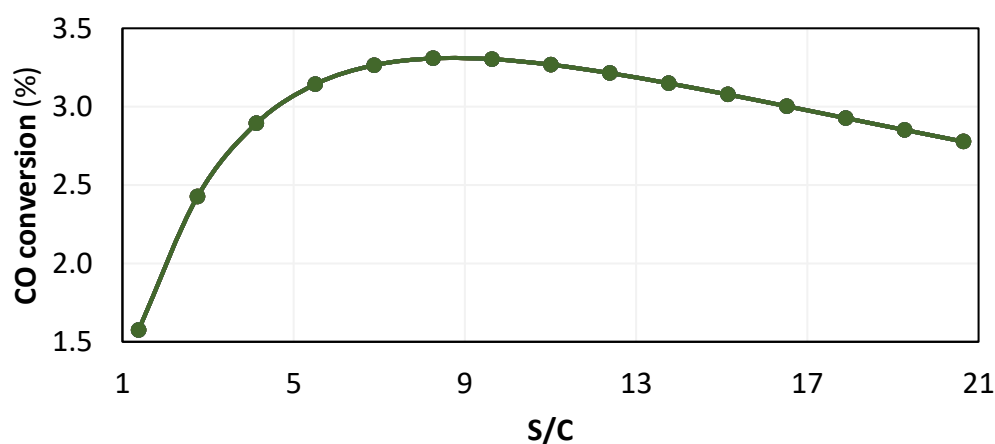


Fig. 4.5. Impact of variation in S/C on CO conversion in plug flow reactor (no effect from T)

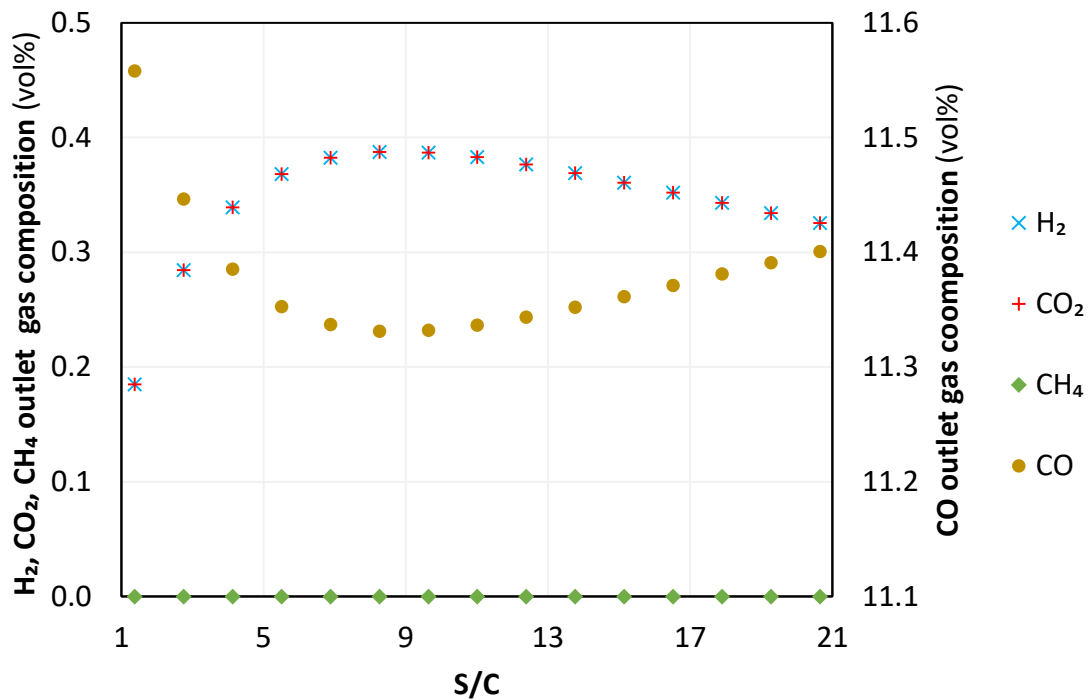


Fig. 4.6. Impact of variation in S/C on outlet gas composition in plug flow reactor (no effect from T)

For the Gibbs reactor, conversion increased with increasing S/C and decreasing T (Fig. 4.7). It was still above 99% and is coherent with thermodynamic calculations and equilibrium principles [52]. Inversely, increasing S/C and T increased CO₂ selectivity (Fig. 4.8) and therefore decreases CH₄ selectivity. Values for S_{CO_2} remain above 75%, meaning WGS is favored compared to methanation and this is exacerbated by the increase in \dot{V}_{H_2O} that forces WGS towards the production of CO₂ and T that when increased favors the least exothermic reaction between WGS and MET (MET: $\Delta H_{298}^0 = -206.0 \text{ kJ/mol}$, [52,53]). The gas composition (not represented) is also an illustration of the conversion, as well as the selectivity, with mainly CO₂ and CH₄ in proportion to the selectivity, little CO due to high conversion, and little H₂ due to methanation.

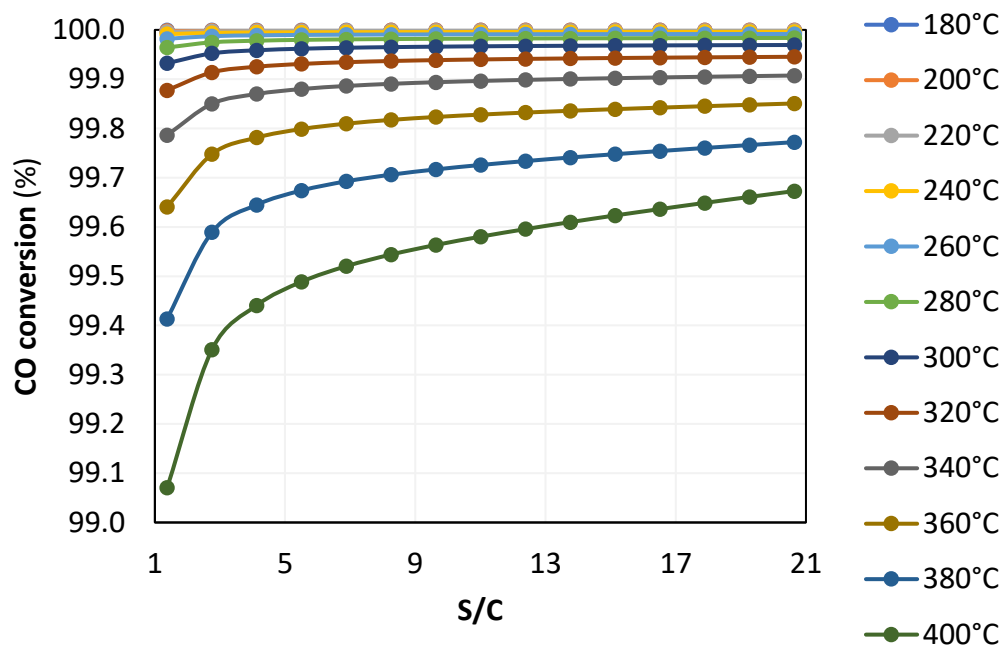


Fig. 4.7. Impact of variation in S/C and T on CO conversion in Gibbs reactor

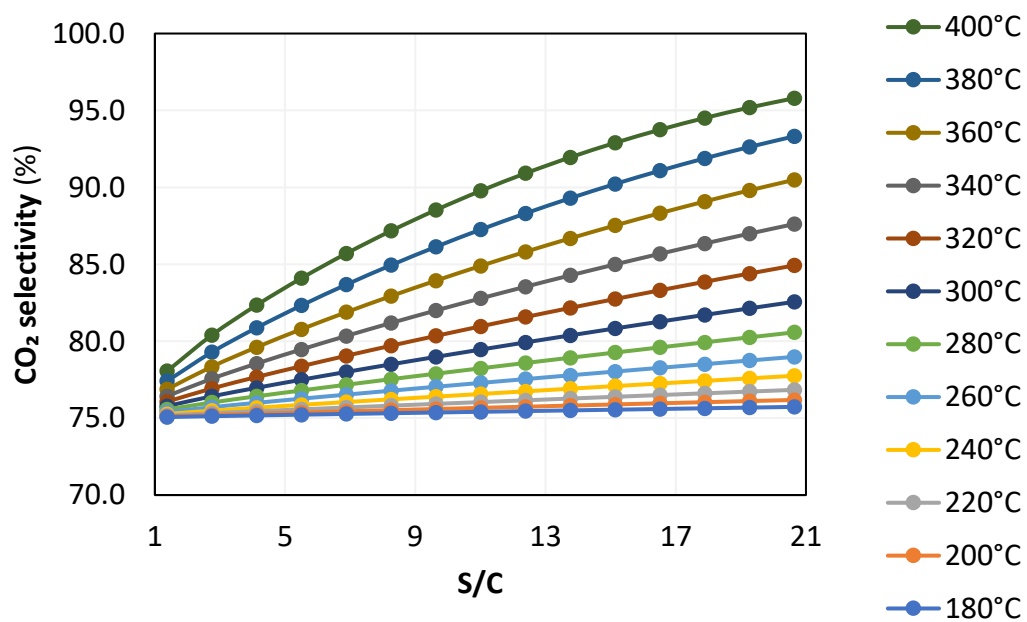


Fig. 4.8. Impact of variation in S/C and T on CO₂ selectivity in Gibbs reactor

Both scenarios tend to have opposite results, with conversion being either close to 100% when the reaction is thermodynamically driven or close to 0% when kinetically driven. The methanation reaction is also more or less dominant in terms of CO selectivity. Therefore, depending on experimental results, operating conditions and the catalytic effect of the studied catalysts, the reaction can be either kinetically driven, in which case the conversion should be low and selectivity high, or thermodynamically driven, where conversion is high and selectivity is impacted but still directed towards CO (>75%). The corrected simulated gas composition will be summarized after presentation of these experimental results (Table 4.7).

4.3.2. WGS reaction

Fern-based biocarbon catalysts were tested in WGS to observe the influence of the impregnation type (before and after pyrolysis), the impregnated metal (Fe and Ni) and WGS operating conditions, namely temperature and water flow. They were also compared to rust (Fe_2O_3) as a significant activity was reported in the literature (around 10-20% CO conversion under comparable temperatures, pressure, GHSV and S/C) and even higher activity when the catalytic metal is promoted and supported (reaching 70%) [34,54,55].

4.3.2.1. Influence of the temperature

The influence of the temperature was evaluated by the CO_2 production in WGS from 180°C to at least 280°C by increasing temperature in intervals of 20°C approximately every 1h30 for nickel and iron biocarbon catalysts, as well as rust. The visualization of the impact of this increase in temperature (T), and the modification of steam excess (S/C) on gas production is facilitated by the representation of the time-dependent evolution of CO_2 production (Fig. 4.9). The experience was repeated for the most active catalysts, which resulted in a relative standard deviation (RSD) of 9.6%. Additionally, the μGC can detect gases up to 0.001 vol%.

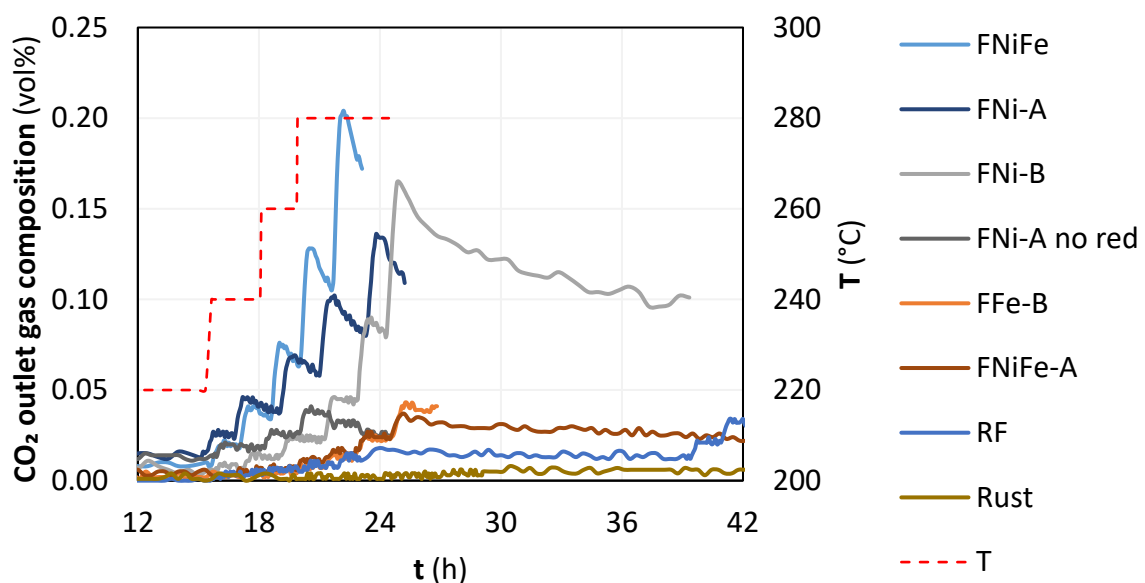


Fig. 4.9. Evolution in time of CO_2 production by catalyzed WGS, T and S/C varied but not represented

According to the results, Ni-based catalysts were shown to be more active, while rust (Fe_2O_3) was the least active. It showed the lowest activity with the maximum concentration of CO_2 being 0.04 vol% at 360°C (Fig. 4.9). In comparable conditions between the simulated results and reported values of literature (S/C = 3.5, GHSV = 60000 h^{-1} , T = 400°C), the value for CO_2 concentration should be close to 2.2 vol%. This value was obtained as a result of a cross-multiplication between the maximal simulated

CO₂ concentration (0.37 vol%, **Fig. 4.6**), the maximal reported CO conversion (20%) and the maximal simulated conversion (3.3%, **Fig. 4.5**) [34,55]. The CO₂ concentration obtained in this study reached 0.20 vol% so the 11-fold difference in experimental and reported values could be related to a difference in unmentioned operating conditions (pressure, presence of inert gas, bed size). The quantity of produced CO₂ (max. 0.20 vol%) compared to that of the simulated results (kinetic: 0.37 vol%) shows the kinetically driven nature of WGS in our conditions. The limitations associated with these conditions are therefore an important factor associated to these low values. This is however accompanied by stronger kinetic properties on behalf on the biocarbon catalysts that outperformed rust. Additionally, the observation of the temporal evolution of CO₂ concentration (**Fig. 4.9**) seems to indicate a deactivation of the catalysts (decrease in value over time) that is steeper as the temperature is increased.

To compare the performances of biocarbon catalysts, the maximum CO₂ production reached at each temperature was represented (Table 4.6).

Table 4.6. Impact of reactor temperature on peak production of CO₂ (vol%) of biocarbon catalyst and rust

T (°C)	Rust	FFe-B	RF	FNiFe-A	FNi-A no red	FNi-B	FNi-A	FNiFe
	CO ₂ outlet gas composition (vol%)							
180	0.007	0.008	0.001	0.006	0.003	0.012	0.047	0.013
200	0.004	0.004	0.005	0.008	0.029	0.010	0.028	0.022
220	0.004	0.005	0.006	0.009	0.019	0.015	0.046	0.041
240	0.005	0.007	0.008	0.013	0.021	0.026	0.069	0.076
260	0.006	0.010	0.011	0.018	0.028	0.046	0.102	0.128
280	0.008	0.015	0.015	0.027	0.041	0.090	0.136	0.204

Under 240°C, the activity of FNi-A (reduced or not), FNiFe and FNi-B appears to be slightly higher. This points out a low temperature activity that might be related to the presence of Ni. At low temperatures, the catalysts and the reaction are not stable due to activation required from both catalyst and reacting gases, and so the reaction is sensible to the ability of the active sites to have an electronic activity. This could be related to the ability to reversibly transform from an oxidated to a reduced state allowing activity in WGS, which is supported by TPR results (Table 4.7) where weaker reducible sites are represented by low peak temperature and the quantity of these sites is represented by the amount of H₂ desorbed [34,56–58]. In this study, the biocarbon catalysts were reduced at 500°C which could justify higher activity from FNi-A and FNiFe. This could also be correlated to the ability to easily adsorb CO or steam where Ni catalysts showed stronger adsorbative capacities for NH₃ and CO₂ respectively (Table 4.8). This is further amplified as Ni-based biocarbon catalysts present a higher amount of reducible sites, evidenced by the quantity of desorbed H₂, that once reduced are sourced of O vacancies that complement and facilitate the adsorption and reactivity of O from CO and steam.

Table 4.7. First H₂ peak from the TPR of the best biocarbon catalysts to determine their reducibility

Biocarbon catalyst	Amount of H ₂ (mmol/g)	Temperature peak #1 (°C)
FNi-A	0.484	355
FNiFe	1.524	514
FNi-B	0.651	601

Table 4.8. Chemical surface groups versus specific surface area of the biocarbon catalysts before WGS

Sample	TPD-NH ₃		TPD-CO ₂		TPD-H ₂		Specific surface area (m ² /g)
	Total adsorption (mmol/g)	T _{max} (°C)	Total adsorption (mmol/g)	T _{max} (°C)	Total adsorption (mmol/g)	T _{max} (°C)	
RF	0.779	913	12.003	915	2.545	993	8.8
FFe-B	0.553	951	8.258	905	0.158	981	309.6
FNi-B	1.480	912	16.207	920	2.921	986	151.6
FNi-A	0.847	945	11.956	923	1.673	989	100.0
FNiFe	1.088	923	15.980	924	0.994	1000	367.9

Above 240°C, the catalytic activity in relation to the CO₂ production increases by approximately 50% according to the following order: rust < FFe-B < RF < FNiFe-A < FNi-A not pre-reduced (no red) < FNi-B < FNi-A < FNiFe. There are similar trends as for lower temperatures: Ni catalysts are generally more active for WGS which could be related to their lower activation energies [59,60]. This activity is further amplified when considering the presence of other metals with promoting and supporting effects (alkali and alkaline earth metals, Co, Cu, Zn, Al, ...) that help reduce even further energy barriers. The performance of FNi-A could be improved through reduction as the CO₂ production of the pre-reduced FNi-A is 3 times higher than that of its not pre-reduced counterpart. This can be expected because through reduction the biocarbon catalyst gains O vacancies which act as reaction sites for both steam and CO [61,62]. On another hand, impregnation and pyrolysis could induce a loss of activity and specific surface area due to blocking of the access to pores containing active sites, induced by the metals in solution and carbon deposit respectively [63,64]. Here, pores and especially active sites are exposed as the specific surface area increases but the unhindered metals maintain their respective activities that are unaffected by this increase in surface area (Table 4.6 and 8). The high surface developed by Fe-based biocarbon catalysts, possibly related to catalyzed graphitization, does not therefore benefit its activity [65,66].

CO conversion was generally under 10% but seemed to increase by approximately 2% from 180 to 280°C (Table 4.9). Given the kinetic-driven nature of the reaction, an increase in temperature can only increase conversion as the reaction has yet to reach thermodynamic equilibrium [23,24,33–36]. As mentioned previously, in studies with similar operating conditions, rust can reach up to 20% conversion but did not exceed 7% in this study. This is indicative of the dominance of the kinetic nature of WGS in our conditions [34,54,55]. It also reflects the potential of the biocarbon catalysts who will

and currently are able to compete with commercial catalysts [67]. Additionally, the biocarbon catalysts outperformed rust with the most active being fern biocarbon impregnated with Fe and Ni before pyrolysis (FNiFe) and reaching 10% conversion. This could be explained by the biomass inherent metals that enhance the electronic state of reactive metals and improve their activity at lower temperatures [68].

Table 4.9. Impact of reactor temperature on CO conversion of biocarbon catalyst and rust

T (°C)	Rust	FFe-B	RF	FNiFe-A	FNi-A no red	FNi-B	FNi-A	FNiFe
	CO conversion (%)							
180	6.4	8.2	7.2	8.4	8.4	8.1	8.3	8.4
200	6.7	8.3	7.0	8.3	7.6	7.9	8.3	8.0
220	6.7	8.0	6.9	8.2	8.2	7.9	8.4	8.4
240	6.6	8.0	7.1	8.4	8.2	8.1	8.9	8.6
260	6.6	7.9	7.0	8.4	8.2	8.5	9.0	9.5
280	6.9	7.9	7.0	8.5	8.5	9.0	9.6	10.3

Selectivity towards CO₂ was globally above 85% and nearing 100% when performing the reaction at high temperatures (>240°C) with active catalysts (Table 4.10). This proved that the conditions were favorable to inhibit the side reaction producing CH₄. Thermodynamically, methanation is more exothermic than WGS so increasing temperature should be more inhibiting to the formation of CH₄ [25].

Table 4.10. Impact of reactor temperature on CO₂ selectivity of biocarbon catalyst and rust

T (°C)	Rust	FFe-B	RF	FNiFe-A	FNi-A no red	FNi-B	FNi-A	FNiFe
	CO ₂ selectivity (%)							
180	100.0	100.0	22.6	96.7	100.0	100.0	100.0	100.0
200	100.0	93.8	84.6	95.8	100.0	95.8	97.3	100.0
220	96.0	98.1	100.0	92.1	89.6	92.3	92.6	100.0
240	100.0	100.0	98.2	92.2	90.0	86.8	94.8	100.0
260	97.0	88.9	100.0	100.0	95.8	93.7	95.1	100.0
280	100.0	100.0	96.7	100.0	97.3	94.3	98.5	99.7

4.3.2.2. Influence of the steam excess

S/C was varied between 1.4 to 20.7. This variation was carried out at the end of the experiment for RF (360°C) and FNi-A not pre-reduced (280°C, Table 4.11).

Table 4.11. Impact of steam excess on peak production of CO₂, CO conversion and CO₂ selectivity of biocarbon catalyst

	CO ₂ outlet gas composition (vol%)		CO conversion (%)		CO ₂ selectivity (%)	
	RF (360°C)	FNi-A no red (280°C)	RF (360°C)	FNi-A no red (280°C)	RF (360°C)	FNi-A no red (280°C)
1.4	0.039		7.4		99.1	
2.8		0.031		8.0		100.0
5.5	0.048	0.038	7.6	8.4	100.0	98.7
20.7	0.056	0.041	7.7	8.5	98.3	97.3

It was observed that the production of CO₂ increased by approximately 20% with increasing S/C. This is coherent with literature as an increase in S/C shifts WGS towards the production of CO₂ and H₂ due to the excess of one reactant (steam in this case) and the resulting displacement in equilibrium. This increase continues at higher values of S/C but the increase lessens above 10 [18,23,24,37,39,40].

The water flow rate seemed to slightly increase conversion by 2.5% (<RSD) which could be due to the displacement of equilibrium. A peak of CO₂ production and therefore CO conversion should be observed at S/C = 8.4 based on the simulated kinetic results (Fig. 4.5 and 6), but this was not the case with the experimental results since the increase continued at 20.7.

According to the literature, an increase in flow rate reduces contact time allowing formation of CH₄ and an increase in S/C drives the consumption of CH₄ through SMR [69–72]. Therefore, CO₂ selectivity should improve with excess steam and high GHSV. In our case, the variation in flow rate did not show an influence on the selectivity. However, selectivity was close to 100% which is comparable to the simulated kinetic results (Fig. 4.5 and 6).

4.3.2.3. Reaction performances

The performance of the biocarbon catalysts was evaluated in WGS reaction through CO conversion and selectivity towards CO₂ and CH₄. The results obtained at 280°C and S/C = 5.5, in terms of concentration of reactive gases (CO) and product gases (CO₂, H₂ and CH₄) was indicated (Table 4.12), and facilitated comparison between the previously simulated results (Fig. 4.5 and 6) and the experimental results (Table 4.6, 9 and 10). This temperature is the highest studied for all catalysts and for which the CO₂ production and CO conversion are sufficiently high to allow a more precise comparison.

Table 4.12. Summary of averaged values of concentrations, selectivity and conversion for all trialed catalysts

Conditions: 280°C, S/C = 5.5			Outlet gas composition (vol%)				Conversion	Selectivity (%)		
			CO	CO ₂	H ₂	CH ₄	X _{CO} (%)	S _{CO₂}	S _{CH₄}	
Biocarbon catalysts and rust			Initial composition	11.76	-	-	-	-	-	
			WGS kinetic simulation	11.35	0.37	0.37	<0.00	3.1	100	<0.0
Sample	Biomass	Metal	Impregnation before/after pyrolysis	Outlet gas composition (vol%)				Conversion	Selectivity (%)	
				CO	CO ₂	H ₂	CH ₄	X _{CO} (%)	S _{CO₂}	S _{CH₄}
RF	fern	-	-	9.70	0.01	0.01	<0.00	7.0	96.7	3.3
FFe-B	fern	Fe	before	9.69	0.01	0.02	<0.00	7.9	100	<0.0
FNiFe-A	fern	Fe,Ni	after	9.63	0.02	0.03	<0.00	8.5	100	<0.0
FNi-B	fern	Ni	before	9.57	0.08	0.09	0.01	9.0	94.3	5.7
FNi-A	fern	Ni	after	9.52	0.12	0.14	<0.00	9.6	98.5	1.5
FNiFe	fern	Fe,Ni	before	9.46	0.17	0.21	<0.00	10.3	99.7	0.3
FNi-A no red.	Fern	Ni	after	9.64	0.04	0.04	<0.00	8.5	97.3	2.7
Fe ₂ O ₃	-	Fe	-	9.67	0.01	0.01	<0.00	6.9	100	<0.0

To summarize, CO₂ and H₂ gas production and inversely CO consumption is higher with Ni-biocarbon catalysts than with Fe-biocarbon catalysts or rust. The most performant catalyst FNiFe combines the properties of both metals. Ni-based catalysts in particular are functional for low temperature WGS as then can alternate between reduced and oxidized states at low temperatures with little energy [34,56–58]. CO conversion is improved as CO consumption is increased and follows this same tendency. CO₂ selectivity decreases as CH₄ production increases. This is mostly the case with Ni-based biocarbon catalysts but CO selectivity in this instance is above 94%.

When compared to the kinetic simulation results, experimental gas production shows to be lower. This is at most 0.17 vol% CO₂ and 0.21 vol% H₂ experimentally (reminder: μ GC sensitivity = 0.001 vol% and RSD = 10%) compared to 0.37 vol% simulated for both gases. The difference in gas production could be due to lower WGS activity as the kinetic parameters used in the simulation (Table 4.5) are based on highly efficient and optimized catalysts such as Pt based catalysts [25,45,47–51]. Additionally, it is possible that some gas is adsorbed by the biocarbon and the moisture trap [73]. The experimental CO conversion, of at least 6.9%, is however higher than the simulated one of 3.1%. The difference in kinetic and experimental conversions could be due to lower values of CO concentration (11.35 compared to 9.70 vol% respectively) for which the variation of content, that is consequently higher as values are lower, results in higher conversion (Eq. 4.6). This conversion is low compared to other reported values of at least 10%, but similar trends have been identified where Ni-based catalysts are more active at lower temperatures than Fe-based catalysts [67]. This conversion can be improved further by changing the kinetic parameters (catalyst) and displacing equilibrium through increase of temperature and steam excess (operating conditions). This increase in temperature will however be limited by

thermodynamic equilibrium (Fig. 4.7) that diminishes as temperature increases, in addition to the loss of catalyst stability. Also, the impact of excess steam stagnates as it is increased [24,36,37].

These results differ from previously studied RWGS where the reaction was partially thermodynamically-driven (namely at 400°C, Chapter 3). In this work, rust was the most active but least stable catalyst whereas biocarbon catalysts performed well as high conversions were maintained for the duration of the experiment (72h) and the catalyst did not suffer deactivation. The most active catalysts were fern-based catalysts which contained both Fe and Ni. Their activity was related to the synergetic effect of inherent metals with O vacancies resulting in improved electronic properties. In the case of WGS, inherent metals allow minimal activity but are confronted to energy barriers that limit their activity. Therefore, a low-temperature functioning metal that can overcome these barriers easily (Ni) is not as limited as other metals (Fe). In both RWGS and WGS, biocarbon catalysts presented interesting properties that resulted in high performance, stability and selectivity. Further modifications may help to improve their performance respective to the tested reaction.

4.3.2.4. Kinetic parameters

Kinetic parameters were estimated via power law and Arrhenius equations (Table 4.2, Eq.4.3 and 7). By assuming nearly constant partial pressures and high CO selectivity, equations were obtained (Eq.4.11-12) and kinetic parameters were deduced (Table 4.13) [33].

$$\ln(r_{CO_2}) = -\frac{E_a}{RT} + \ln(k_0) + constant \quad \text{Eq.4.11}$$

$$\frac{k_{0,biosourced\ catalyst}}{k_{0,rust}} = e^{\ln(r_{CO_2,biosourced\ catalyst}) - \ln(r_{CO_2,rust})} \quad \text{Eq.4.12}$$

Table 4.13. Estimated kinetic parameters for biocarbon catalysts and rust in pre-established decreasing order of performance

Catalyst	E_a (kJ/mol)	$k_0, \text{biocarbon catalyst}/k_0, \text{rust}$
FNiFe	59.5	$5.6 \times 10^5 = e^{11.6}$
FNi-A	26.8	$1.8 \times 10^2 = e^{5.8}$
FNi-B	92.1	$2.2 \times 10^8 = e^{19.2}$
FNi-A not pre-reduced	22.1	$1.4 \times 10^1 = e^{2.7}$
FNiFe-A	43.3	$1.3 \times 10^3 = e^{7.2}$
RF	7.5	$3.9 \times 10^{-1} = e^{-1.0}$
FFe-B	5.2	$2.2 \times 10^{-1} = e^{-1.5}$
Rust	9.5	$1 = e^0$

The most performant catalysts present relatively high kinetic constants, which is beneficial for kinetic-driven WGS, but also present high activation energy. This phenomenon is inverted for the least performing catalysts and indicates the importance of the dual effect from both parameters. No

immediate conclusion can be drawn based on a comparative factor accounting for the contribution of both parameters (such as comparing rates). However, this underlines the importance of the intrinsic characteristics of the biocarbon catalysts that have no immediate catalytic impact (thermal, electric and electronic conductivity). Regardless, the experimental values obtained for the activation energy and the preexponential factor, compared to literature, are of the same order of magnitude [13,15,27]. Furthermore, the assumptions to obtain these parameters are insufficient to completely describe the rate law, for example the orders for each reactant and product were not determined. Indeed, CO formation rates are highly dependent on the partial pressures of formed gases and their respective orders, and do not consider possible methane production (Table 4.2) [13–21]. Nevertheless, the comparison between the obtained results for WGS simulation and experiments was summarized (Table 4.14).

Table 4.14. Synthesis of the comparison between the obtained results for WGS simulation and experiments

Parameters	Result	Discussion
Simulated plug flow reactor	Kinetic simulations result in low conversion (<3.3%) with maximal conversion reached at specific value of water flow and nearly 100% selectivity; no impact from T	Kinetic simulations are regulated by the set of kinetic parameters resulting in WGS being dominant but not quite active; too much liquid water results in use of reaction energy to form steam, optimum at S/C = 8.4
Simulated Gibbs reactor	Thermodynamic simulations tend towards high conversion (>99%) and selectivity (>75%)	Conversion increases with excess steam but decreases with temperature and inversely for selectivity: equilibrium principles and exacerbation of CH ₄ producing reactions (more exothermic than WGS) by steam
T	<ul style="list-style-type: none"> •Biocarbon catalysts are more active than rust and when reduced •Ni-based biocarbon catalyst are more active especially at lower T •11-fold difference between experiments and literature •Instability below 240°C •Increase in conversion and high selectivity 	<ul style="list-style-type: none"> •O vacancies caused by reduction of O-containing biocarbon surface groups could improve CO and steam uptake and reactivity; other inorganic element namely AAEM and co-catalytic metals may help reduce energy barriers •Ni may be active and accessible at low T thanks to low T reversibility and to sufficiently developed porosity •Difference experiment-literature could be related to not addressed studied operating conditions •Instability may be related to electronic sensitivity and competition between activation of catalyst and reacting gases •Promotion of kinetics by T increasing consumption of CO and inhibiting of methanation as it is more exothermic than WGS
S/C	<ul style="list-style-type: none"> •Increase of CO₂ production •Increase in conversion even at higher S/C values (20.7) •Little influence of selectivity but close to 100% 	<ul style="list-style-type: none"> •Displacement of equilibrium towards the products of WGS due to excess of steam •Contradiction with simulation as maximum observed at 8.4 S/C but coherent with displacement of equilibrium •Coherent with simulation, excess steam that promotes CH₄ reforming and increase in GHSV that limits time to form CH₄
Kinetic (global)	<ul style="list-style-type: none"> •The reaction is kinetically driven with high conversion (<10%) and selectivity (>85%) •Biocarbon catalysts outperformed rust 	<ul style="list-style-type: none"> •Inherent metals, facilitated reducibility and O vacancies could improve biocarbon performance but a change in operating conditions could enable thermodynamic equilibrium •E_a = 5.2 kJ/mol and k₀/k_{0, rust} = 2.2 x 10⁸ for biocarbon catalysts compared to 9.5 kJ/mol and 1 for rust, respectively: high kinetic performance observed at low T (<400°C) for biocarbon catalysts in WGS

4.4. Conclusion and perspectives

Biocarbon catalysts from fern were tested in original WGS conditions with increments in temperatures ranging 180 to 400°C and in S/CO from 1.4 to 20.7, every 1h30. Results showed that WGS is kinetically-driven: conversion increased as temperature increased. Biocarbon catalysts outperformed rust, which shows promising results compared to commercial catalysts. Ni-based biocarbon catalysts showed the best activity. This could be attributed to their activation from lower temperatures. This is especially the case of the fern catalyst impregnated with Ni and Fe before pyrolysis, which resulted in a conversion above 10%. CO conversion and consequently CO_2 and H_2 gas production increased with S/CO ratio due to improved kinetics and displacement of equilibrium, respectively. Selectivity was above 85% and was slightly affected by temperature and S/CO , where their increase inhibits the side reaction producing CH_4 . Kinetic parameters were determined for the biocarbon catalysts relative to rust and are comparable to literature values. No explicit relation between the order of the biocarbon catalysts' activity and these parameters was established. Characteristics with subtle impact on the kinetics may therefore need to be brought to light. Future work should observe these characteristics and optimize operating conditions to direct WGS towards thermodynamic equilibrium, as well as analyze the impact of biocarbon catalysts on other environmental applications. Additionally, further tests should be performed to precise the kinetic laws (including power law) that apply to these catalysts, and their respective parameters, by modifying the gas flows and the contact time between the gas and the catalyst bed.

References

- [1] About — IPCC n.d. <https://www.ipcc.ch/about/> (accessed July 24, 2023).
- [2] Pal DB, Chand R, Upadhyay SN, Mishra PK. Performance of water gas shift reaction catalysts: A review. *Renewable and Sustainable Energy Reviews* 2018;93:549–65. <https://doi.org/10.1016/j.rser.2018.05.003>.
- [3] Chen W-H, Chen C-Y. Water gas shift reaction for hydrogen production and carbon dioxide capture: A review. *Applied Energy* 2020;258:114078. <https://doi.org/10.1016/j.apenergy.2019.114078>.
- [4] Ratnasamy C, Wagner JP. Water Gas Shift Catalysis. *Catalysis Reviews* 2009;51:325–440. <https://doi.org/10.1080/01614940903048661>.
- [5] Shen Y. Chars as carbonaceous adsorbents/catalysts for tar elimination during biomass pyrolysis or gasification. *Renewable and Sustainable Energy Reviews* 2015;43:281–95. <https://doi.org/10.1016/j.rser.2014.11.061>.
- [6] Wang G, Jiang L, Zhou Y, Cai Z, Pan Y, Zhao X, et al. Investigation of the kinetic properties for the forward and reverse WGS reaction by energetic analysis. *Journal of Molecular Structure: THEOCHEM* 2003;634:23–30. [https://doi.org/10.1016/S0166-1280\(03\)00209-4](https://doi.org/10.1016/S0166-1280(03)00209-4).
- [7] Plata JJ, Graciani J, Evans J, Rodriguez JA, Sanz JF. Cu Deposited on CeO_x-Modified TiO₂(110): Synergistic Effects at the Metal–Oxide Interface and the Mechanism of the WGS Reaction. *ACS Catal* 2016;6:4608–15. <https://doi.org/10.1021/acscatal.6b00948>.
- [8] Lambert M, Leven BA, Green RM. New Methods of Cleaning Up Heavy Metal in Soils and Water. *ENVIRONMENTAL SCIENCE AND TECHNOLOGY BRIEFS FOR CITIZENS* n.d.:3.
- [9] Said M, Cassayre L, Dirion J-L, Joulia X, Nzihou A. Effect of Nickel Impregnation on Wood Gasification Mechanism. *Waste Biomass Valor* 2017;8:2843–52. <https://doi.org/10.1007/s12649-017-9911-3>.
- [10] Pahija E, Panaritis C, Gusarov S, Shadbahr J, Bensebaa F, Patience G, et al. Experimental and Computational Synergistic Design of Cu and Fe Catalysts for the Reverse Water–Gas Shift: A Review. *ACS Catal* 2022;12:6887–905. <https://doi.org/10.1021/acscatal.2c01099>.
- [11] Lèbre É, Stringer M, Svobodova K, Owen JR, Kemp D, Côte C, et al. The social and environmental complexities of extracting energy transition metals. *Nat Commun* 2020;11:4823. <https://doi.org/10.1038/s41467-020-18661-9>.
- [12] Yuan X, Cao Y, Li J, Patel AK, Dong C-D, Jin X, et al. Recent advancements and challenges in emerging applications of biochar-based catalysts. *Biotechnology Advances* 2023;67:108181. <https://doi.org/10.1016/j.biotechadv.2023.108181>.
- [13] Saeidi S, Fazlollahi F, Najari S, Iranshahi D, Klemeš JJ, Baxter LL. Hydrogen production: Perspectives, separation with special emphasis on kinetics of WGS reaction: A state-of-the-art review. *Journal of Industrial and Engineering Chemistry* 2017;49:1–25. <https://doi.org/10.1016/j.jiec.2016.12.003>.
- [14] Ayastuy JL, Gutiérrez-Ortiz MA, González-Marcos JA, Aranzabal A, González-Velasco JR. Kinetics of the Low-Temperature WGS Reaction over a CuO/ZnO/Al₂O₃ Catalyst. *Ind Eng Chem Res* 2005;44:41–50. <https://doi.org/10.1021/ie049886w>.
- [15] Yan H, Qin X-T, Yin Y, Teng Y-F, Jin Z, Jia C-J. Promoted Cu-Fe₃O₄ catalysts for low-temperature water gas shift reaction: Optimization of Cu content. *Applied Catalysis B: Environmental* 2018;226:182–93. <https://doi.org/10.1016/j.apcatb.2017.12.050>.
- [16] Zhu M, Wachs IE. Iron-Based Catalysts for the High-Temperature Water–Gas Shift (HT-WGS) Reaction: A Review. *ACS Catal* 2016;6:722–32. <https://doi.org/10.1021/acscatal.5b02594>.
- [17] Palma V, Pisano D, Martino M. CFD modeling of the influence of carrier thermal conductivity for structured catalysts in the WGS reaction. *Chemical Engineering Science* 2018;178:1–11. <https://doi.org/10.1016/j.ces.2017.12.035>.

- [18] Gosiewski K, Tańczyk M. Applicability of membrane reactor for WGS coal derived gas processing: Simulation-based analysis. *Catalysis Today* 2011;176:373–82. <https://doi.org/10.1016/j.cattod.2010.11.042>.
- [19] Živković LA, Pohar A, Likozar B, Nikačević NM. Kinetics and reactor modeling for CaO sorption-enhanced high-temperature water–gas shift (SE–WGS) reaction for hydrogen production. *Applied Energy* 2016;178:844–55. <https://doi.org/10.1016/j.apenergy.2016.06.071>.
- [20] Seo Y-S, Seo D-J, Seo Y-T, Yoon W-L. Investigation of the characteristics of a compact steam reformer integrated with a water-gas shift reactor. *Journal of Power Sources* 2006;161:1208–16. <https://doi.org/10.1016/j.jpowsour.2006.05.039>.
- [21] Ghasemzadeh K, Zeynali R, Basile A. Theoretical study of hydrogen production using inorganic membrane reactors during WGS reaction. *International Journal of Hydrogen Energy* 2016;41:8696–705. <https://doi.org/10.1016/j.ijhydene.2015.12.117>.
- [22] Peppley BAD. A comprehensive kinetic model of methanol-steam reforming on Cu/ZnO/Al₂O₃ catalyst. Royal Military College of Canada, 1997.
- [23] Cornaglia L, Múnera J, Lombardo E. Recent advances in catalysts, palladium alloys and high temperature WGS membrane reactors: A review. *International Journal of Hydrogen Energy* 2015;40:3423–37. <https://doi.org/10.1016/j.ijhydene.2014.10.091>.
- [24] Park YM, Son M, Park M-J, Bae JW. Effects of Pt precursors on Pt/CeO₂ to water-gas shift (WGS) reaction activity with Langmuir-Hinshelwood model-based kinetics. *International Journal of Hydrogen Energy* 2020;45:26953–66. <https://doi.org/10.1016/j.ijhydene.2020.06.296>.
- [25] Phatak AA, Koryabkina N, Rai S, Ratts JL, Ruettinger W, Farrauto RJ, et al. Kinetics of the water–gas shift reaction on Pt catalysts supported on alumina and ceria. *Catalysis Today* 2007;123:224–34. <https://doi.org/10.1016/j.cattod.2007.02.031>.
- [26] Angeli SD, Monteleone G, Giaconia A, Lemonidou AA. State-of-the-art catalysts for CH₄ steam reforming at low temperature. *International Journal of Hydrogen Energy* 2014;39:1979–97. <https://doi.org/10.1016/j.ijhydene.2013.12.001>.
- [27] Mendes D, Mendes A, Madeira LM, Iulianelli A, Sousa JM, Basile A. The water-gas shift reaction: from conventional catalytic systems to Pd-based membrane reactors—a review. *Asia-Pacific Journal of Chemical Engineering* 2010;5:111–37. <https://doi.org/10.1002/apj.364>.
- [28] VAN DER LAAN GP, BEENACKERS AACM. Kinetics and Selectivity of the Fischer–Tropsch Synthesis: A Literature Review. *Catalysis Reviews* 1999;41:255–318. <https://doi.org/10.1081/CR-100101170>.
- [29] Ghanekar P, Kubal J, Cui Y, Mitchell G, Delgass WN, Ribeiro F, et al. Catalysis at Metal/Oxide Interfaces: Density Functional Theory and Microkinetic Modeling of Water Gas Shift at Pt/MgO Boundaries. *Top Catal* 2020;63:673–87. <https://doi.org/10.1007/s11244-020-01257-4>.
- [30] Ding K, Gulec A, Johnson AM, Schweitzer NM, Stucky GD, Marks LD, et al. Identification of active sites in CO oxidation and water-gas shift over supported Pt catalysts. *Science* 2015;350:189–92. <https://doi.org/10.1126/science.aac6368>.
- [31] Majima T, Kono E, Ogo S, Sekine Y. Pre-reduction and K loading effects on noble metal free Co-system catalyst for water gas shift reaction. *Applied Catalysis A: General* 2016;523:92–6. <https://doi.org/10.1016/j.apcata.2016.05.025>.
- [32] Patlolla A, Carino EV, Ehrlich SN, Stavitski E, Frenkel AI. Application of Operando XAS, XRD, and Raman Spectroscopy for Phase Speciation in Water Gas Shift Reaction Catalysts. *ACS Catal* 2012;2:2216–23. <https://doi.org/10.1021/cs300414c>.
- [33] Pastor-Pérez L, Gu S, Sepúlveda-Escribano A, Reina TR. Bimetallic Cu–Ni catalysts for the WGS reaction – Cooperative or uncooperative effect? *International Journal of Hydrogen Energy* 2019;44:4011–9. <https://doi.org/10.1016/j.ijhydene.2018.12.127>.
- [34] Rodriguez JA, Senanayake SD, Stacchiola D, Liu P, Hrbek J. The Activation of Gold and the Water–Gas Shift Reaction: Insights from Studies with Model Catalysts. *Acc Chem Res* 2014;47:773–82. <https://doi.org/10.1021/ar400182c>.

- [35] Khan A, Smirniotis PG. Relationship between temperature-programmed reduction profile and activity of modified ferrite-based catalysts for WGS reaction. *Journal of Molecular Catalysis A: Chemical* 2008;280:43–51. <https://doi.org/10.1016/j.molcata.2007.10.022>.
- [36] Babatabar MA, Saidi M. Hydrogen production via integrated configuration of steam gasification process of biomass and water-gas shift reaction: Process simulation and optimization. *International Journal of Energy Research* 2021;45:19378–94. <https://doi.org/10.1002/er.7087>.
- [37] Daly H, Goguet A, Hardacre C, Meunier FC, Pilasombat R, Thompsett D. The effect of reaction conditions on the stability of Au/CeZrO₄ catalysts in the low-temperature water-gas shift reaction. *Journal of Catalysis* 2010;273:257–65. <https://doi.org/10.1016/j.jcat.2010.05.021>.
- [38] Cheula R, Maestri M. Nature and identity of the active site via structure-dependent microkinetic modeling: An application to WGS and reverse WGS reactions on Rh. *Catalysis Today* 2022;387:159–71. <https://doi.org/10.1016/j.cattod.2021.05.016>.
- [39] Baraj E, Ciahotný K, Hlinčík T. The water gas shift reaction: Catalysts and reaction mechanism. *Fuel* 2021;288:119817. <https://doi.org/10.1016/j.fuel.2020.119817>.
- [40] Živković LA, Pohar A, Likozar B, Nikačević NM. Reactor conceptual design by optimization for hydrogen production through intensified sorption- and membrane-enhanced water-gas shift reaction. *Chemical Engineering Science* 2020;211:115174. <https://doi.org/10.1016/j.ces.2019.115174>.
- [41] Francesconi JA, Mussati MC, Aguirre PA. Analysis of design variables for water-gas-shift reactors by model-based optimization. *Journal of Power Sources* 2007;173:467–77. <https://doi.org/10.1016/j.jpowsour.2007.04.048>.
- [42] Munirathinam R, Pham Minh D, Nzihou A. Effect of the Support and Its Surface Modifications in Cobalt-Based Fischer–Tropsch Synthesis. *Ind Eng Chem Res* 2018;57:16137–61. <https://doi.org/10.1021/acs.iecr.8b03850>.
- [43] Lee JS, Kim HS, Park N-K, Lee TJ, Kang M. Low temperature synthesis of α -alumina from aluminum hydroxide hydrothermally synthesized using [Al(C₂O₄)_x(OH)_y] complexes. *Chemical Engineering Journal* 2013;230:351–60. <https://doi.org/10.1016/j.cej.2013.06.099>.
- [44] Ghogia AC, Machado BF, Cayez S, Nzihou A, Serp P, Soulantica K, et al. Beyond confinement effects in Fischer-Tropsch Co/CNT catalysts. *Journal of Catalysis* 2021;397:156–71. <https://doi.org/10.1016/j.jcat.2021.03.027>.
- [45] Yang L. CO₂ conversion via reverse water-gas shift using multicomponent catalysts - University of Surrey. University of Surrey, 2021.
- [46] Puig-Gamero M, Pio DT, Tarelho LAC, Sánchez P, Sanchez-Silva L. Simulation of biomass gasification in bubbling fluidized bed reactor using aspen plus®. *Energy Conversion and Management* 2021;235:113981. <https://doi.org/10.1016/j.enconman.2021.113981>.
- [47] Kosky P, Balmer R, Keat W, Wise G. Chapter 14 - Mechanical Engineering. In: Kosky P, Balmer R, Keat W, Wise G, editors. *Exploring Engineering (Fifth Edition)*, Academic Press; 2021, p. 317–40. <https://doi.org/10.1016/B978-0-12-815073-3.00014-4>.
- [48] Elsaddik M. Hydrogen-rich syngas from steam gasification of cellulose in a biorefinery approach. These de doctorat. Ecole nationale des Mines d'Albi-Carmaux, 2022.
- [49] Solli K-A, Kumar Thapa R, Moldestad BME. Screening of Kinetic Rate Equations for Gasification Simulation Models 2018.
- [50] Abdelouahed L, Authier O, Mauviel G, Corriou JP, Verdier G, Dufour A. Detailed Modeling of Biomass Gasification in Dual Fluidized Bed Reactors under Aspen Plus. *Energy Fuels* 2012;26:3840–55. <https://doi.org/10.1021/ef300411k>.
- [51] LaMont DC, Thomson WJ. Dry reforming kinetics over a bulk molybdenum carbide catalyst. *Chemical Engineering Science* 2005;60:3553–9. <https://doi.org/10.1016/j.ces.2005.01.021>.
- [52] Klose J, Baerns M. Kinetics of the methanation of carbon monoxide on an alumina-supported nickel catalyst. *Journal of Catalysis* 1984;85:105–16. [https://doi.org/10.1016/0021-9517\(84\)90114-3](https://doi.org/10.1016/0021-9517(84)90114-3).
- [53] Er-rbib H, Bouallou C. Modeling and simulation of CO methanation process for renewable electricity storage. *Energy* 2014;75:81–8. <https://doi.org/10.1016/j.energy.2014.05.115>.
- [54] Butterman HC, Castaldi MJ. Influence of CO₂ Injection on Biomass Gasification. *Ind Eng Chem Res* 2007;46:8875–86. <https://doi.org/10.1021/ie071160n>.

- [55] Reddy GK, Boolchand P, Smirniotis PG. Unexpected Behavior of Copper in Modified Ferrites during High Temperature WGS Reaction—Aspects of $\text{Fe}^{3+} \leftrightarrow \text{Fe}^{2+}$ Redox Chemistry from Mössbauer and XPS Studies. *J Phys Chem C* 2012;116:11019–31. <https://doi.org/10.1021/jp301090d>.
- [56] Reddy GK, Gunasekara K, Boolchand P, Smirniotis PG. Cr- and Ce-Doped Ferrite Catalysts for the High Temperature Water–Gas Shift Reaction: TPR and Mossbauer Spectroscopic Study. *J Phys Chem C* 2011;115:920–30. <https://doi.org/10.1021/jp102959p>.
- [57] Si R, Raitano J, Yi N, Zhang L, Chan S-W, Flytzani-Stephanopoulos M. Structure sensitivity of the low-temperature water-gas shift reaction on Cu–CeO₂ catalysts. *Catalysis Today* 2012;180:68–80. <https://doi.org/10.1016/j.cattod.2011.09.008>.
- [58] Gokhale AA, Dumesic JA, Mavrikakis M. On the Mechanism of Low-Temperature Water Gas Shift Reaction on Copper. *J Am Chem Soc* 2008;130:1402–14. <https://doi.org/10.1021/ja0768237>.
- [59] Burch R. Gold catalysts for pure hydrogen production in the water–gas shift reaction: activity, structure and reaction mechanism. *Physical Chemistry Chemical Physics* 2006;8:5483–500. <https://doi.org/10.1039/B607837K>.
- [60] Dou X, Veksha A, Chan WP, Oh W-D, Liang YN, Teoh F, et al. Poisoning effects of H₂S and HCl on the naphthalene steam reforming and water-gas shift activities of Ni and Fe catalysts. *Fuel* 2019;241:1008–18. <https://doi.org/10.1016/j.fuel.2018.12.119>.
- [61] Pati RK, Lee IC, Hou S, Akhuermonkhan O, Gaskell KJ, Wang Q, et al. Flame Synthesis of Nanosized Cu–Ce–O, Ni–Ce–O, and Fe–Ce–O Catalysts for the Water-Gas Shift (WGS) Reaction. *ACS Appl Mater Interfaces* 2009;1:2624–35. <https://doi.org/10.1021/am900533p>.
- [62] Namiki T, Yamashita S, Tominaga H, Nagai M. Dissociation of CO and H₂O during water–gas shift reaction on carburized Mo/Al₂O₃ catalyst. *Applied Catalysis A: General* 2011;398:155–60. <https://doi.org/10.1016/j.apcata.2011.03.029>.
- [63] Kundakovic Lj, Mullins DR, Overbury SH. Adsorption and reaction of H₂O and CO on oxidized and reduced Rh/CeO_x(111) surfaces. *Surface Science* 2000;457:51–62. [https://doi.org/10.1016/S0039-6028\(00\)00332-0](https://doi.org/10.1016/S0039-6028(00)00332-0).
- [64] Tomczyk A, Sokołowska Z, Boguta P. Biochar physicochemical properties: pyrolysis temperature and feedstock kind effects. *Rev Environ Sci Biotechnol* 2020;19:191–215. <https://doi.org/10.1007/s11157-020-09523-3>.
- [65] Akhil D, Lakshmi D, Kartik A, Vo D-VN, Arun J, Gopinath KP. Production, characterization, activation and environmental applications of engineered biochar: a review. *Environ Chem Lett* 2021;19:2261–97. <https://doi.org/10.1007/s10311-020-01167-7>.
- [66] Béguerie T, Weiss-Hortala E, Nzihou A. Calcium as an innovative and effective catalyst for the synthesis of graphene-like materials from cellulose. *Sci Rep* 2022;12:21492. <https://doi.org/10.1038/s41598-022-25943-3>.
- [67] Ghogia AC, Romero Millán LM, White CE, Nzihou A. Synthesis and Growth of Green Graphene from Biochar Revealed by Magnetic Properties of Iron Catalyst. *ChemSusChem* 2023;16:e202201864. <https://doi.org/10.1002/cssc.202201864>.
- [68] Shrestha P, Chun DD, Kang K, Simson AE, Klinghoffer NB. Role of Metals in Biochar Production and Utilization in Catalytic Applications: A Review. *Waste Biomass Valor* 2022;13:797–822. <https://doi.org/10.1007/s12649-021-01519-6>.
- [69] Iriarte-Velasco U, Sierra I, Gutiérrez-Ortiz MA, Ayastuy JL. Bioapatite derived from animal bones as support for environmentally concerned catalysts: WGS with suppressed methanation activity. *Journal of Environmental Chemical Engineering* 2023;11:110677. <https://doi.org/10.1016/j.jece.2023.110677>.
- [70] Arzamendi G, Diéguez PM, Montes M, Odriozola JA, Sousa-Aguiar EF, Gandía LM. Methane steam reforming in a microchannel reactor for GTL intensification: A computational fluid dynamics simulation study. *Chemical Engineering Journal* 2009;154:168–73. <https://doi.org/10.1016/j.cej.2009.01.035>.
- [71] Sheu W-J, Chu C-S, Chen Y-C. The operation types and operation window for high-purity hydrogen production for the sorption enhanced steam methane reforming in a fixed-bed reactor.

International Journal of Hydrogen Energy 2022;47:37192–203.
<https://doi.org/10.1016/j.ijhydene.2021.11.112>.

[72] Abbas SZ, Dupont V, Mahmud T. Kinetics study and modelling of steam methane reforming process over a NiO/Al₂O₃ catalyst in an adiabatic packed bed reactor. International Journal of Hydrogen Energy 2017;42:2889–903. <https://doi.org/10.1016/j.ijhydene.2016.11.093>.

[73] Chen Y, Zhang X, Chen W, Yang H, Chen H. The structure evolution of biochar from biomass pyrolysis and its correlation with gas pollutant adsorption performance. Bioresource Technology 2017;246:101–9. <https://doi.org/10.1016/j.biortech.2017.08.138>.

General conclusion

The Paris Agreement, signed in 2015 by 195 nations, aims to limit global warming to 2°C and decrease greenhouse gas emissions, primarily carbon dioxide and methane. Nitrous oxide, a minor greenhouse gas, contributes to environmental issues and is responsible with nitrogen oxides for health-related problems. Hydrogen, produced through carbon-neutral thermal processes like biogas reforming, may also help reduce GHG emissions. These processes however requiring catalysts that are currently expensive and environmentally and sanitarly damaging. This work therefore aims at producing biocarbon catalysts from bioresources that contain metals with a catalytic capacity for three reactions: water-gas shift, reverse water-gas shift and direct decomposition of nitrogen oxides (WGS, RWGS and deNO_x respectively). The catalysts can be produced by thermal treatment that could enhance catalytic properties.

Fern and willow were selected as feedstocks for the biocarbon catalysts. They were impregnated before and after pyrolysis through wetness impregnation of iron and nickel nitrates. Optimal conditions for heating rate and pyrolysis operating temperature were determined through literature, thermogravimetric analysis and thermodynamic simulations. Both unimpregnated and impregnated biomass were pyrolyzed and the resulting biocarbon were tested for reverse and direct water-gas shift and direct decomposition of nitrogen oxides. Optimal preheating temperature for water-gas shift was simulated. The biocarbon catalysts were characterized in terms of organic element content (CHNS analysis), inorganic element content (ICP-AES) and its dispersion on the carbonaceous matrix (SEM, TEM), thermal stability (TGA-DSC), specific surface area (BET, N₂), textural properties and surface chemical functions (TPD, TPR, TPO, XRD). The changes in the structure of the biocarbon catalyst were analyzed before and after the chemical reaction to determine the influence of these properties of the reactions. Two set-ups, for deNO_x and for WGS/RWGS, were respectively completely developed and assembled during this PhD thesis, in addition to being optimized through on-line gas analysis.

Fern and willow catalysts impregnated before pyrolysis were tested for deNO_x. NO was decomposed by these catalysts and better removal was observed as temperature was increased from 200 to 500°C. The removal ratio, a criterion defined by observing the removal of NO, reached 31% in presence of Ni-impregnated willow biocarbon at 500°C and in presence of Fe-impregnated willow biocarbon at 200°C. This NO reduction may be facilitated by the presence of reductive and basic functions that enhance NO adsorbability and reactivity in coordination with high specific surface area that allow further dispersion of active sites. High amounts of metal impregnated may decrease the performances of the

catalysts due to pore blocking. A production of N_2 and O_2 was detected, as well as CO and CO_2 that may result from the degradation of the biocarbon catalysts and could lead to selective reduction of NO . Mass loss was indeed reported, but it was not correlated to deactivation as the removal ratio was maintained for the duration of the experiment.

The produced biocarbon catalysts were tested in RWGS at $400^\circ C$ with a ratio H_2/CO_2 of 3 and compared to rust and Fe-doped alumina. This resulted in highly stable conversion (little deactivation over 72h) with high selectivity towards CO ($>84\%$) on behalf of the biocarbon whereas rust was more active with conversion reaching equilibrium ($30<35\%$) in less than 24h followed by deactivation due to carbon fouling. Fern biocarbon were reported to impact more RWGS than willow biocarbon. This was attributed to higher inorganic content especially K, Mg and Ca that have known promotion effects on catalysts and may diminish energy limitations for the adsorption and transformation of reactive gases. This complements the high CO_2 adsorptive properties of the biocarbon as this can enhance adsorption of CO_2 and facilitate its reaction, due to electron transfer, with proximate reactive sites. The best performing biocarbon was tested for long-term stability (288h) and little deactivation was observed with a slight increase in conversion. This contrasts with rust and reported catalysts that are more active for RWGS but cannot sustain this activity for long periods. The highest time over stream reported was at most 120h, and rust did not last more than 24h in our conditions. Similarly, the impact of prereduction on the best performing reducible biocarbon catalyst was assessed and had a negative impact on reactivity related to increase in particle size and loss of active sites during reduction.

Fern-based biocarbon catalysts were tested in WGS. Operating conditions were modified approximately every 1h30 with $20^\circ C$ increases in temperature from $180^\circ C$ and S/C was adjusted to 5.5, 1.4, 2.8, 20.7 with a resulting GHSV of 30744, 21686, 24705, 63959 h^{-1} respectively. WGS was simulated by process software Aspen Plus with representation of thermodynamic and kinetic phenomena. It was determined that the reaction was kinetically driven by comparison of experimental results with simulated results and literature, and Ni-catalysts were more performant than their Fe counterparts namely rust. The presence of other inherent metals in the biocarbon catalysts such as K allowed activity by promoting electronic properties and the facilitated reducibility of Ni catalysts allowed them to be the most active. Therefore, more energy could be provided to react with steam and carbon monoxide, who were additionally adsorbed and activated by the high quantity of O deficient sites provided by reduction of the functional groups of biocarbon. The combination of these biocarbon catalytic properties resulted in their higher activity and selectivity compared to rust (least active and reference catalyst). All catalysts were highly selective of CO ($>95\%$). Variation of temperature allowed the determination of kinetic constants through Arrhenius law equation and no explicit order was determined implying influence of other properties on kinetics. Despite this, they are coherent with

values reported in the literature, where the activation energy varies from 0.5 to 186 kJ/mol and the kinetic constant figures between 1.9×10^{-9} and 4.3×10^{12} .

Biocarbon from phytoremediation plants combine and group extremely interesting properties for catalysis. The presence of inherent metals influences the catalytic metals by providing sites that further the adsorption of reactive gases and could facilitate the dispersion of electrons due to difference in charge, resulting in improved activation of these gases. This is further amplified as the biocarbon can develop high specific surface area that disperses active sites and basic, acidic and oxygen functions that once reduced are a source of active sites that also help adsorb and transform the reactants. These properties make heavy metal-loaded biocarbon an effective biocarbon catalyst in deNO_x, RWGS and WGS. Biocarbon catalysts show potential as substitutes for commercial catalysts. Indeed, their production and use are directly inscribed in a circular economy approach due to the reuse of biocarbon and metals as catalysts. That is the reason why they would require further studies to improve this potential. Once perfected, this could be a means of limiting and even reducing the environmental and health problems that are raised by extraction of commercial catalysts as well as greenhouse gas emissions.

Perspectives

As mentioned, biocarbon catalysts and the processes in which they were involved require further studies to further adjust the properties of these catalysts towards its given application, and to improve the understanding of how they behave during these processes.

Future studies could observe more in depth the catalytic impact of a selected property on a selected reaction. For instance, the presence of inherent metals was able to improve RWGS and WGS. Therefore, testing biocarbon with high inherent ash content and without metal-loading could be a means of identifying the exact nature of the metals that impact these reactions (K, Ca, Mg, Fe, Ni) and the type of biomass that should be searched for catalytic applications. In the case of deNO_x, the specific surface area and high gas adsorption properties allowed better performance of the biocarbon catalyst. While studying varying bioresources, looking at these properties could allow identification of interesting resource types for this process. Additionally, the carbon structure behavior may vary depending of the presence of metals, inherent or incorporated. Coupled with life cycle analyses, it may be possible to identify the most interesting bioresources in terms of environmental and financial impact and with activity in reaction identify the most environmentally friendly and cost-effective catalyst. This has already begun as newer catalysts, such as algae and mine residues, are starting to be tested in both set-ups that were finalized during the thesis.

Given the complex nature of bioresources, attributing improvement of the processes to only one characteristic might deter from other equally interesting properties. Ergo, further characterizations are needed, such as FTIR that could provide additional information on the surface functions in conjunction with gas desorption during TPD, Raman for more information concerning the nature of the bonds between metal and biocarbon surface or OSC and XPS measurements that could provide more insights on oxygen vacancies and their nature. This includes in situ techniques (ex. DRIFTS) that could allow determination of the mechanistic phenomenon that occur during the process and observe real time degradation or deactivation of the catalysts. Once determined, it may be possible to isolate the characteristics that constitute good catalytic properties and seek these in future biocarbon catalysts.

Currently, the biocarbon catalysts are stable at 500°C, limiting possible use for high temperature reactions such as reforming of CH₄. To stabilize them, many axes could be considering such as post-treatment activation using a none O₂ oxidizing gas (H₂O, CO₂, ...) or modifying the conditions of production of the biocarbon (graphitization, gasification, ...). This would allow for a little degradable

catalyst but could be source of potential deactivation in case of sintering or carbon fouling. Studies could therefore test progressively the change in production conditions of an identified active catalyst and observe how the modifications affect activity. Once high temperature stability is established, studies could research the regenerability of the biocarbon catalysts. In absence of high temperature stability, it is also possible to study lower temperatures processes such as FTS or CAMERE. In a factory approach, it is also possible to identify the most performant catalysts for a given application and then integrate these applications together to achieve a common objective, such as improving and purifying biosourced H₂ production.

Finally, some model-based studies such as DFT focus on the interaction between metals or metal and support, how they react with gases and how they affect these reactions, as well as the hydrodynamic to better understand the flow regime of the reactor. Additionally, iso-selectivity or -conversion experiments could be performed to isolate the intrinsic influences of the catalysts on the reactions. New studies could go more in depth about the electronic state of metals on biocarbon, especially during the reaction. This is the case with reactions with in-situ techniques such as XANES, EXAFS and DRIFTS.

Appendix A

Non-retained biocarbon: preparation and characteristics

A.1. Operating conditions, description and initial choice

The different impregnation as well as their conditions are reminded in the following tables (Table A.1-3). The biomass that were impregnated before pyrolysis are mentioned along with the impregnation conditions and the content in the impregnation metal after pyrolysis (Table A.1). This is followed by the conditions and metal content of biocarbon (BC) impregnated after pyrolysis (Table A.2). The last table contains information about mass loss of impregnated biomass during pyrolysis with relative standard deviation (RSD) (Table A.3). An objective of 3 wt% of metal in biocarbon was selected to imitate phytoremediation conditions [1].

To decide the concentrations necessary for the 1st batches, conditions are derived from preestablished protocols [2,3]. Fern was impregnated first then willow was impregnated based on the results obtained for fern. To initially impregnate biomass, in Said's thesis, it was found for 1 wt% Ni in solution, there was 0.36 mol of Ni per kg of willow. For 3 wt%, this was 0.95 mol/kg. This content was then converted, 2.11 wt% of Ni in biomass was obtained for 1wt% Ni in solution, 5.58 wt% for 3 wt% in solution. Using a linear regression between these 2 values, for an objective of 3 wt% of Ni in biomass, 1.5 wt% of Ni in solution was required. This same percentage was used for iron. 750 mL then 1 L of distilled water were used for these impregnations. To first impregnate biocarbon, calculations based on insipient wetness impregnation was used: wettable volume of biocarbon was determined by adding drops of water on a known mass of biocarbon until water was no longer adsorbed. The difference in mass divided by density of water is then equal to the wettable volume. To reach an objective of 3 wt% in biocarbon, the mass of metal nitrate (powder) to add was determined considering that metal content in the biocarbon remained the same because the effect of leaching is limited (Eq.A.1). From this, a concentration of powder in the solution was deduced by dividing this mass by the wettable volume. Wetness impregnation was then realized in this same concentration and at first for 3h. At first, 100 mL of distilled water was used for these impregnations due to limited quantities of biocarbon, this was then increased while conserving the concentration of biocarbon and nitrate in water. Solubility was not an issue due to the high solubility of nitrates in water.

$$3 \text{ wt\% of metal in biocarbon} = \frac{m_{\text{powder added}} \times \text{wt\%}_{\text{metal in powder}} + m_{\text{metal in biocarbon}}}{m_{\text{initial of biocarbon}} + m_{\text{powder added}}} \quad \text{Eq.A.1}$$

Once the first batches were complete and characterized, the following impregnations were then optimized following time of contact and quantities of sample and metal nitrate in solution. The samples which were chosen for deNO_x, RWGS and WGS reactions are in bold writing.

Table A.1. Impregnation of fern and willow before pyrolysis, conditions and content after pyrolysis

Impregnated BC (before pyrolysis)	Abbreviation	Impregnation conditions Powder = nitrate	Metal content (wt%, BC)
Fern BC impregnated with Ni before pyrolysis #1	FNi*	2 days stirring, 38.884+19.738g powder and 51.984g biomass (BM) for 500+250mL distilled water	37.96
Fern BC impregnated with Ni before pyrolysis #2	FNi-B2	3 days stirring, 20.873g powder and 21.329g BM for 1L distilled water	20.51
Fern BC impregnated with Ni before pyrolysis #3	FNi-B	3 days stirring, 9.838g powder and 21.790g BM for 1L distilled water	3.96
Fern BC impregnated with Ni before pyrolysis #4	FNi-B4	3 days stirring, 4.757g powder and 21.830g BM for 1L distilled water	3.84
Fern BC impregnated with Fe before pyrolysis #1	FFe*	3 days stirring, 55.446g powder and 21.942g BM for 500mL distilled water	64.17
Fern BC impregnated with Fe before pyrolysis #2	FFe-B	3 days stirring, 25.669g powder and 21.666g BM for 1L distilled water	13.17
Fern BC impregnated with Fe & Ni before pyrolysis #1	FNiFe-B1	3 days stirring, 28.360g (Fe) & 21.615g (Ni) powder respectively and 21.865g BM for 500mL distilled water	19.34 & 17.81
Fern BC impregnated with Fe & Ni before pyrolysis #2	FNiFe	3 days stirring, 12.748g & 10.404g powder respectively and 21.373g BM for 1L distilled water	10.30 & 8.08
Willow BC impregnated with Ni before pyrolysis #1	WNi-B	3 days stirring, 4.397g powder and 21.626g BM for 1L distilled water	2.41
Willow BC impregnated with Fe before pyrolysis #1	WFe-B	3 days stirring, 4.112g powder and 20.378g BM for 1L distilled water	4.64
Willow BC impregnated with Fe & Ni before pyrolysis #1	WNiFe-B1	3 days stirring, 3.346g & 4.342g powder respectively and 21.276g BM for 1L distilled water	2.97 & 3.00
Willow BC impregnated with Fe & Ni before pyrolysis #2	WNiFe-B2	3 days stirring, 6.674g & 8.552g powder respectively and 21.891g BM for 1L distilled water	-

Table A.2. Impregnation of fern and willow after pyrolysis, conditions and content from BC

Impregnated BC (after pyrolysis)	Abbreviation	Impregnation conditions Powder = nitrate	Metal content (wt%, BC)
Fern BC impregnated with Ni after pyrolysis #1	FNi-A1	3h stirring, 9.107g powder and 1.998g biocarbon (BC) for 100mL distilled water	0.35
Fern BC impregnated with Ni after pyrolysis #2	FNi-A2	6 days stirring, 3.067g powder and 2.005g BC for 100mL distilled water	6.64
Fern BC impregnated with Ni after pyrolysis #3	FNi-A	7 days stirring, 1.340g powder and 2.004g BC for 100mL distilled water Then 7 days stirring, 8.043g powder and 12.031g BC for 600mL distilled water	1.43
Fern BC impregnated with Ni after pyrolysis #4	FNi-A4	10 days stirring, 0.666g powder and 2.036g BC for 100mL distilled water	2.94
Fern BC impregnated with Fe after pyrolysis #1	FFe-A1	3h stirring, 13.466g powder and 1.990g BC for 100mL distilled water	0.64
Fern BC impregnated with Fe after pyrolysis #2	FFe-A	13 days stirring, 13.469g powder and 1.986g BC for 100mL distilled water	0.51
Fern BC impregnated with Fe after pyrolysis #3	FFe-A3	3 days stirring, 4.436g powder and 2.004g BC for 100mL distilled water	0.59
Fern BC impregnated with Fe after pyrolysis #4	FFe-A4	7 days stirring, 4.422g powder and 1.996g BC for 100mL distilled water	0.31
Fern BC impregnated with Fe after pyrolysis #5	FFe-A5	10 days stirring, 4.423g powder and 2.012g BC for 100mL distilled water	0.25
Fern BC impregnated with Fe & Ni after pyrolysis #1	FNiFe-A	3h stirring, 6.685g (Fe) & 4.583g (Ni) powder respectively and 1.997g BC for 100mL distilled water	0.76 & 0.36
Fern BC impregnated with Fe & Ni after pyrolysis #2	FNiFe-A2	7 days stirring, 4.770g & 1.665g powder respectively 2.010g BC for 100mL distilled water	0.31 & 0.02
Willow BC impregnated with Ni after pyrolysis #1	WNi-A	10 days stirring, 1.311g powder and 2.016g BC for 100mL distilled water	1.81
Willow BC impregnated with Fe after pyrolysis #1	WFe-A1	3 days stirring, 4.435g powder and 2.003g BC for 100mL distilled water	0.06
Willow BC impregnated with Fe after pyrolysis #2	WFe-A	10 days stirring, 4.812g powder and 5.003g BC for 250mL distilled water	0.23
Willow BC impregnated with Fe & Ni after pyrolysis #1	WNiFe-A1	10j, 2.102g & 1.355g powder respectively and 2.050g BC for 100mL distilled water	0.51 & 0.06

Table A.3. Mass loss after pyrolysis of the aforementioned impregnated biomass

BC	Mass loss	
	Average (wt%)	RSD (%)
FNi*	72.0	0.8
FNi-B2	66.4	0.8
FNi-B	66.7	1.7
FNi-B4	68.0	2.1
FFe*	69.7	0.3
FFe-B	67.0	1.5
FNiFe-B1	66.7	6.2
FNiFe	67.4	0.2
WNi-B	71.2	2.2
WFe-B	72.1	6.4
WNiFe-B1	72.1	-
WNiFe-B2	-	-

A.2. Conclusion

The selected biocarbon catalysts are presented in bold. The tables represent the different steps which created the catalysts used in this thesis. This optimization of operating conditions attests the difficulty to impregnate biocarbon versus biomass, biocarbon requiring on average 10 days compared to 3 and 3 times the quantity of metal nitrate in solution.

References

- [1] A global database for plants that hyperaccumulate metal and metalloid trace elements - Reeves - 2018 - New Phytologist - Wiley Online Library n.d. <https://nph.onlinelibrary.wiley.com/doi/full/10.1111/nph.14907> (accessed October 26, 2020).
- [2] M. Said, Comportements et rôles des métaux lourds au cours de la pyro-gazéification de la biomasse : études expérimentales et thermodynamiques, phdthesis, Ecole des Mines d'Albi-Carmaux, 2016. <https://tel.archives-ouvertes.fr/tel-01541337> (accessed June 9, 2021).
- [3] R. Munirathinam, D. Pham Minh, A. Nzihou, Effect of the Support and Its Surface Modifications in Cobalt-Based Fischer–Tropsch Synthesis, *Ind. Eng. Chem. Res.* 57 (2018) 16137–16161. <https://doi.org/10.1021/acs.iecr.8b03850>.

List of figures

Fig. I.1. Different types of thermochemical conversion [4].....	21
Fig. I.2. Pyrogasification steps [6].....	22
Fig. I.3. Wordmap by VOSviewer of 100 most used terms related to WGS catalysts from 1649 articles from ScienceDirect since 2022, focus on the catalytic cluster.....	24
Fig. I.4. Wordmap by VOSviewer of 100 most used terms related to deNO _x catalysts from 1197 articles from ScienceDirect since 2022, focus on the catalytic cluster.....	26
Fig. I.5. Macromolecules composing lignocellulosic biomass [25].....	27
Fig. 1.1. 10 mm fern on the left, 6 mm willow on the right.....	34
Fig. 1.2. Speciation of Fe, Ni and Cu at thermodynamic equilibrium depending on temperature and gaseous atmosphere of pyrolysis of fern simulated using FactSage.....	36
Fig. 1.3. TGA of willow biomass under N ₂ with increase from 30 to 1000°C at 2, 5 and 10°C/min.....	36
Fig. 1.4. Oven providing heat and N ₂ for biocarbon production on the left, diagram of the setup on the right.....	37
Fig. 1.5. Decreasing distribution of particle size of milled unimpregnated biocarbon.....	39
Fig. 1.6. Remaining solid mass by TGA of aforementioned biocarbon to observe 24h stability under N ₂	39
Fig. 1.7. Example of N ₂ adsorption-desorption isotherm of one of the applied biocarbon.....	47
Fig. 1.8. TPD and TPO program.....	49
Fig. 1.9. TPR program.....	49
Fig. 1.10. Scheme and picture of the setup for deNO _x experiments, 1 st campaign.....	53
Fig. 1.11. Picture of the different components of the NO _x analyzer.....	54
Fig. 1.12. Scheme and picture of the setup for deNO _x experiments, 2 nd campaign.....	56
Fig. 1.13. New and optimized program for deNO _x	56
Fig. 1.14. Scheme and picture of the setup for RWGS and WGS experiments, 1 st campaign.....	58
Fig. 1.15. Scheme and picture of the setup for RWGS and WGS experiments, 2 nd campaign.....	60
Fig. 2.1. Experiment set-up for testing deNO _x performance of biocarbon catalysts.....	74
Fig. 2.2. Temperature program of the oven during one standard experiment.....	75
Fig. 2.3. SEM imagery of different biocarbon catalysts (RW, FNi and WNi biocarbon).....	79
Fig. 2.4. SEM imagery of FNi biocarbon showing encapsulation of metals.....	79
Fig. 2.5. NO removal ratio X _{NO} of different biocarbon catalysts (RF, FNi, FFe, RW, WNi, WFe) under 1021 ppm NO/Ar.....	80
Fig. 2.6. X _{NO} of fern biocarbon at 500°C.....	82
Fig. 2.7. X _{NO} of fern-based biocarbon catalyst impregnated with higher Fe content and used in deNO _x at 200 and 500°C (left), and impregnated with higher Ni content and used in deNO _x at 500°C (right).....	82
Fig. 2.8. NO concentration curves of selected biocarbon catalysts (WNi, WFe, FNi and blank test) during 500°C deNO _x experiments for extended time (4h), under 1021 ppm NO/Ar.....	83
Fig. 2.9. Normalized N ₂ concentration of different biocarbon catalysts (RF, FNi, FFe, RW, WNi, WFe), under 1021 ppm NO/Ar.....	84
Fig. 2.10. CO ₂ concentration of different biocarbon catalysts (RF, FNi, FFe, RW, WNi, WFe), blank area: Ar; shadow area: 1021 ppm NO/Ar.....	85
Fig. 2.11. CO concentration of different biocarbon catalysts during 500°C deNO _x experiments (a: fern biocarbon; b: willow biocarbon), blank area: Ar; shadow area: 1021 ppm NO/Ar.....	86

Fig. 2.12. H ₂ concentration of different biocarbon catalysts during 350 and 500°C deNO _x experiments (a: fern biocarbon at 350°C; b: willow biocarbon at 350°C; c: fern biocarbon at 500°C; d: willow biocarbon at 500°C), blank area: Ar; shadow area: 1021 ppm NO/Ar	86
Fig. 2.13. Graphical representation of deNO _x mechanism	87
Fig. 3.1. Set-up for the Reverse Water-Gas Shift (RWGS) experiments	110
Fig. 3.2. Selectivity in CO (top) and conversion of CO ₂ (bottom) of fern biocarbon catalysts tested in RWGS at 400°C	112
Fig. 3.3. Selectivity in CO (top) and conversion of CO ₂ (bottom) of willow biocarbon catalysts tested in RWGS at 400°C	112
Fig. 3.4. HRTEM images of unimpregnated fern biocarbon (RF) before its use in RWGS	115
Fig. 3.5. XRD diffractogram of unimpregnated fern biocarbon (RF) not spent and spent by RWGS (and Al ₂ O ₃)	116
Fig. 3.6. HRTEM images of fern biocarbon impregnated with Ni after pyrolysis (FNI-A) before its use in RWGS	116
Fig. 3.7. HRTEM images of fern biocarbon impregnated with Fe before pyrolysis (FFe-B) before its use in RWGS	117
Fig. 3.8. CO ₂ desorbed while increasing temperature of FNI-Fe before RWGS (left) and after RWGS (right)	121
Fig. 3.9. XRD diffractogram of FFe-B not spent and spent by RWGS (and Al ₂ O ₃)	121
Fig. 3.10. HRTEM images of alumina after RWGS with RF, loss of metals on alumina	122
Fig. 3.11. Selectivity in CO (top) and conversion of CO ₂ (bottom) of reference and biocarbon catalysts tested in RWGS at 400°C, with test of the effects of the duration and the reduction on the biocarbon catalysts	122
Fig. 3.12. XRD diffractogram of rust not spent and spent by RWGS (and Al ₂ O ₃)	123
Fig. 3.13. HRTEM images of rust after RWGS	123
Fig. 3.14. XRD diffractogram of FNI-A not spent and spent by RWGS (and Al ₂ O ₃)	124
Fig. 3.15. HRTEM images of fern biocarbon impregnated with Fe before pyrolysis (FFe-B) after RWGS	125
Fig. 4.1. Set-up for the Water-Gas Shift (WGS) experiments	148
Fig. 4.2. Aspen Plus flowsheet for simulation of pre-heating temperature	151
Fig. 4.3. Impact of pre-heating temperature and pressure on vaporization rate before entering reactor	151
Fig. 4.4. Addition of WGS reactors to preheating flowsheet	152
Fig. 4.5. Impact of variation in S/C on CO conversion in plug flow reactor (no effect from T)	153
Fig. 4.6. Impact of variation in S/C on outlet gas composition in plug flow reactor (no effect from T)	154
Fig. 4.7. Impact of variation in S/C and T on CO conversion in Gibbs reactor	155
Fig. 4.8. Impact of variation in S/C and T on CO ₂ selectivity in Gibbs reactor	155
Fig. 4.9. Evolution in time of CO ₂ production by catalyzed WGS, T and S/C varied but not represented	156

List of tables

Table I.1. Product distribution for different types of thermochemical conversion [5].....	22
Table I.2. Examples of reactions that can occur during pyrogasification [8]	23
Table I.3. Inorganic species and their role (inhibition or catalysis) in pyrogasification and RWGS, presented in Chapter 3.....	25
Table I.4. Product distribution from fast pyrolysis (>100°C/min) depending on lignocellulosic material [7]	27
Table I.5. Metal thresholds for hyperaccumulation in plants [40].....	28
Table 1.1. Unimpregnated biocarbon, names, pyrolysis conditions and mass loss.....	37
Table 1.2. Impregnated biocarbon, names, impregnation conditions.....	38
Table 1.3. Mass losses of biocarbon due to increase to 500°C and 24-h isotherm	40
Table 1.4. Organic content (wt%) of biocarbon catalysts	41
Table 1.5. Inorganic content (µg/g) of biocarbon employed as catalysts	42
Table 1.6. MC and AC of biocarbon catalysts.....	43
Table 1.7. Different TGA-DSC programs used in this work	45
Table 1.8. Temperature and energy of desorption of possible adsorbed molecules due to applications	46
Table 1.9. Desorption temperatures and gases associated to functional groups from literature [11,27–30].....	50
Table 2.1. Steady state deNO _x ratio (X_{NO}) of different biocarbon catalysts, from a preliminary study .	72
Table 2.2. Mass of biomass and metal nitrates used for impregnation	73
Table 2.3. CHNS elemental composition of biocarbon catalysts characterized before and after 500°C deNO _x experiments	76
Table 2.4. Inorganic composition of biocarbon catalysts before deNO _x experiments.....	77
Table 2.5. Surface chemical groups and specific surface area of biocarbon catalysts before deNO _x	78
Table 2.6. Steady state X_{NO} (averaging from t = 75 to 90 min)	80
Table 2.7. Mass loss of biocarbon catalysts after standard deNO _x experiments (1h)	83
Table 3.1. Inorganic species and their role (inhibition or catalysis) in pyrogasification and RWGS ...	107
Table 3.2. Biocarbon catalysts, names, impregnation conditions and metal content in biocarbon...	109
Table 3.3. Summary of averaged concentrations, selectivity and conversion for the trialed catalysts	113
Table 3.4. Inorganic composition (µg/g biocarbon) of willow and fern biocarbon catalysts before RWGS	114
Table 3.5. Chemical surface groups versus specific surface area of the biocarbon catalysts, before RWGS.....	119
Table 3.6. Desorption temperatures and gases associated to functional groups from literature [43,119,127–129]	120
Table 4.1. Inorganic species and their role (inhibition or catalysis) in pyrogasification and RWGS, from Chapter 3	138

Table 4.2. Expression of reaction rates ($\text{mol g}^{-1} \text{s}^{-1}$) for WGS with associated parameters and references	139
Table 4.3. Summary of the influence and impact of operating conditions on WGS.....	146
Table 4.4. Biocarbon catalysts, names, impregnation conditions and metal content in biocarbon...	147
Table 4.5. Set of parameters to kinetically simulate WGS process [25,45,47-51]	153
Table 4.6. Impact of reactor temperature on peak production of CO_2 (vol%) of biocarbon catalyst and rust	157
Table 4.7. First H_2 peak from the TPR of the best biocarbon catalysts to determine their reducibility	158
Table 4.8. Chemical surface groups versus specific surface area of the biocarbon catalysts before WGS	158
Table 4.9. Impact of reactor temperature on CO conversion of biocarbon catalyst and rust	159
Table 4.10. Impact of reactor temperature on CO_2 selectivity of biocarbon catalyst and rust	159
Table 4.11. Impact of steam excess on peak production of CO_2 , CO conversion and CO_2 selectivity of biocarbon catalyst	160
Table 4.12. Summary of averaged values of concentrations, selectivity and conversion for all trialed catalysts.....	161
Table 4.13. Estimated kinetic parameters for biocarbon catalysts and rust in pre-established decreasing order of performance.....	162
Table 4.14. Synthesis of the comparison between the obtained results for WGS simulation and experiments.....	164
Table A.1. Impregnation of fern and willow before pyrolysis, conditions and content after pyrolysis	177
Table A.2. Impregnation of fern and willow after pyrolysis, conditions and content from BC.....	178
Table A.3. Mass loss after pyrolysis of the aforementioned impregnated biomass	179

Production de catalyseurs biosourcés pour élimination de NO_x, WGS et RWGS

Ce travail propose une approche innovante pour la production, caractérisation et utilisation de catalyseurs biosourcés pour des applications dans les domaines de l'énergie et de l'environnement, afin de réduire le coût et l'impact des catalyseurs commerciaux actuellement utilisés. Le travail développé ici promeut une approche d'économie circulaire dans la mesure où des plantes issues de la phytoremédiation ont été employées pour la production de catalyseurs biosourcés, respectueux de l'environnement. Ces catalyseurs ont été utilisés pour produire des vecteurs énergétiques tels que l'hydrogène à partir des réactions de gaz à l'eau direct (water-gas shift, WGS) et indirect (reverse water-gas shift, RWGS), et pour la décomposition des polluants de NO_x (deNO_x). Les catalyseurs biosourcés ont été produits à partir de saule et fougère avec un contenu contrôlé en métaux introduit par imprégnation avant ou après pyrolyse à 800°C afin d'imiter l'hyperaccumulation (>3 g métal /kg biocarbone) dans un support carboné poreux. Les catalyseurs ainsi produits ont été testés pour les réactions de deNO_x, ainsi que dans WGS et RWGS, et les dispositifs expérimentaux associés ont été développés et optimisés pendant la thèse. Ils ont été caractérisés en termes de composition, structure et stabilité thermique, ceci avant et après utilisation. Pour les trois réactions, les catalyseurs ont montré une sélectivité et une conversion élevées et maintenues dans les conditions de réaction, facilitées par le contenu en métaux catalytiques dont l'activité a été renforcée par les métaux inhérents. La présence de fonctions oxygénées de surface et d'une surface spécifique élevée (<419 m²/g) ont amélioré l'adsorption et la dissociation des gaz réactifs grâce à des sites supplémentaires formés par réduction et à une meilleure activité électronique. Avec ces caractéristiques, les catalyseurs biosourcés ont montré des performances meilleures que celles de catalyseurs références de la littérature en raison d'une meilleure stabilité ou activité catalytiques (conversion maintenue pour plus de 120h, énergie d'activation entre 0.5 et 186 kJ/mol, constante cinétique entre 1.9×10^{-9} et 4.3×10^{12}). Le catalyseur de saule imprégné au Ni avant pyrolyse et le catalyseur bimétallique (Ni/Fe) de fougère ont montré les meilleures performances pour les réactions de deNO_x, et RWGS et WGS, respectivement.

Mots clés : Catalyseurs biosourcés, Nickel, Fer, Pyrolyse, Réaction de gaz à l'eau, Élimination d'oxydes d'azote

Production of biocarbon catalysts for NO_x decomposition, WGS and RWGS

This work proposes an innovative approach to the production, characterization and use of biocarbon catalysts for energy and environment-related applications, in order to reduce the cost and impact of the commercial catalysts currently in use. The work developed here promotes a circular economy approach in the way that plants from phytoremediation have been used for the production of eco-friendly biocarbon catalysts. They were used for the production of energy vectors such as hydrogen by direct and reverse water-gas shift reaction (WGS and RWGS respectively), as well as for the decomposition of NO_x pollutants (deNO_x). Biocarbon catalysts were produced from willow and fern with a controlled metal content introduced by wet impregnation before or after pyrolysis at 800°C to imitate hyperaccumulation (>3 g metal/kg biocarbon) in a porous carbon support. The resulting catalysts were tested in deNO_x, as well as WGS and RWGS reactions, and the associated experimental equipments were developed and optimized during this thesis work. They were characterized in terms of composition, structure and thermal stability, before and after use. For the three reactions, the catalysts showed high selectivity and conversion, facilitated by the catalytic metals whose activity was enhanced by the inherent metals. The presence of surface oxygen functions and a high specific surface area (<419 m²/g) improved adsorption and dissociation of reactive gases thanks to additional reactive sites formed by reduction and enhanced electronic activity. With these characteristics, biocarbon catalysts showed better performances than literature-based reference catalysts as they were either more stable or active (conversion maintained for more than 120h, activation energy from 0.5 to 186 kJ/mol, kinetic constant between 1.9×10^{-9} and 4.3×10^{12}). Willow biocarbon impregnated with Ni before pyrolysis and bimetallic (Ni/Fe) fern biocarbon showed the best performances for the deNO_x, and RWGS and WGS reactions, respectively.

Keywords: Biocarbon catalysts, Nickel, Iron, Pyrolysis, Water-Gas Shift, Nitrogen oxide decomposition